Development of new methods to study collisions of OH radicals with liquid surfaces

Robert Henry Bianchini

Submitted for the degree of Doctor of Philosophy

Heriot-Watt University

School of Engineering and Physical Sciences

August 2018

ABSTRACT

This thesis presents a new experimental method for studying the dynamics of collisions between the gas-phase radical OH (or OD for technical reasons) and an organic liquid surface acting as proxy for the surface of aerosol particles. This new experimental method consists of two configurations. The first introduces a molecular beam source of OD radicals, generated via an electric discharge, and probes them via conventional laser-induced fluorescence (LIF) measurements. This allows the user to set the angle of incidence and control the speed, and thus the collision energy, with which the radicals hit the liquid surface. The second arrangement is an extension of the first, in which OD is detected via planar-LIF. This allows images of OD fluorescence from the plane of detection to be acquired, thus providing information on the speed and angular distribution of the radicals scattered off the surfaces.

The collision-energy dependence of the inelastic scattering dynamics and survival probability of OD from the long-chain, saturated hydrocarbon, squalane ($C_{30}H_{62}$), and its partially unsaturated analogue, squalene ($C_{30}H_{62}$), was studied with the molecular beam set-up. The results were compared with scattering off a liquid perfluoropolyether (PFPE) used as an inert reference. The molecular-beam source allowed collision energies close to atmospheric conditions to be accessed, for the first time. The results provide the first direct evidence of OD uptake on squalene being negatively activated due to addition reactions of OD with the unsaturated sites. More surprisingly, the positively activated behaviour expected for squalane on the basis of analogous OH + alkane gas phase reactions was not observed, which is speculated to be the result of trapping-enhanced reactivity at lower collision energies.

The collision-energy and angle-of-incidence dependence of the scattering dynamics of OD off liquid surfaces was investigated using, for the first time in gas-liquid scattering experiments, the planar-LIF image acquisition approach. Preliminary findings show that OD scatters off all surfaces with an unexpectedly broad angular distribution. Nevertheless, the observed above-thermal speeds and hot rotational distributions of the scattered OD confirm that a substantial fraction of the scattering is directly impulsive at an incident translational energy of 30 kJ mol^{-1}. More subtle differences indicate that impulsively scattered radicals are still present, even at the lower collision energy of 7.5 kJ mol^{-1}.

ACKNOWLEDGMENTS

First and foremost, I'd like to thank my supervisor Prof. Kenneth McKendrick for introducing me to the world of gas-liquid interface scattering, and for the many detailed discussions we had on all aspects of the experiment, which have been of great help for understanding a wide range of related subjects. I am also equally grateful to Prof. Matthew Costen for his help and advice on lasers and many other practical aspects of the experiment.

Heartfelt thanks go to all past and present members of the McKendrick-Costen group for their help and support throughout these years, and especially Dr Maria Tesa-Serrate for her help on the experiment in the first year of my PhD, Dr Thomas Sharples for his invaluable advice on LabVIEW™ programming, and Dr Simon Purcell for his practical advice and help in the lab.

Special thanks go to Dr Stuart Greaves for providing us with the electric discharge device and his valuable advice on how to operate it, without which many of the experiments in this thesis would not have been possible. I'd also like to thank Dr Paul Lane and Erasmus student Mira Rupp for all their help with designing and characterizing the optimized components of the electric discharge device.

I am also grateful to Matthew Bain and Vanessa Tang for their early work in developing the image acquisition code and optimizing the imaging detection set-up, respectively, and Maksymilian Roman for taking over the experiment from me these last few months. I hope that the imaging set-up continues to provide exiting new 'movies' and interesting data in this and future iterations of the gas-liquid scattering experiment.

Of course, none of this would have been possible if it weren't for my Italian chemistry high school teachers Marina Scandola and Raffaella Di Guardo, whose interesting lessons and lab experiments inspired me to continue studying chemistry at Heriot-Watt University, and onwards to complete my PhD.

Finally, I'd like to thank my parents, my brother and my sister for their encouragement and patience through all these years.

ACADEMIC REGISTRY
Research Thesis Submission

Name*:*	Robert Henry Bianchini		
School:	Engineering and Physical Sciences		
Version: *(i.e. First, Resubmission, Final)*	Final	Degree Sought:	Doctor of Philosophy

Declaration

In accordance with the appropriate regulations I hereby submit my thesis and I declare that:

1) the thesis embodies the results of my own work and has been composed by myself
2) where appropriate, I have made acknowledgement of the work of others and have made reference to work carried out in collaboration with other persons
3) the thesis is the correct version of the thesis for submission and is the same version as any electronic versions submitted*.
4) my thesis for the award referred to, deposited in the Heriot-Watt University Library, should be made available for loan or photocopying and be available via the Institutional Repository, subject to such conditions as the Librarian may require
5) I understand that as a student of the University I am required to abide by the Regulations of the University and to conform to its discipline.
6) I confirm that the thesis has been verified against plagiarism via an approved plagiarism detection application e.g. Turnitin.

* *Please note that it is the responsibility of the candidate to ensure that the correct version of the thesis is submitted.*

Signature of Candidate*:*		Date:	

Submission

Submitted By *(name in capitals):*	ROBERT HENRY BIANCHINI
Signature of Individual Submitting:	
Date Submitted:	

For Completion in the Student Service Centre (SSC)

Received in the SSC by *(name in capitals):*			
Method of Submission *(Handed in to SSC; posted through internal/external mail):*			
E-thesis Submitted (mandatory for final theses)			
Signature:		Date:	

Please note this form should be bound into the submitted thesis.

TABLE OF CONTENTS

Chapter 1 – Introduction

1.1 Objectives

The interactions that occur between a gas-phase chemical species and the surface of a liquid play a key role in many processes of scientific and technological importance. Examples of such processes include respiration, distillation, multiphase catalysis, combustion and heterogeneous atmospheric chemistry. Despite the importance of these interactions for both natural phenomena and industrial processes, far less is known about the boundary between the gas phase and the liquid phase compared with reactions in bulk liquids, in the gas phase, or at the gas-solid interface. This is partly due to the fact that, unlike the gas-solid interface, liquid surfaces are disordered, dynamic, aperiodic, and more prone to thermal roughening [1-2], which makes an analysis of these surfaces more challenging. There are also a number of practical issues involved in setting up a gas-liquid interface experiment, a number of which are outlined throughout this chapter. Nevertheless, the past two decades has seen a significant increase in the amount of data collected in this area of research [3-9].

To gain a better understanding of the processes that occur at the gas-liquid interface, it is important to determine the microscopic structure of the liquid surfaces, and the fundamental dynamics of gas-liquid interfacial reactions. The liquid surface itself can be studied with a number of different techniques, such as sum frequency generation, X-ray photoelectron spectroscopy, and X-ray, light, neutron, electron and ion scattering [9]. The dynamics of gas-liquid interfacial reaction, on the other hand, can be studied by colliding gas-phase atomic or molecular projectiles with the surface, and detecting the species scattering back into the gas phase [8-9]. The latter approach has been used within the group to study the collisions of OH radicals with organic and perfluorinated liquid surfaces [10-12]. The aim of the work presented in this thesis is to expand on the previous work done within the group, using a new experimental set-up. Specifically, rotationally cold OH radicals will be scattered off liquid surfaces via a molecular beam set-up, which allows the user to change the collision energy and the angle of incidence of the projectiles. In the first set of experiments, the collision energy dependence of the scattering dynamics and uptake of the radicals on a given surface will be studied via a conventional Laser-Induced Fluorescence (LIF) detection set-up. In the second set, a planar-LIF detection set-up will be used to image the OH radicals in the

scattering plane. From those images, the collision-energy dependence of the speed and angular distributions of the scattered OH radicals off a given surface will be determined. Both experiments will expand the current understanding of gas-liquid scattering dynamics of OH radicals on organic surfaces at relatively low collision energies that are most relevant to ambient environments, particularly the atmosphere.

1.2 Motivation

The research presented in this thesis is mainly fundamental in nature, though the results obtained here may be of interest in a number of applications, such as multiphase catalysis and combustion. One of these areas of interest is atmospheric chemistry, specifically the reactions that occur on the surfaces of aerosols. Atmospheric aerosols are particles typically consisting of an inorganic, hydrophilic core coated by a layer of organic molecules in an inverse micelle structure [13] (Figure 1.1). They are generated from a wide variety of natural and anthropogenic sources, such as sea sprays, wax emissions from vegetation, combustion or industrial processes. The organic layer on the surface has a complex and dynamic structure that can contain a wide variety of functional groups, including alkyl, vinyl and aromatic groups [13-14]. At the surface, this structure is similar to that of organic liquids, which makes them suitable proxies for studying the reactions and scattering dynamics occurring on aerosols.

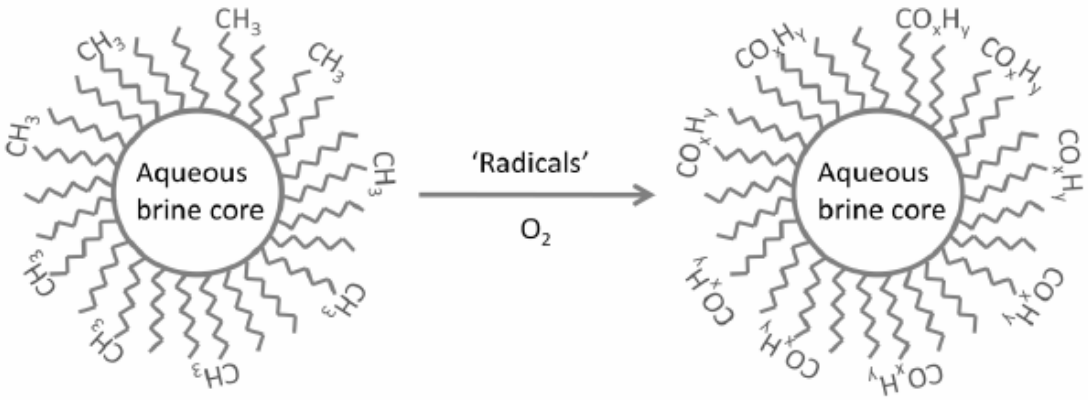

Figure 1.1: A schematic representation of the proposed structure of atmospheric aerosols, before and after processing with OH and other oxidants in the atmosphere. Figure adapted from reference [13].

Reactions with oxidants in the atmosphere can alter the properties of the aerosols, such as the particle size, and the functional groups present on the surface (as shown in Figure 1.1). This chemical 'ageing' process produces so-called secondary organic aerosols (SOAs), which have a more oxidized and polar surface that, in turn, increases the uptake of water on the surface, making them more effective as cloud condensation nuclei [13, 15-17]. The modified surface also has a significant influence on how light is absorbed or reflected from the aerosols, altering the balance between incoming and outgoing solar radiation. Both effects have a significant impact on atmospheric chemistry, and have thus been studied extensively in the literature [14, 18-19].

The major oxidizing agents present in the atmosphere are O_3, NO_3, and OH. Their reactions with organic molecules such as volatile organic compounds (VOCs) and the surfaces of aerosols have been extensively studied and reviewed by Heard and Pilling [20] and more recently by Morris and co-workers [21]. Of the three oxidants, only the OH radical reacts efficiently with a number of functional groups such as alkanes, alkenes and aromatic groups. NO_3 can also react with these functional groups, but the reactions proceed much slower than with OH, with the exception of reactions with alkenes. Ozone, on the other hand, reacts selectively with alkenes.

OH radicals are generated indirectly via photodissociation of ozone in the troposphere, which produces $O(^1D)$ atoms that react with water vapour, according to the following equations:

$$O_3 + h\upsilon\ (\lambda < 320\ \text{nm}) \rightarrow O_2(^1\Delta) + O(^1D) \qquad (1.1)$$

$$O(^1D) + H_2O \rightarrow 2\ OH \qquad (1.2)$$

The OH radicals produced in this reaction will be rapidly thermalized, then collide with aerosols and other species in the atmosphere with a thermal distribution of collision energies distributed around an average of ~4 kJ mol^{-1}. The typical daytime concentration of OH is of order ~10^6 cm^{-3}, as compared to a total number density at atmospheric pressure and temperature of ~3 x 10^{19} cm^{-3}. OH radicals are also highly reactive with many species in the atmosphere, and as such, they have a short lifetime, of order ~1 s in clean air and 10 ms in polluted air [20]. Both features have made it

challenging to measure the exact concentration of the radicals directly in the atmosphere, although many measurement techniques have since been developed and used [20, 22]. These measurements have revealed that there are discrepancies between theoretical models and actual OH densities measured, of up to 80%, suggesting that there are still OH loss processes that have yet to be accounted for [22]. In this context, the study of OH scattering off organic liquid surfaces may provide further insights as to the nature of this discrepancy. These fundamental studies have also been used recently to gain a better understanding of the effect of oxidants and SOAs on human health, such as how antioxidants in the epithelial lining fluids change after reaction with OH radicals [23].

1.3 Previous OH Measurements

The oxidation processes of organic molecules in the atmosphere by OH radicals are known to be very complex. Furthermore, there are significant differences between the homogeneous reactions that occur between gas phase species, and the heterogeneous reactions occurring at the gas-surface interface. To gain a better understanding of these processes, many measurements of OH radicals have been taken both in the laboratory and in the field [13-14, 18, 20, 22]. Laboratory studies of gas-liquid surface reactions usually employ a variety of organic surfaces such as organic liquids, waxes, sub-micron particles and self-assembled monolayers. Amongst these, squalane (a long, branched liquid alkane at ambient conditions [24]) is often used as the liquid of choice to model the surface of aerosols. This field has been recently reviewed by Morris *et al.* [21], providing many examples of OH reactions on surfaces highly relevant to particles in the atmosphere, alongside more fundamental studies to determine the reaction mechanisms. A selection of relevant examples will be discussed in the sections below.

In many of these studies, the reactivity of OH on the surfaces is quantified by an uptake coefficient, γ, defined as the probability of reaction per collision with the surface [25-26]. The uptake coefficient can be obtained either by measuring the loss of OH directly, or by measuring a change in the concentration of a species present at the surface. Measurements using the latter method have been known to result in uptake coefficients greater than unity, indicating that sequences of secondary reactions are also producing or removing the species being detected. Direct loss of OH can also be quantified as a survival probability, σ, defined as the fraction of incident species that are elastically or

inelastically scattered off a surface compared to an inert reference. As defined by Houle *et al.* [26] the survival probability is the complement of the sticking coefficient, *S*, which quantifies the fraction of molecules that do not scatter or re-desorb off the surface without reaction, as defined by the equation:

$$S = 1 - \sigma \tag{1.3}$$

When comparing these measurements, it is important to note that *S* is related to, but not necessarily the same as, the reactive uptake coefficient [21, 25-26]. It is also important to note that γ is not a constant, but is dependent on a number of factors such as the concentration of gas species, the number of reactive sites available on surface and the rate of delivery of the gas reactant.

1.3.1 Reactions at surfaces on particles of atmospheric relevance

One of the more common experimental methods for studying reactions of OH on surfaces and particles that are highly relevant to atmospheric processes involves the use of a flow tube reactor. In the flow tube, the radicals react with particles created via a nucleation process prior to entering the flow tube reactor itself. The loss of OH and/or the identification of reaction products is then usually conducted via mass spectrometry.

This method has been used in a study by Smith *et al.* [27], where OH radicals were generated in the flow tube via photolysis of O_3 in the presence of H_2O, and went on to react with squalane aerosol particles created via nucleation in an N_2 stream. The composition of the aerosol particles was monitored via a custom-built aerosol mass spectrometer. The reactive uptake coefficient was obtained by measuring the reactive loss of squalane in the particle phase, and was determined to be 0.30 ± 0.07. This value is several orders of magnitude higher than equivalent values for O_3 and NO_3 reported in previous studies [28-30], and is consistent with the relatively high chemical potential of the OH radical and the smaller barriers for hydrogen abstraction involved [31-32]. It also indicates that almost 70% of the radicals escape the surface without reacting. At low exposure of OH, the authors propose that sequential oxidation processes preferentially occur on the surface, whereas at atmospherically relevant levels of exposure, squalane molecules are preferentially volatilized into various gas-phase

functionalized organic products. These processes will compete over time depending on OH exposure.

The later study by Ruehl *et al.* [33] also made use of the photo-oxidation flow-tube method with MS measurements to determine the effect of the aerosol surface structure on the reactivity. Particles formed from nucleation processes using squalane as the organic liquid were compared with particles formed from octacosane, a straight chain alkane with a slightly smaller molecular weight than squalane. The reactive uptake coefficients obtained were 0.36 ± 011 for squalane and 0.18 ± 011 for octacosane. The lower uptake coefficient on octacosane is presumably due to the linear structure of the molecule and the fact that octacosane is solid at room temperature, resulting in a slower diffusion of unreacted molecules from the bulk to the surface than for the branched squalane, which is liquid at room temperature. The same group also found that functionalized products are more likely to occur on the terminus of the octacosane backbone, indicating that the molecules prefer to orient themselves normal to the surface, a phenomenon known in the literature as the 'surface freezing' effect.

The flow-tube method was later improved on by Che *et al.* [24], who replaced the stationary flow-tube used previously with a chamber containing an impeller to provide a continuous-flow stirred tank reactor, while retaining the same method of creating the aerosols and OH radicals. With the stirred tank reactor, the uptake coefficient obtained for squalane exposure to OH was found to be higher (0.51 ± 0.10) than the previous values reported by Smith *et al.* [27]. The authors attribute this difference to the influence of secondary reactions where more than one squalane molecule reacts with OH, which the new experimental method is more sensitive to than the stationary flow-tube reactor.

The studies described so far have looked at particles acting as proxies to the primary organic aerosols (POA) present in the atmosphere, i.e. aerosols that have yet to be oxidized. To study the extent of secondary chemistry of OH with SOAs, Kolesar *et al.* [34] exposed a squalane aerosol in a flow-tube experiment to a viscous SOA material, which was itself the product of α-pinene ozonolysis. The group found that the presence of the SOA coating increased the loss of squalane particles by up to a factor of ~2 with respect to the reactive uptake coefficient reported by Smith et al. [27] This suggested

that the radicals formed at the particle surface were able to migrate through the SOA coating to the core squalane layer of the aerosol, where further reactions occurred.

The follow-up flow-tube experiments done by Wilson *et al.* [35-36] provided further insight into the role of surface structure on OH reactions with the unsaturated organic molecules, as well as the effect of the presence of O_2. The particles were coated with either squalene, a branched alkane similar to squalane but with six C=C double bonds, or linoleic acid, a linear carboxylic acid with three C=C double bonds. The particles then reacted with OH in the presence of low (1%) and high (10%) concentrations of O_2 in the flow tube reactor. The reactive uptake coefficients were found to be 2.34 ± 0.07 for squalane and 3.75 ± 0.18 for linoleic acid, indicating that secondary chain chemistry plays a key role in these reactions. The uptake coefficient for squalene is lower than for linoleic acid despite it having more unsaturated sites. It was also noted that the uptake coefficient for squalene increased with increasing O_2 concentration, suggesting that O_2 promotes chain propagation reactions from the initial OH + squalene reaction. By contrast, at higher O_2 concentrations the uptake coefficient for linoleic acid decreases, indicating that chain termination reactions are promoted instead. Low concentration of O_2 were also found to promote functionalization products in reactions with squalene, whereas at higher concentrations, fragmentation products occur. Functionalization products were found to dominate in reactions with linoleic acid aerosols regardless of the level of O_2 present, suggesting that the fragmentation reaction channels are minor for linear molecules.

Many other organic aerosol surfaces, such as those present in soot [30, 37-40], biomass-burning aerosols [41-43], and those emerging from the use herbicides [44], pesticides [45-46], and flame retardants [47-48], have also been studied via the flow-tube method, obtaining a wide range of information on the product structure [30, 36, 39, 45, 49], yield and volatilization [39, 46], changes in particle size [40, 46] and hygroscopic properties [40], as well as kinetic information such as the reactive and degradative rate constants [37, 41, 43-48]. Aerosols of n-hexacosane and of organic molecules present in motor oils have also been studied by Donahue *et al.* [50-52], using a smog chamber instead of a flow-tube reactor. OH reactive uptake coefficients measured for these systems were found to range significantly between 0.19 and 2.0, with values as high as 8 also reported in the literature [51], providing evidence of the complexity of the secondary chemistry occurring on the surface.

1.3.2 Reactions on larger scale surfaces

Another way to use the flow-tube reactor outlined above is to coat the flow-tube itself with organic molecules. This method was adopted by Bertran *et al.* [53] to study a wide range of surfaces, including halocarbon wax (used as an inert surface), methyl- and vinyl- terminated SAMs, and several solid organic surfaces such as paraffin wax, stearic acid-palmitic mixtures, pyrene, and soot. Unlike many of the experiments reported in the previous section, the reactive uptake coefficient was determined by monitoring the loss of OH radicals. The average value of the uptake coefficient for the potentially reactive surfaces was found to be ~0.3 for many of the surface studied, the exceptions being the vinyl-terminated SAMs (0.60) and soot (0.88).

The higher value for the vinyl-terminated SAM in the previous experiment was likely due to the extreme reactivity of OH with vinyl groups. This was confirmed in the work done by Moussa and Finlayson-Pitts [54] on a SAM containing vinyl groups, obtained by depositing 7-octenyltrichlorosilane on a germanium attenuated total reflectance (ATR) crystal. The reaction of OH radicals with the surface in the presence of O_2 was followed in real-time using ATR-IR spectroscopy to monitor the loss of C=C double bond, obtaining a reaction probability of 1.1 ± 0.9 for addition of OH with the vinyl groups. The unit reaction probability indicates that every OH radical, regardless of its translation energy, orientation, or impact parameter, reacts with the surface. In a later study, Dilbeck and Finlayson-Pitts [55] studied how OH radicals reacted with unsaturated and saturated phospholipid molecules adsorbed on an NaCl surface, also in the presence of O_2, identifying functional groups both with diffuse reflection infrared Fourier transform spectrometry (DRIFTS), and MALDI-TOF mass spectrometry measurements. DRIFTS allowed the loss rate of specific vibrational modes during the gas phase reaction to be determined, from which they derived a reaction probability of $(4 \pm 1) \times 10^{-3}$ for OH addition to the C=C double bond on the unsaturated phospholipid surface, and a H-abstraction probability from the methylene groups on the saturated phospholipids of $(8 \pm 1) \times 10^{-3}$. The authors suggested that these low reaction probabilities were due to the phospholipid aggregation during the preparation process of the surface, which therefore restricted the availability of surface molecules for reaction.

Another method of studying thin films of organic molecules was X-ray photoelectron spectroscopy (XPS). Mysak *et al.* [56] have used this method to observe the reactions of OH radicals with a 5-Å thick film of coronene, and measure the changes in film

thickness and the functional distribution of the surface (determined as a ratio of surface oxygen-to-carbon) as a function of exposure to OH over time. The authors determined that both functionalization and volatilization processes played a role in the changes of the coronene film via reaction, and established that the changes in film thickness were dominated by functionalization processes at low O/C ratios (~0.1), whereas carbon loss processes started dominating at ratios more than 0.3, with decomposition of the film via loss of both carbon and oxygen atoms occurring when the O/C ratio on the film reaches 0.5. The results imply that the only 'ageing' process of POAs is the formation of oxygenated functional groups, whereas carbon and oxygen loss processes are more likely to occur once the POAs have been converted to SOAs via reaction. This is consistent with the chemistry reported in previous flow-tube studies by Wilson *et al.* [27, 33, 36], described in the previous section.

1.3.3 Fundamental experimental and theoretical work on specific gas-liquid surface

Given the complexity of the reactions occurring on the surfaces of aerosols, experimental methods and theoretical models were developed to gain a better understanding of the primary elementary encounters of OH with a liquid surface. On the experimental side, the work by McKendrick *et al.* [10-12] provided direct measurement, in isolation, of the OH survival probability after scattering off the surface. This was achieved by creating the radicals via photolysis of a precursor molecule at a short distance from a liquid surface, and then detecting the scattered molecules via LIF at the same distance. This method was adapted from a similar scattering experiment used extensively by the group to study OH emerging from reactions of atomic O with the surface [57-78], and will be described in further detail in section 1.4.4 of this chapter.

In the first scattering experiment detecting the inelastic scattering of OH [10], a low pressure of HONO above the liquid surfaces was photolyzed by a 355-nm laser, producing radicals with a mean translational energy [79] of 53.7 kJ mol^{-1} and a near-thermal rotational temperature of 329 ± 35 K. These were then scattered off the liquid surface squalane and compared with the results from scattering off a perfluoropolyether (PFPE), used as an inert reference. Of the OH radicals that survive encounter with the liquid surface, the McKendrick group determined that the dominant, faster component with the higher rotational temperature from both liquids was

consistent with a direct, impulsive scattering mechanism (see section 1.4.3). They also detected a slower, thermalized component consistent with a trapping-desorption mechanism, which was larger for squalane than for PFPE. Relative to PFPE, the survival probability of OH after encounter with the squalane surface was found to be 0.51 ± 0.04, which was assumed to be from H-abstraction reactions forming H_2O. A broader range of liquid surfaces, including squalene and oleic acid (a linear carboxylic acid with one unsaturated site), were then studied in the second scattering experiment [11]. Subtle differences in the arrival time of detected OH, and more noticeable differences in the rotational temperatures of the impulsively scattered OH, were observed from scattering off the different surfaces. The survival probabilities were also found to differ between the surfaces, ranging from 0.61 ± 0.07 for squalene, to 0.76 ± 0.10 for oleic acid. A comparison of the appearance profiles and rotational temperatures between squalane and squalene suggested that the additional loss of OH on squalene was due to the slower-moving and more thermally accommodated radicals reacting via an addition reaction to the unsaturated sites. This was later confirmed in the third experiment [12]. In this scattering experiment, the photolysis of allyl alcohol at 193 nm produced OH radicals with a hyperthermal rotational temperature of 1920 ± 120 K and a higher collision energy distributed between 70-80 kJ mol^{-1}. This allowed McKendrick and co-workers to distinguish the rotational energy distribution of both the impulsively scattered and thermally desorbed components of OH scattered off the surfaces, from which it was observed that the OH emerges with slower speeds and a higher thermal component from the squalane surface, compared to the squalene surface. The sticking probabilities obtained from the survival probabilities reported above were found to be remarkably consistent with the uptake coefficient results obtained flow-tube experiments [33].

From the results outlined above, it was assumed that the thermal-desorption fraction of the desorbing OH flux could potentially react with the organic liquid surfaces via a Langmuir-Hinshelwood mechanism. This idea was explored in further detail in the work by Enami and co-workers [23, 80-81], where OH radicals (from photolysis of O_3 in an $O_3/O_2/H_2O$ gas mixture) reacted with microjets of carboxylic acids in a vacuum chamber, and the products detected via electrospray ionization mass spectrometry. From those experiments, Enami and co-workers were able to determine that the initial reaction mechanisms occurs precisely at the gas-surface interface, and inferred from the extent of acid depletion during reaction that there is always an excess of OH available to

react at the outermost layer of the surface, which is consistent with the theoretical studies by Roeselová *et al.* [82].

Fundamental reactions of OH with vinyl-terminated and methyl-terminated functional groups were also investigated by D'Andrea *et al.* [83] using alkane- and alkene-thiol SAMs attached to a gold surface. OH radicals were produced in a molecular beam set-up by a corona discharge striking an Ar/H_2O_2/water mixture. The reactivity on the surface was monitored via reflection/absorption infrared spectroscopy (RAIRS) over time. The results from those experiments showed that a 10-minute dose of OH would destroy all CH_3- groups at the interface. Oxidation of the vinyl groups was found to proceed more rapidly, with all vinyl groups eliminated within 5 minutes. Based on the spectral changes observed and the rapid degradation of the surface, the authors suggested that the initial reaction of OH with the surface were also likely to cause radical-induced polymerization reactions onto the surface, which may explain the nature of the higher than unity reactive uptake coefficients reported in section 1.3.1.

Monte-Carlo simulations of reactions of OH with squalane, chosen as a model for alkane aerosols surfaces, were performed by Houle and co-workers [26] to gain a better understanding of the early stages of oxidative aging of the aerosols. Using a simulation that coupled free radical reactions and Fickian diffusion, the group determined that the reaction of OH with squalane is initiated by H-abstraction leading to the formation of H_2O and an alkyl free radical, which in the presence of O_2 in the gas phase or dissolved in the particle forms a peroxy radical, which accumulates on the surface until second-order reactions become significant, leading to formation of ketones and/or alcohols. The simulations also revealed that the experimentally determined reactive uptake coefficients do not represent the sticking or accommodation coefficient for a well-mixed system, but depends in a complex way on the OH density in the gas phase and the size and material characteristics of the aerosol studied.

1.4 Previous Work on Gas-Liquid Dynamics

The remainder of this chapter will focus on studies that scatter atoms and molecules off the liquid surface, and how this combined body of work provides information on the scattering dynamics of the gas species. A summary of the key experimental features and the theoretical models used to interpret the data will be provided in sections 1.4.1 and 1.4.2, respectively, followed by a review of experiments scattering neutral (section 1.4.3) and reactive (section 1.4.4) projectiles off the surface. Information from the scattering dynamics of both types of projectiles has also been used to 'interrogate' the composition and structure specific to the surface of the liquid itself. These experiments will be reviewed in section 1.4.5. Though not the primary focus in this thesis, scattering dynamics results from SAMs will also be reviewed where relevant to understanding the results presented in this chapter.

1.4.1 Experimental common features

Many experiments studying the gas-liquid surface collision dynamics have a few basic features in common, chief amongst them are the preparation of the liquid surface itself, a means to generate the projectiles in the gas phase, and a method to detect the scattered products.

The key requirement for these studies to succeed is that the nascent products that scatter from the surface must be detected before they encounter other molecules present in the gas phase, to avoid an exchange of energy between the gas phase molecules that will result in loss of information specific to the interfacial interactions. To ensure that molecules have a reasonably large mean free path, the experiment must be performed under vacuum. However, without the use of additional special measures, this requirement restricts the choice of liquids that can be studied to those that have a low vapour pressure, such as glycerol, long linear ($n > 20$) or branched hydrocarbon chains such as oleic acid and squalane (respectively), liquid polymers such as PFPE, concentrated acids, salt solutions, and ionic liquids. The chosen liquid is either placed in a static reservoir or coated onto a wheel in the vacuum chamber. The wetted wheel method (Figure 1.2), pioneered by Lednovich and Fenn [84], is the most popular method used for gas-liquid scattering experiments, and consists of a disc of suitable material immersed in a bath with the liquid to be studied. When the wheel rotates, the surface becomes coated with the liquid, generating an interface that is refreshed on each

rotation. A scraper is often added to the set-up to provide an evenly covered smooth surface. Recently, Nathanson and co-workers have developed a method of scattering gas phase projectiles off the surface of a microjet of the chosen liquid [5]. Though this method is still currently being developed and optimized, preliminary results show that it can used to study the gas-liquid interface of liquids with high vapour pressure, such as aqueous solutions.

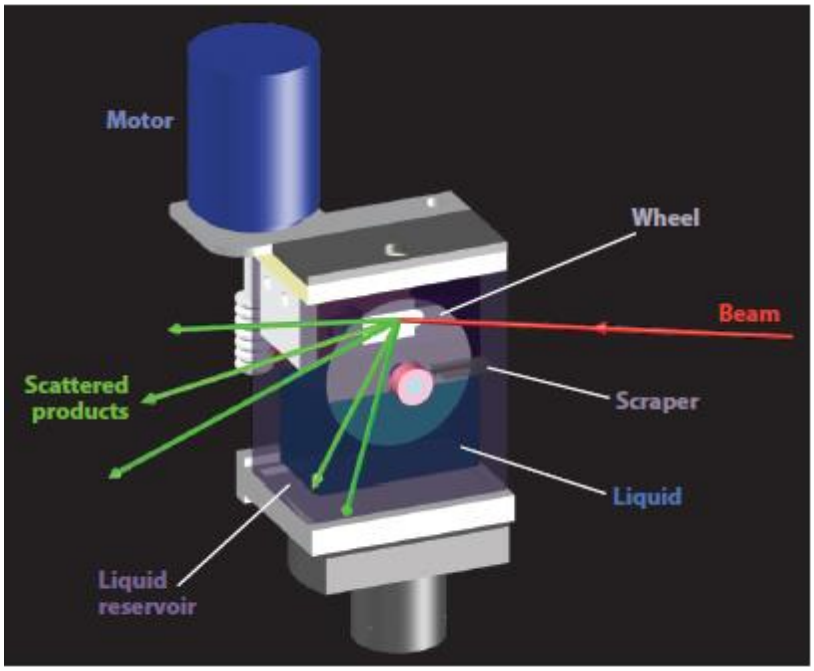

Figure 1.2: A rotating wheel partially immersed in a liquid reservoir. The wheel rotates to provide a continually refreshed liquid surface for molecular beam scattering experiments. Reprinted from reference [8].

In many of the experiments, the gas phase projectiles are introduced in the vacuum chamber via a molecular beam directed towards the surface. This method provides incident atoms and molecules with a defined speed and angle of incidence towards the surface. The supersonic expansion of the projectiles in the vacuum chamber can be used to cool the internal-state distribution, often effectively into a single quantum state, allowing the user to obtain well-resolved information of energy transfer between translation and internal energy distribution. Temporal resolution is dependent on the gas mixture that enters the chamber [85], but can be improved by chopping or pulsing the beam. Neutral species can be introduced as-is into the molecular beam, whereas radical species need to be generated *in situ*. Methods used to create the radicals include,

but are not limited to, chemical reaction, radiofrequency discharge, photolysis, and direct current (DC) discharge [86].

An alternative approach of creating radical projectiles is the 'bulk photolysis' method mentioned in section 1.3.3 above. The method involves introducing a bulk pressure of the precursor molecule in the experimental chamber, ensuring that the pressure is low enough to maintain the single-collision conditions. The molecule is then photodissociated via a short laser pulse fired at a short distance from the wheel. Unlike the molecular beam method, the radicals are produced with a broad distribution of speeds and internal energy distributions. The latter may be advantageous to certain scattering experiments, as it allows the investigation of scattering from high-energy initial states, though the resulting dynamical information may be convoluted over the initial state distributions.

The two main methods for detecting the scattered products are mass spectrometry (MS) and laser spectroscopy techniques, such as LIF, IR absorption, and resonance-enhanced multiphoton ionization (REMPI). MS provides well-resolved information on the translational energy of the scattering products. By paring it with an incident molecular beam in a set-up where both the angle of incidence, θ_i, and the angle of detection, θ_f, with respect to the surface normal can be varied, the user can also determine the velocity distribution of the products as a function of angle via time-of-flight (TOF) measurements. By contrast, detection by laser spectroscopy provides the internal-state distribution of the products, as well as translational energy information, although with more limited resolution. Angular distribution of the scattered products can also be obtained via planar-LIF, a variation of the LIF technique where the probe beam is expanded into a sheet to probe a 2D region in the scattering plane, as demonstrated by Lundgren *et al.* [87] for solid surfaces, and by our own group for liquid surfaces in Chapter 5 of this thesis.

1.4.2 Theoretical models and simulations

The gas-liquid scattering events detected experimentally with the methodology described above are the sum of many individual atomic interactions with the surface. The methodology used is unable to resolve each individual interaction with the surface,

and so to obtain a better understanding of what occurs at the gas-surface interface, theoretical simulations are used to model these interactions.

The simplest models used to simulate the trajectories of the scattered projectiles treat the incident projectiles and the surfaces as two spheres of defined mass, m_{gas} and m_s (respectively). The mass of the surface used in these models is not the same as the mass of the molecule in the liquid [88-91], but is dependent on other parameters, as described below. In the early work by Nathanson *et al.* [4] the interaction is assumed to be hard-sphere collision, analogous to similar interactions occurring in the gas-phase. The energy transferred to the surface, $\Delta E = E_f - E_i$, is obtained as a function of the deflection angle, $\chi = 180° - (\theta_f + \theta_i)$, via the equation:

$$\left(\frac{\Delta E}{E_i}\right)_{HS} = \frac{2\mu}{(1+\mu)^2}\left[1 + \mu(sin\chi)^2 - cos\chi\sqrt{1-\mu^2(sin\chi)^2}\right]\left[1 + \frac{V-2RT_{liq}}{E_i}\right] \qquad (1.4)$$

where $\mu = m_{gas}/m_s$, V is the depth of the gas-surface interaction potential, and T_{liq} is the liquid surface temperature. In this model, m_s is dependent on the collision energy E_i and the angle of incidence of the projectile. From Equation (1.4), it can be inferred that "head-on" collisions corresponding to large values of χ increase the energy transfer, whereas "glancing" collisions at smaller χ lead to smaller ΔE. This model was found to work well for heavy atoms or molecules impacting the liquid surface. However, the later work by Minton and co-workers found that this model breaks down for collisions of hyperthermal oxygen and argon atoms with squalane, PFPE and SAMs [3, 90], as the values of m_s were found to be greater for hydrocarbon surfaces despite the fact that they lead to higher ΔE. To account for this, the group adjusted the hard-sphere model equation by introducing E_{int}, indicating the internal modes of energy in molecules, or all other motions of surface atoms other than direct recoil in the case of atomic projectiles. This produced the 'soft sphere' binary-collision model, which was found to be in better agreement with the experimental results. The model is represented by the equation:

$$\left(\frac{\Delta E}{E_i}\right)_{SS} = \frac{2\mu}{(1+\mu)^2}\left[1 + \mu(sin\chi)^2 - \cos\chi\sqrt{1-\mu^2 sin^2\chi - \frac{E_{int}}{E_i}(\mu+1)} + \frac{E_{int}}{E_i}\left(\frac{\mu+1}{2\mu}\right)\right] \qquad (1.5)$$

To obtain further information on inelastic gas-liquid scattering interactions, more realistic models of the surface were generated via classical molecular dynamics (MD) simulations [92-94]. These simulations can also be used to observe how the surfaces dissipate energy from collisions, which is not currently observable via experimental methods. Another application where MD simulations are used is to estimate which atoms at the gas-liquid interface are geometrically accessible to the gas phase projectiles [75, 95]. Simulating a liquid such as squalane can often be a computationally demanding process, so many of the earlier theoretical work use SAMs as a model for the liquid surfaces [96-99]. SAMs possess flexible chains and intermolecular interactions typical of liquid surfaces, though their much more ordered structure helps simplify the simulations. Since then, improvements in the simulations model and in readily available computer power have made it feasible to simulate the liquid surface of squalane [94-95, 100]. Simulations were run with either a united-atom (UA) model, where each CH_x unit is treated as a single atom [96, 99, 101], or an explicit atom (EA) model where each atom was simulated explicitly [102]. The accuracy of the scattering trajectories could also be improved by fitting force field parameters to high level quantum calculations [96, 103-105].

In order to simulate reactive atom scattering events such as bond formation, bond breaking and electron transfer processes, quantum mechanics need to be applied in "on-the-fly" direct dynamics simulations methods, that steer the gas-liquid motion with successive electronic structure calculations of the energies and forces involved [106]. However, a full quantum mechanical treatment of the simulation for either a liquid or a SAM remains computationally prohibitive. To minimize the computational cost, the size of the liquid surface was reduced either by approximating the liquid to a cluster [107], or by employing a hybrid quantum mechanics/molecular mechanics (QM/MM) method [108-115]. In this method, the gas-liquid systems are partitioned into regions treated classically, and regions treated with QM, where the atoms are treated with semi-empirical Hamiltonians to further simplify and hence accelerate the calculations.

1.4.3 Inelastic gas-liquid scattering dynamics

The basic foundations of the gas-liquid scattering methodology described in section 1.4.1 above, were developed by the pioneering work done by Nathanson *et al.* [1-2, 4, 92, 116-120]. Nathanson's group have scattered a range of non-reactive molecules, including rare gases (He, Ne, Ar, and Xe), and molecules such as CH_4, NH_3, and D_2O, from a range of surfaces including PFPE, squalane and glycerol, with the projectiles emerging from a molecular beam source. The scattered projectiles were then detected via TOF mass spectrometry profiles, with the detector placed at a fixed final scattering angle with respect to the surface. In the course of these experiments, the group deduced several key features on the scattering dynamics and on the properties of the surface that have been applied to many gas-liquid scattering experiments, which will be summarized here.

With regards to the gas phase projectiles, the group found that the velocity distributions of the scattered products can be characterized as resulting from the combination of two limiting mechanisms. The first is the direct impulsive scattering (IS) mechanism, where the scattered species leave the surface with high translational energies and a narrow angular distribution that is correlated with the incident angle. The other is the thermal desorption (TD) mechanism, where the scattered species leave with a Maxwell Boltzmann distribution of speeds and a $cos(\theta)$ angular distribution centred around the surface normal. A representative time-of-flight (TOF) distribution of the two components obtained from experimental data is shown in Figure 1.3. The IS and TD terminology has previously been used to describe similar bimodal behaviour from scattering off gas-solid surfaces [121]. According to this distinction, the projectiles that scatter with an IS mechanism collide with the surface for a few times at most, and scatter off with high, unaccommodated speeds, and suggest that energy transfer processes with the surface is limited to what might be expected from an equivalent gas phase-like inelastic collision with a localized region of the surface. Projectiles that scatter with a TD-like mechanism, on the other hand, undergo many collisions with the surface, resulting in a larger transfer of energy to the surface and an apparently thermal distribution of products.

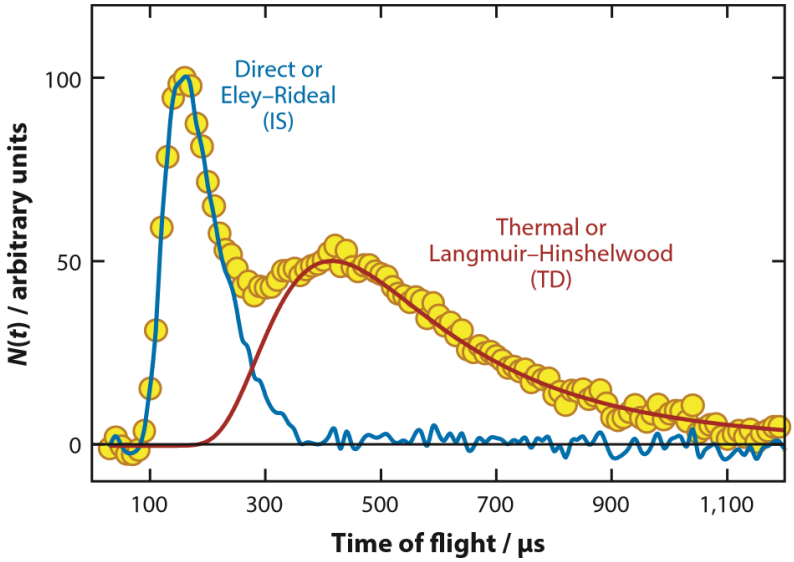

Figure 1.3: Representative TOF profiles for reactively scattered HCl following reaction of an incident Cl-atom with average incident energy of 118 kJ mol^{-1} on a squalane surface (Section 1.4.4). The angle of incidence θ_i and final angle θ_f with respect to the surface normal are 60° and 45°, respectively. Data points are represented by yellow circles, the red curve is a Maxwell-Boltzmann (MB) fit to the slow TD component, and the blue curve is the fast IS component, obtained as the difference between the data and the MB fit. Figure reprinted from reference [8], data and caption adapted from reference [89]

The IS and TD labels have been widely used to characterize the experimental observations from both non-reactive and reactive products in this field. Theoretical work on the subject, however, cautions users from ascribing each component to either one of the limiting mechanisms. Hase and co-workers [94, 96-97, 99, 101] have simulated the scattering of inert gases from H-SAMs (SAMs with terminal H-atoms at the gas-SAM interface) and squalane surfaces, and found that although the simulated scattered products follow a bimodal distribution, roughly agreeing with the IS/TD model, the colder fraction of the products was not well fitted by the surface temperature [99]. The thermalized products were ascribed to coupling of the projectiles with the internal modes of the liquid molecules. Furthermore, single-collision products expected to follow an IS distribution were found to be best described by a sum of two Maxwell-Boltzmann distributions, which indicates that thermalization does not necessarily imply trapping at the surface [101].

Other key concepts determined by Nathanson *et al.*, related to the properties of the liquid surface, are its *roughness* and its *stiffness*. The stiffness of the surface is described by the effective surface mass m_s obtained via Equations (1.4) or (1.5) above, which, in turn, is influenced by the mass of the incident projectile, and the collision energy and angle of incidence with which it impacts the surface. Surfaces that absorb less energy from the collision are referred to as *hard* surfaces, whereas surfaces that promote a larger transfer of momentum are referred to as *soft* surfaces. PFPE, with its heavy CF_x groups and denser structure, was determined to be a *hard* surface [117, 122-123], whereas squalane, with its relatively lighter aliphatic chains, is an example of a *soft* surface [124]. Application of the soft-sphere model to recent experiments and simulations [125] has shown that m_s values for the hydrocarbon surfaces were much larger than those for perfluorinated surfaces, which was explained as being the participation of many atoms in the hydrocarbon chain in the scattering process, which dissipates the projectile's energy more efficiently within the surface. The *roughness* of the surface, on the other hand, is a description of the structure and fluctuation of the surface itself at a molecular level [1]. *Rough* liquid surfaces, such as squalane, promote multiple encounters of the incident projectiles with the molecules at the surface, thereby increasing the TD fraction of the scattered products, as well as contributing to larger out-of-plane scattering with respect to the probed region. *Smooth* surfaces, such as PFPE, have a less structured gas-liquid interface which promotes more single-impact collisions and IS-like trajectories. Scattering experiments using different projectiles with the liquid surface set at different temperatures showed that increases in temperature increase the thermal motion of the molecules, generating a rougher and less dense interface [1-2, 61].

To obtain a complete picture of the scattering dynamics, the internal energy distributions of the scattered products were probed with several laser spectroscopy techniques. The earliest experimental work relevant to soft surfaces was done by Cohen *et al.* [124, 126] and involved scattering of NO radicals from fluorine terminated SAMs and hydrogen terminated SAMs. The NO radicals were cooled in a molecular beam expansion, and the scattered products probed via REMPI. The incident radicals were rotationally cold, with a narrow distribution of translation energies, from which the translational-to-rotational energy transfer could be resolved. The authors found that radicals scattering with IS trajectories were more rotationally excited than those in the TD channel, which were in turn warmer than the incident species. They also found that

NO scattered of F-SAMs gave hotter rotational and translational distributions than H-SAMs. McCaffery *et al.* [122, 127-128] observed similar results from inelastic scattering of rotationally cold I_2 from PFPE, squalane, and PDMS (perfluorodimethylsiloxane). These experiments also marked the first use of LIF for detecting scattered products.

Further spectroscopic information was obtained by Nesbitt and co-workers, who inelastically scattered a rotationally cold beam of CO_2 off liquid surfaces and probed them via IR absorption spectroscopy [102, 123, 129-133]. Nesbitt's group have investigated the collision dynamics using different liquids, collision energies, angles of incidence, and liquid temperatures. In all cases, the rotational distribution of scattered CO_2 was hotter than the incident beam, indicating translation-to-rotation energy transfer processes. The group also found that vibration excitation of CO_2 at the surface was less efficient, and attributed this result to the fact that vibrational accommodation at the surface requires more time than rotational energy transfer. Polarization-modulated IR spectroscopy was used to study orientation and alignment effects resulting from scattering, from which it was found that the highly corrugated PFPE surface induced impulsive torques on the scattered CO_2 promoting forward end-over-end tumbling. The rotational distributions were found to be strongly bimodal in nature, which were described by a two-temperature Boltzmann fit (Chapter 2 Section 2.9.2). In this model, the cold temperature T_1 was ascribed to the TD component, whereas the hot temperature T_2 was associated with the IS component. The fraction of molecules in the TD component, α, was interpreted as being the fraction of molecules that have been thermally accommodated at the surface. The translational energies of the products, obtained from so-called 'Dopplerimetry' measurements, further indicated that the products accommodate both their translational energy and rotational energy at the surface. The translational and rotational temperatures obtained for the IS component were found to be similar, however, the TD fraction inferred from the Doppler profiles were found to not match the α fraction from the two-temperature fit, which suggests that the two temperature model is not sufficient to fully describe the scattering dynamics.

Scattering simulations of CO_2 on F-SAM surfaces done by Hase *et al.* [102-103, 134] and by Perkins *et al.* [135] provided further insights into the results obtained by Nesbitt and co-workers. The simulations found that a direct interaction with the surface lasted typically less than 10 ps, whereas vibrational accommodation at the surface occurred on

a timescale of ~50 ps, explaining why energy transfer to vibrational energy modes is less efficient than transfer to rotational modes [103]. Some deviations from the IS/TD binary model were also identified. The trajectories identified in the simulations were of three types: direct scattering, penetration into the SAM, and physisorption. The physisorption trajectories, expected to correspond to a TD mechanism, were nevertheless found to be superthermal when high collision energies were used [103]. Direct scattering trajectories were also found to include single and multiple collisions. Finally, the α for the TD fraction obtained from the bimodal temperature fits were not equivalent to the fraction of physisorption and/or penetration trajectories.

The theoretical results used to interpret both Nathanson's and Nesbitt's data both indicate that a simplistic IS/TD bimodal model does not describe the scattering events effectively, but rather the two mechanisms must be treated as extremes of a range of possible mechanisms with which the projectiles can scatter off the surfaces. The dynamical information obtained from scattering OH radicals off liquid surfaces described in previous sections further reinforced this argument [10-12]. Specifically, the experiments where near thermal OH was produced via photolysis of HONO resulted in scattered products with rotational distributions that could be fitted to a single Boltzmann temperature. The rotationally and translationally hotter OH radicals produced via photolysis of allyl alcohol allowed the IS and TD components to be identified by their rotational energy distribution using the two-temperature Boltzmann fit. However, the α values obtained strongly disagreed with the TD fractions inferred from the translational energy distributions.

1.4.4 Reactive gas-liquid scattering dynamics

Many of the observations on gas-liquid scattering dynamics determined from non-reactive scattering events were found to also be applicable to scattering events that lead to reaction [70, 88, 136]. The interpretation of the results, however, is complicated by the reaction dynamics of the nascent products, and the fact that they can accommodate their energy totally or partially with the surface. This section will primarily focus on the reactions of radicals with liquid surfaces, as these are more relevant to the experimental work reported in this thesis. Proton exchange and solvation processes, as well reactions initiated by encounters with metastable species, have also been studied, and a summary of this work will be presented in this section.

The most widely studied gas-liquid scattering reaction is hydrogen abstraction from liquid hydrocarbons, with reactions of $O(^3P)$ + squalane being the most extensively characterized example. This reaction has been studied in parallel by Minton and co-workers [68, 88-91] and by McKendrick *et al.* [58-67, 69, 95]. In Minton's group, $O(^3P)$ was generated in a molecular beam, and the scattered products were detected via MS at various scattering angles with respect to the angle of incidence. The major product identified from reaction with squalane was found to be OH, analogous to similar reactions occurring in the gas-phase [57]. OH radicals scattered in two distinct velocity distributions, consistent with the IS and TD model of inelastic scattering. The TD component of the scattering could have emerged either from a thermal accommodation of the nascent OH product after a reaction from an impulsive scattered mechanism, or accommodation of $O(^3P)$ to a C-H moiety on the surface, although the latter mechanism was not observed in practice. Additionally, the OH radicals may abstract a second hydrogen from the surface to form H_2O. Analysis of the scattering angle distributions showed that H_2O emerged from the surface with both superthermal and thermal translational energies. The complexities of the reactions leading to formation of H_2O suggests that it is more likely to be formed via a TD mechanism, which explains the larger thermal component of this product compared to others. The superthermal component, on the other hand, is a rare example of a two-step Eley-Rideal reaction [121]. Similar reaction dynamics were also observed from interfacial H abstraction by Cl radicals [89]. In both H-abstraction reactions, backwards and sideways scattering in the centre-of-mass (c.m.) frame was favoured in contrast to analogous gas-phase reactions, due to the geometric constraints imposed by the surface. A representative analysis of the angular distribution of the scattered products is shown in Figure 1.4.

Minton and co-workers have also scattered O-atoms at much higher collision energies (451-472 kJ mol^{-1} in the c.m. frame) using a laser detonation method of creating the radicals [89-91]. At the higher collision energies, additional reaction channels were available, including a C-C bond breaking reaction that lead to the formation of CH_3O as a product. Related theoretical studies corroborating the experimental observations [108, 115] suggest that H-atom elimination reactions should also be observed, though in practice the detection sensitivity for H was insufficient to detect the H-atom products. Using the soft-sphere model (Equation (1.5)) in a kinematic analysis of the IS component showed that the effective surface mass for squalane when O-atoms are

scattered on its surface is 76 a.m.u. for the low collision energy, and 46 a.m.u. at the higher collision energy.

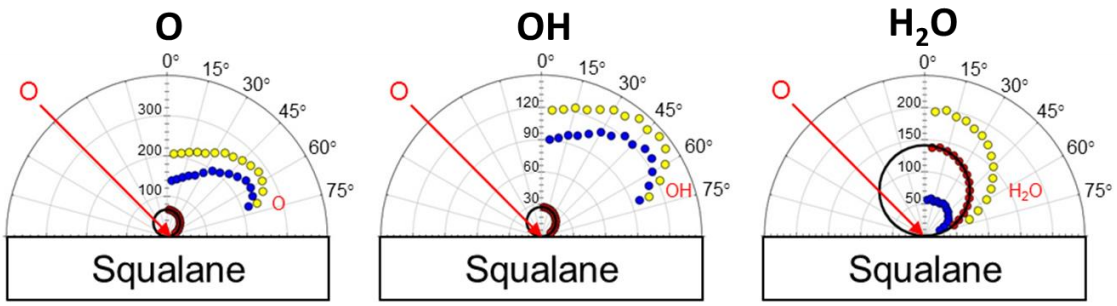

Figure 1.4: Flux angular distribution of scattered O, OH and H_2O off a squalane surface. O atoms impact the surface with an average translational energy ranging from 504 to 511 kJ mol^{-1}, at an angle of incidence θ_i of 45°. Total signal size is represented in yellow circles. Red circles represent the TD component, obtained via a Maxwell-Boltzmann fit of the slow component in TOF profiles. The TD component is well described by a cosine distribution about the surface normal, shown as black lines. Blue circles represent the IS component, derived from subtraction of the TD component from the data. Figure and caption adapted from reference [78]

The work by McKendrick *et al.* [58-67, 69, 95] provided complementary information on the internal distribution of the OH products. In their experiments, $O(^3P)$ was produced via photolysis of a bulk pressure of NO_2 at a short distance from the surface. The O-atoms would then scatter off the surface with superthermal collision energies. The OH radicals that formed as a product of the reaction of O-atoms with the surface were probed via LIF. The translational energy distribution was probed via TOF profiles by varying the delay between the firing of the photolysis beam and the probe beam. The resolution provided by these experiments was limited, but, nevertheless, an IS component was identified by fitting the profiles to a Monte-Carlo simulation which included IS and TD components [59]. The presence of both components was more clearly identified from the rotational energy distribution of the products. The overall rotational distribution obtained could be fit to a single Boltzmann temperature, found to be above the liquid temperature but below that of related gas-phase scattering processes with smaller hydrocarbons [137]. This suggested that not all scattered produces had IS-like properties, and that a significant TD component was present. This was further

confirmed by probing the rotational distribution at different points of the TOF profile [60]. Superthermal, IS-type behaviour was observed at the early delays when the products start to appear, whereas more thermal distributions, found to be dependent on the surface temperature, were observed at later delays, strongly suggesting that TD-like products strongly contribute to the tail end of the TOF profile.

Throughout these experiments, a significant fraction of the OH products in the first vibrationally excited state (v = 1) was observed [59]. The ratio of OH in the excited state with respect to the ground state (v = 0) was determined to be 0.07 ± 0.02 for scattering off squalane. This value is lower than analogous gas-phase experiment with smaller hydrocarbons [137], although it should be noted that absolute vibrational branching ratios are notoriously difficult to obtain even in gas-phase experiments [57]. The vibrationally excited products result from reaction of O(^{3}P) with the secondary and tertiary hydrocarbon sites. MD simulations confirm that such sites are accessible, although there is a slight preference for the methyl groups to preferentially occupy the gas liquid interface [95, 108]. The vibrationally excited OH had slower translational energies than OH (v = 0), and further experimental work showed that the yield of OH (v = 1) was sensitive to the surface temperature, whereas OH (v = 0) yields were independent of this property [61]. This suggested that OH (v = 1) were produced via a TD mechanism. The MD simulations show that increases in surface temperature cause the squalane surface to become more open [61], which suggested that OH (v = 1) was lost via collisional relaxation rather than vibrationally enhanced secondary reactions. The lack of liquid-temperature dependence on the yield of OH (v = 0) further suggests that thermally accommodated O(^{3}P) was not the most significant source of the TD OH component observed in the Minton experiments described above. Further insights into the reaction mechanisms of OH radicals with the surfaces were provided from the inelastic scattering of OH experiments [10-12] described earlier in section 1.3.3.

The scattering dynamics of the O(^{3}P)/OH reactions with squalane are dominated by the collision energy, which is higher than the chemical energy released into the products emerging from reaction with the surface. As a result, the trends observed in those reactive experiments are not dissimilar to the inelastic scattering experiments reported in section 1.4.3. To gain a better understanding of the reaction energetics on the interfacial dynamics, highly exoergic reactions were studied by scattering projectiles at low collision energies. One such system is the reaction of F + squalane, which was

studied by Nesbitt and co-workers experimentally by detecting HF via IR spectroscopy [136, 138] and compared with results from QM/MM simulations by Troya *et al.* [139] and Schatz *et al.* [109]. In the gas-phase reactions, F + hydrocarbons give rise to HF products with high translational and internal energies. The gas-surface experiments observed a fraction of hot products in agreement with the gas-phase results, but also a rotationally and translationally cold product, which was determined to arise from thermalization at the surface. A similar situation was observed in suitably adapted 'bulk photolysis' scattering experiments done by the McKendrick group, involving reactions of $O(^1D)$ + squalane [70] and $O(^3P)$ + squalene [74]. The analogous reactions in the gas phase were found to produce rotationally hot OH, via a transient insertion mechanism ($O(^1D)$ + squalane), or due to the higher available energy on breaking the allylic C-H bond ($O(^3P)$ + squalene). In the gas-liquid experiments, rotational energy distributions obtained via LIF spectroscopy were found to be bimodal, with a cold component presumed to emerge from secondary encounters with the surface. The $O(^3P)$ + squalene reaction was noted to produce a lower yield of OH radicals than the $O(^3P)$ + squalane reaction, despite the greater exothermicity of reactions with the allylic C-H. Analogous reactions with alkenes in the gas phase [140-142] found that addition reactions to double bonds compete efficiently with H-abstraction reactions, and so this suggests that the unsaturated sites in squalane are also available at the surface, as discussed previously.

More complex interactions and reactions with the surface, proceeding via many reaction pathways, have also been observed experimentally by Nathanson and co-workers. In an extensive set of experiments, protic acids such as HCl, HBr and HCOOH were scattered off glycerol and water, using deuterium labelling to distinguish proton exchange events [143-152]. The projectiles were found to react either via proton exchange, solvation into the bulk, or they could become temporarily trapped without it leading to reaction. Interactions between the projectiles and the surface could cause many of the molecules to thermalize, leading to a substantial amount of TD products. Using interfacial ions reduced the trapping while increasing rapid interfacial exchange by disrupting the H-bond network between OH groups in salty glycerol surfaces [146, 150-151, 153-154], whereas using salty water instead of glycerol increased the probability of solvation and eliminated the rapid interfacial proton reaction [147]. In another study, the group scattered Na atoms from a glycerol surface to study the effect of ionization of Na on the surface, once again using selective deuteration of glycerol to identify the reaction

pathways [107, 155]. Interaction of Na with the surface was found to produce Na^+ ions and solvated electrons, triggering a series of reactions leading to a range of scattered products, identified via MS. The distribution of Na that survives the scatting encounter was found to match an IS-type distribution entirely, indicating that thermalized Na atoms undergo ionization and solvation with the surface, and therefore do not scattered back in the gas phase.

1.4.5 Gas-liquid scattering as an analytical probe of surfaces

The experiments reported in the previous sections have characterized a wide range of gas-liquid processes, providing an extensive amount of information on the fundamental scattering dynamics of the projectiles. Throughout the analysis of this combined body of work, it was noted that the scattered products can also provide information specific to the outermost layer at the gas-liquid interface, which may not be easily obtained via more conventional methods of studying surfaces. As such, gas-liquid scattering experiments have recently been used to 'interrogate' the surfaces of the liquids studied, yielding information such as the preferential orientation of the molecules and the availability of specific functional groups at the surface. They have also been used to probe more complex surfaces obtained from mixtures and solutions, such as ionic liquids or solutions of glycerols and salts. This section covers experimental work focusing on the surface structural effects rather than the scattering dynamics, highlighting the work done on pure molecular liquids relevant to the experiments reported in the thesis.

The first studies of surface structural effects on scattering dynamics were done by Donaldson *et. al.* [156], who were investigating the inelastic scattering of I_2 from the surface of 4-cyano-4'-pentylbiphenyl (5CB). 5CB is a thermotropic liquid crystal, with a nematic phase at room temperature and an isotropic phase above 35° C. In the nematic phase, the molecules are preferentially oriented along a unit vector known as the director. Donaldson and co-workers have scattered I_2 off the liquid surface at both phases and detected the scattered products via LIF. From these experiments, it was observed that the TD fraction of the scattered products had substantial internal excitation, consistent with multiple encounters with the surface. When the liquid was in the isotropic phase, the internal energy distribution of the TD fraction was found to be similar to analogous results from scattering off other organic liquids [122, 128, 157],

indicating that the liquid molecules are disordered. By contrast, when scattered off the liquid in the nematic phase, a higher degree of accommodation to the surface, dependent on the direction of incidence with respect to the alignment of the molecules, was observed. As the incidence angle approached perpendicular to the director vector, the surface was found to be microscopically rougher, which induced the scattered products to be more internally excited.

In another early study by McKendrick *et al.* [63], O(^{3}P) was scattered off a range of branched (pristane and squalane) and linear (*n*-docosane, *n*-tetracosane and *n*-octacosane) hydrocarbon chains, detecting the reactive product OH via LIF. The barriers of H-abstraction from primary, secondary and tertiary H-atoms have been previously studied from scatting experiments with hydrocarbons in the gas-phase [137]. A comparison of the barriers of reaction with the collision energy distribution available from the 'bulk photolysis' experiment showed that O(^{3}P) is more likely to abstract H-atoms from secondary and tertiary sites, whereas only a smaller fraction of O-atoms with high translational energies was able to abstract H-atoms from primary sites. When O(^{3}P) was scattered off the liquid surfaces, the yield of OH products was found to be higher for the branched organic molecules. For the linear alkanes, the yield of OH decreased with the decreasing length of the chain. The higher yield from branched liquid was likely due to the tertiary C-H sites being available at the surface, whereas the difference in yield for the linear hydrocarbons was interpreted as arising from the supermolecular ordering of the chains perpendicular to the surface, resulting in the primary C-H bonds being more exposed. This effect was found to be similar to the 'surface freezing' effects reported from earlier independent studies [158], and was found to be enhanced for shorter chains at lower temperatures.

The inelastic scattering of OH radicals off liquid surfaces [10-12] reported previously in section 1.3.3 also provided information on the structure of the surface, and especially on what functional groups are readily accessible at the gas-liquid interface. The experiments detected a decrease in the survival probability of OH when scattered off squalene, which must have been caused by the presence of vinyl sites at the surface with which OH can undergo addition reactions.

Both inelastic and reactive scattering experiments have been used to characterize more complex surfaces, such as ionic liquids (IL) and mixtures of glycerol with salts, or of

hydrocarbon chains with concentrated acids. Ionic liquids are low-temperature molten salts composed of a large organic cation and an inorganic anion. Since their discovery in 1914, these liquids have been used in a wide variety of industrial applications, as reviewed by Plechkova *et al.* [159]. Due to the potential for fine-tuning the surfaces of the ionic liquids by changing the cation or the anion, there is a growing interest in gaining a full understanding of the principles that govern the surface composition of these liquids. Because of this, their surfaces have been studied via a wide range of techniques [160-161], amongst which the gas-liquid scattering experiments provide a method to study the structure of the gas-liquid interface specifically. Many of the scattering experiments use ionic liquids that have a 1-alkyl-3-methylimidazolium cation ([C$_n$mim], where *n* indicates the number of C atoms in the alkyl chains).

Inelastic scattering experiments were performed by Nesbitt *et al.*, who scattered NO [162] and CO_2 [111, 163] off $[C_4mim]^+$ ILs using a range of different anions. The values of the TD fraction were found to depend on the anion used, suggesting indirectly that anions are present on the surfaces. The cationic group was found to provide similar inelastic scattering dynamics to hydrocarbon liquids such as squalane [68]. Different degrees of accommodation on the surface were determined to arise from different fractions of the alkyl coverage, which is in turn dependent on the identity of the anion and the alkyl chain length [164]. The effect of the alkyl chain length was more incisively characterised via reactions with a chemically specific atomic probe. This method, now known as reactive atom scattering (RAS), provides high surface specificity, as well as selective probing of the alkyl chains depending on the projectile used and the collision energy. $O(^3P)$ reactions with ionic liquids have been studies both via the 'bulk photolysis' method by the McKendrick group [66-67, 69], and with the higher collision energies provided by the laser detonation method used by Minton *et al* [68]. The 'bulk photolysis' experiment in particular produce $O(^3P)$ with a range of collision energies that make it more sensitive to secondary and tertiary C-H bonds, as discussed above, whereas the higher collision experiments accessible by Minton and co-workers, provide a similar level of reactivity towards all H atoms. The complementary work done by the two groups has shown that the alkyl chains orient themselves towards the vacuum phase, though contrary to previous conclusions observed through other surface analytical measurements [165-167], the surface does not become completely saturated with alkyl chains, even when the longer [C_{12}mim] cation. Further experiments on the effect of anions on alkyl coverage [75] show that anions

with smaller ionic volume pack more efficiently, allowing more alkyl chains to cover the surface. A more recent set of experiments studying the effect of mixing two cations of different chain lengths show that the yield of OH products do not simply change proportionally to the amount of each cation present in the mix, but that the cation with the longer chain preferentially occupies the surface even at low concentrations in the mixture [168-169].

Mixtures of inorganic salts with glycerol were studied by scattering hyperthermal Ar [146, 151, 153] and CO_2 [170] off the liquid surface. The studies found that ions were present at the interface of glycerol, disrupting the hydrogen bond network by bonding to its OH groups. This disruption resulted in smoother and stiffer liquid surfaces compared to pure glycerol, with an increased surface mass that led to higher kinetic energies in IS channels, and hotter rotational distributions (for CO_2). The rotational excitation was also found to be sensitive to the identity of the salt anion, but not its cation, which would indicate that the anions are more surface active than cations, assuming that the rotational distributions are equally sensitive to the cation and anion identity.

Nathanson and co-workers have also scattered Ar [171] and HCl [172-174] off linear alcohols located on the surface of H_2SO_4, measuring the properties of the scattered species as a function of the chain length of the alcohol used. When Ar was scattered off mixtures containing 1-butanol, the IS channel of the scattered products was found to become slower and less significant with increased butanol coverage, suggesting an increase in surface roughness and a reduction in effective surface mass. With HCl as the projectile, the group observed an enhanced uptake, leading to higher probability of H exchange, when butanol was present in the mixture. Similar results were also observed for mixtures of hexanol on H_2SO_4, although as the layer of hexanol became more compact, H exchange processes decreased back to values observed when scattered off pure H_2SO_4. Finally, when a branched chain alcohol (2-ethylbutanol) was mixed with H_2SO_4, the interfacial reaction was found to be hindered more effectively, due to the larger surface area covered by the branched surfactant, compared to the linear one.

The work presented in this thesis aims to provide new insights into the scattering dynamics of the gas-phase species at relatively low collision energies relevant to ambient environments, and particularly the atmosphere. It will also help establish new

ways to obtain information on the structure of organic liquid surfaces. This was at first achieved by introducing a molecular beam source of OH radicals to the chamber. The optimization of the properties of the molecular beam source will be discussed in Chapter 3, while the results obtained with the new set-up will be reported in Chapter 4. Finally, a new detection set-up was then used to image OH LIF photons from a 2D region in the scattering plane, the results of which are shows in Chapter 5. This is the first experimental study where the detection method is used to observe a gas species scattering off a liquid surface. As such, the proof-of-concept custom analysis programs and methodology will determine how much information can be reliably obtained from the imaging results and lay the groundwork for further improvements to this new detection set-up.

Chapter 2 - Experimental Methods

2.1 Introduction

This chapter covers the general experimental approach. OH and OD radicals were generated in a molecular beam by applying a high voltage DC discharge to a pulsed beam of D_2O seeded in a rare gas at high backing pressure. The mixture of carrier gas and radical species supersonically expands into the chamber, where it scatters off a rotating wheel coated in the liquid to be studied. Both the ingoing and any scattered OD were detected by laser-induced fluorescence, using two alternative methods: either a single-point, liquid light guide (LLG) and photo-multiplier tube (PMT) set-up, or an image acquisition set-up based on a system of lenses with image-intensifier and camera.

The following sections provide details on the vacuum system, the liquids studied, both detections methods, a general outline of the DC discharge device, and the types of experimental outputs obtained. The specific details of the optimisation of the discharge device and molecular beam source will be covered in Chapter 3, whereas those of the optimisation of the imaging set-up and the analysis of the images will be covered in Chapter 5. Specific further details for each study, and any deviations from the general method, will be provided in the relevant chapters.

An overview photograph of the experimental chamber using the imaging detection set-up is shown in Figure 2.1, alongside a schematic of the main chamber's internal components with the single point detection set-up, in Figure 2.2

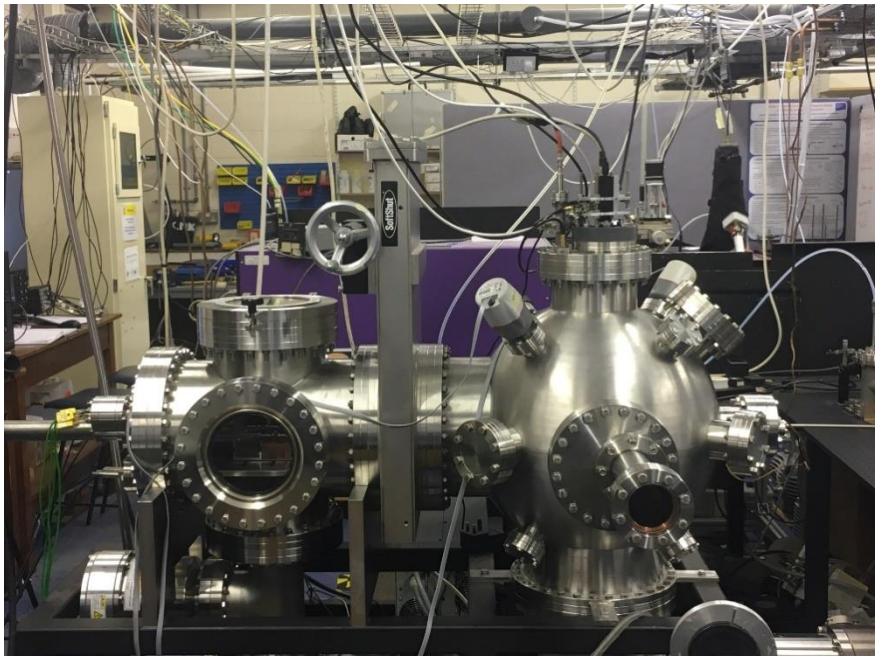

Figure 2.1: Photograph of the experimental chamber with the image acquisition set-up described in section 2.7.2. The load lock chamber lies to the left, whereas the main chamber lies to the right. A black cloth would cover the camera at the top of the main chamber when the experiment is running.

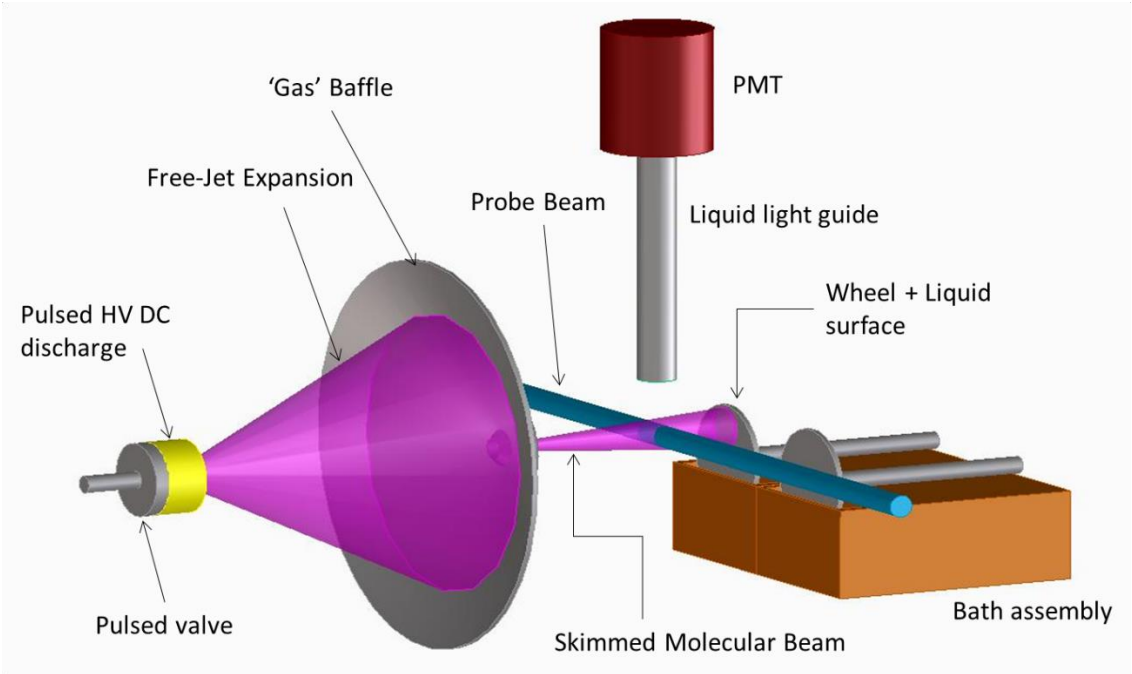

Figure 2.2: 3D schematic diagram of the internal components of the main chamber, using the single point detection set-up described in section 2.7.1

2.2 Vacuum Chambers

Two stainless steel vacuum chambers were used to form the body of the experimental set-up. The scattering experiments and the detection of OH and OD radicals were performed in a spherical chamber, referred to as the main chamber. A cylindrical chamber, referred to as the load lock, was connected to the main chamber via a gate valve, and was used to house the bath assembly, described below. The main and load-lock chamber were pumped by two separate systems of pumps, which consisted of turbo pumps (Edwards STP-A1303C and STP-301, respectively) each mounted at a 90º elbow at the bottom of the chamber, in order to prevent any spilled liquid from the baths from dropping into the turbo pump and damaging it. Each pump was connected via a backing line to dry scroll pumps, one for each chamber (Edwards XDS 35i and XDS 10, for the main chamber and load lock chamber, respectively). Isolating valves (Edwards SP Speedivalves) were added to the backing line, so that the line could be isolated from the rest of the chamber while keeping the scroll pumps on. When bringing the chamber under vacuum from atmospheric pressure, the chambers were first evacuated separately with the scroll pumps, generating a vacuum pressure of circa 10^{-2} mbar, at which point the turbo pumps were switched on, lowering the vacuum pressure even further to circa 10^{-6} mbar. Once the desired vacuum pressure was achieved in both chambers, the gate valve was opened. Dry nitrogen was used to bring the chamber back to atmospheric pressure, and care was taken to minimise external contamination when the chamber was open. The pressure in each chamber was monitored separately by active wide-range gauges (Edwards WRGS-NW35) for values in the high vacuum range and close to atmospheric pressure.

When closed, the gate valve would seal the main chamber from the load lock chamber, allowing the user to vent it without turning off the vacuum pumps in the main chamber. This gives the user the ability to access the bath assembly retracted into the load lock chamber, via a quick-access door sealed with an O-ring, in order to change the liquids in the baths without having to interrupt any ongoing experiments, such as the characterization of incident OD radicals in the molecular beam. Rails were mounted into both the main chamber and the load lock, providing a means for the bath assembly to be moved between both chambers.

The fluorescence detection set-ups (Section 2.7) were mounted on the top flange of the main chamber. Additionally, two view-ports were mounted onto nipples at a 45º angle from the top of the chamber, allowing the user to view the inside of the chamber under vacuum, and check for any issues with the devices inside the chamber, such as whether the liquid-covered wheel is properly aligned with the molecular beam, or whether the discharge is striking. The probe beam enters the chamber via quartz fused silica windows (Kurt J. Lesker, VPZL-450Q) mounted onto 21 cm arms, with the beam directed to pass at a carefully controlled distance from the liquid-covered wheel when positioned inside the chamber. In certain experiments, laser baffles were added to the arms to minimise scattered laser light. The main chamber also included three nipples onto which the user can mount the molecular beam set-up at various angles of incidence to the surface. The position of these nipples was set so that the focus of the three alternative molecular beam ports would be found in the exact centre of the chamber. The angles of incidence with respect to the liquid covered wheel provided by these ports were at 0º, 30º and 45º. Feedthroughs for the electrical connections to the molecular-beam valve and discharge components were mounted on the closest un-used nipple to the one where the molecular beam assembly was mounted.

2.3 Creating the Liquid Surfaces

The liquid surface was generated on a 5 cm diameter stainless steel wheel, which was partially immersed into a copper bath capable of containing up to 5 mL of the liquid to be studied. The wheel was attached to a rotating axel, driven by a motor (Phytron VSS Stepper Motor VSS42.200.2.5) placed inside the chamber with the copper bath, and set to rotate at typically 0.5 Hz. As it rotated, the wheel was continuously coated by a fresh layer of the liquid in the bath, which helped prevent the issue of the surface being excessively exposed to reaction with the OD radicals from the molecular beam. The copper bath rested on a copper heating block, with a cartridge heater (Watlaw Firerod cartridge heater, G1E93-G10J84T) inserted in it to allow the bath and the liquid to be heated to a desired temperature. This method does not allow for the temperature of the bath to be actively cooled back to room temperature (or below) once heated. Cooling was achieved by letting the heat dissipate via thermal conductivity. The temperatures of the bath and the motor driving the rotation of the stainless-steel wheel were monitored with thermocouples.

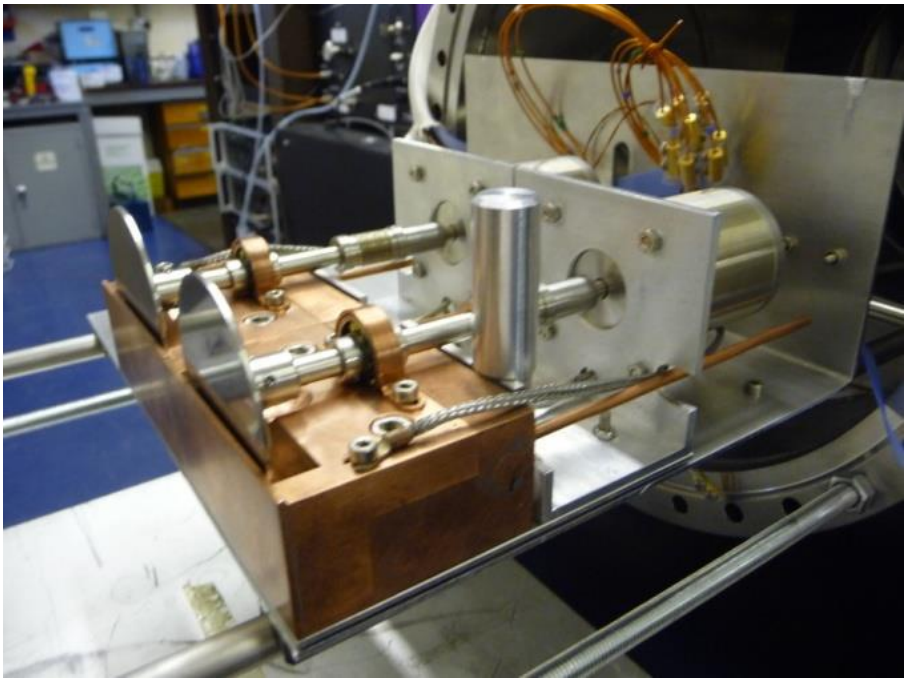

Figure 2.3: Photograph of the bath assembly

The bath assembly was made up of two separate copper baths, each with its own wheel and motor set-up (Figure 2.3). Both baths were mounted onto a translation stage, which was in turn mounted onto a static platform on rails. The platform with the copper wheels could be moved from side to side via the use of a wobble stick rotary pincer (MDC Vacuum Products llc., DG-275, 150 mm) in the load lock chamber, allowing the user to change which liquid is exposed to the molecular beam without having to vent the chamber. A linear motion power probe (Kurt J. Lesker, PP-306-H, 620 mm) was used to move the entire bath assembly into the main chamber and back into the load lock, with rails on the bath assembly allowing it to bridge the gap between the static rails in both chambers. When fully extended, the mechanical arm took the liquid surfaces to the focus point of the three molecular beam ports, ensuring that the molecular beam would scatter off the same point of the liquid surface regardless of angle of incidence. The linear motion power probe is set on the same axis as the molecular beam port for 0º, allowing for the distance between the surfaces and the probe beam to be adjusted in that set-up without changing the spot where the molecular beam hits the liquid surface. When changing liquids, the baths and respective wheels were thoroughly cleaned with methanol and acetone in a sonicator bath, to avoid cross-contamination.

2.4 Liquid Surfaces

The liquids investigated in this thesis were the saturated hydrocarbon squalane (2,6,10,15,19,23-hexamethyltetracosane) and its unsaturated analogue squalene ((6E,10E,14E,18E)-2,6,10,15,19,23-hexamethyltetracosa-2,6,10,14,18,22-hexane,). A liquid perfluoropolyether (PFPE), sourced from DuPont (Krytox 1506, (F-[$CF(CF_3)CF_2O]_{14ave}$-CF_2CF_3)), was also used as an inert reference, allowing the survival probabilities of OD radicals off the hydrocarbon surfaces to be extracted by comparison, as explained further below. PFPE also provided an internal reference to calibrate the results due to day-to-day variations, as also explained below.

The liquids were used directly as purchased without further purification, other than extensive degassing under vacuum as part of the experimental procedure to remove dissolved gases or other volatile components. All liquids were chosen due to their low vapour pressure at room temperature and low melting points, which makes them suitable to use in the vacuum chamber. Their physical properties are reported in Table 2.1, whereas the corresponding molecular structures are provided in Figure 2.4.

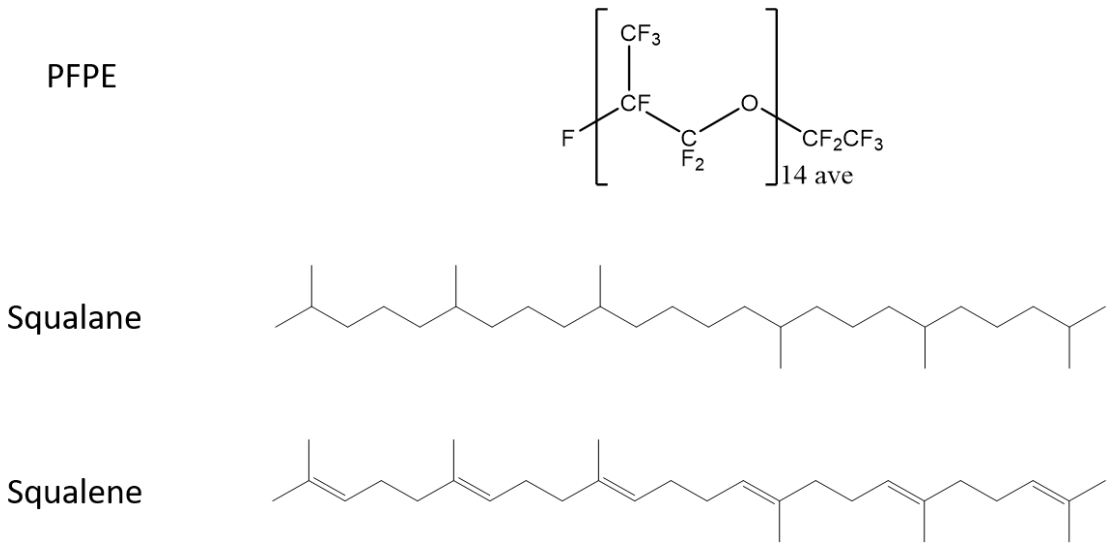

Figure 2.4: Common names and chemical structures for liquids used

Liquid	**Source**	**Purity**	**Vapour pressure/ Torr (at 298 K)**	**Melting point/ K**
PFPE (Krytox 1506)	DuPont	-	$\sim 10^{-7}$	213 (pour point)
Squalane	Sigma-Aldrich	≥99%	$\sim 10^{-7}$	235
Squalene	Sigma-Aldrich	≥98%	$\sim 10^{-7}$	198

Table 2.1: Key properties of the liquids used

2.5 Molecular Beam Set-Up

2.5.1 Previous method used: Bulk Photolysis

The experimental method most commonly used previously in the McKendrick group for gas-liquid scattering experiments was the 'bulk photolysis' method [8]. In this method, a precursor gas was introduced into a vacuum chamber via a needle valve, carefully adjusted to obtain a constant pressure in the chamber. The precursor was then photolyzed by a pulsed laser beam of suitable wavelength at a chosen distance, typically 5 – 10 mm, from the liquid surface. Some of the radicals generated would then scatter off the surface. Both the initially generated radicals and the ones that scattered off the surface were probed by a laser beam counter-propagating the photolysis beam, and detected via laser-induced fluorescence. The scattered radicals can generally be discriminated from the incident radicals by their later appearance times.

This methodology has been used successfully to look at OH radicals generated from hydrogen abstraction reactions by $O(^3P)$ and $O(^1D)$ atoms interacting with organic liquid surfaces [57-64, 66-75]. The radicals were generated from photolysis of a precursor gas, in this case NO_2. Using a reactive atom to scatter off a surface is a method more generally known as Reactive Atom Scattering (RAS). The inelastic scattering of OH radicals can also be looked at using this methodology, by substituting HONO as the precursor gas [10-12]. While the group was able to obtain interesting results from these experiments (as explored in more detail in Chapter 1 Section 1.3.2),

the methodology has some limitations to it. For one thing, there is no control over the direction from which the radicals will scatter off the surface, which makes it difficult to establish the scattering angle distribution of the radicals. Furthermore, the collision energy and rotational energy distribution of the generated radicals is determined by the choice of the precursor and the photolysis wavelength used. The group had previously generated OH radicals with high collision energy and thermal [10-11] or hyper thermal [12] rotational energy distribution from readily available combinations of precursor gases and photolysis wavelengths. However, there are no suitable and conveniently available combinations able to provide collision energies more relevant to atmospheric conditions. Finally, there's the practical problem that the probe beam will detect all the OH radicals present in the chamber, including all the radicals generated at the point where the photolysis beam is fired, and the background signal size at later times where the scattered OH appears. Both problems were addressed by taking data without the surface in the chamber, and subtracting this 'background' signal contribution from the data taken with the surface in.

2.5.2 New method: Molecular beam

To obtain more information on the inelastic scattering dynamics and the uptake of OH radicals with the surface, a molecular beam set-up was introduced into the experimental chamber presented in the current work. A molecular beam is generally obtained by allowing a high pressured gas mixture containing the particles to be studied (which can be atoms, radicals, ions or molecules), often seeded in a carrier gas, to expand through a small orifice into a chamber at low pressure, either continuously or via a pulsed valve. When the valve opens, the gas leaves the high pressure reservoir with a mean velocity equivalent to the speed of sound, and undergoes many collisions, resulting in the 'cooling' of the rotational and vibrational energy distribution, which are often reported as temperatures (T_{rot} and T_{vib}, respectively). As the ratio between reservoir and vacuum pressure increases beyond a critical value G (typically 2.1 or lower for gases [175]), the molecular speed exceeds the local speed of sound, resulting in the formation of a supersonic free-jet expansion of the gas. At a sufficient distance from the nozzle, the molecules have spread far apart enough to form a beam with a near constant velocity where very few intermolecular collisions occur. The supersonic expansion continues until it reaches the Mach disk shock barrier, a region where turbulence causes supersonic expansion to break down, resulting in a molecular beam with subsonic

speeds. In the region between the valve nozzle and the Mach disk shock barrier (referred to as the 'cone of silence'), a conical skimmer is placed at the centreline of the expansion in order to extract the coldest and densest part of the free-jet expansion, resulting in a collimated molecular beam with a well-defined direction, a supersonic mean speed, a narrow spreads of speeds about the mean, and a small transversal speed distribution. The latter parameter is often reported as a translational temperature T_{trans}, which for molecular beams is usually of the order of a few K. The rotational and vibrational temperatures of the molecules in the molecular beam are determined by the thermodynamics of the expansion, which is itself dependent on the temperature of the reservoir, the heat capacity of the gas, and its molecular mass.

In this experiment, the molecular beam was generated by a high-pressured gas mixture entering the main chamber via a pulsed valve (General Valve series 9), to which a nozzle faceplate with a 1 mm orifice was attached. The valve was secured to the main chamber via supporting rods attached to a flange, either directly or indirectly via an aluminium valve holder plate. It was then connected to the source of the gas mixture via a stainless-steel gas line through an in-build feedthrough on the flange. This flange was mounted onto the selected one of the three nipples which determined the angle of incidence of the molecular beam with respect to the surface. The pulsed valve was connected via suitable feedthroughs to a control box (Iota One Pulse Driver, Part 60-1-900, General Valve Corporation), from which the pulse duration and activation time of the valve opening was set.

After exiting the pulsed valve, the gas mixture expanded supersonically into the main chamber, forming a free jet with a wide angular range. A collimated molecular beam was formed by inserting a skimmer (Beam Dynamics, inc), which was itself mounted on an aluminium skimmer holder attached to supporting rods in line with the valve nozzle. A simple 'gas baffle' made of several layers of aluminium foil in a roughly rectangular shape was also attached to the skimmer holder, to prevent the free jet from passing around the skimmer holder into the detection region. A 5 mm diameter skimmer was used for the scattering experiments described in Chapter 4, whereas a 2 mm diameter skimmer was used in Chapter 5. Further details on the optimization of the skimmer distance with respect to the valve, as well as the size of the gas baffle, are described in Chapter 3 Section 3.6 of the thesis.

2.5.3 Creating the radicals: photolysis method

In the first iteration of the molecular beam set-up, a photolytic method of creating OH radicals from a suitable precursor in the gas mixture was tested by previous Ph.D students in the McKendrick group. This involved using a 193 nm beam generated from an ArF excimer laser (GAM EX350) to photodissociate the precursor molecule at the throat of the expansion of the molecular beam into the chamber. Several precursors were tested, with the best results obtained by using 1% allyl alcohol seeded in a rare gas. Although their work was successful at obtaining a rotationally cold species, with a rotational temperature as low as 30 K, this method did not provide a sufficiently high and reproducible OH density close to the liquid surfaces to be used in scattering experiments, and so a DC discharge method of creating the radicals (described below) was adopted.

2.5.4 Creating the radicals: DC discharge set-up

The DC discharge device, shown in Figure 2.5, was attached onto the nozzle faceplate. This device is based on a design developed by Dr Stuart Greaves (Heriot-Watt University) and outlined by Ondřej Tkáč in his thesis thesis [176], and will henceforth be referred to as the Greaves device. This device was in turn inspired by the discharge device used by ter Meulen and van Beek [177] and Ikejiri *et al.* [178]. The Greaves device consists of two stainless-steel electrodes, separated from each other and from the valve faceplate by Macor® ceramic insulators, and encased in a Teflon body. The electrode closest to the pulsed valve, referred to as the grounding electrode, has a cone-shaped nozzle with a 1 mm diameter to match the orifice of the valve faceplate. A Kapton wire, attached to a metal tag soldered onto the electrode itself, connected the electrode to a feedthrough in the vacuum chamber, which was then set to ground. The front electrode, placed furthest from the pulsed valve, has an orifice with rounded edges on both sides in line with the gas flow. A high negative DC voltage from a PMT power supply (Bertan model 353) was applied to the front electrode via a separate feedthrough and Kapton wire connection, which was secured to the electrode via a spade connector and a bolt that screws into a threaded hole on the electrode itself. When the chamber was under vacuum, an electrical discharge would initiate between the front and ground electrode by the rise in local pressure caused by the pulsed valve opening. The discharge would then remain active for as long as the negative voltage was kept on or until the pulsed valve closed, whichever came first.

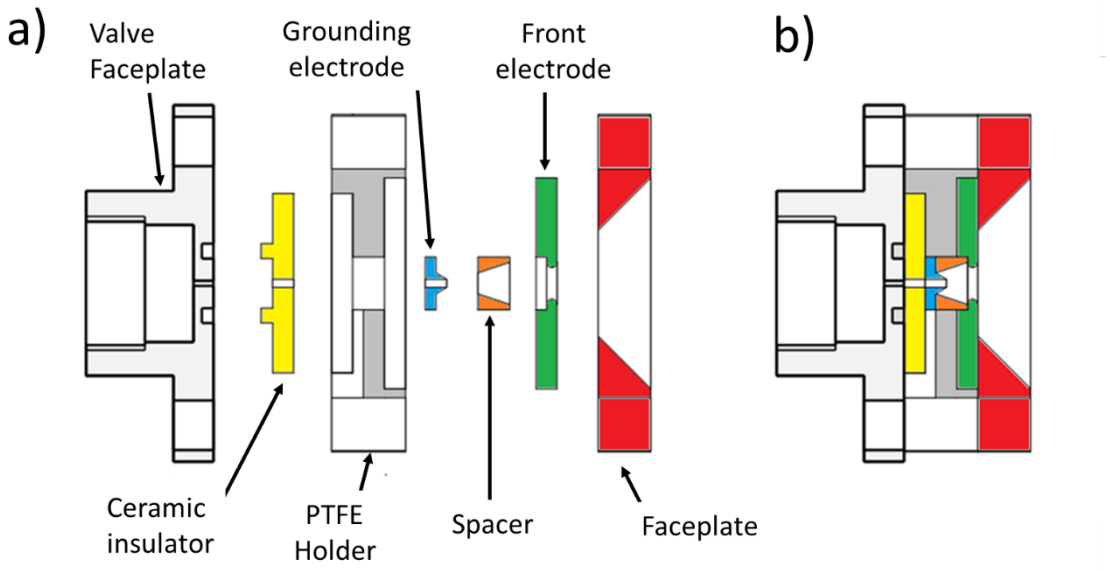

Figure 2.5: An expanded (a) and collapsed (b) schematic diagram of the original DC discharge device design from the Greaves group attached to the valve faceplate. Schematic adapted from reference [176].

The negative high voltage (HV) can be applied either continuously (by attaching the electrode directly to the power supply), or in a pulsed mode using a fast switch (PVX-4140, Directed Energy, Inc.), switching between the PMT power supply in the active state and another power supply (Fluke model 412B) set to ground or positive voltage, in the passive state. In a typical experiment, the fast switch was set to trigger to the active state circa 100 μs after the pulsed valve had opened, for a period of 10 μs. Other combinations of activation time and HV pulse duration could be programmed via a delay generator (Section 2.8), and have been explored in more detail in Chapter 3.

Conventional wisdom suggests that a source of electrons is needed to seed the discharge device in order for the discharge to strike at voltage pulses less than circa 60 μs long. It was found in practice that the Edwards wide-range gauges on their own provided enough electrons for the discharge to strike at short pulses, so long as the gauge was sufficiently near the discharge device, or positioned to provide a direct line of sight to the device itself. Where necessary, the discharge was further stabilized by applying a high current to a filament positioned close to the pulsed valve, or by applying a positive 'bias' voltage to the front electrode. This will be covered in more detail in section 3.5 of Chapter 3.

Multiple variations of the discharge device components and discharge conditions, such as voltage, gas pulse length, backing pressure and start time of the discharge, as well as the distance between the valve and the skimmer, were explored to optimise the molecular beam conditions used for subsequent gas-liquid scattering experiments. Further details on the results of these optimisation tests will be covered in Chapter 3, and the configurations used for the experiments reported in this thesis will be reported in their respective chapters.

2.5.5 Choosing the right radicals: OH or OD?

The majority of previous experiments done in the McKendrick group have primarily looked at OH radicals, either as the product of reaction between oxygen atoms and a hydrocarbon surface, or as the inelastically scattered particle off the surface itself. In the following experiments, however, OD radicals were inelastically scattered off the liquid surfaces and detected instead.

The group has previously detected OD radicals in a number of scattering experiments, such as scattering $O(^3P)$ off deuterated squalane [58-59] to confirm that the radicals could only have emerged via reaction with the liquid surface, or scattering off selectively labelled SAMs [65] to find out which sites on the alkyl chains were reactive. In the scattering experiments reported in this thesis, the choice to detect OD was motivated by the switch to using the DC discharge to create OH radicals. Unlike the products of the chosen photolysis routes, which have been well characterised in previous experiments, it was unclear from proof-of-concept experiments using the discharge device whether the discharge itself might also generate oxygen (most likely $O(^3P)$) atoms alongside OH, and, if so, in what proportion. As thoroughly explored in previous experiments in the group [57-64, 66-75], at high-enough collision energy $O(^3P)$ abstracts hydrogen atoms from organic liquid surfaces to form OH. It would thus be possible to inadvertently detect the reactive OH products concurrently with the OH inelastically scattered from the molecular beam. These two sources of OH would not be easily distinguished. To isolate the products of inelastic scattering unambiguously, OD radicals were therefore used in the following experiments. An alternative approach would involve scattering OH radicals off the fully deuterated versions of the liquid surfaces; however, this would be considerably more expensive than generating OD

using relatively cheap D_2O as the precursor, and scattering it off the non-deuterated liquid surfaces.

2.5.6 Creating the gas mixture

The high-pressure gas mixture was prepared using a bubbler set-up. Circa 10-15 g of liquid D_2O (99.9% purity, Cambridge Isotope Laboratories, Inc.,) was placed inside a glass vial contained into a sealed stainless-steel CF40 T-piece. An inner tube with Swagelok fittings was immersed in the liquid in the glass vial and connected to the carrier gas line via a soldered feedthrough. A 0.5 mm hole was drilled through a blank Swagelok cap and attached to the tube, allowing the carrier gas to bubble through the liquid and providing a mixture of ~3% D_2O at atmospheric pressure in the carrier gas. Rare gases (CP grade, 99.99%) were used as carrier gases. Cylinders of helium and neon (BOC Gases) were attached to the bubbler via regulated supplies. Typical backing pressures used in the experiment were of between 1.6 and 3 bar for either carrier gas. The effects of the backing pressure on the conditions of the molecular beam will be explored in Chapter 3 section 3.3.2, while specific backing pressures for each scattering experiment will be reported in the experimental sections of Chapters 4 and 5.

2.6 Detection Method

Both the incident OD radicals in the molecular beam, and those that scattered off the surface, were detected by laser-induced fluorescence (LIF) The following sections contain an introduction to LIF spectroscopy and provide details on the two experimental detection systems used.

2.6.1 Fundamentals of Laser-Induced Fluorescence

Pioneered by Zare and co-workers in 1974 [179], LIF is a widely used spectroscopic technique, where the molecules to be detected are electronically excited by means of a short laser pulse. The excited molecules then spontaneously emit fluorescence photons as they fall to various levels in the electronic ground state. The emission is collected via a suitable optical arrangement, usually at right angles to the excitation laser beam. If a tuneable laser with sufficiently narrow bandwidth is used, single rovibrational transitions between energy levels can be probed. The LIF intensity as a function of

probe wavelength, λ, is known as an excitation spectrum. By analysing such excitation spectra, the desired relative population distribution over rovibrational states in the electronic ground state can be extracted, provided that the intensity factors (Franck-Condon factors and rotational line strengths) are known. The fact that this technique provides information on the internal energy distribution of the molecules makes it particularly useful for studying gas-phase collision dynamics.

One of the main advantages of LIF is that it is, in principle, a zero-background technique, allowing it to detect signals from very low number densities (of the order of $<1 \times 10^6$ molecules cm^{-3}), such as low concentrations of radical intermediates in flames and plasmas [180]. Another advantage is that, since fluorescence takes place in all directions, 2D and 3D images of the fluorescent light can be taken with the appropriate set-up, such as with planar-LIF (discussed below). Polarised LIF can also be used to obtain information about the stereodynamics of a reaction [181]. As only a small proportion of photons are absorbed by the species to be detected, the method requires a significant initial number of photons. This is usually provided by pulsed lasers, which also gives the technique good time resolution. A disadvantage of LIF is that it cannot be used on its own to obtain the absolute number densities of the species, due to a number of experimental factors, such as the strength of the transition, the collection efficiency of the optics, the quantum efficiency and wavelength dependence of the detector, and the pulse energy of the laser, which are difficult to quantify. Other factors, such as the target species predissociating, having a very short lived excited state, or having the excited state quenched via collisions, also make it difficult to detect certain molecules and radicals. Therefore, to be successfully detected by LIF, a species must have a known spectrum, a sufficiently strong electronic absorption band within the wavelength range of the probe laser, and good fluorescence quantum yields with ideally no predissociation in the excited state. These conditions are satisfied by a wide range of molecules [182], including the lower-lying rovibrational levels of OH and OD radicals, as discussed in the following section.

The LIF technique is often used with a cylindrical probe beam, with fluorescence emissions of the molecules studied usually detected by a photomultiplier tube (PMT), often used in combination with a system of lenses, though liquid light guides have also been used. While a lot of information can be and has been obtained via this technique, it does not provide vectorial information (speed and direction) on the incident and

scattered molecules directly. To get that additional information, a variation of LIF, called planar-LIF (PLIF) or 2d-LIF, will be used here. This technique was first mentioned in 1982 independently by Dyer and Crosley [183], and by Kychakoff *et al.* [184] in their studies of combustion species in flames, and consists of expanding the probe laser beam in one direction to form a sheet. This allows for a 2D area in the detection region to be probed via some form of real-space detection. An imaging set-up, described below, will be used to study the temporal variation of the real-space density of OD radicals as they move through the detection region.

2.6.2 Spectroscopy of OH and OD radicals

OD radicals are good candidates to be studied by LIF as, like OH radicals, they have convenient fluorescence lifetimes (~700 ns) and do not dissociate upon transition to low rotational levels. Predissocation becomes a significant factor at rotational levels higher than $N' = 28$, however rotational levels higher than $N' = 8$ will not be considered for the purpose of the scattering experiments reported in this thesis. OD radicals in the ground vibrational state were probed by excitation on the (1,0) band around 287 – 289 nm, and the photons emitted were detected on the (1,1) band around 310 – 313 nm, on the A $^2\Sigma^+$ -X $^2\Pi$ electronic transition. Using different bands for excitation and detection helps prevent the scattered probe light from affecting the LIF signal.

In the electronic ground state, OH and OD radicals have the electronic configuration $(1\sigma)^2(2\sigma)^2(3\sigma)^2(1\pi)^3$ which gives rise to a molecular term symbol of $X^2\Pi_i$ (as $\Sigma = \pm 1/2$ and $\Lambda = \pm 1$). In the low rotational levels, OD $^2\Pi_i$ is in an intermediate case between Hund's case (a) and (b), while in higher rotational levels, it is best described by Hund's case (b). Because of this, both coupling cases need to be considered when interpreting the spectroscopy. In Hund's case (a), the electronic orbital angular momentum L couples strongly with the electrostatic field of the nuclei. The electron spin angular momentum S is coupled to the internuclear axis by the internal magnetic field due to the orbital motion of electrons. Their projections onto the internuclear axis ($\Lambda\hbar$ and $\Sigma\hbar$, respectively) combine to form the electronic angular momentum, $\Omega = |\Lambda + \Sigma|$. This gives rise to two spin-orbit manifolds in the X state, $^2\Pi_{3/2}$ (F_1) and $^2\Pi_{1/2}$ (F_2). Of the two, rotational levels in the F_1 manifold are lower in energy. Coupling of L to nuclear rotation R produces a further splitting known as Λ-doubling. As a result of Λ-doubling and spin-orbit coupling, each rotational J level of the OH/OD X state is split into four.

As J increases, the splitting in energy between the doublets increases, while the splitting between Ω components decreases, and Hund's case (b) (described below) becomes a better descriptor of the OH/OD X state.

The OH A state has electronic configuration $(1\sigma)^2(2\sigma)^2(3\sigma)^1(1\pi)^4$, and a corresponding term symbol of $^2\Sigma^+$. For this state, $\Lambda = 0$, so there is no projection of the orbital angular momentum along the nuclear axis, and no Λ-doubling. This state is best described by Hund's coupling case (b), whereby the spin angular momentum S couples to nuclear rotation R, resulting in two components f_1 ($J = N + ½$) and f_2 ($J = N - ½$).

The selection rules that apply to the OD A-X transition are:

1. $\Delta J = 0, \pm 1$

2. $+ \leftrightarrow -$, but $+ \nleftrightarrow +$ and $- \nleftrightarrow -$

3. $\Delta \Lambda = 0, \pm 1$

4. $\Delta S = 0$

Rules 3 and 4 are specific to Hund's cases (a) and (b) and are satisfied by the A – X transition. Applications of rules 1 and 2 results in six main branches. These are labelled (in absorption) P_1 ($\Delta J/\Delta N = -1$ from F_1), P_2 ($\Delta J/\Delta N = -1$ from F_2), Q_1 ($\Delta J/\Delta N = 0$ from F_1), Q_2($\Delta J/\Delta N = 0$ from F_2), R_1 ($\Delta J/\Delta N = 1$ from F_1), R_2 ($\Delta J/\Delta N = 1$ from F_2). When Hund's case (a) applies, the selection rule $\Delta J = 0, \pm 1$ is still obeyed, but values of ΔN other than 0 or ±1 are allowed. As a result, six satellite branches appear, labelled P_{12}, Q_{12}, R_{12} (arising from the F_2 manifold), and P_{21}, Q_{21}, and R_{21} (from F_1). A schematic representation of the energy levels and the main-branch transitions is shown in Figure 2.6 below.

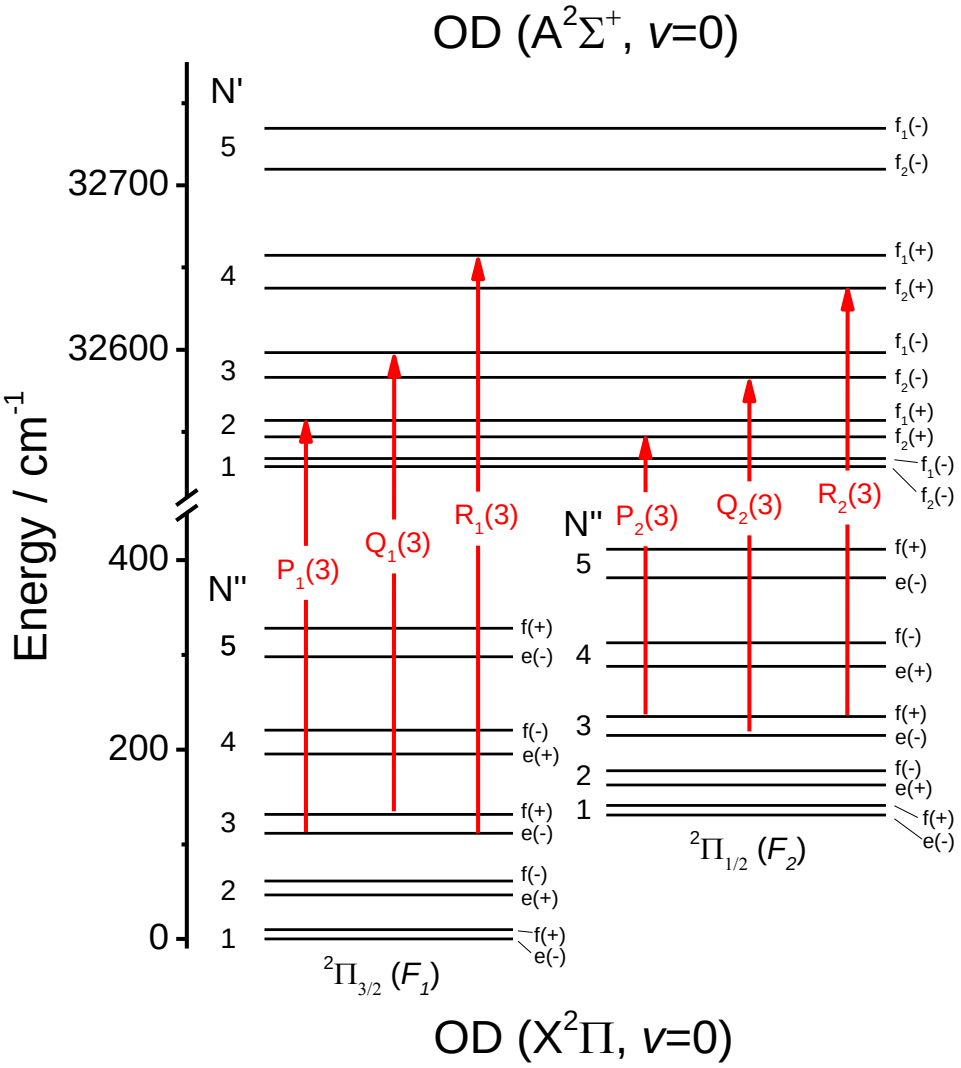

Figure 2.6: Main-branch A-X transitions for OD, arising from same N level in the ground state (N = 3). Satellite branches have been omitted, and Spin-rotation splitting and Λ-doubling exaggerated for clarity.

2.6.3 Probe laser

The LIF excitation probe beam was produced by a pulsed dye laser (Sirah Cobra-Stretch, CSTR-LG-24), using a gain medium consisting of an organic dye solution circulating through two quartz cuvettes. The dye laser was pumped by the 532 nm light from a frequency-doubled pulsed Nd:YAG laser (Continuum Surelite II-10). The vertically-polarised 532 nm beam was split into three components, pumping three different stages of the pulsed dye laser: resonator, preamplifier, and amplifier. The emission wavelength was selected by a diffraction grating in the resonator stage. The

grating has a groove density of 2400 lines/mm, so the approximate line width obtained is 0.0012 nm. The light transmitted through the output coupler was then rotated by 180° with two prisms and passed again through the resonator cell at a different height than the resonator (preamplifier stage). The light was then further amplified in the final stage by passing through a second cuvette, before entering the frequency conversion unit (FCU). In the FCU, a KDP second-harmonic crystal produced frequency-doubled laser light in the UV region, which was then separated out from the fundamental wavelength by means of Pellin-Broca prisms.

To detect OD radicals on the A-X (1,0) band, a mixture of fluorescent dyes was used. This was obtained by making a rhodamine 6G dye solution for the resonator and amplifier dye cells, and then adding an empirically determined quantity of concentrated rhodamine B dye solution in both dye cells, maintaining the same proportions as used for making up the main dye. In the case of rhodamine 6G, the recommended concentration of dye for the amplifier cell is 1/3rd of the concentration used for the resonator dye. The power of the UV laser light of the base rhodamine 6G dye laser in the typical frequency doubled range of 280-285 nm region was checked using a power meter (Gentec-e ED- 100A UV). A small amount of Rhodamine B was then added to both dye solutions, monitoring the peak UV power output over a range of wavelengths after each addition of the dye. The process was repeated until a power output close to that of the base dye was obtained in the frequency doubled range between 286-290 nm, where the excitation of OD radicals on the (1,0) band occurs.

The output beam of the dye laser was horizontally polarised and approximately 4-6 mm in diameter. This cylindrical beam was used for the single-point detection experiments, and for initial tests with the image acquisition set-up, probing at circa 10 mm from the liquid surface. To image a wider area of the scattering plane, the cylindrical beam was expanded into a 2D sheet via the use of concave and convex lenses. Further information on the optimisation of the probe sheet can be found in Chapter 5.

The output energy of the probe beam could be adjusted by varying the Q-switch delay of the pump laser, and via the use of an external polariser and a $\lambda/2$ waveleplate combination to further attenuate and fine-tune the UV output. The energy was kept constant over the range of wavelengths used by recording a suitable FCU calibration curve for each laser dye. The calibration involved varying the angle of the FCU crystal

and compensator to change its conversion efficiency to the desired constant output energy.

2.7 Detection Set-Ups

2.7.1 Single point detection set-up

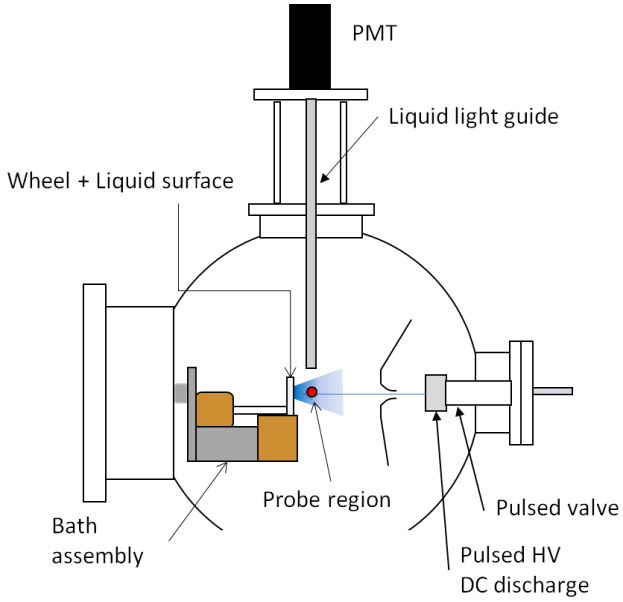

Figure 2.7: Schematic of the experimental set-up of the main chamber, with the PMT and liquid light guide set-up

Two detection set-ups were used in the acquisition of data from this experiment. In the first set-up (Figure 2.7), referred to as the single point detection set-up, OD radical fluorescence was detected via a liquid light guide (Ultrafine Technology Ltd. Series 300, length 500 mm, width 80 mm) pointing at the centre of the main chamber, perpendicular to the probe beam axis. The liquid light sat inside a stainless-steel tube, with an O-ring-sealed window on its end, at 10 mm above the laser axis. The collection angle was $2\alpha = 72°$, so photons could only be detected if they were emitted from a ~10 mm segment of the laser axis. Additionally, a dichroic optical filter, centred at λ = 317 nm with FWHM = 8 nm (Laser Components) was placed between the liquid light guide and the PMT. This ensured that the photons transmitted were on the corresponding emission band, while filtering out scattered light from the probe beam. The PMT (EMI, 9813QB) was operated at a typical gain voltage of 1.5 kV. The signal from the PMT was then transmitted to a digital oscilloscope. The experiments reported in Chapters 3 and 4 were acquired with this detection set-up.

2.7.2 Image acquisition set-up

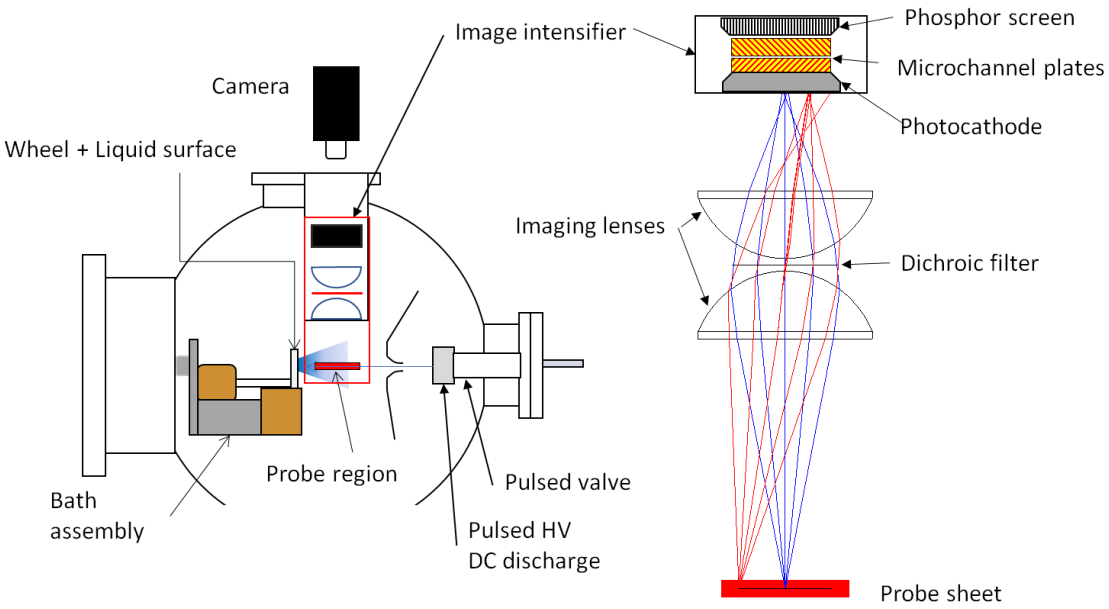

Figure 2.8: Schematic of the main chamber with the image acquisition set-up. A zoomed in version of the optical stack is shown on the right. Red and blue lines indicate pathways of the fluorescence photon travelling though the lenses to the image intensifier

The image acquisition set-up is made up of several components that were put inside the main vacuum chamber, and a camera placed outside the chamber. All of the components in the chamber were placed in aluminium holding plates and secured to rods attached to the bottom of a flange, aligned so that the components were placed directly under the CF63 view port built in the flange. A black Delrin plastic casing was used to cover the imaging components inside the vacuum chamber, to prevent scattered light from reaching the detector from the sides of the imaging-optics stack.

The imaging set-up inside the vacuum chamber consisted of an image intensifier (Photek, MCP240/Q/S20/P43/GL), two fused silica lenses (Thorlabs La4384), and a dichroic optical filter, also centred at λ = 317 nm with FWHM = 8 nm (Laser Components). These components were arranged as shown in Figure 2.8. The optimal distances between each component were determined by previous students in the McKendrick group [185], and will be described in further detail in Chapter 5 Section 5.2. The image intensifier was powered by a power supply unit and a gating module provided by the manufacturer and installed into a custom-made power supply unit outside the vacuum chamber. This unit allowed the user to vary the gain voltage

applied to the micro-channel plates (MCP) in the image intensifier, which was typically set between 1.400 and 1.475 kV. The phosphor screen was set at a voltage of 5 kV with respect to the MCP, while the gating unit was set to apply -200 V to the photocathode when triggered externally, resting at +50 V when not being triggered. When a photon hits the photocathode when it's being gated on, it releases primary photoelectrons into the MCP, where they collide with the channel walls to produce secondary electrons. These electrons then get accelerated along the channel, producing further electrons with each collision with the wall. The high voltage on the phosphor screen accelerates these electrons into the screen, producing phosphorescence light; this is then detected by a CCD camera (The Imaging Source, DMK 21BF618.H or Basler Scout FireWire Camera, scA780-54fm) placed outside the main chamber, through the port in the flange. An avalanche photodiode SPM detector (MicroFM-10035-X18 sensor on a MicroEVB-1mm board) was placed alongside the camera to monitor, via an oscilloscope, the total light level produced by the phosphor screen. The optimization of the imaging set-up, the analysis procedures of the results obtained, and the experimental results will be covered in Chapter 5.

2.8 Instrument Control and Data Acquisition

All the devices were triggered by an 8-channel delay generator (BNC 565). These generated a primary trigger (T_0) at 10 Hz. Channels producing TTL pulses were used to trigger both the flashlamp and Q-switch delay for the Nd:YAG laser, and the cameras in the image acquisition set-up. The pulsed valve driver, the fast switch, the gating unit for the image intensifier and the oscilloscopes were triggered by pulses with different amplitudes set by the delay generator. All the channels in the delay generator used positive trigger pulses, with the sole exception of negative trigger pulse used for the fast switch to trigger between the resting state (at ground or at positive voltage), and the active state (the negative HV pulse). The delay of each channel with respect to T_0 was varied using custom-made software.

The oscilloscopes (LeCroy Wavesurfer 434) operated at a sample rate of 2 GS/s. One was triggered synchronously with the fast switch and used to observe the current draw from the power supplies when a discharge occurs, as described in further detail in section 3.2 of chapter 3. The other oscilloscope, used for data acquisition, was set to trigger synchronously with the probe beam, so that the laser pulse was always detected

at the same point in the acquired waveform. When using the single point detection set-up, the time base of the oscilloscope was set to 1 μs per division, and the LIF signal was collected by the software in a circa 3 μs gate after the probe pulse. In addition, an electronic baseline was recorded via a shorter gate (typically 0.5 μs) before the probe pulse. The data in the signal and baseline gates were averaged by the internal program of the oscilloscope, with multiple laser shots averaged before transfer to the data acquisition PC via an Ethernet connection (TCP/IP) for further processing of the data. A similar arrangement was used for the signal from the photodiode; with suitable adjustments to the time base and delay settings, as further described in Chapter 5 (Section 5.2). A sample waveform trace from the image acquisition set-up is shown in Figure 2.9.

Custom data-acquisition and experimental control software were programmed on the data acquisition PC using LabVIEW™ [186]. The experimental control software, also referred to as the tune-up software, allowed the user to set the start delays of each channel in the delay generator, and vary the probe-laser wavelength and the gates for acquiring data from the waveform, as described above. This was done to find the peak signal of a given LIF transition prior to data acquisition. The parameters set in the tune-up software were then saved and used by the data-acquisition software. Separate programs were used to record time-of-flight profiles (Section 2.9.1) and excitation spectra (Section 2.9.2), as described in each section. The tune-up program was later modified to display the images acquired by the CCD cameras, and acquire images as described in Section 2.9.3. The shutter mode of the cameras was set so that the timing of the trigger pulse and the exposure time of the camera were controlled by the delay generator, and thus by the tune-up software. Other parameters of the camera, such as the gain, brightness, frame rate, exposure, gamma parameters, trigger parameters, were set by the camera software prior to data acquisition to maximise the signal observed.

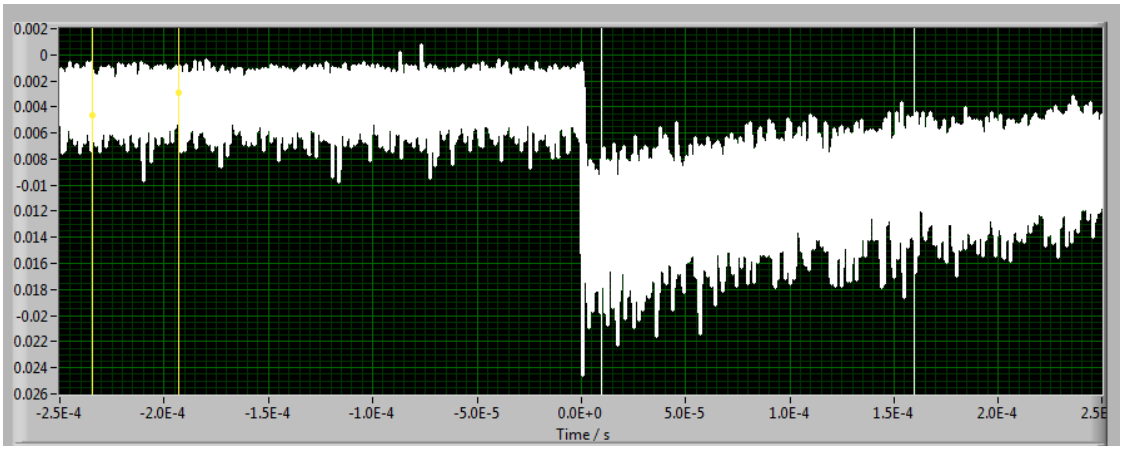

Figure 2.9: A sample screenshot of the LabVIEW™ data acquisition program, displaying an acquired waveform from the avalanche photodiode of the image acquisition set-up. The vertical axis represents voltage in V. The waveform is an average of 20 laser shots. The voltage spike at time = 0 μs is caused by scattered light from the Nd:YAG pump laser detected through the cloth covering the imaging-set up. The subsequent decay corresponds to the phosphorescence from the image intensifier's phosphor screen. The signal (white) and baseline (yellow) gates are delimited by vertical lines.

2.9 Experimental Outputs

Three different data acquisition programs were used to obtain three types of experimental outputs: time-of-flight (TOF) profiles, excitation spectra, single images and sequences of images. The TOF profiles and both types of image outputs were obtained at a fixed wavelength on a given transition. Single images collected the OD fluorescence signal at a fixed delay between the start of the discharge and the probe beam pulse. TOF profiles and the sequences of images output also collected OD fluorescence while varying the discharge-probe beam delay. Excitation spectra were recorded by scanning the excitation wavelength at a fixed discharge-probe delay, collecting OD fluorescence at different transitions. TOF profiles and excitation spectra can be acquired with both detection set-ups, whereas the image outputs can only be acquired via the image acquisition set-up. The general features of each type of output will be discussed below. A more in-depth look at the analysis of the image outputs will be covered in Chapter 5.

2.9.1 Time-of-flight profiles

Experimental Time-of-flight Profiles

Time-of-flight (TOF) profiles are records of the relative OD LIF signal intensity as a function of the delay between the start of the high voltage (HV) discharge pulse and the probe laser pulse, recorded on a given LIF transition. The LIF signal intensity provides information on the OD density in the level probed by that transition, whereas the shape of the profile provides information on the speed, and hence translational energy, of the radicals, both those present in the incident molecular beam and those scattered off a liquid surface. With appropriate normalization, the intensities of TOF profiles taken on different transitions also provide the relative populations in different product rovibrational states.

Before acquiring TOF profiles, the probe laser wavelength was tuned to a given transition with the LabVIEW™ tune-up software, by varying the wavelength of the laser and the discharge-probe beam delay to find the maximum LIF signal for that transition. The "tune-up" procedure was carried out at regular intervals of approximately 30 minutes between acquiring sets of TOF profiles, to correct for any potential wavelength drifts of the probe laser. In practice, it was found that the wavelength drift would stabilize over the course of the day once the probe beam set-up had warmed up, allowing the user to increase the interval between tuning the laser without affecting the OD LIF signal intensity detected.

TOF profiles were then acquired at the probe wavelength set by the tune-up program. To make optimum use of a given acquisition time, different step sizes were used for three different sections of the TOF profile, with shorter steps over the range where the peak of the ingoing beam and scattered OD were likely to appear, and longer steps for the range of delays before and after that section. For each delay, the LIF signals for several laser shots (typically 30) were acquired and averaged. To ensure reproducibility, several profiles were recorded, alternating between a profile with the surface out (i.e the incident OD profile) and a profile with the surface in. These individual profiles were then averaged.

Figure 2.10 show representative raw OH TOF profiles on the $Q_1(5)$ transition, with and without a surface present. By overlapping the profiles, it can be seen that those with the

surface in have additional OD density after the falling edge of the incident OD profiles, and that the delays where this signal is detected often have an underlying incident OD signal contribution. To extract the scattered OD profile, both the averaged surface in and surface out profiles were normalised to the OD signal at the delay corresponding to the peak of the associated incident OD profile, and then the incident OD profile was subtracted from the profile with the surface in. Further improvements to the experimental conditions, such as making the incident OD packet shorter and rotationally colder, can help to better distinguish the incident OD contribution from the scattered OD contribution to the profiles with surface in, and thus improve the subtraction process. These improvements will be discussed in Chapter 3 of this thesis.

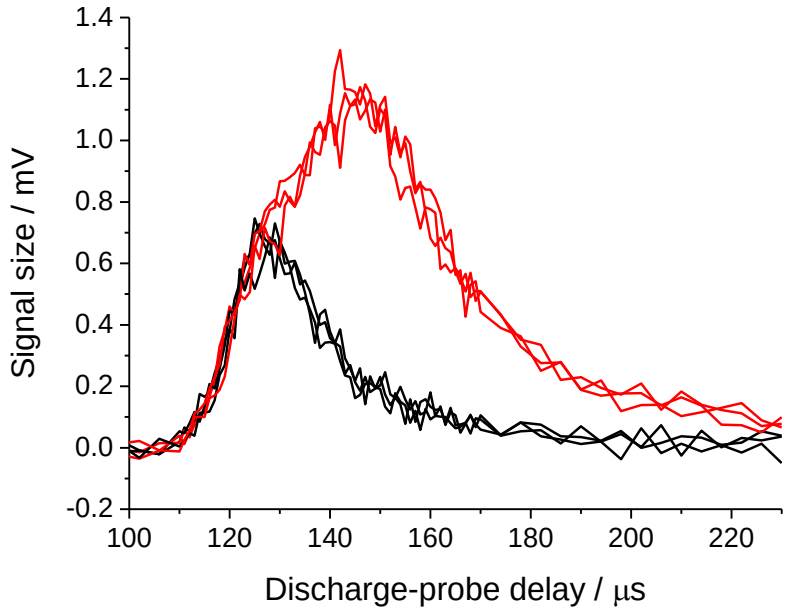

Figure 2.10: Representative OD TOF profiles taken on the $Q_1(5)$ transition, including surface in (PFPE, red lines) and surface out (black lines). The probe laser background has been subtracted from the profiles

The main source of background noise in the data is due to scattered light from the probe laser pulse that appears in the signal gate. Additional background noise may also be generated by contaminants in the liquids that emit fluorescence when excited by the probe beam. To correct for this factor, several points were included in the TOF profiles at delays before the rising edge of the incident OD. The average of these points was then subtracted from the signal at all other delays.

2.9.2 Excitation spectra

Experimental Excitation spectra

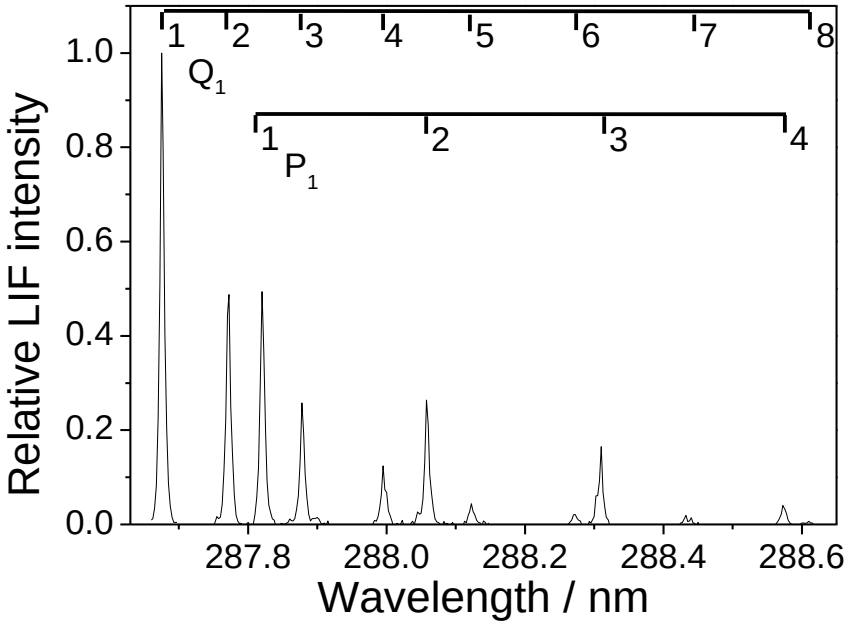

Figure 2.11: A representative experimental excitation spectrum of OD radicals, taken at a discharge-probe beam delay corresponding to the peak signal size of the incident beam profile using He as the carrier gas. The data acquisition software was set to scan discontinuous wavelength regions corresponding to selected transitions of the Q_1 and P_1 branches, as labelled.

OD excitation spectra were obtained by scanning the wavelength of the probe laser over a relevant region at a constant discharge-probe pulse delay and recording the OD LIF signal size at each wavelength. A representative example of an OH excitation spectrum is shown in Figure 2.11. Several laser shots (typically 20) were averaged for each wavelength. The probe wavelength was typically varied in steps of 0.0025 nm, omitting regions that did not contain any transitions of interest to reduce the data acquisition time. This was done because drifts in the chamber pressure, discharge conditions and probe-laser energy can affect the relative intensities of the different spectral lines. A short data acquisition time ensures that the conditions remain relatively constant over the course of a spectrum. Taking multiple excitation spectra at the same discharge-probe beam delay also helped to ensure that the excitation spectra are consistent and representative of that delay.

Fitting of rotational distributions

The ground-state OD rotational state distributions were obtained by fitting the experimental spectra in the spectral simulation program LIFBASE [187]. The program can simulate LIF excitation spectra using previously known spectroscopic constants, in this case for OD, taking into account experimental factors such as probe-laser resolution, line broadening and shift in wavelength and baseline between the experimental data and the simulation. A simulated spectrum of OD with a rotational temperature, T_{rot}, of 300 K is presented in Figure 2.12.

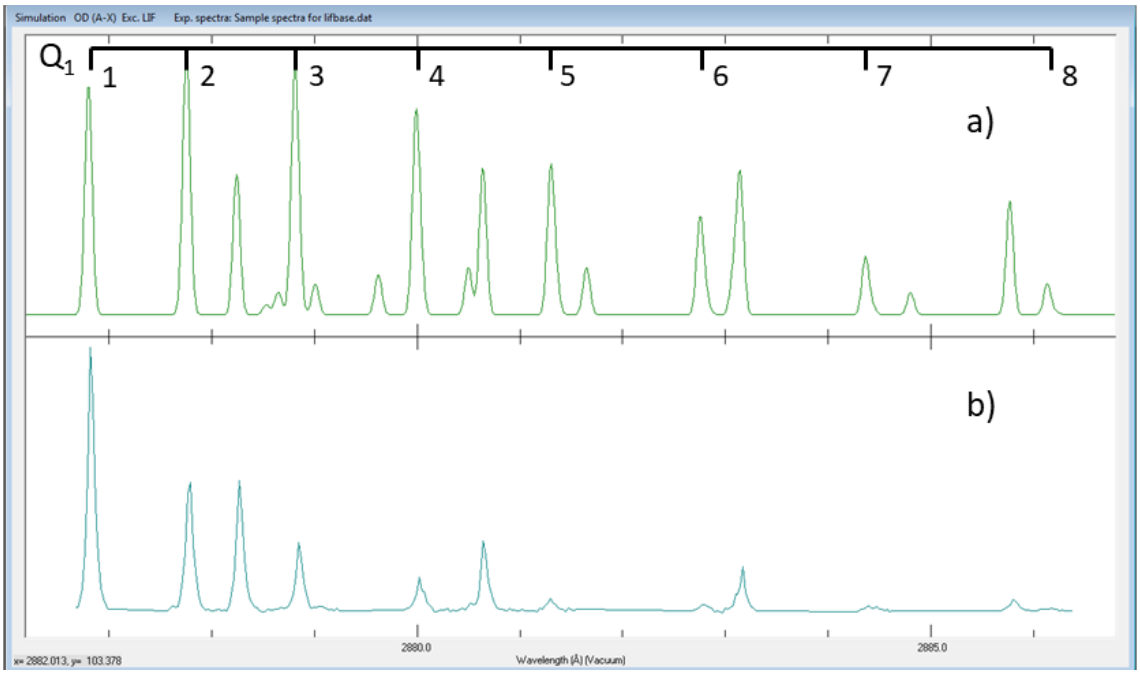

Figure 2.12: LIFBASE screenshot of a) a simulated LIF excitation spectrum of OD with T_{rot} = 300 K, and b) a representative experimental spectra, obtained from Figure 2.11. Q_1 transitions are labelled as indicated, all other transition labels have been omitted for clarity.

The populations of the individual N levels for each spin-orbit and Λ-doublet manifold was manipulated in the simulation to match the experimental spectrum. The populations of the first eight N rotational levels of the Q_1 branch lines were then obtained from the simulations program, and each value was renormalized to the sum of the populations. Where multiple spectra have been taken for the same discharge-probe delay and same experimental conditions, the populations obtained from individual spectra were then averaged and used in the Boltzmann analysis described below.

In a sample at thermal equilibrium, the population of a particular quantum state is related to the energy of that state via the Boltzmann distribution:

$$P(N_i) = \frac{g_i}{Z} e^{-\frac{E_i}{k_B T}} \tag{2.1}$$

where $P(N_i)$ is the relative population in the rotational level N_i, E_i is the energy of that level, g_i is its degeneracy, k_B is the Boltzmann constant, and T_{rot} is the temperature of the distribution. Z is the partition function, defined as $Z = \sum_i g_i e^{-\frac{E_i}{k_B T}}$

To provide a simple single measure characterising the rotational populations extracted from experimental results, Boltzmann plots were often formed; these consist of the natural logarithm of the population divided by the degeneracy plotted against the energy of the rotational level. The resulting points could, in some cases, be fitted adequately to a straight line of slope $-\frac{1}{k_B T}$. However, this does not imply that they were truly thermal distributions at temperature T. In some cases, particularly the spectra from the ingoing beams, it was found that the points in the Boltzmann plots did not fit a line. In these cases, a two-temperature model fit was applied. The two temperature fit is analogous to that used, for example, by Nesbitt and co-workers [123], and is based on the equation:

$$\frac{P(N_i)}{2J+1} = C\left[\frac{\alpha}{T_1} e^{-\frac{E_i}{k_B T_1}} + \left(\frac{1-\alpha}{T_1}\right) e^{-\frac{E_i}{k_B T_2}}\right] \tag{2.2}$$

Where T_1 and T_2 are the two rotational temperatures used in the fit, α is the fraction of the population with the lower temperature T_1, and C is an arbitrary scaling factor. This equation assumes that the rotational partition function takes its classical value proportional to T. This is valid so long as the population spans a reasonable number of levels.

The fitting functions for both the linear and two-temperature fit to the Boltzmann plots provided the standard error in the fit for each of the parameters, from which the errors in the temperatures were derived. The errors in the fit were estimated according to the error propagation formula. The reduced chi-squared statistic was excluded from the calculation of the error. In order to improve the fitting of the Boltzmann plots, and thus

the accuracy of errors in the temperatures, an instrumental weighting was applied to the data set, whereby each data point was weighted according to the inverse of the square of their error values.

The simulations used to extract the populations from the experimental spectra all assume the ideal case where there is no spectral line saturation, the probe-laser intensity is flat across the region probed, and the population of the excited state is linearly proportional to the probe-laser intensity. In practice, the populations in an experimental spectrum can potentially differ from the actual distribution due to variations in detection sensitivity as a function of wavelength (mostly given by the transmission curve of the dichroic filter), variations in the probe laser energy with wavelength, and saturation.

To account for all these factors, thermal OD spectra were acquired and analysed for each dye calibration curve used throughout the scattering experiments. The spectra were taken at a delay of circa 1 ms from the start of the discharge, with the discharge conditions set to strike over the entire gas pulse. This ensured that the OD detected had undergone a large number of gas-phase collisions (~40 for a gas pulse length of 350 μs, and ~60 for a gas pulse length of 500 μs) so that the rotational distribution was fully thermalized. The correction factor for each rotational level was determined via the equation

$$f_{p(N')} = \frac{p(N')_{therm}}{p(N')_{sim}} \tag{2.3}$$

where $p(N')_{therm}$ is the relative population obtained from the thermal calibration spectra, and $p(N')_{sim}$ is the expected rotational population obtained from a simulated LIFBASE spectra of OD with a rotational temperature of ≈ 295 K, equivalent to the ambient temperature at the time of the experiments. The correction factor was then applied to the experimental results.

2.9.3 Images

The images that the cameras acquire are the primary experimental output from the imaging detection set-up. This output was acquired via the modified tune-up program, as described in Section 2.8. As with the TOF profiles, the probe laser was tuned to a given transition, with the discharge-probe delay set so that the signal from the incident

beam covered a wide area of the probed region viewed by the collection lenses and image intensifier. The signal intensity was monitored both via the avalanche photodiode and from the camera in a 'live feed' mode, where the images obtained after each trigger pulse it received were shown in the tune-up program.

Before acquiring any images, the camera was set to acquire a limited section of the entire field of view. A 420-by-420 pixel region, centred around the phosphor screen of the image intensifier, was set up. Each pixel from the camera can assume an intensity value between 0 and 255. To remove as much of the noise generated by the camera as possible, a threshold was applied to the images acquired. If the intensity of any given pixel in the image was below the threshold value (typically set at 12), then its intensity was reset to 0.

The tune-up software could be set to acquire either a 'single-shot' image, or a 'summed image'. The 'single-shot' image is simply the last image displayed in the 'live feed' mode when the shot is acquired, whereas the 'summed image' is obtained from the sum of several 'single-shot' images (typically 500) determined by the user. The intensity of a given pixel in the 'summed image' is the sum of the intensities in the same pixel position from each individual shot acquired. The summed images were the preferred image output acquired in the scattering experiments, due to the resulting higher signal-to-noise ratio. Both the single-shot and summed images could be acquired at a fixed discharge-probe delay set via the tune-up program. Additionally, the tune-up program could also be set to acquire a sequence of summed images over a range of different discharge-probe delays, in a method similar to the data acquisition of TOF profiles.

The images thus obtained were initially analysed and processed using the most recent version of ImageJ (specifically the Fiji distribution of ImageJ) available [188-189]. The program allowed the user to apply a false-colour mapping to the images to better visualize the data. A sample summed image with the false-colour mapping applied is shown in Figure 2.13 below. When comparing sequences of images obtained from scattering OD off different liquid surfaces, the false-colour mapping parameters were set using the PFPE sequence of images and applied to all other liquids to highlight the differences in scattered OD signal size.

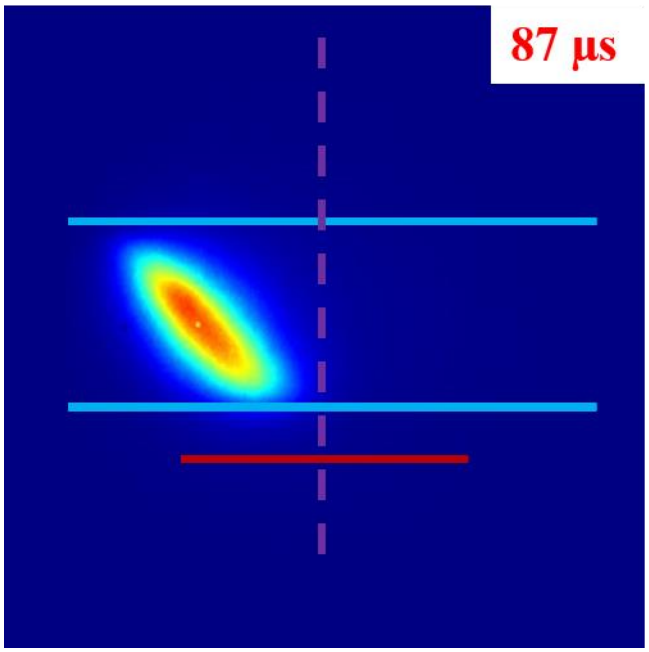

Figure 2.13: A sample false-colour summed image of the signal detected from the incident OD beam. The molecular beam is set at a 45° angle of incidence from the surface, indicated by the red line. The discharge-probe delay is reported in the top-right corner. The cyan lines indicate the area probed by the probe sheet, while the purple dashed line indicates the normal angle of incidence axis.

To obtain the speed and angular distribution of scattered OD, the images were also analysed using custom-made LabVIEW™ programs. These will be covered in further detail in Chapter 5 Section 5.3.

Chapter 3 – Optimization and Characterizaton of the Molecular Beam

3.1 Introduction

Electrical discharges are one of the most common methods used to create OH (or OD) radicals in a molecular beam [86]. The discharges are produced at the throat of the expansion via devices attached to the pulsed valve. The design of the device determines the type of electrical discharge produced, and can be generally divided into corona-excited discharge devices [83, 190-193], Dielectric Barrier discharge (or DBD) devices [194-196], and DC electric discharge (also known as 'glow' discharge) devices [177-178, 197-202]. The experiments reported in this thesis were conducted using a 'glow' type discharge device designed by the Greaves group [176] described in further detail in Section 2.5.4. This chapter will describe a series of characterization experiments aimed at identifying the conditions required to achieve a stable electric discharge and optimal molecular beam properties, as described in further detail in Section 3.2.

The parameters that can be changed to optimize the stability of the discharge and the properties of the molecular beam can be classified into three different groups: the components of the discharge device itself, the positioning of the skimmer and gas baffle with respect to the pulsed valve in the chamber, and the *in situ* discharge conditions that can be modified while the discharge is firing. Each of these groups and the individual parameters within them will be expanded on throughout the course of this chapter, providing details on the changes made and their effect on the molecular beam. Some of these parameters, such as the optimization of *in situ* properties of the molecular beam (Section 3.3) and the design of different components of the device (Section 3.4), have been described in a project report by ERASMUS project student Mira Rupp [203], and so a summary of the results from the report will be provided in this thesis. Many of those parameters have also been characterized by other groups using similar 'glow' discharge devices [177-178, 197-202]. These will be discussed alongside the results described in this chapter to gain further insight into how the molecular beam properties are being modified.

The results and observations from this chapter provide some useful guidelines for optimising the properties of the incident beam in the gas-liquid scattering experiments

reported in this thesis. However, obtaining optimal molecular beam properties and a stable discharge was not always possible depending on the carrier gas used for molecular beam, and on other factors yet to be accounted for. In such cases, the parameters were adjusted to be as close to the optimal conditions as possible. These specific conditions will be included in the experimental details section of Chapters 4 and 5 of this thesis.

3.2 Key Features of an Ideal Molecular Beam

For the molecular beam conditions to be considered as suitable for the gas-liquid scattering experiments reported in this thesis, it needs to have the following features: a) the discharge must be stable, b) the Full Width at Half Maximum (FWHM) of the TOF profiles must be short, and c) the rotational temperature of the OD radicals must be 'cold', i.e. the radicals must preferentially populate the low N rotational levels. Maximising the number density of OD produced by the discharge is also desirable for the experiment; however, the conditions at which it is achieved do not always correspond to conditions suitable for a stable discharge, which in turn affects the reliability of the results obtained. In such cases, obtaining a stable discharge was prioritised over having a larger signal.

Of these features, having a stable discharge is necessary to achieve a reliable and reproducible incident number density of OH (or OD) radicals, which in turn affects the characterization of all the other properties listed in this chapter. A stable discharge is achieved when it fulfils the following conditions: a) the discharge strikes every time the pulsed valve opens, and b) the discharge is active for the full length of the HV pulse applied to the front electrode. Checking whether the discharge is striking every pulse is easily done by observing with the naked eye whether a glow emerges from the discharge device. However, more accurate detection methods need to be used to determine the delay at which the discharge strike starts within the HV pulse. This can be monitored either via a direct measurement of the light produced by the discharge plasma with a highly sensitive optical detector, or by measuring the properties of the electric circuit powering the discharge device while the discharge is striking. Early measurement of the discharge stability were conducted by measuring the discharge plasma glow via an avalanche photodiode viewing the discharge device through a view port in the main chamber. However, the main chamber lacked view ports from which

the device could be observed unobstructed by the gas baffle (discussed in Section 3.6.2), therefore the photodiode could only be used to measure the discharge glow under free jet expansion conditions. The fast switch device used to supply the HV pulse, on the other hand, came with in-build probes in the electrical circuit from which both the current draw and the voltage of the power supplies could be measured without any further modification of the experimental set-up, by connecting the appropriate output to an oscilloscope. As such, the current draw output was used to monitor the stability of the discharge throughout the characterization and optimization experiments reported in this chapter, and in the experiments reported in later chapters.

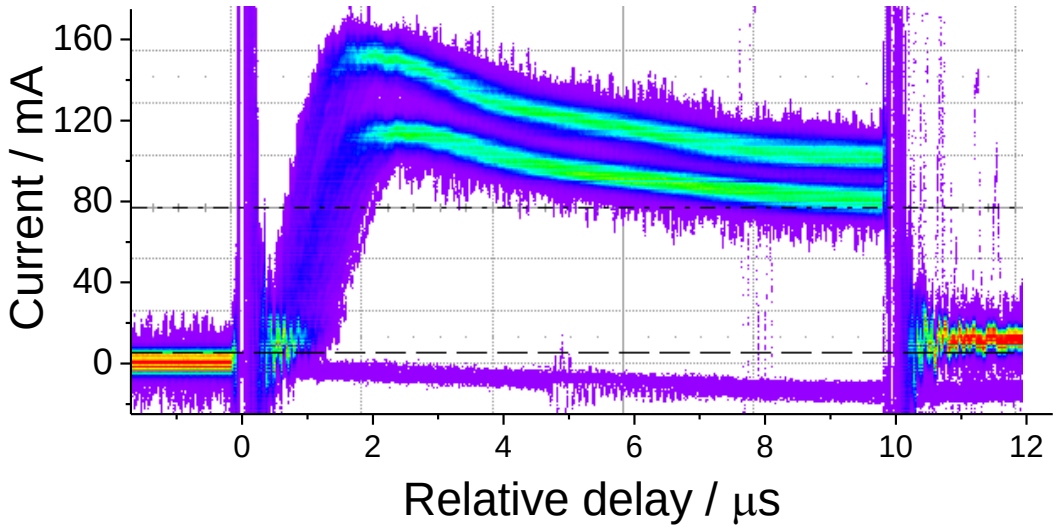

Figure 3.1: Representative persistence trace graph of the current draw from a discharge striking in a molecular beam of D_2O seeded in He. Vertical purple lines at 0 and 10 μs emerge from electrical noise caused by the fast switch device at the start and stop delay of a 10 μs HV pulse. The rise in the trace within the HV pulse indicates that the discharge is striking, drawing current from the power supply. The trace shows that the discharge strikes draw current with two clearly distinguishable modes, as described in the text.

To compare the discharge stability between different set-ups and conditions, persistence plots of the current draw from the fast switch were obtained from the oscilloscope. An example of a persistence plot is shown in Figure 3.1. A persistence plot is the sum of individual discharge pulse traces acquired over a user-determined interval, typically of ~60 s. A false-colour map was then applied to the resulting sum of traces, ranging from

red, to yellow, followed by green, blue and purple. Red indicates the most intense part of the plot, corresponding to a large number of individual traces being observed in the same position, whereas purple indicates a low intensity in the plot, equivalent to a small number of traces.

The persistence plot in Figure 3.1 shows a rise in the current trace within the HV pulse delimited by the two vertical purple lines, indicating that the discharge is striking and OD radicals are being produced. The current draw of the discharge strike occurs in two clearly distinguishable modes, with noticeable differences in the amount of current drawn, and more subtle difference in the rising edge of the trace. The fact that the two modes are distinguishable in the persistence plot suggests that the discharge strike regularly switches between the two modes. This was confirmed through live observation of the current draw traces, which further indicated that the discharge strike was alternating between the two modes with each laser shot. This bi-stability in the discharge striking conditions is present regardless of the carrier gas used, and regardless of the other *in situ* conditions and discharge components used, as described in this and later chapters, although the two modes can only clearly be distinguished at sufficiently high voltages for the HV pulse.

The example persistence graph shown in the figure above is also a good representation of the ideal discharge conditions outlined above, as the rise in current draw starts within 1 μs of the start of the HV pulse, and only one shot was missed. Measurements of the discharge stability conducted with the photodiode showed that the discharge strike would always stop at the end of the HV pulse. However, under unstable discharge conditions, the start time of the discharge strike may occur at any delay after the start of the HV pulse. A discharge starting more than 1 μs later after the start of the HV pulse would therefore lead to a reduction in the OD number density, and thus a reduction in the LIF signal detected. It would also result in the OD packet first appearing at later delays in both TOF profiles and sequences of images, compared to when the discharge strikes for the full HV pulse. Even if the discharge activated for the full HV pulse, the average signal acquired at a given delay can decrease significantly if there are many missed discharge shots. In practice, obtaining a fully stable discharge just by varying the *in situ* conditions (Section 3.3) and the discharge device components (Section 3.4) was not always possible, especially when using carrier gases heavier than helium. In such cases, a first attempt to stabilize the discharge was made by introducing a source of

seed electrons or optimizing the effect of the sources already present (Section 3.5). If the discharge still failed to strike for the reliably over the full HV pulse, the conditions were adjusted to maximize the discharge strike length within the HV pulse, and/or minimize the number of missed shots, in order to reduce the variability in the LIF signal size detected.

An analysis of the persistence plots obtained under a range of different *in situ* conditions revealed that when the voltage of the HV pulse and the backing pressure of the carrier gas were set to obtain the maximum OD number density for a given variation of the discharge device design (discussed in Section 3.4), the peak current output of the corresponding trace was usually found at between 100 and 200 mA in almost every circumstance. This feature turned out to be useful as an empirical guideline to identify, to a first approximation, the range of optimal *in situ* conditions without the need to acquire TOF profiles or excitation spectra, though a full experimental characterization was still required to fine-tune the properties of the molecular beam.

With regards to the other features characteristic of an ideal beam, each of them can be monitored via the TOF profiles and excitation spectra outputs, described earlier in Chapter 2 Section 2.9. Information on the spread of velocities of the radicals can be obtained by measuring the FWHM of the TOF profiles [175], provided that the discharge pulse is shorter than the spread of arrival times corresponding to the physical spread of speeds determined by the carrier gas used, the expansions conditions in the chamber, and the resulting speed ratio. Further details are provided in section 3.3.4. Furthermore, if the incident OD TOF profile has a small FWHM, then the spread of arrival times where the incident and scattered OD signal overlap in a TOF profile will be significantly reduced. This, in turn, reduces the subtraction error in TOF profiles obtained from removing the incident beam contribution from profiles obtained with the surface in, as described in Section 2.9.1.

Excitation spectra, on the other hand, provide information on the rotational state distribution of the radicals in the incident beam, allowing the user to establish whether the radicals are sufficiently rotationally ‘cold’, i.e. whether they preferentially populate the lower rotational N levels. This information can in principle allow the user to evaluate translation-to-rotational energy transfer in collisions with the liquid surface by comparing the incident OD rotational distribution with that of the scattered OD.

However, the analysis becomes intractably complex the more rotational levels are populated in the incident beam, and so these correlations are only practical to consider when essentially all the incident OD radicals populate the lowest N state. In the experiments presented in this thesis, such a rotational distribution for a molecular beam was not achieved, and therefore the energy transfer process was only evaluated qualitatively. Nevertheless, a 'cold' rotational distribution does still provide an advantage in acquiring TOF profiles, as the scattered OD radicals are more likely to occupy the higher rotational N levels than the incident radicals, therefore minimizing, if not outright removing, the incident OD signal contribution in the 'surface in' profiles acquired.

3.3 Optimising the Molecular Beam *In Situ*

The molecular beam experimental set-up has several parameters that can be changed while the pulsed valve and HV pulse are active. These parameters were varied while detecting OD LIF signal in order to find the optimal conditions that produce a stable discharge, a high OD number density and optimal molecular beam properties for a given carrier gas (Section 3.3.1) and set of discharge device components (Section 3.4) used. The following section will list each of the *in situ* parameters and outline a summary of the effect they have on the properties of the molecular beam, using representative results from a molecular beam using He as the carrier gas, and using the original, unmodified Greaves discharge device design (Figure 2.5), unless otherwise noted. In all cases, experimental data was acquired for conditions where the discharge was stable and active for the entire HV pulse, unless otherwise noted. The characterization and optimization tests of the incident beam in this section were done both under free-jet expansion conditions, and with the skimmer, supporting rods, and gas baffle (described in Section 3.6) in place. The representative data shown in this section will be taken from characterization experiments using a free-jet expansion of the beam, unless otherwise noted. With regards to the TOF profiles shown in this and later sections, the delays are set relative to the start of the HV pulse, unless otherwise noted.

3.3.1 Carrier gas

Of the experimental conditions that can be changed without modifying any component in the main chamber, the identity, pressure and temperature of the carrier gas used for the molecular beam plays a key role in determining all the other properties of the incident OD radicals, such as the speed and collision energy of the molecular beam, and the rotational energy distribution of the OD radicals contained within it. The carrier gases used is typically an inert gas, used at pressures above atmospheric pressure. In the gas-liquid scattering experiments reported in this thesis, the radicals were seeded in a high pressure of either He or Ne. Ar was also used during initial proof-of-concept tests to determine the effectiveness of the Greaves discharge device in creating OD radicals compared to the photolysis method described in Section 2.5.3, and subsequently for selected characterization experiments reported in this chapter.

The relation between the pressure of the carrier gas in the discharge region, the discharge voltage and the distance between the electrodes is described by Paschen's law [204], which states that

$$V_B = \frac{Bpd}{\ln(Apd) - \ln[\ln(1+\frac{1}{\gamma_{SE}})]} \tag{3.1}$$

where V_B is the breakdown voltage necessary to light the discharge, p is the pressure of the gas between the electrodes, d is the distance between electrodes, A and B are experimentally determined constants, and γ_{SE} is the secondary electron emission coefficient at the cathode, which depends on various parameters such as the material of the electrodes, the pressure, the gas and the current [204]. Plotting the breakdown voltage V_B against the pressure of the gas at a set distance between electrodes results in a plot called a Paschen curve. Example plots for different noble gases can be seen in Figure 3.2

From the Paschen curve, it is observed that the breakdown voltage for a discharge to strike is dependent on the gas being used, and its pressure. It is also noted that lighter carrier gases such as He and Ne require a higher minimum pressure and higher minimum breakdown voltage than heavier gases, such as Ar. Both features were observed in all the experiments reported in this thesis, and will be expanded on in later

parts of this chapter, specifically in Section 3.3.2 for the backing pressure of the carrier gas used and Section 3.3.3 for the voltage applied to the front electrode.

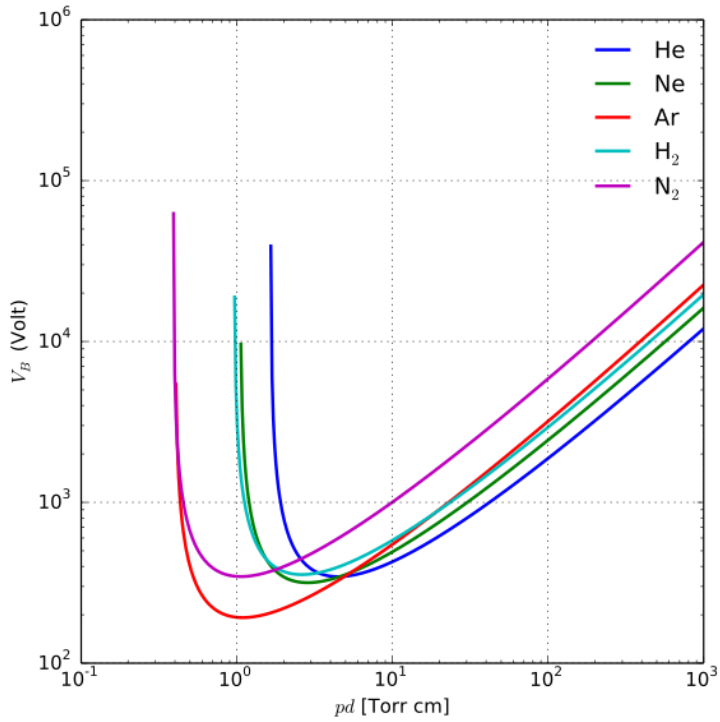

Figure 3.2: Representative Paschen curves obtained for different noble gases (as shown in legend on top-right corner), using the expression for the breakdown voltage (Equation (3.1)) and typical values of the remaining parameters. Image reprinted from reference [205].

When switching carrier gas, several changes were observed both visually and in the diagnostic results. The most apparent change was the colour of the discharge plasma, which was light blue when using He, and orange-red when using Ne. With regards to the stability of the discharge, it was observed that the He carrier provided a more stable discharge over the whole HV pulse with the vast majority of *in situ* conditions and discharge device components tested, whereas it was more difficult to find suitable conditions to obtain a reliable discharge strike with the Ne carrier without an additional source of electrons to seed the discharge region, as discussed in Section 3.5.

Close inspection of several persistence plots, such as those presented in Figure 3.3, indicate that the current drawn from the power supply by the discharge strike follows the same pattern regardless of the conditions used. This pattern consists of an initial

rise in the current draw to a plateau value, followed by a further increase to a peak current output, before returning once again to the plateau value, which remains constant to the end of the HV pulse. While this pattern is observed in the persistence plots obtained for both carrier gases, there are noticeable differences in the delay at which the peak current output occurs and in the relative size of the peak with respect to the plateau current output between different carrier gases. Figure 3.3 shows that with He, the peak current output is small compared to the plateau current output and occurs within the first 10 μs of the start of the discharge strike, whereas for Ne, the peak current output is much higher and occurs at a later delay compared to the start of the discharge strike, requiring HV pulses longer than 10 μs in order to be observed.

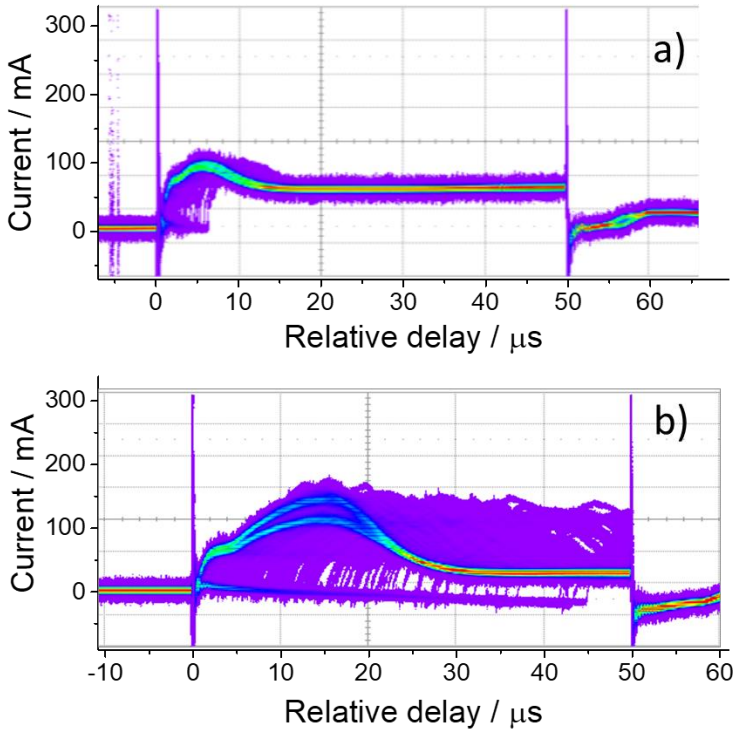

Figure 3.3: Representative persistence plots of current draw for a 50 μs discharge using He (a) and Ne (b) as the carrier gas, where conditions are set to produce the highest OD number density without stabilizing the discharge with the hot filament (described in Section 3.5). Delays are relative to the start of the HV pulse.

From an experimental point of view, the most important changes lie in the speed of the incident radicals, extracted from the TOF profiles, and the rotational energy distribution

extracted from the excitation spectra. The speed of the incident radicals can be estimated from the terminal velocity equation [206], which states that:

$$V_\infty = \sqrt{\frac{2R}{W}\left(\frac{\gamma}{\gamma - 1}\right)T_0} \tag{3.2}$$

where R is the gas constant, W is the molecular weight of the pure gas, or the molar average molecular weight for a gas mixture, γ is the heat capacity ratio, and T_0 is the temperature of the gas in the stagnation state. The estimated speeds for each of the carrier gases used in this thesis are shown in Table 3.1, alongside the experimentally obtained speeds of incident OD radicals reported in Chapter 4 Section 4.3 .

Carrier Gas	**Theoretical speed (a) / m s^{-1}**	**Experimental speed (b) / m s^{-1}**
Helium	1751	1811 ± 8
Neon	783	894 ± 3
a) From Equation (3.2) assuming a molecular beam of pure carrier gas, and T_0 = 295 K; b) From Chapter 4 Section 4.3		

Table 3.1: Terminal speeds of the carrier gas estimated from the prescription of Scoles [206] compared with experimental speeds of OD radicals obtained in Chapter 4

The results shown in Table 3.1 indicate that the experimentally obtained speeds of incident OD radicals are generally faster than the predicted terminal velocities for the pure carrier gas. This difference in speeds is likely due to the OD radicals being accelerated into the main chamber by the electric field generated by the electrodes in the discharge device, or by other conditions in the discharge plasma itself. Nevertheless, the relative magnitude of experimental speeds of incident OD were found to be in good agreement with the relative magnitude of the predicted speeds. In addition, it was found that the TOF profiles of incident OD did not change significantly for a given HV pulse length, regardless of discharge components or *in situ* conditions used, therefore indicating that any change in the average speed will be minimal.

More noticeable changes were observed with the rotational temperatures obtained via a two-temperature fit to the Boltzmann plots (Section 2.9.2) extracted from excitation spectra at the delays corresponding to the peak of the TOF profiles. Nevertheless, the colder temperatures obtained from this analysis were always lower than 100 K for either carrier gas. OD radicals seeded in He would, in general, have a relatively warm rotational temperature of ~80 K; whereas OD radicals seeded in Ne have a colder rotational temperature of ~40 K. The trend in rotational temperatures is consistent with previously obtained results in the literature [177-178, 197-202], where heavier carrier gases were found to produce rotationally colder radicals in a molecular beam due to rotational-to-translational energy transfer caused by collisions of the species being studied with the carrier gas. Specific values of the incident velocities of OD radicals and their rotational temperatures will be reported in the experimental sections of Chapters 4 and 5, with the exact conditions used for each set.

3.3.2 Backing pressure

As can be seen from the example Paschen curves drawn in Figure 3.2, the breakdown voltage for a given carrier gas is dependent on the pressure within the discharge region. This is mainly determined by the backing pressure behind the valve, though the amount of gas present in the discharge region can also be varied by modifying the tension behind the pulsed valve, which in turn changes how far the poppet in the valve is pushed back from the nozzle. In fact, optimal discharge conditions can be obtained at different backing pressures for the same carrier gas simply by adjusting the valve tension. The poppet of the valve can also change shape over time due to wear and tear, changing the optimal conditions over time. Because of these factors, the right backing pressure needed for given experimental conditions can't be worked out *a priori* but needs to be adjusted accordingly for each experimental set-up. This was done by regularly checking the signal sizes and current output at various voltages for several backing pressures, and selecting the one that gave the best results.

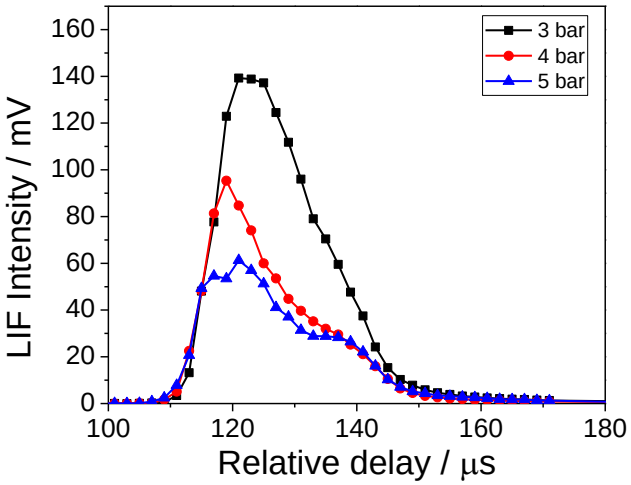

Figure 3.4: Representative TOF profiles of incident OD radicals, showing variations of the profile shape and LIF intensity with backing pressure around an optimal backing pressure of 3 bar. The profiles were acquired on the $Q_1(1)$ transition for a molecular beam seeded in He under free jet expansion conditions. Discharge voltage was set at -1550 V, HV pulse length was 15 μs. Lines between points in the TOF profiles were added to highlight the presence of a shoulder on the falling edge of the.

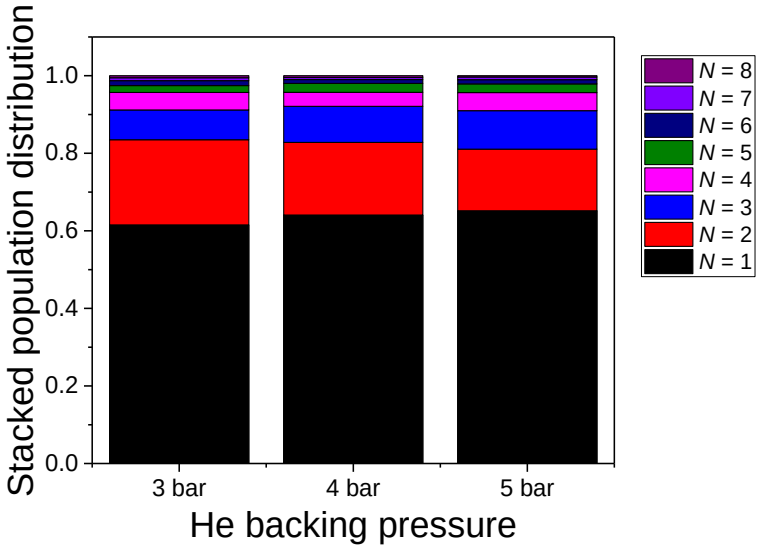

Figure 3.5: Stacked rotational population distributions extracted from single excitation spectra taken at the peak of the TOF profiles shown in Figure 3.4. Populations shown are from $N = 1$ to 8, normalized to the sum of their populations.

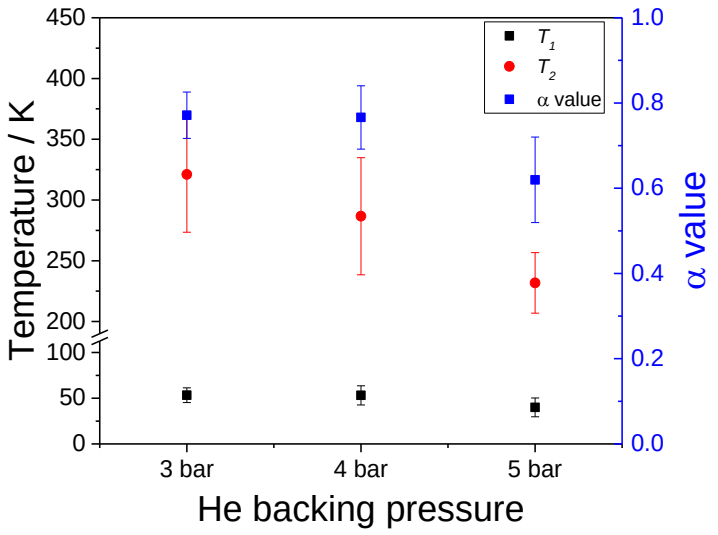

Figure 3.6: Rotational temperatures and α values obtained from a two temperature fit (Chapter 2 Section 2.9.2) to the populations shown in Figure 3.5. Errors are derived from the two temperature fit.

Throughout these optimization tests, it was observed that the signal size of the incident OD at a fixed voltage generally increased proportionally to the increase in backing pressure up to the optimal conditions, beyond which the signal size would then decrease. In addition, a shoulder on the falling edge of the TOF profiles would become more prominent above the optimal pressure, as shown in Figure 3.4. The rotational energy distribution for each backing pressure was extracted from single excitation spectra taken at the peak of the respective TOF profiles (Figure 3.5). Rotational temperatures and α values were then obtained from a two-temperature fit (Chapter 2 Section 2.9.2) to those populations (Figure 3.5). Both the rotational energy distribution and the values obtained from the two-temperature fit analysis suggest that changing the backing pressure of the carrier gas has a minimal effect on the rotational cooling of the OD radicals, and so the backing pressure can be freely adjusted in order to optimize other properties of the molecular beam.

3.3.3 Discharge voltage

The discharge strike in the Greaves device was obtained by applying a high negative voltage to the front electrode and setting the other electrode to ground. Conventional wisdom indicates that, out of all the possible combinations in which the voltage can be applied to a discharge device, this combination is the one most likely to provide a discharge that strikes reliably each time the pulsed valve opens. Anderson *et al.* [207] suggest that this is likely caused by the difference in mobility between electrons and buffer gas cations, where a flux of heavy cations is less likely to propagate effectively upstream against the supersonic gas flow compared to the flow of electrons.

The Paschen curves in Figure 3.2 also suggest that, for a given carrier gas and pressure within the discharge region, there is an optimal voltage at which a discharge strikes is likely to occur. This optimum voltage was determined empirically for each carrier gas by varying the HV pulse voltage in order to maximize the OD number density produced by the discharge strike. Through several characterization experiments reported in this chapter, it was determined that the optimum breakdown voltage also depends on other experimental conditions, such as the discharge device components used (Section 3.4), or the method employed to seed the device with electrons (Section 3.5). The specific optimal discharge voltage for each set-up will be reported in the appropriate section within this chapter, and in the experimental methods section in Chapters 4 and 5. Nevertheless, the variation of LIF signal size and rotational energy distribution with HV pulse voltage was found to follow a similar trend regardless of the conditions used, which will be discussed below.

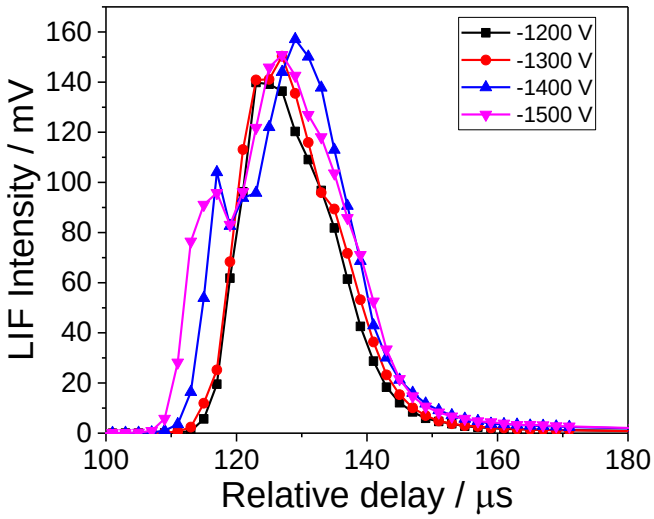

Figure 3.7: Representative TOF profiles of incident OD radicals, showing variations of the profile shape and LIF intensity with discharge voltage around an optimal voltage of -1300 V. The profiles were acquired on the $Q_1(1)$ transition for a molecular beam seeded in He at 3 bar, under free jet expansion conditions. HV pulse length was 15 μs. Lines between points in the TOF profiles were added in order to highlight the presence of a shoulder in the profile on the rising edge, as described in text.

As observed in the representative TOF profiles (Figure 3.7), the LIF signal size was found to generally increase with increasing voltage up to the point where the peak current draw reaches 200 mA. Beyond this point, increasing the voltage would decrease of the overall LIF signal, despite a continuing increase in the current draw. At higher voltages, an additional shoulder in the TOF profiles is observed at delays earlier than the peak of the profile This behaviour was also observed by Lewandowski *et al.* [208]. When the peak of the current draw increased above circa 400-500 mA, there was also the risk of the glow discharge switching to an arc discharge regime, where the current draw increased dramatically to values of several amps, which usually triggered the in-built trip of the fast switch, set at 10 A.

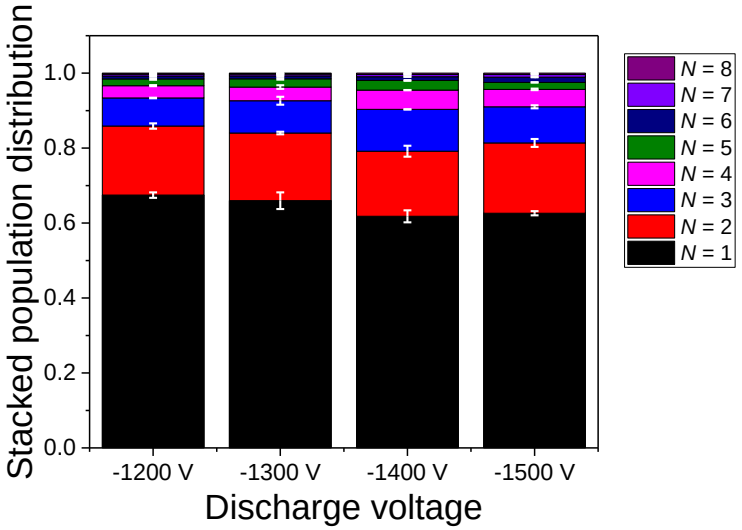

Figure 3.8: Stacked rotational population distribution extracted from excitation spectra taken at the peak of the TOF profiles shown in Figure 3.7. Populations shown are from $N = 1$ to 8, normalized to the sum of their populations. The populations are the result of an average of two excitation spectra. The standard error of the mean for each population is shown in white.

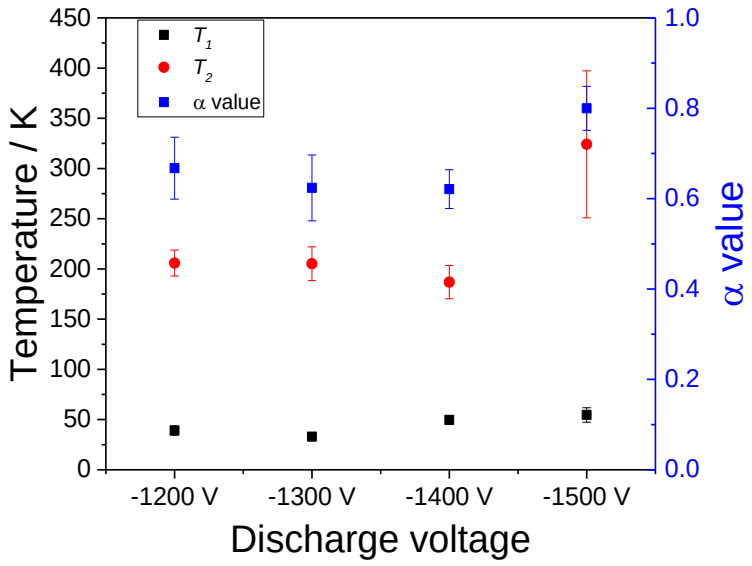

Figure 3.9: Rotational temperatures and α values obtained from a two temperature fit (Chapter 2 Section 2.9.2) to the populations shown in Figure 3.8. Errors represent the errors in the fit, using an instrumental weighting of the errors in the populations.

The rotational population distributions of the incident OD radicals were extracted from excitation spectra taken at the peak of the TOF profiles shown in Figure 3.7, and shown in Figure 3.8. Rotational temperatures and α values were then obtained from a two-temperature fit to those populations, and the results are shown in Figure 3.9. The differences in the stacked relative populations as a function of discharge voltage were found to be small and within error of each other, which corresponds to small differences in the two temperature fit values, as shown in Figure 3.9. It was therefore concluded that the discharge voltage does not significantly affect the rotational cooling of the molecular beam, and therefore it can be freely optimised to obtain the maximum signal size.

3.3.4 HV pulse length

The maximum length for which the discharge can be active, provided all other *in situ* conditions have been optimised to obtain a stable discharge, is determined by the duration of the HV pulse applied to the front electrode. The HV pulse length can, in turn, be set independently via the delay generator. Using the experimental set-up described in Chapter 2, the HV pulse length could be as short as 2 μs within the gas pulse, up to a maximum length equivalent to the length of the gas pulse. The latter arrangement, referred to as a Continuous-Wave (CW) discharge, can also be achieved by connecting the power supply directly to the electrode.

The advantages of using a short HV pulse to generate the OD radicals were first demonstrated by Lewandowski and co-workers [208]. In their experiment, OH radicals were generated in a molecular beam seeded in Xe at 3 bar backing pressure, with the pulsed valve opened for 100 μs. By varying the length of the HV pulse, Lewandowski's group showed that, under CW discharge conditions, OH radicals in the molecular beam had a rotational temperature of 198 K, whereas when the HV pulse was reduced to 1 μs, the rotational temperature of the radicals was reduced to 28 K. The higher rotational temperature for OH under CW discharge conditions was ascribed to heating caused by the violent discharge process, therefore having shorter HV pulses will reduce the heating effect of the discharge plasma on the radicals. Similar improvements were also reported by other groups in the literature [198, 209-210]. Though cold molecular beams of OH below 50 K have been previously obtained under CW discharge conditions [177-178, 197], these results were achieved using heavier carrier gases than the ones used in

the experiments reported in this thesis, and with commercial pulsed valves capable of shorter gas pulses than those achievable with the General valve used in this experimental set-up.

The majority of experiments reported in this thesis were carried out with a HV pulse length of 10 μs. CW discharges were also used throughout the data acquisition, initially for proof-of-concept experiments to test the effectiveness of the discharge device, and to obtain thermal calibration spectra (Section 2.9.2) and the instrument function for the image acquisition set-up (Section 5.3) in later experiments. The optimal short HV pulse length was initially determined via characterization experiments conducted prior to the single-point detection experiments reported in Chapter 4. At the time, the current draw of the discharge was not monitored, and so the shot-to-shot stability of the discharge was determined by monitoring the peak LIF signal size over several laser shots with the tune-up program. From these and other characterization experiments, it was determined that the 10 μs HV pulse length provided a good compromise between discharge stability, OD number density, and the optimal properties of the molecular beam.

Following the experiments reported in Chapter 4, the optimization of the molecular beam reported in this chapter enabled the user to test and characterise shorter HV pulses. These tests were carried out using He as the carrier gas, in order to determine whether the cooling of the OD radicals using the 10 μs HV pulse could be improved by either shortening the pulse length down to 1.25 or 2 μs, using trains of short pulses separated by gaps to make up an overall pulse length of 10 μs, or using a combination of the two. Persistence plots obtained from a representative set of these attempts are shown in Figure 3.10, with the associated TOF profiles shown in Figure 3.11. The rotational population distribution extracted from those conditions are shown in Figure 3.12, and the temperatures and α values obtained from a two temperature fit to the populations is shown in Figure 3.13.

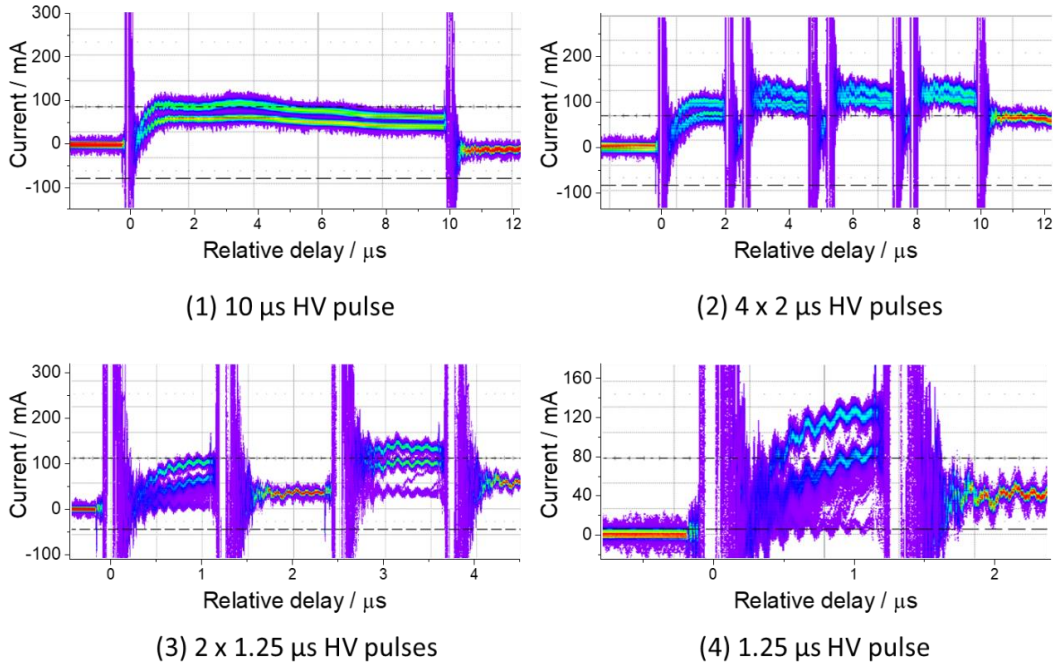

Figure 3.10: Representative persistence plots obtained from a molecular beam of OD seeded in 3 bar of He, firing 1) a 10 μs HV pulse, 2) four 2 μs HV pulses / 0.5 μs gaps, 3) two 1.25 μs HV pulses / 1.25 μs gap, 4) a 1.25 μs HV pulse within a nominal gas pulse length of 500 μs. Discharge pulse length was set as – 800 V. The discharge device used a 2 mm hole front electrode, a faceplate with a 12 mm channel, and a 3 mm diameter spacer, as described in Section 3.4.

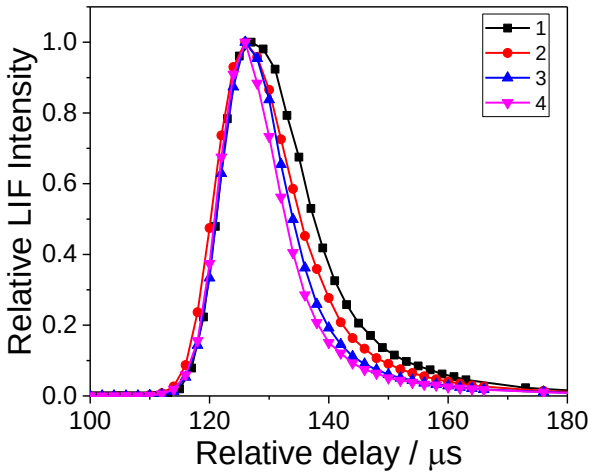

Figure 3.11: Representative peak normalized TOF profiles of the incident OD radicals obtained for different HV pulse combinations, as shown in Figure 3.10. Profiles were acquired on the $Q_1(1)$ transition.

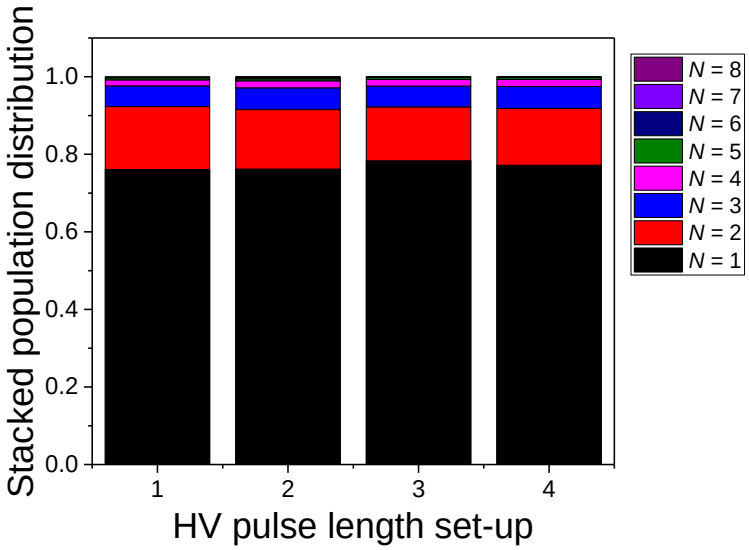

Figure 3.12 Stacked rotational population distribution extracted from single excitation spectra taken at the peak of the TOF profiles shown in Figure 3.11. Populations shown are from $N = 1$ to 8, normalized to the sum of their populations.

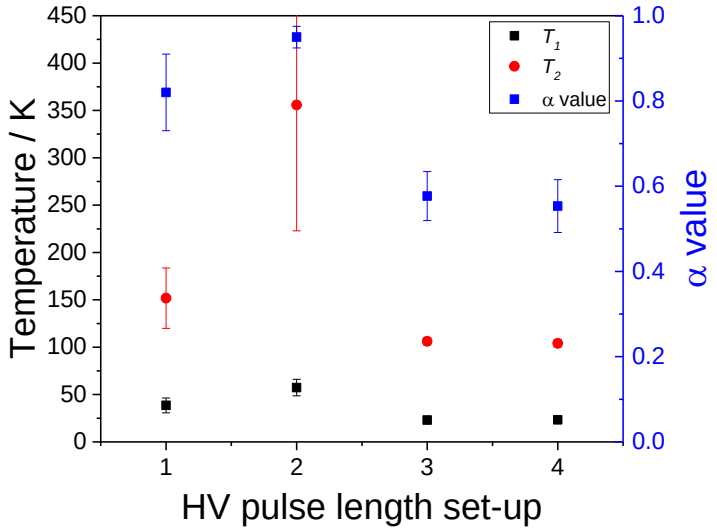

Figure 3.13: Rotational temperatures and α values obtained from a two temperature fit (Chapter 2 Section 2.9.2) to the populations shown in Figure 3.12 above, with associated errors in the fits.

Both the TOF profiles (Figure 3.11) and the rotational populations (Figure 3.12) and temperatures (Figure 3.13) show that the beam properties can be further optimized by using a shorter HV pulse. However, these improvements are marginal, amounting to a difference of circa 4-5 μs in the FWHM compared to the 10 μs pulse length and about 10-15 K in the colder rotational temperature, which is the more predominant temperature obtained from the two-temperature fit. Using a shorter pulse also reduces the OD number density produced by the discharge, and runs the risk of increasing the number of missed discharge strikes, as shown by the persistence plots in Figure 3.10, which would in turn lead to a further decrease in the average OD LIF signal acquired at a given discharge-probe delay. As for using a train of pulses, the results show that the differences between them and with the continuous HV pulses tested are very small and within error. These results confirm that a HV pulse length of 10 μs provides a good compromise between discharge stability, OD number density, and the properties of the molecular beam, and thus this pulse length was used for the gas-liquid scattering experiments reported in Chapter 5.

3.3.5 Gas pulse-discharge delay

If the HV pulse length is shorter than the duration of the gas pulse, then the discharge can be applied to different portions of the gas pulse. This was achieved by changing the delay between the start of the HV pulse and the opening time of the pulsed valve, hence referred to as the gas pulse-discharge delay. A representative set of TOF profiles, taken by applying a 15 μs HV pulse at different discharge-gas pulse delays at fixed voltages and backing pressures, is shown in Figure 3.14. Rotational population distributions obtained from those profiles are shown in Figure 3.14, and the resulting rotational temperatures and α values obtained from a two temperature fit are shown in Figure 3.16.

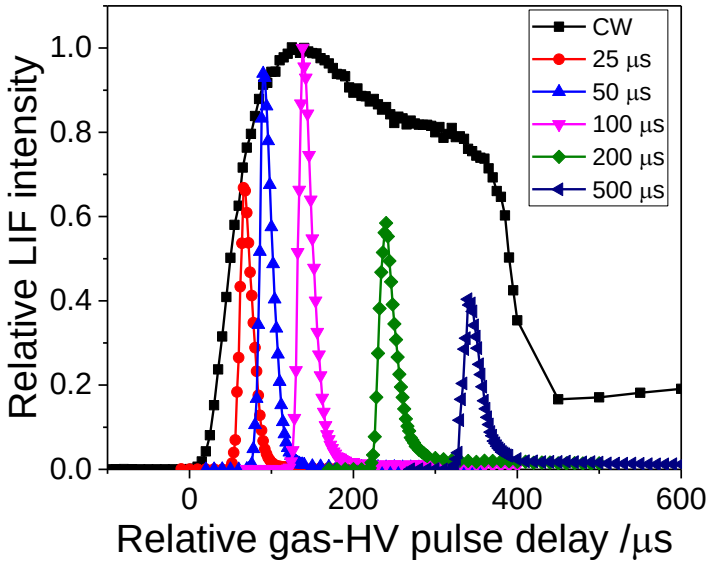

Figure 3.14: Representative TOF profiles of incident OD LIF signal obtained from a 15 µs HV pulse fired at different gas-discharge pulse delays within a nominal gas pulse length of 500 µs. Profiles have been normalized to the peak of the profile obtained at the gas-discharge pulse delay of +100 µs. A TOF profile obtained with a CW HV pulse (black squares), normalized to the LIF signal at the gas-discharge pulse delay of +100 µs, is included for comparison. The profiles were acquired on the $Q_1(1)$ transition for a molecular beam seeded in He with backing pressure of 3 bar, with a 5 mm diameter skimmer placed at a skimmer-pulsed valve distance of 167 mm (see Section 3.6.1). The discharge voltage was set at -1700 V.

The differences in LIF signal size between the profiles obtained with the short HV pulses at early gas-discharge delays shown in Figure 3.14 is consistent with the expected relative density of the gas pulse at the corresponding delays, shown by the TOF profile obtained with the CW discharge. The differences in relative LIF signal between the short HV pulse TOF profiles obtained at later gas-discharge delays and the CW discharge profile is likely due to the earlier OD generated in the CW pulse reappearing in the detection region after collisions with the walls of the main chamber and/or other components present in the chamber such as the skimmer holder plate. This issue will be addressed in further detail in Section 3.6. It was also noted that the discharge was more unstable when starting right at the rising edge of the gas pulse, which indicates that the pulsed valve might not always open at the same time between pulses.

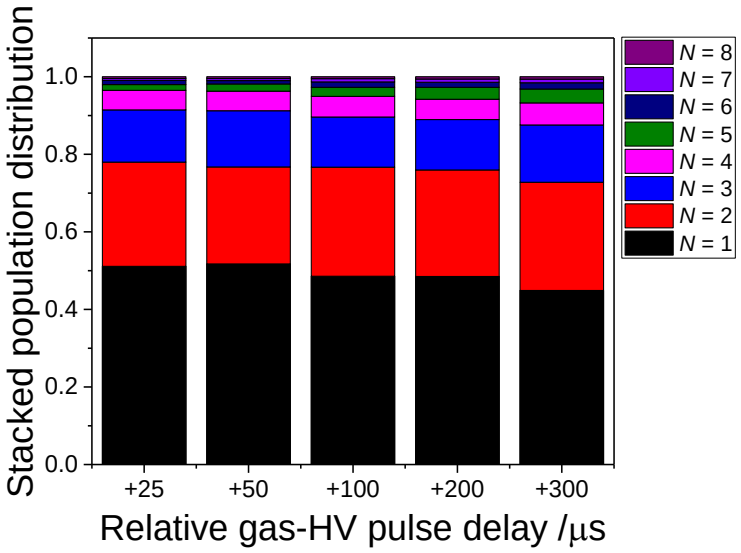

Figure 3.15: Stacked rotational population distribution extracted from single excitation spectra taken at the peak of the TOF profiles for the short HV pulse lengths shown in Figure 3.14. Populations shown are from $N = 1$ to 8, normalized to the sum of their populations.

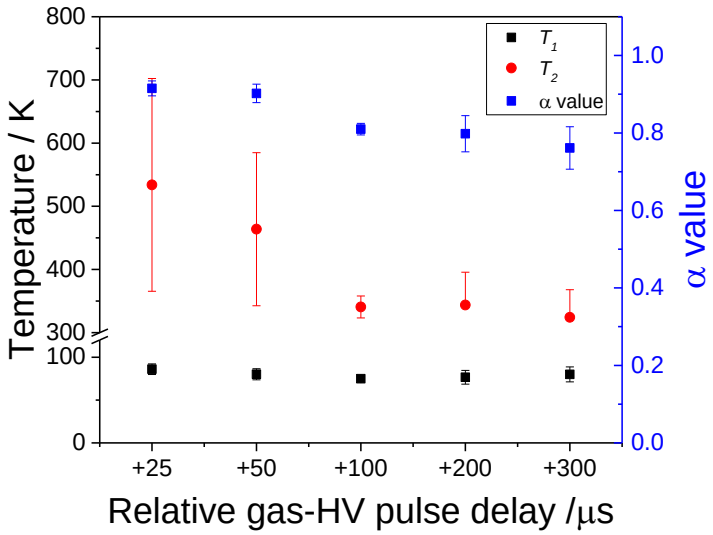

Figure 3.16: Rotational temperatures and α values obtained from a two temperature fit (Chapter 2 Section 2.9.2) to the populations shown in Figure 3.15, with associated errors in the fit.

The rotational population distributions (Figure 3.15) and associated temperatures and α values (Figure 3.16) extracted from the peak of the TOF profiles, however, were found to not be significantly different (within error) when varying the discharge-gas pulse delay. Based on these results, the discharge-gas pulse delay of the HV pulse was set as close to the rising edge of the gas pulse as possible while maintaining a stable discharge and a high signal size. In practice, this corresponded to a discharge-gas pulse delay of ~100 μs. This also had the advantage of minimizing the amount of gas in the molecular beam that collides with the surface prior to the arrival of the radicals created by the discharge, thus reducing any gas phase collisions that may occur above the surface.

3.3.6 Rotational temperatures at different discharge-probe delays

The rotational temperatures used to compare different settings were usually extracted from excitation spectra taken at the delays corresponding to the peak of the associated TOF profile from the lowest *N* level. While this provides some consistency when comparing data, it does not necessarily imply that the rotational energy distribution is the same at all delays. Conventional wisdom would indicate that, if the OD radicals generated from a short HV pulse suffered no additional collisions before entering the detection region, then the resulting TOF profile could be fit to a Gaussian distribution. However, at low *N* levels, the TOF profiles obtained experimentally feature an additional 'tail' at later delays compared to the rising edge of the profile. This tail becomes more prominent at higher rotational levels. This would suggest that a small fraction of rotationally cold OD radicals undergo gas phase collisions where translation-to-rotational energy transfer processes occur prior to entering the detection region, resulting in slower, rotationally warmer OD radicals appearing at later delays.

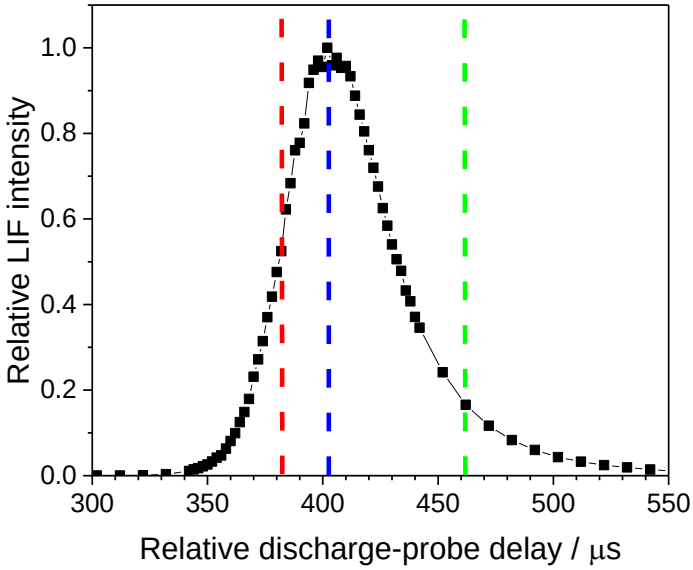

Figure 3.17: Representative peak-normalized TOF profile of incident OD LIF signal. The profiles were acquired on the $Q_1(1)$ transition for a free-jet expansion of a molecular beam seeded in Ar, with backing pressure of 1.3 bar, using a 10 μs HV pulse fired within a nominal gas pulse length of 500 μs. Discharge device used the original Greaves design components, but with a 2 mm diameter front electrode hole and a faceplate with a 12 mm channel (see Section 3.4). Dashed lines indicate the discharge-probe delays at which excitation spectra were taken, corresponding to the rising edge (red line, at -20 μs from the peak), the peak of the profile (blue line), and the tail (green line, at + 60 μs from the peak)

To check this assumption, excitation spectra were taken at the delays corresponding to the 'rising edge' (roughly at the mid-point of the rise in signal of the profile), the 'peak', and the 'tail' (roughly at the point where the 'tail' begins to appear) of the TOF profile, shown by the red, blue and green lines in the representative TOF profile obtained using Ar as the carrier gas and shown in Figure 3.17. A set of rotational populations taken at those representative conditions is shown in Figure 3.18, and the rotational temperatures and α values derived from those populations is shown in Figure 3.19.

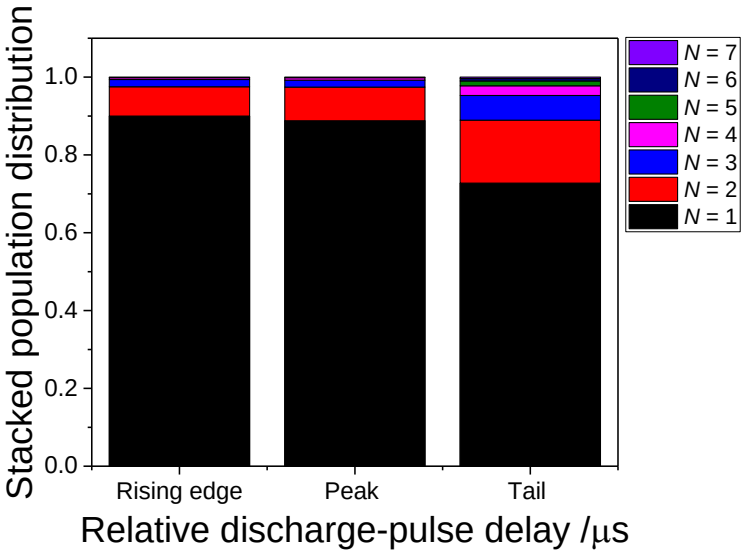

Figure 3.18: Stacked rotational population distribution extracted from single excitation spectra obtained from a molecular beam using the same conditions as the representative TOF profile shown in Figure 3.17. The excitation spectra were taken at different discharge-probe delays, also shown in Figure 3.17. Populations shown are from $N = 1$ to 8, normalized to the sum of their populations.

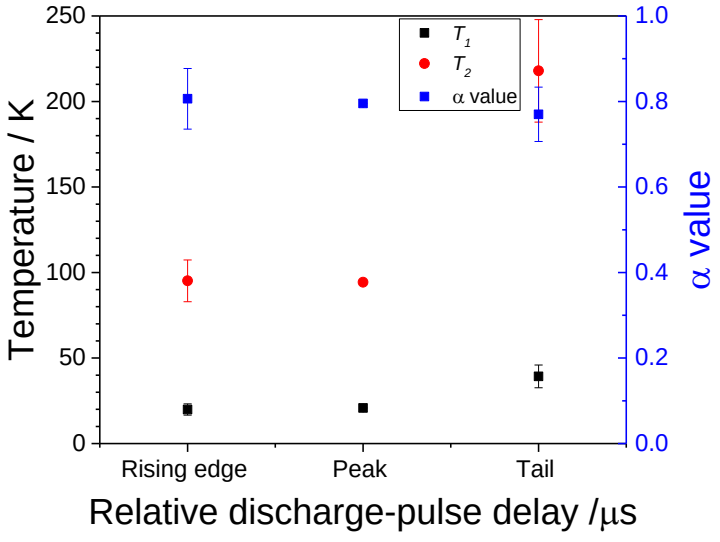

Figure 3.19: Rotational temperatures and α values obtained from a two temperature fit (Chapter 2 Section 2.9.2) to the populations shown in Figure 3.18, with associated errors in the fit.

The data show that, while the rotational temperatures remain almost constant up to the peak of a given TOF profile, they increase slightly towards the tail of the profile. Despite the increase in temperature, the rotational populations of OD at the 'tail' of the profile (Figure 3.18) shows that the majority of OD radicals in the beam still populate the lower N level. When related to the OD number density at the 'tail' of the profile with respect to its peak (Figure 3.17), the results indicate that only a small fraction of the overall incident OD packet has become rotationally warmer compared to the rest of the packed. Thus, the results confirm that slower moving, rotationally hotter OD radicals appear after the core part of the profile containing the rotationally colder OD has passed through. Reassuringly, the results also confirm that this rotationally warmer fraction of OD is unlikely to make a significant contribution to the OD signal scattered from a liquid surface, so it can be safely assumed that the majority of scattered OD LIF signal at higher rotational energies emerges from the large fraction of cold incident OD radicals undergoing translational-to-rotational energy transfers to higher N levels.

3.4 Discharge Device Design

In this section, several variations of the Greaves discharge device described in section 2.5.4 and shown in Figure 2.5 will be described. Each variation of the device was then tested with the beam operating in a free-jet expansion set-up. Helium was used as the carrier gas for all the experiments reported in this section. For some components, additional tests were conducted using neon as the carrier gas. For each variation of the device, TOF profiles were acquired at the $N = 1$ level, while rotational temperatures were extracted from excitation spectra acquired at the delay corresponding to the peak of the TOF profile. The results were compared with a previously optimized set of experiments using the original Greaves device, under the same optimal *in situ* conditions. From those comparisons, the effect of each modified component on the stability of the discharge and the properties of the molecular beam was determined.

The components of the discharge device that were changed were the PTFE faceplate, the front electrode, the grounding electrode, and the ceramic spacer between electrodes. All other components of the device were unlikely to influence the molecular beam properties, and so could be freely altered to accommodate any major change in the design of the previously listed components (e.g. when the base of the grounding electrode was widened to allow for a metal tag to be soldered onto it). The following

sections will describe the variations for each of the listed components in turn, and their effect on the molecular beam properties.

3.4.1 Faceplate

In the original design of the discharge device (Figure 2.5) the faceplate design was such that it did not constrain the molecular beam once it had exited the front electrode. As the rotational cooling of the radicals in the molecular beam is caused by collisions with the carrier gas, a new set of faceplates was designed to further constrain the molecular beam before it entered the vacuum chamber. This was done by including a channel in the faceplate, starting just after the front electrode and extending to 6 mm (in the first design) and 12 mm (in the second design), before opening up into a 40° cone. An example of a faceplate design with the channel is shown in Figure 3.20. The diameter of the channel was set to match the diameter of the inner hole of the front electrode. The 40° cone aperture was chosen based on results reported in the literature [175].

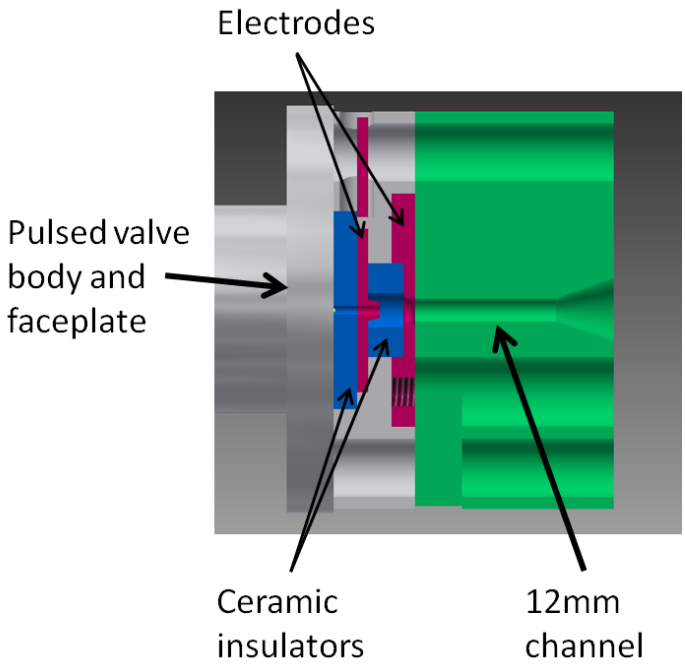

Figure 3.20: Discharge device assembly, using a faceplate with a 12 mm channel. The faceplate is highlighted in green.

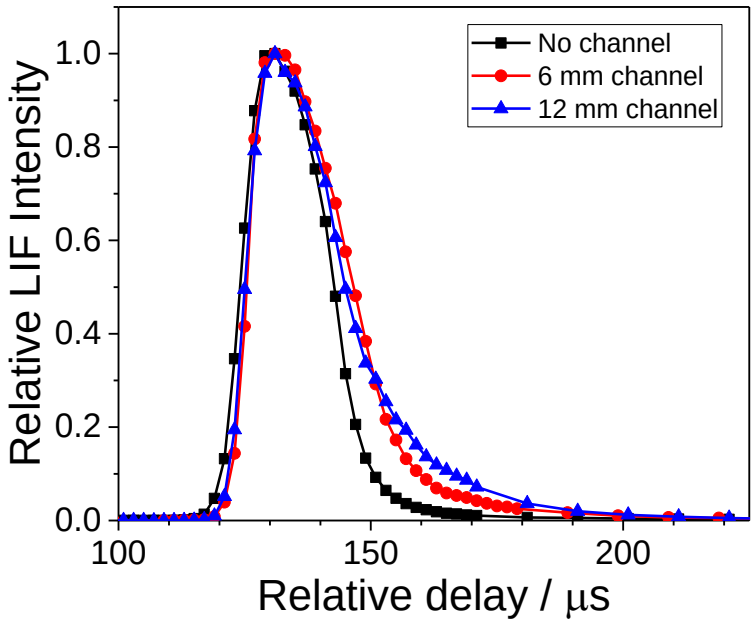

Figure 3.21: Representative peak-normalized TOF profile of incident OD LIF signal. The profiles were acquired on the $Q_1(1)$ transition for a free-jet expansion of a molecular beam seeded in He, with backing pressure of 3 bar, using a 10 μs HV pulse fired within a nominal gas pulse length of 500 μs. Discharge device used the original Greaves design components, but with a 2 mm diameter front electrode hole and a faceplate with no channel (black), a 6 mm channel (red) and a 12 mm channel (blue).

The faceplates with the two different channel lengths were tested and compared with the equivalent no-channel faceplate, using different carrier gases and a range of different discharge device components. The first set of experiments was carried out using He as the carrier gas. A representative set of TOF profiles obtained from this arrangement is shown in Figure 3.21. The rotational population distribution from each set of data is shown in Figure 3.22 while the rotational temperatures derived from those populations are shown in Figure 3.23.

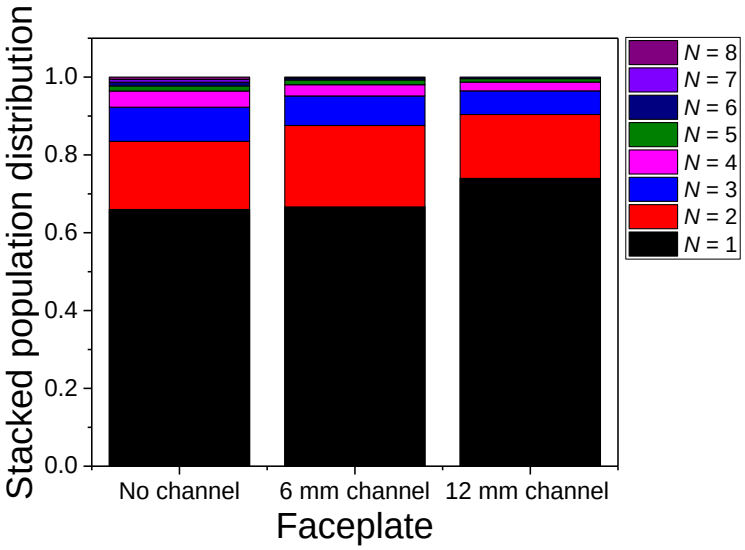

Figure 3.22: Stacked rotational population distribution extracted from single excitation spectra taken at the peak of the TOF profiles using different discharge device faceplates under the conditions described in Figure 3.21. Populations shown are from $N = 1$ to 8, normalized to the sum of their populations.

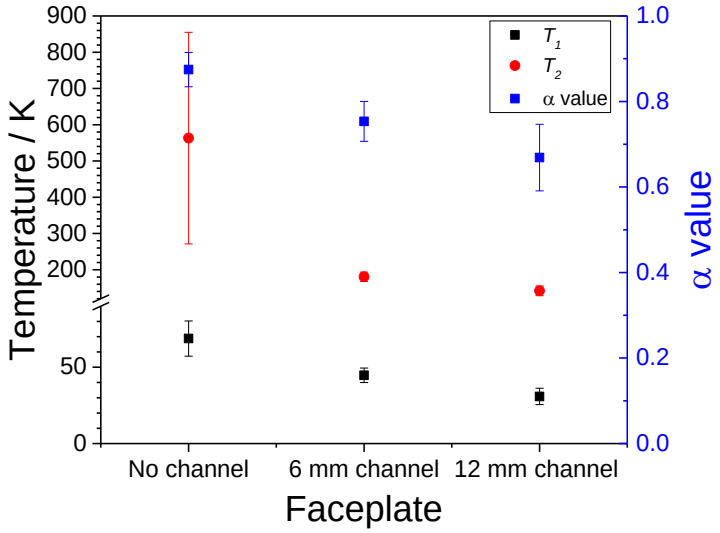

Figure 3.23: Rotational temperatures and α values obtained from a two temperature fit (Chapter 2 Section 2.9.2) to the populations shown in Figure 3.21, with associated errors in the fit.

The results show that the rotational temperature of the OD radicals is colder when using faceplates with a channel. They also show that having a longer channel does provide some improvements in the cooling over the 6 mm channel faceplate, though the improvements are smaller when compared with the results from using the faceplate with no channel. This gain in rotational cooling, however, comes with some disadvantages. The TOF profiles in Figure 3.21 show that adding the channel increases the length of the tail in the profile, which may marginally increase the FWHM of the profile and the amount of hotter OD radicals appearing at later times, as discussed earlier in section 3.3.6, whereas the results from the no channel faceplate gave an almost Gaussian shaped TOF profile. Using the faceplate with a channel was also found to restrict the use of the hot filament method of stabilising the discharge via electron seeding (as explained in more detail section 3.5 below).

Throughout the experiments carried out with He as the carrier gas, the discharge was found to strike reliably for the entire HV pulse regardless of the faceplate used. When the faceplates were then tested with Ne as the carrier gas, however, the discharge failed to strike reliably for HV pulses shorter than 100 µs when using the faceplates with either the 6 mm or 12 mm. Furthermore, when using HV pulses of 100 µs or longer, the discharge start time was found to vary frequently within a range of up to 30 µs from the start of the HV pulse, with the peak current output part of the trace (Section 3.3.1) increasing as the delay between the start of the HV pulse and the discharge strike increased. These issues were not observed when using the faceplate with no channel. The instability of the discharge strike when using the faceplates with channels was therefore assumed to be the result of choking of the molecular beam inside the discharge device itself, caused by the heavier Ne carrier gas being constrained by the channel itself.

Based on these results, the faceplate with the 12 mm channel was only used for the scattering experiments with the image acquisition set-up using He as the carrier gas (described in Chapter 5 of this thesis), while for all other experiments, a faceplate with no channel was used.

3.4.2 Front electrode

In previous discharge device designs, the front electrode consisted of a thin ring located outside of the discharge device casing, mounted onto a support connected to the pulsed valve that ensured it was on-axis with the valve nozzle [177-178]. By contrast, the front electrode of the Greaves discharge device consists of a larger stainless steel disk encased inside the body of the device, with a hole at a set diameter in the centre of the disk, and a recess on one side to accommodate the ceramic spacer. The design of the discharge device ensures that the central hole of the electrode is always located on-axis with respect to the pulsed valve nozzle, regardless of the variations in the electrode's design. The large disk size also made it easier to connect the electrode to the negative HV supply, by securing a Kapton wire with a spade connector to an additional off-centred tapped hole drilled in the disk via a small bolt.

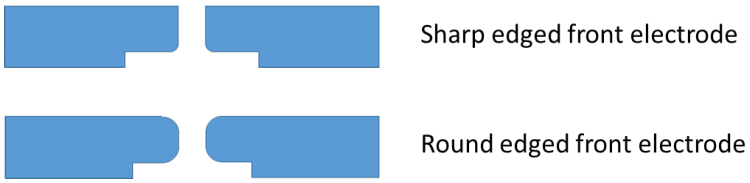

Figure 3.24. Side-view schematic designs of the two variations of front electrodes used for testing the effect of various diameter sizes for the inner hole. Adapted from reference [203]

To determine the optimum diameter for the hole in the front electrode, several front electrodes with varying diameters were made, based on two different designs shown in Figure 3.24. In both designs, the side that was facing the grounding electrode, i.e. the side with the recess for the ceramic spacer, has rounded inner hole edges. The main difference between the two designs lies instead in the edges of the 'exit' side of the hole facing the inside of the main chamber, where one design has sharp edges, while the other has rounded edges. Electrodes with the inner hole diameter of 1 mm, 2 mm, and 3 mm were made up with the sharp edge design, while electrodes with inner hole diameter of 2 mm and 3 mm were made with the rounded edge design. Both sets of electrodes were tested using the original Greaves device components. Additional tests were also conducted with different faceplate designs. A summary of the results from these tests will be discussed below.

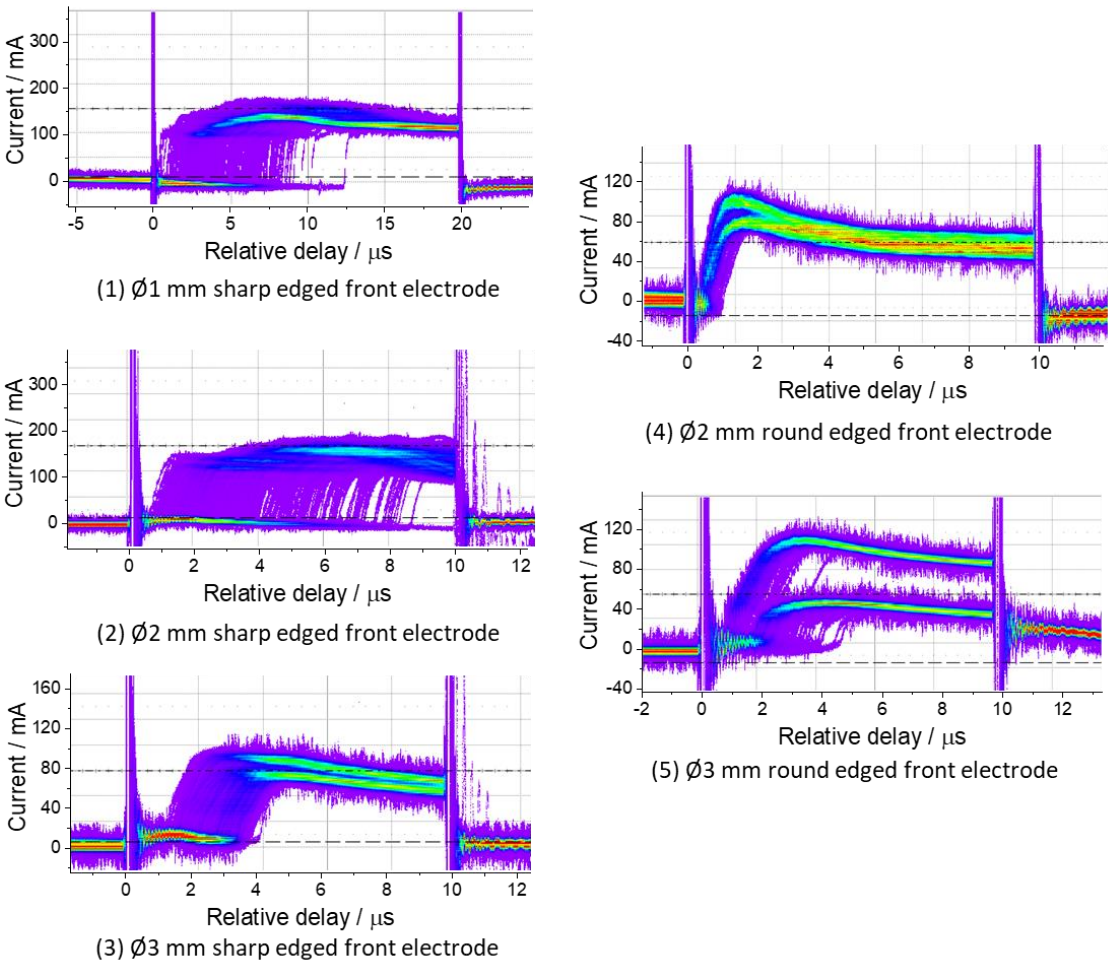

Figure 3.25: Representative persistence plots obtained from applying the discharge to a molecular beam of OD, seeded in 3 bar of the He carrier, using a 1 mm (1), 2 mm (2), and 3 mm (3) diameter sharp edged front electrode, and a 2 mm (4), and 3 mm (5) rounded edge front electrode, under the best *in situ* conditions available to achieve the most stable discharge for the electrode. The experiments were carried out using the original Greaves device grounding electrode and spacer and a faceplate with no channel.

The effect each electrode had on the discharge stability is shown in Figure 3.25. In general, the results show that the discharge stability electrodes with sharp edges on one side has generally much poorer stability than the equivalent electrodes with rounded edges on both sides. The stability of the electrodes with sharp edges does seem to improve with the larger diameter hole of 3 mm, whereas the opposite is true for the electrodes with rounded edges.

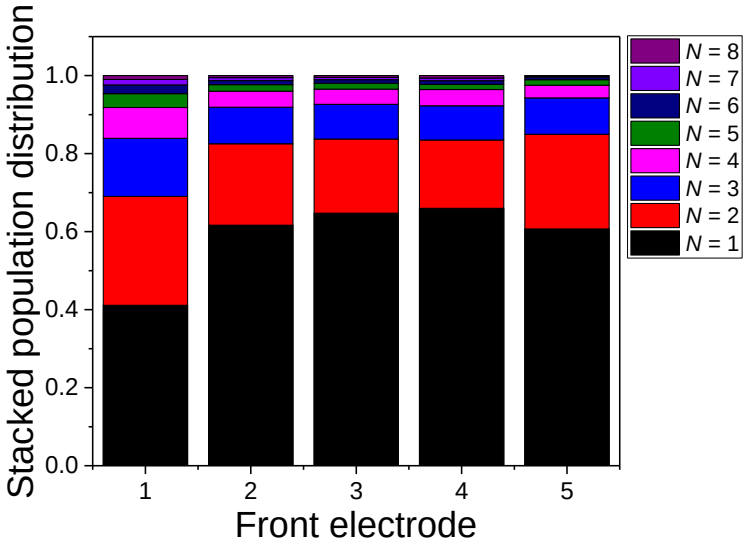

Figure 3.26: Stacked rotational population distribution extracted from single excitation spectra taken as close to the peak of the TOF profiles as possible (accounting for the instability of the discharge at the rising edge of the TOF profile), using different discharge device front electrodes as indicated in Figure 3.25. Populations shown are from $N = 1$ to 8, normalized to the sum of their populations.

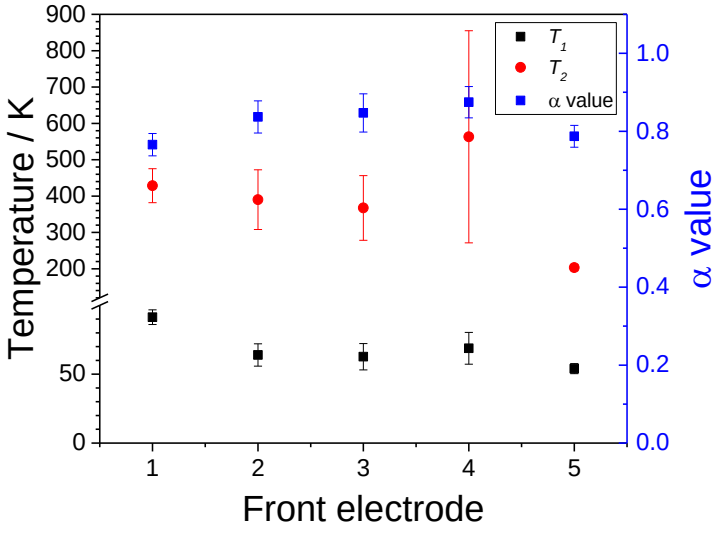

Figure 3.27: Rotational temperatures and α values obtained from a two temperature fit (Chapter 2 Section 2.9.2) to the populations shown in Figure 3.26, with associated errors in the fit.

The rotational populations (Figure 3.26) and extracted rotational temperatures and α values (Figure 3.27) obtained from each set-up show that there is little difference in the cooling of the radicals when using either the 2 mm or 3mm diameter hole for either electrode design, indicating that none of the front electrode designs influences the properties of the molecular beam significantly, other than the stability of the discharge strike itself. Of all the variations tested, the 2 mm diameter hole front electrode, with the edges of the hole rounded on both sides, provided the most stable electric discharge conditions, and was thus used in all the experiments reported in this thesis

One final note is that, when using the discharge device over a period of months, a brown-coloured substance, likely arising from the discharge plasma partially eroding the ceramic insulator between electrodes, starts to accumulate around the inner hole of the outer electrode, though not on the rounded edges or the inside of the hole itself. This causes the discharge conditions to become progressively unstable over time and so the substance needed to be removed from the electrode regularly, or the electrode itself needed to be replaced if cleaning it is not possible.

3.4.3 Grounding electrode

The grounding electrode used in this device has a cone shaped nozzle emerging from a stainless steel base, similar to the design used by van Beek *et al.* [177]. The main difference between the van Beek design and the Greaves device is that the van Beek design had sharp edges at the tip of the cone, whereas the Greaves design uses a cone nozzle with a flat tip. In order to test the effectiveness of each grounding electrode design, several variants with different internal diameters were made for both the sharp and flat edge cone shapes. Each electrode was tested with a range of different Greaves device components. A representative set of results for each grounding electrode design will be shown below.

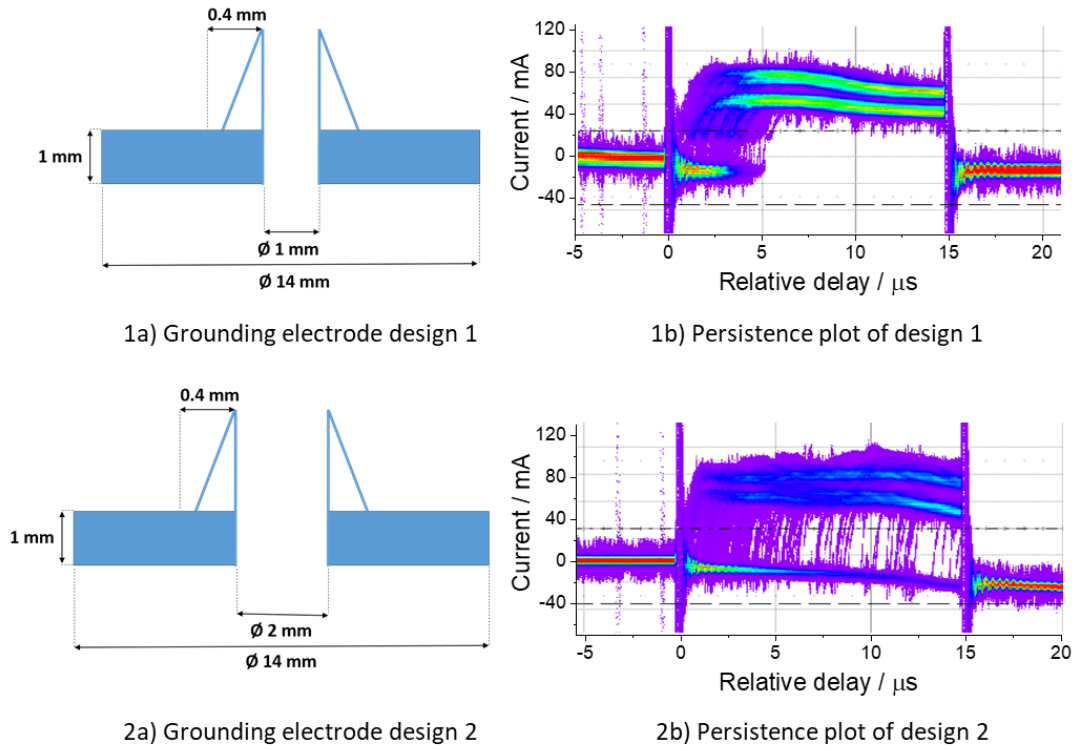

Figure 3.28: Schematic designs of the grounding electrodes with sharp cone tips, and representative persistence plots associated with the design. The persistence plots were obtained from experiments carried out using He as the carrier gas, under optimal *in situ* conditions. The components used by the discharge device include a 2 mm diameter ceramic spacer, a 2 mm diameter front electrode, and a faceplate with no channel (Design 1) and a 6 mm channel (Design 2). Schematics adapted from reference [203]

For the sharp-edge cone designs, two grounding electrodes with orifice diameters of 1 mm and 2 mm were tested. The designs are shown in Figure 3.28, alongside a representative set of persistence plots. These plots show that neither design achieves a fully stable discharge over a short HV pulse. However, of the two electrodes, the 1 mm diameter orifice design ensured that the discharge struck reliably for at least 10 µs with each laser shot, whereas with the 2 mm orifice design, the discharge was less likely to strike reliably and with a consistent pulse length.

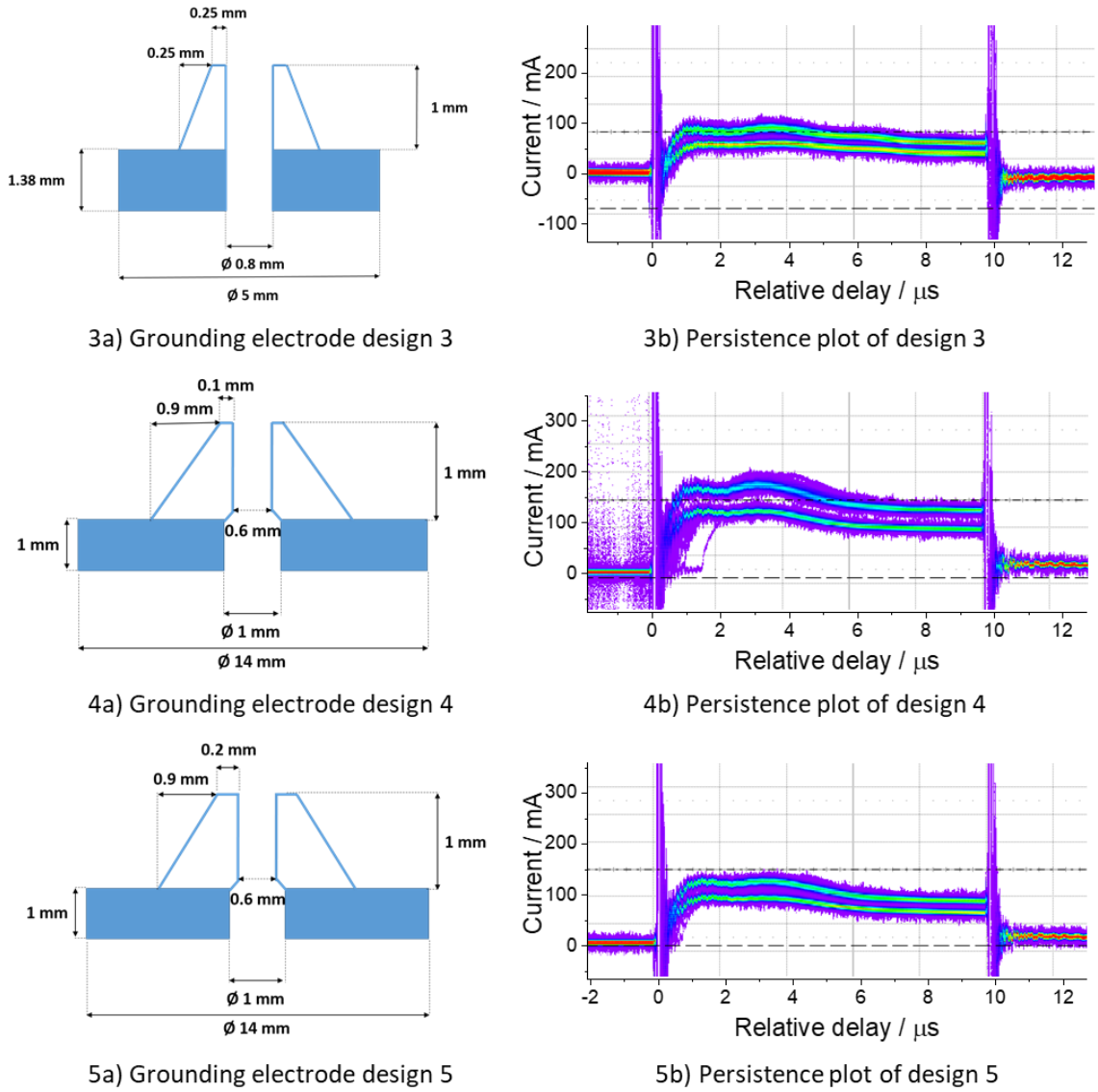

3a) Grounding electrode design 3 | 3b) Persistence plot of design 3

4a) Grounding electrode design 4 | 4b) Persistence plot of design 4

5a) Grounding electrode design 5 | 5b) Persistence plot of design 5

Figure 3.29: Schematic designs of the grounding electrodes with flat cone tips, and representative persistence plots associated with the design. The persistence plots were obtained from experiments carried out using He as the carrier gas, under optimal *in situ* conditions. The components used by the discharge device include the conical ceramic spacer, a 2 mm diameter front electrode, and a faceplate with a 12 mm channel. Schematics adapted from reference [203]

As for the flat cone tip grounding electrode designs, three electrodes were made, one with an orifice of 1 mm diameter throughout the electrode, and two electrodes with a smaller orifice of 0.6 mm within the cone itself, and different sized flat tips. The designs are shown in Figure 3.29, alongside a representative set of persistence plots. As is apparent from the figure, all of the designs used provide an overall much more stable HV pulse compared to the sharp-edged tips design.

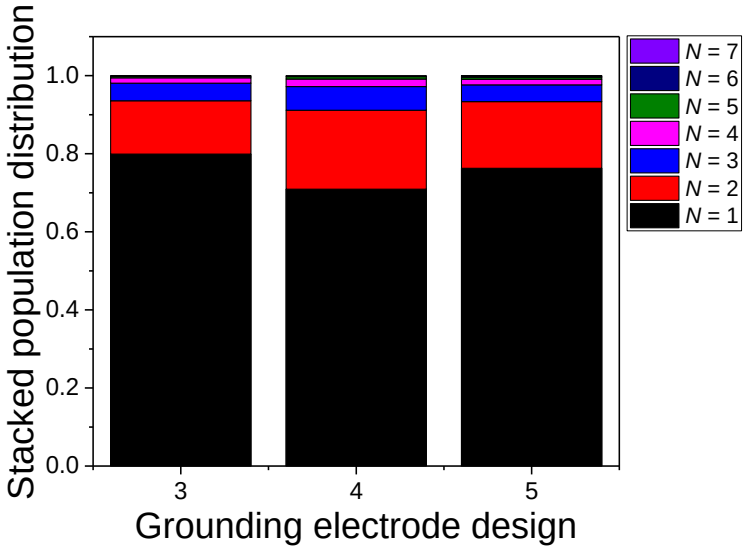

Figure 3.30: Stacked rotational population distribution extracted from single excitation spectra taken at the peak of the TOF profiles, using different discharge device grounding electrodes under the conditions indicated in Figure 3.29. Populations shown are from $N = 1$ to 7, normalized to the sum of their populations.

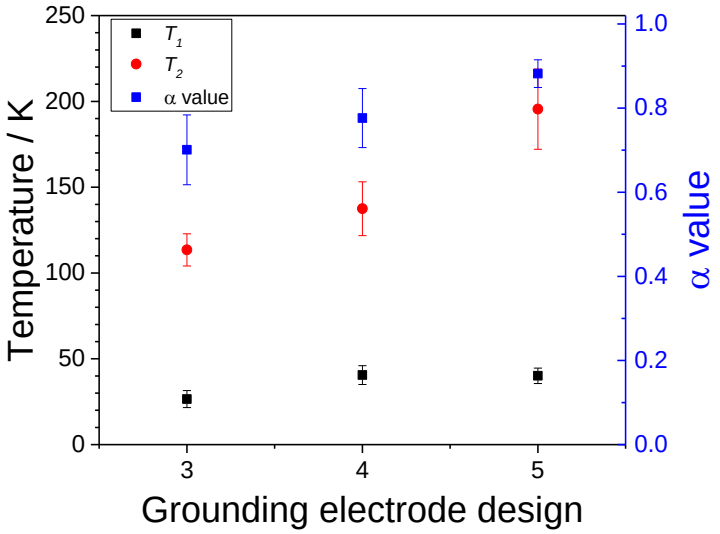

Figure 3.31: Rotational temperatures and α values obtained from a two temperature fit (Chapter 2 Section 2.9.2) to the populations shown in Figure 3.30, with associated errors in the fit.

To test whether the narrower nozzle diameters of designs 4 and 5 improved the rotational cooling of radicals with respect to design 3, the relative population distribution of the incident OD radicals was obtained from LIF excitation spectra taken at the peak arrival time of the radicals and plotted in Figure 3.30. The resulting rotational temperatures and α values are displayed in Figure 3.31. Contrary to expectations, it was design 3, with the 1 mm orifice through the electrode, that gave the colder molecular beam, though the improvement it provides is relatively small, of the order of about 10 K.

To summarise, the results showed that grounding electrodes with a 1 mm diameter orifice or smaller and with a flat cone tip provide a much more stable discharge pulse over designs with larger orifices or cones with sharp tips. Of those electrodes, the design with a 1 mm orifice diameter throughout the length of the cone provided a marginally colder beam compared to the other designs. As with the front electrode design discussed in section 3.4.2 above, the results also show that when sharp edges are present on tip of the cone on the grounding electrode, the discharge conditions become more unstable. As such, sharp edges need to be removed as much as possible from the flat cone tip designs. Even so, jagged edges may still form on the flat cone tip due to imperfections in the manufacturing of the electrode, or through repeated exposure of the cone tip to the discharge plasma over several months of continuous usage, leading to a progressively unstable discharge. Because of this, the flat cone tip of the electrode was inspected regularly with a microscope, and if jagged edges were confirmed to be present, the electrode was replaced.

3.4.4 Spacer

To protect the PTFE body housing the electrodes from the discharge occurring between the cone of the grounding electrode and the inner hole of the front ring electrode, a ceramic spacer was placed between the two. The original Greaves device was designed with a conical spacer, with a hole diameter of 2 mm close to the cone, extending out to 3 mm on the front electrode side, as shown in Figure 2.5. The effect of this ceramic spacer on the molecular beam was compared against two other ceramic spacers, with cylindrical holes of diameter 2 mm and 3 mm respectively. Each spacer was tested with a range of different components for the Greaves device, whilst ensuring that the

diameter of the spacer was equal or bigger than the diameter of the inner hole in the front electrode. A representative set of results is shown below.

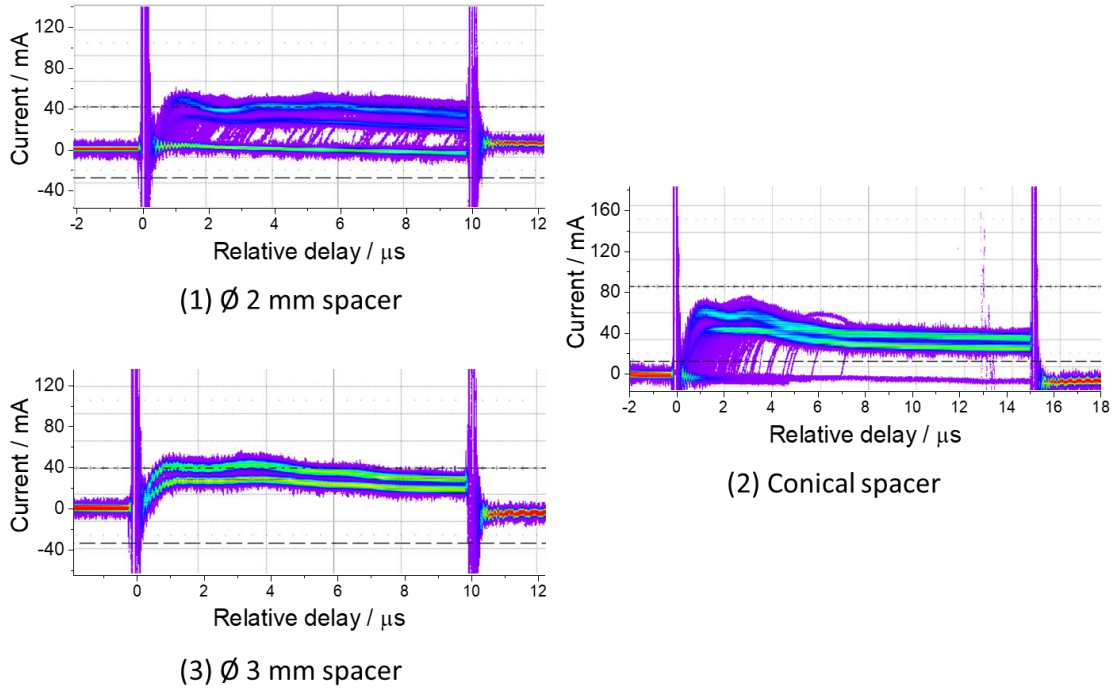

Figure 3.32: Representative persistence plots of the discharge stability when using different ceramic spacers. The plots were recorded for a free-jet expansion of a molecular beam seeded in He, with backing pressure of 3 bar, using a 10 or 15 μs HV pulse fired within a nominal gas pulse length of 500 μs. Discharge device used the original Greaves design ground electrode, a 2 mm diameter front electrode hole and a faceplate a 12 mm channel (blue). Spacers used: 2 mm diameter spacer (1), conical spacer (2) and 3 mm diameter spacer (3).

The persistence plots obtained for each of the spacers tested (Figure 3.32) indicate that using the 3 mm cylindrical spacer gives a very stable discharge compared to the other options. The conical spacer could also provide a stable discharge if the 3 mm cylindrical spacer is not available, with suitably adjusted *in situ* conditions. Surprisingly, there appears to be a slight but noticeable change in the width of the TOF profiles when using the conical spacer as opposed to the cylindrical spacers, as seen in Figure 3.33. It is as yet unclear how the shape of the spacer may have had this effect.

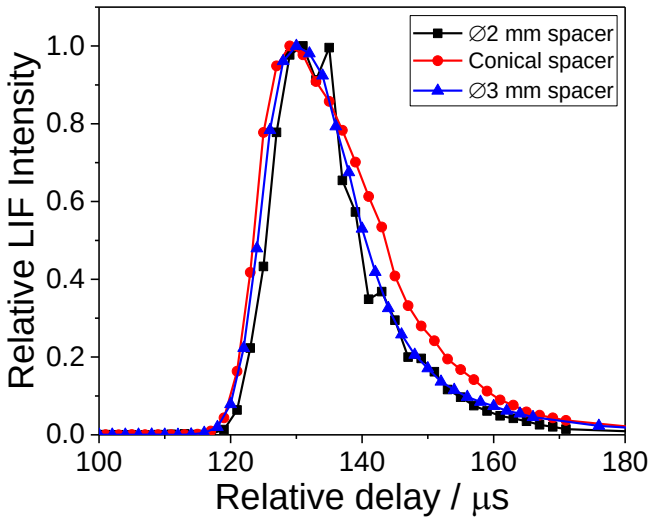

Figure 3.33: Representative peak-normalized TOF profiles of incident OD radicals, probed on the $Q_1(1)$ transition, taken under the same conditions as the persistence plots from Figure 3.32, using the 2 mm diameter spacer (black), conical spacer (red) and 3 mm diameter spacer (blue)

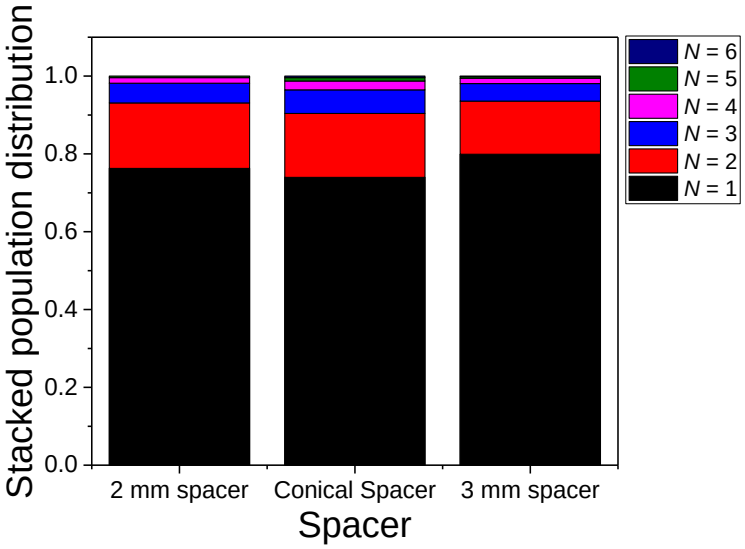

Figure 3.34: Stacked rotational population distribution extracted from single excitation spectra taken at the peak of the TOF profiles from Figure 3.33, using different ceramic spacers for the discharge device. Populations shown are from $N = 1$ to 6, normalized to the sum of their populations.

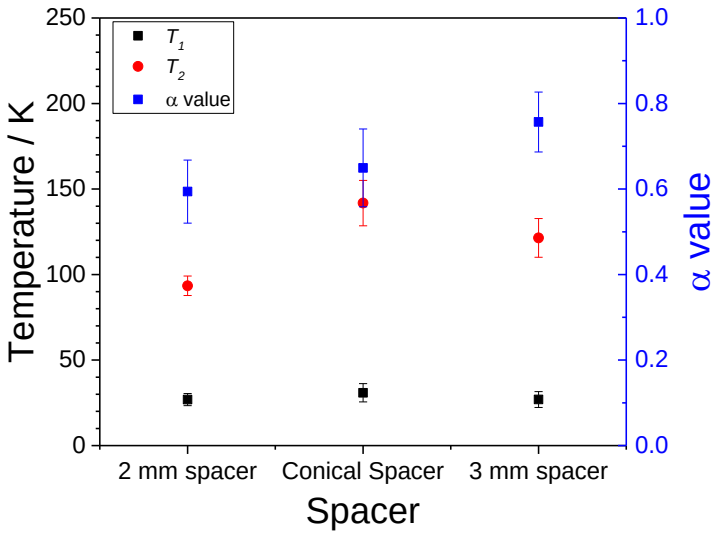

Figure 3.35: Rotational temperatures and α values obtained from a two temperature fit (Chapter 2 Section 2.9.2) to the populations shown in Figure 3.34, with associated errors in the fit.

Despite the slight differences in the TOF profiles, both the rotational population distributions (Figure 3.34) and the corresponding rotational temperatures (Figure 3.35) show that there is no significant change in the cooling of the radicals in the molecular beam. The results suggest that having a spacer with a diameter wider than that of the inner hole of the front electrode is desirable to obtain a stable discharge, and that a cylindrical spacer is preferable over a conical one. The conical spacer was used for the experiments reported in Chapter 4, whereas the 3 mm diameter cylindrical spacer was used for the experiments reported in Chapter 5.

3.5 Seeding the Discharge

In an attempt to obtain discharge pulse lengths shorter than the gas pulse to improve the cooling of the molecular beam (Section 3.3.4), Lewandowski and co-workers introduced a tungsten filament close to the pulsed valve in their experimental chamber [208]. By applying a high current to the filament, the group was able to achieve a reliable and reproducible discharge for HV pulses as short as 1 µs. They also showed that the presence of the hot filament reduced the minimum voltage required to obtain a stable discharge at short HV pulses by a factor of ~ 4, which in turn produced a significantly colder molecular packet. This method of stabilizing the discharge has been

adopted by other groups using short discharge pulse lengths in their experiments [198, 209-210].

Conventional wisdom would therefore suggest that a source of electrons, such as a filament, would need to be added to our experimental chamber for the discharge to work at short HV pulses. During the first attempts at running scattering experiments with short HV pulses, however, the discharge was found to still strike reliably even at HV pulses lower than 60 μs without the need for a hot filament. Through later optimization experiments involving the gas baffle (discussed in section 3.6.2), it was eventually discovered that the short discharge pulses were being stabilized by the wide range pressure gauges (Edwards WRG-S-DN40CF) mounted on the main chamber. These gauges are Penning-type gauges, also known as cold-cathode ion gauges. The cold-cathode gauges generate electrons between the cathode and the anode of the gauge. The electrons then ionize gas molecules between the two electrodes, which are then accelerated to the grounded cathodes. The pressure is then measured based on the current required to neutralize the ionized gas molecules during each time unit. As both the cathode and anode of the gauges are directly exposed to the vacuum chamber, it is possible for the generated electrons to escape the gauge and enter the vacuum chamber, where they can then access the discharge device, and thus stabilize the discharge strike. This explanation was confirmed by checking the discharge stability after disconnecting the gauge, as shown in Figure 3.36 (a) when comparing with Figure 3.36 (c) and (d). Further testing showed that having two pressure gauges on opposite hemispheres of the main chamber (as shown in Figure 3.37) was optimal for obtaining a stable discharge. This indicates that the discharge device can potentially be stabilized by a pressure gauge on the opposite hemisphere of the main chamber, provided there are no obstructions in between, such as a large gas baffle (described in section 3.6.2). It also suggests that only one pressure gauge, placed close to the discharge device, might be sufficient to stabilize the discharge, though it may require further adjustment of the other conditions.

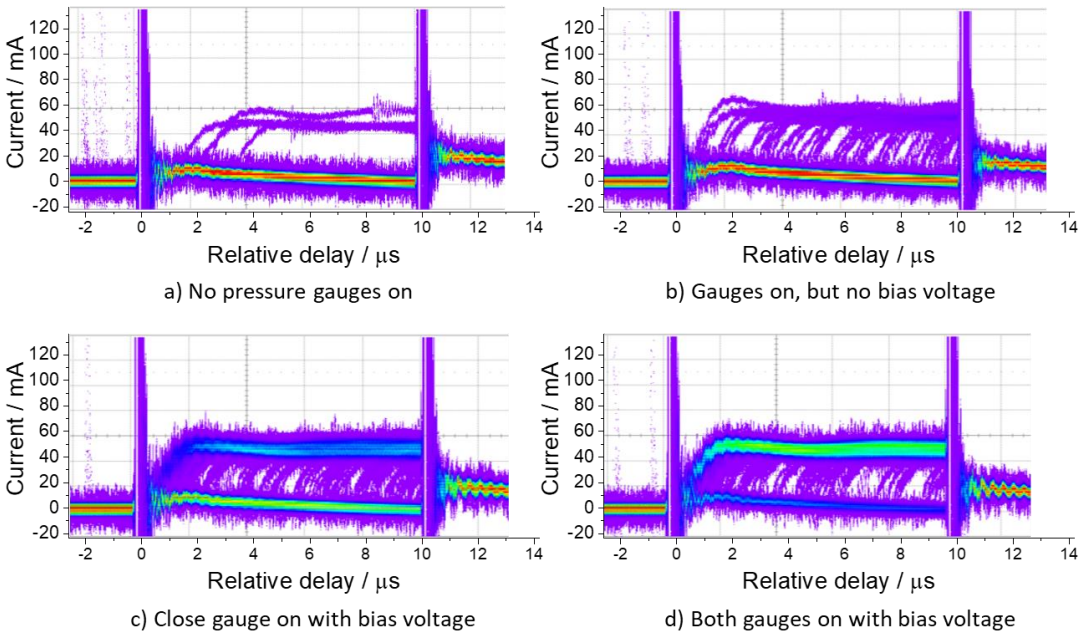

Figure 3.36: Representative persistence plots of the discharge stability using Ne as the carrier gas under optimal *in situ* conditions, with pressure gauges on or off, or with the bias voltage present or absent, as described in the captions under each plot. 'Close gauge' position is shown in Figure 3.37 below

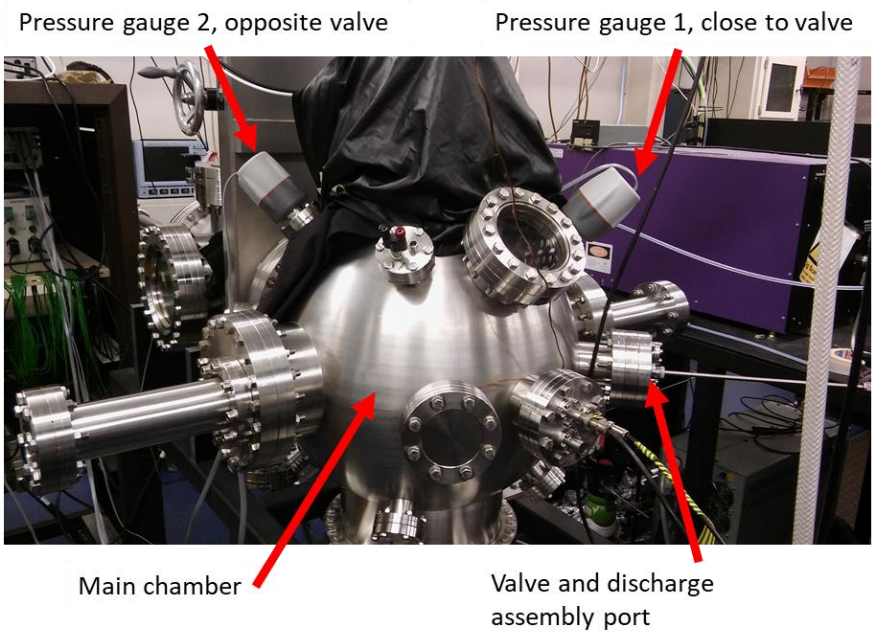

Figure 3.37: Photo of main chamber in the lab, with pressure gauges position highlighted with respect to the valve and discharge device port, set at 45° angle of incidence with respect to the surface

The presence of one or more wide range gauges ensured that the discharge would strike reliably at short HV pulses. However, on their own, the gauges were not enough to guarantee a reproducible discharge over the entire HV pulse under all experimental conditions tested, and especially when using Ne as the carrier gas (as shown, for example, in Figure 3.6). In order to obtain a reproducible discharge that strikes at the start of the HV pulse, two methods were employed to further stabilise the discharge *in situ*.

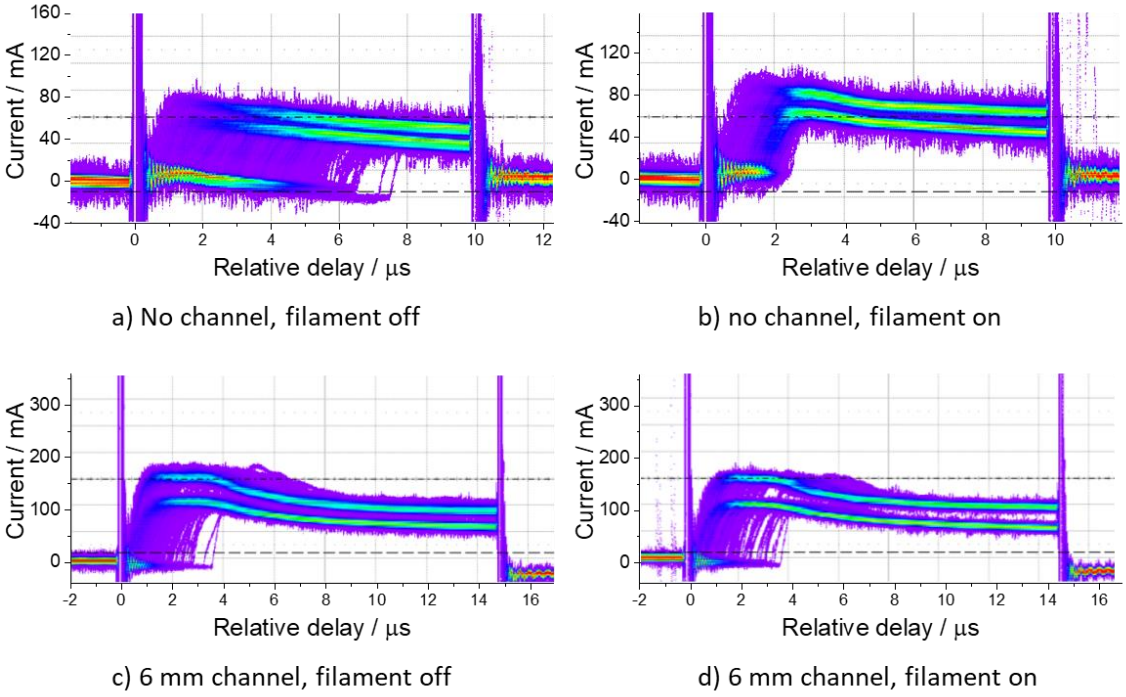

Figure 3.38: Representative persistence plots of the discharge conditions of a He beam, showing stabilizing effect of using the filament (right column) compared to no filament (left column). The discharge faceplates used are the no channel faceplate (top row) and the 6 mm channel faceplate (bottom row)

In the first instance, a hot filament was inserted in the main chamber close to the discharge device, as per the approach pioneered by Lewandowski *et al.* [208]. The current applied to the filament was set at between 0.4 and 1.4 A, adjusting it throughout the course of the day and also between days to obtain a stable discharge. This method was used primarily for the single-point detection set-up reported in this thesis. The stabilizing effect of the hot filament was tested for discharge devices with different faceplate designs (Section 3.4.1). A comparison of the persistence plots (Figure 3.38)

shows that the hot filament is very effective at stabilizing the discharge when a faceplate with no channel is attached to the discharge device (Figure 3.38 (a) and (b)). When a faceplate with a channel is attached to the discharge device, however, no improvement in the discharge conditions is observed. (Figure 3.38 (c) and (d)). This was thought to be due to the constrained line of sight to the electrodes that results from using the faceplates with the channel.

There were also concerns that the light produced from the glowing filament when a high current is applied would also be picked up by the optical detectors used to capture the LIF signals. This was not a problem for the more conventional PMT experiments reported in Chapter 4, as the gas baffle used was large enough to block most of the light going into the detection region of the chamber, and no additional baseline signal was observed. However, it became more of a concern when switching to the image acquisition set up, as the gas baffle used in these experiments was smaller. In this case, it was found that the discharge could also be stabilized by biasing the front electrode with a positive voltage of up to 230V, provided by a second power supply that the fast switch switches to when the high negative pulse is not active, to attract the electrons produced by the gauges to the discharge device. This effect is best shown in Figure 3.36 (b) comparing with Figure 3.36 (d), for an unoptimized molecular beam with neon as the carrier gas.

3.6 Inserting the Skimmer Plate Holder

After the molecular beam passes through the discharge device, it supersonically expands into the main chamber. The OD radicals in the beam can then scatter off any of the components present in the main chamber, including the liquid light guide, the bath assembly, and both liquid surfaces. To ensure that the scattered OD radicals detected by the probe beam emerge exclusively from scattering events with the active liquid surface (i.e. the one placed at the focal point of the molecular beams) the molecular beam was skimmed using a conical skimmer. The rest of the beam was blocked by a gas baffle attached to the skimmer holder. This section will describe the advantages of inserting the gas baffle and skimmer, and how they affected the signal size and rotational cooling of the radicals in the molecular beam.

The experiments reported in this section were all carried out with a Greaves device optimized for OD seeded in He. This consisted of a faceplate with a 12 mm channel, a front electrode with 2 mm inner hole diameter, a grounding electrode with a flat cone tip (design 3, shown in Figure 3.29), and a 3 mm diameter spacer. The *in-situ* conditions of the beam with the He carrier were optimized to obtain a stable discharge with a high OD number density and a 'cold' rotational temperature prior to inserting the skimmer.

3.6.1 Positioning the skimmer

To determine whether the placement of the skimmer affected the properties of the radicals in the molecular beam, a preliminary test was conducted by placing a 5 mm diameter skimmer at a distance of 167 mm from the skimmer tip to the pulsed valve nozzle, which was itself placed at 230 mm from the probe region. This skimmer-to-pulsed valve distance was used for the scattering experiments reported in Chapter 4 (which were completed prior to the optimization experiments reported in this chapter) to ensure that the radicals would dose a ~1 cm^2 area on the liquid surface.

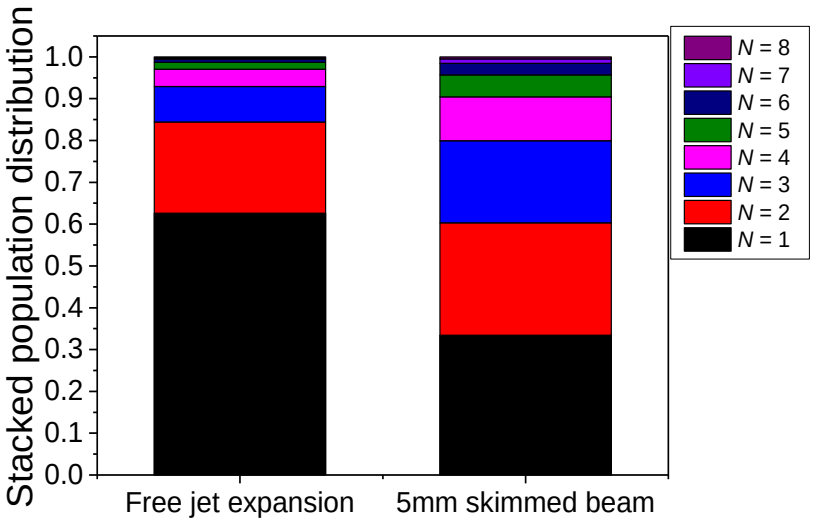

Figure 3.39: Stacked rotational population distributions of rotational levels from $N = 1$ to 8, with the sum normalized to 1, comparing the free jet expansion population distribution with the population distribution of a beam skimmed by a 5 mm skimmer in the set-up outlined in Chapter 4. Rotational populations were obtained from excitation spectra taken at the peak of the TOF profiles obtained on the $Q_1(1)$ transition, using He as the carrier gas, under optimized *in situ* conditions.

Excitation spectra were acquired at the peak of the TOF profiles obtained both for the free jet expansion beam and for the beam with the skimmer in. The relative populations from each spectra are shown in Figure 3.39. The figure showed that the lower *N* levels were significantly less populated, and the higher levels more populated, than the optimized free jet expansion results corresponding with an increase. The results indicated that the improvements obtained via optimization of the free jet expansion had effectively been cancelled out by the placement of the skimmer.

To better understand the reason why the improvements to the beam properties were lost after inserting the skimmer in the chamber, the 5 mm skimmer was placed at several different skimmer-to-pulsed valve distances. These experiments were then repeated using a 2 mm skimmer, one run using a Greaves device with a 3 mm diameter hole front electrode and associated 12 mm channel faceplate, and the second run using the 2 mm diameter hole front electrode and associated 12 mm faceplate. The experiments were carried out without the gas baffle attached to the skimmer holder. TOF profiles were acquired for each of these sets, and the integrated signal size of each profile was plotted against the skimmer-to-discharge device distance. This distance was measured between the tip of the skimmer and the front edge of the faceplate on the discharge device, to account for the fact that the molecular beam is constrained by the discharge device up until it exits the faceplate, and that the point where the beam is last constrained varies when comparing faceplates with different channel lengths.

Comparing the plots of integrated signal size over distance in Figure 3.40 revealed that the largest signal is obtained with the 5 mm skimmer placed at a very short distance from the valve. However, this was likely due to the fact that at such a distance, the 5 mm skimmer is too big to actually skim the molecular beam. The integrated signal then decreases rapidly up to a skimmer-to-discharge device distance of 50 mm, and then no change is observed until the maximum skimmer-to-discharge device distance is reached, where the signal appears to increase again.

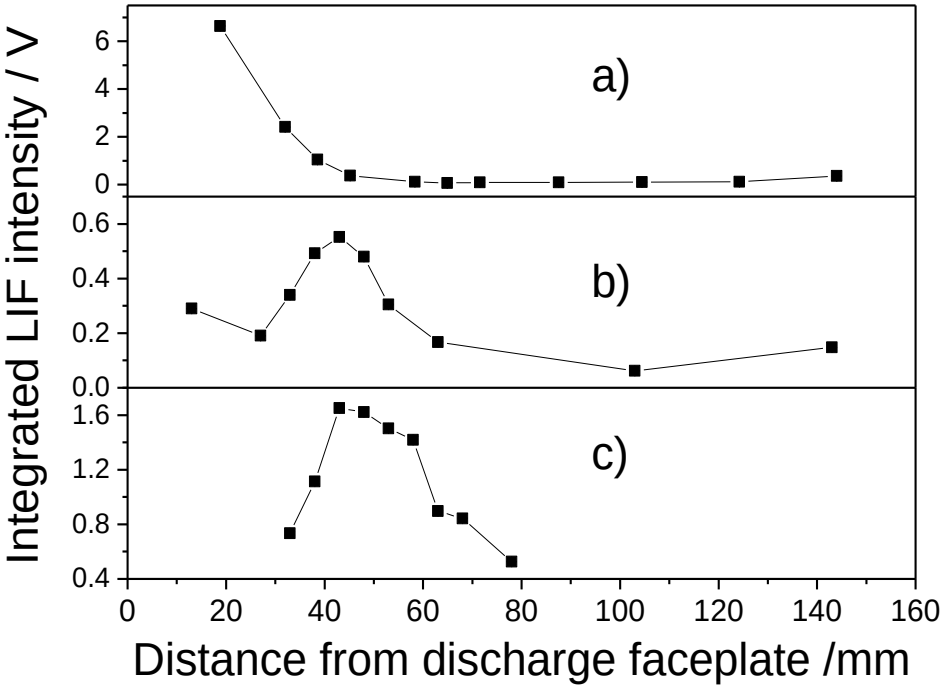

Figure 3.40: Plots of integrated signal size of TOF profiles acquired at select skimmer-to-pulsed valve distances with the 12 mm channel faceplate attached to the discharge device, using a) a 5 mm diameter skimmer and 3 mm diameter hole front electrode, b) a 2 mm diameter skimmer and 3 mm diameter hole front electrode, and c) a 2 mm diameter skimmer and 2 mm diameter hole front electrode. Profiles were acquired on the $Q_1(1)$ transition, using He as the carrier gas, under optimised *in situ* conditions.

The plots obtained with the 2 mm skimmer, on the other hand (Figure 3.40 (b) and (c)), featured a pronounced maximum integrated signal size within a narrow range of intermediate skimmer-to-discharge device distances, centred around an optimal distance of ~ 40-45 mm. The range of optimal distances that give the highest integrated LIF signal with the 2 mm skimmer also changes depending on the front electrode used in the discharge device. With the '3 mm' front electrode (Figure 3.40b) the range of distances is narrower and occurs at shorter skimmer-to-discharge device distances, whereas with the '2 mm' front electrode (Figure 3.40c) the integrated LIF signal starts to rise at slightly longer skimmer-to-discharge device distances, but the range of optimal distances is wider.

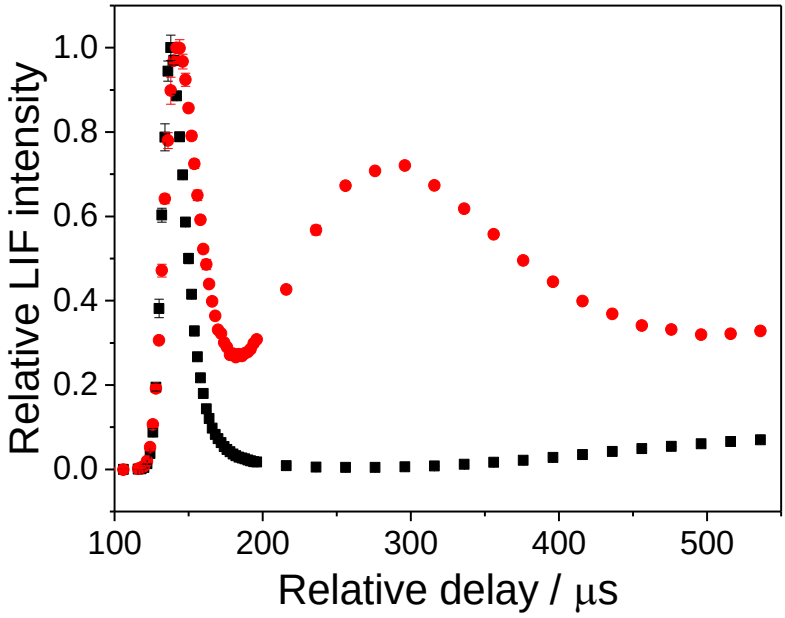

Figure 3.41: Representative peak-normalised TOF profiles of OD LIF signal taken on the $Q_1(1)$ transition using the He carrier with *in situ* parameters optimized for both OD number density and molecular beam properties. The discharge device used a 3 mm front electrode and related 12 mm channel faceplate. A 2 mm skimmer was placed at 43 mm (black squares) and 143 mm (red circles) from the discharge device.

In both Figures 3.30 a) and 3.30 b), a slight increase in the integrated LIF signal size is also observed at the maximum skimmer-to-discharge device probed. A comparison of the shape of the TOF profiles from different set-ups (Figure 3.41) revealed that the increase was due to the appearance of OD signal at later delays, compared to the narrow peak of the profile observed at earlier delays. The peak of the TOF profile corresponds to LIF signal from incident OD radicals that have reached the probed region by passing through the skimmer. The rise in signal size at later delays suggests that the incident radicals were being slowed down as a result of shockwaves occurring in the region between the valve and the skimmer. A further contribution to the OD LIF signal at later delays may also be due to radicals that had travelled around the skimmer plate holder and scattered off other components present in the main chamber before entering the detection region. This will be discussed in further detail in the next section.

Excitation spectra were then obtained from both sets of experiments using the 2 mm skimmer. The results are reported in Figures 3.42 and 3.43. For ease of comparison between the set-ups, the stacked rotational population distribution is shown in these figures. When using the 3 mm hole front electrode, the proportion of radicals populating the lowest rotational *N* level was highest at the skimmer-discharge device distance corresponding to the peak in signal size shown in the earlier Figure 3.40 b), and lowest when the skimmer was closest or furthest away from the valve. For the results where the skimmer is furthest from the valve, a possible explanation for the radicals being warmer may arise as a result of collisions of the molecular beam with the rods supporting the skimmer plate, which then collide with the OD radicals that pass through the skimmer, reheating them before they enter the probe region. Surprisingly, when using the 2 mm front electrode, the radicals retained their 'cold' rotational distribution even when the skimmer-discharge device distance was twice the distance where the optimal signal size was obtained.

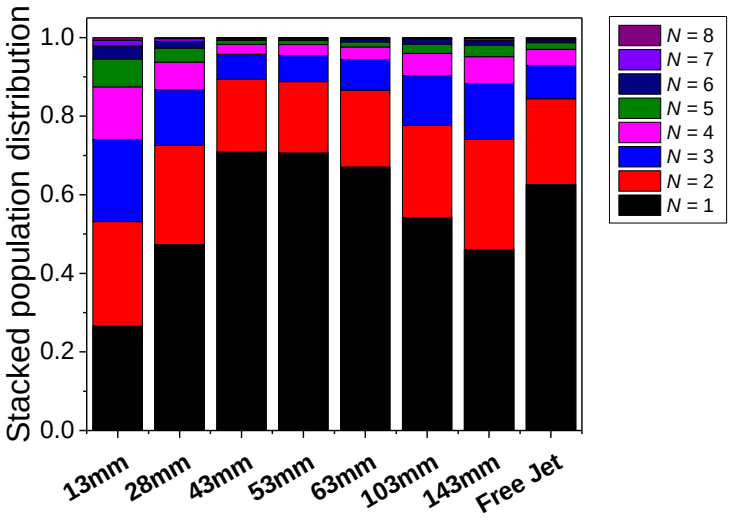

Figure 3.42: Stacked rotational population distributions obtained for the 2 mm skimmer, 3 mm front electrode set of TOF profiles at different skimmer-discharge device distances, with results from the free jet expansion added for comparison. Rotational populations were obtained from excitation spectra taken at the peak of the TOF profiles obtained on the $Q_1(1)$ transition, using He as the carrier gas.

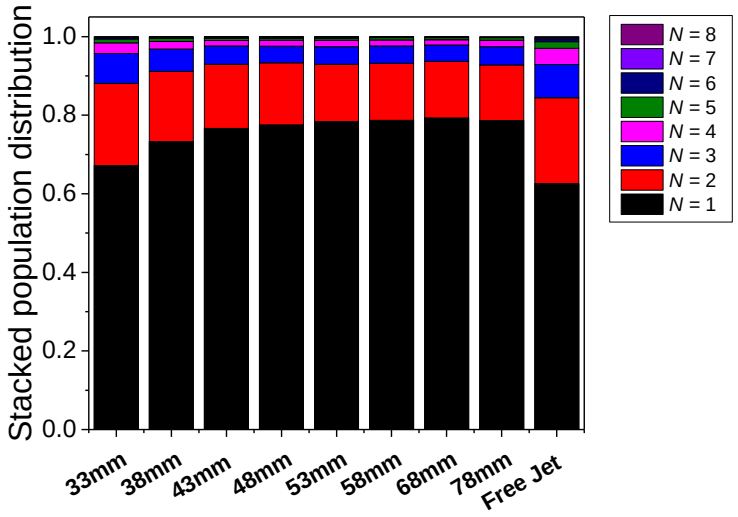

Figure 3.43: Stacked rotational population distributions obtained for the 2 mm skimmer, 2 mm front electrode set of TOF profiles at different skimmer-discharge device distances, with results from the free jet expansion added for comparison. Rotational populations were obtained from excitation spectra taken at the peak of the TOF profiles obtained on the $Q_1(1)$ transition, using He as the carrier gas.

Based on the above considerations, the 2 mm diameter skimmer was found to provide the highest OD number density and the lowest OD rotational temperature when placed at a skimmer-to-discharge device distance of 40 mm, when used in combination with the '2 mm' front electrode for the discharge device. This optimal set-up was used for the experiments reported in chapter 5.

3.6.2 Inserting the gas baffle

As highlighted by Figure 3.41, it is possible for radicals to enter the probe region and be detected via pathways other than passing through the skimmer itself. This presents a number of problems for obtaining unambiguous data in gas-liquid scattering experiments. The most obvious issue is that the 'tail' of the profile occurs at delays where LIF signal from OD radicals scattered off a liquid surface is expected to appear. This feature could potentially be accounted for by inserting a small beam blocker between the skimmer and the skimmer holding plate. TOF profiles of the OD LIF signal from radicals entering the detection region via scattering trajectories that start outside the region on the liquid surface dosed by the molecular beam (see previous

section) can then be acquired at regular intervals between acquiring sets of data. This 'background' OD contribution can then be subtracted from the experimental data. Representative 'background' OD TOF profiles are shown in Figure 3.44 alongside profiles obtained with the skimmer pathway unblocked.

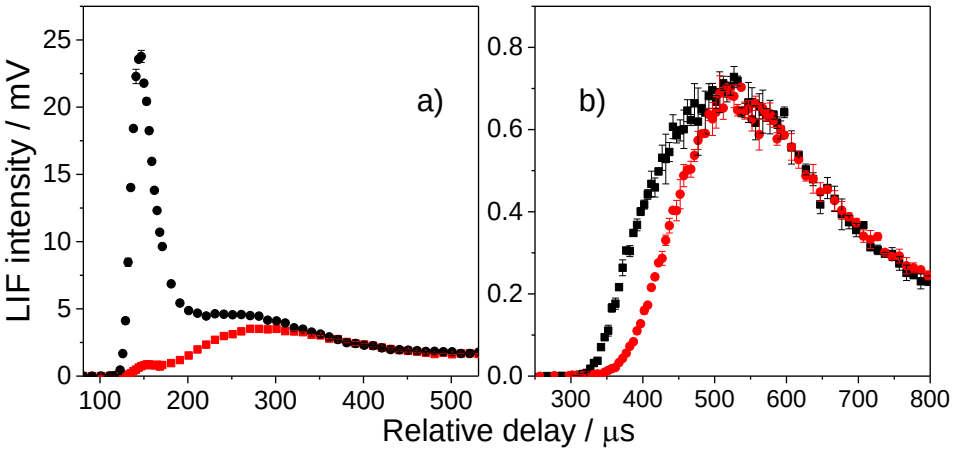

Figure 3.44: Representative TOF profiles showing the effect of blocking the pathway through the skimmer hole (red circles) vs. leaving it unblocked (black squares), for a molecular beam of OD radicals seeded in a) He and b) Ar, taken on the $Q_1(1)$ transition. Profiles were obtained with the liquid surface out, using optimal *in situ* and discharge device conditions

A comparison of the profiles in Figure 3.44 shows that the majority of 'background' OD LIF signal is detected at later delays with respect to the peak of the incident beam. This suggest that most of the radicals in the tail enter the detection region after scattering against physical components in the main chamber, such as the walls of the chamber itself, or via gas-phase scattering events. However, some LIF signal is also detected at delays where OD radicals that pass directly through the unblocked skimmer were expected to appear in the detection region. This signal can only come from radicals that travel with the same speed as the radicals passing through the skimmer and enter the probe region via trajectories other than through the skimmer itself. Furthermore, the profiles show that, while the contribution of those 'background' radicals to the LIF signal from OD that passed through the skimmer may be minimal under certain conditions (e.g. when OD seeded in He is probed at the $N = 1$ level), it becomes much more significant when probing higher rotational levels, or when seeding the radicals

with different carrier gases. Finally, if OD radicals are able to arrive in the probe region via trajectories other than though the skimmer when the bath assembly is out, it follows that the radicals may be able to collide with the rest of the bath assembly. The scattered radicals would then enter the probe region, to be detected alongside the radicals scattered off the liquid surface. Addressing this issue would thus require 'background' TOF profiles to be acquired both with the surface in and the surface out, which would have made the data acquisition impractically laborious to obtain.

An alternative to acquiring 'background' TOF profiles was to stop OD radicals from entering the probe region other than directly through the skimmer. In order to do so, a rectangular 'gas baffle' was attached to the skimmer holding plate. This gas baffle was made out of several layers of aluminium foil to prevent it from folding over in the main chamber, and to allow the baffle to be inserted into the chamber by folding it to fit through one of the ports and unfolding it once it was secured to the supporting rods. It also allowed the shape of the baffle to be adjusted as required, as shown in Figure 3.45 where the baffle was bent to prevent it intersecting the probe beam when the valve assembly was placed at 45° with respect to the surface.

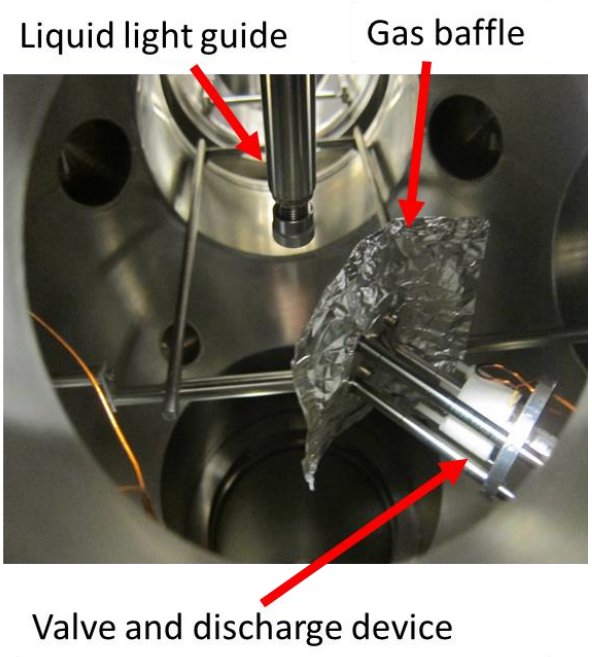

Figure 3.45: Photograph of the inside of the main chamber, showing a small 10 x 10 cm 'gas baffle' attached to the valve and discharge device assembly. The baffle has been folded on the right side to allow the probe beam to pass without intersecting it.

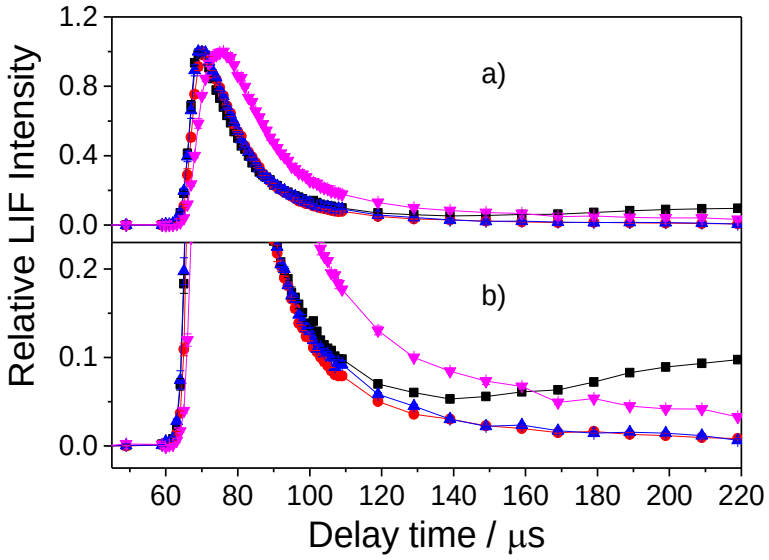

Figure 3.46: Representative TOF profile of incident OD radicals seeded in He and probed on the $Q_1(3)$ transition, using a 10 x 10 cm baffle (red circles), a 20 x 20 cm baffle (blue triangles), and a 30 x 30 cm baffle (pink triangles), compared with no baffle (black squares). Profiles were acquired with optimal discharge components and *in situ* conditions, with a 2 mm skimmer placed at ~ 40 mm from the discharge device, and with the distance between the surface and the valve of ~140 mm. b) is a rescaled version of a) to highlight the 'tail' end of the profile.

When the gas baffle was originally set up for the experiment reported in Chapter 4, it was thought that a large, 30 x 30 cm gas baffle was necessary for blocking the molecular beam with the skimmer placed 160.5 mm away from the discharge device. Experimenting with different size baffles with the skimmer placed at the optimal distance from the discharge device, shown in Figure 3.46, later revealed that a 10 x 10 cm gas baffle was sufficient to prevent radicals from creeping around the skimmer faceplate, even with a bend in the baffle (as shown in Figure 3.45). Indeed, the TOF profiles suggests that having too large a baffle may be detrimental to the molecular beam properties, though this only seems to become significant for the larger 30 x 30 cm gas baffle. Based on these results, the smaller 10 x 10 cm baffle was used for the image acquisition experiments described in Chapters 5.

3.7 Summary Points

1) The electric discharge device used in the experiments reported in this thesis was the Greaves device [176], which was based on the 'glow'-type discharge devices reported in the literature, specifically the devices used by van Beek [177] and Ikegiri [178]. It consists of two electrodes, a 'grounding' electrode with a conical nozzle and a ring electrode with a small hole acting as the 'front electrode'. These are separated by ceramic insulators from each other and from the pulsed valve. All components are encased in a Teflon body.

2) To obtain an optimal molecular beam for gas-liquid scattering experiments, a) the discharge has to strike every time the pulsed valve opens for the full duration of the HV pulse length, b) the FWHM of the TOF profile must be as small as possible, and c) the rotational temperature of the radicals must be 'cold'.

3) When optimizing various experimental parameters, it was noted that for optimal discharge conditions, the peak current draw was usually found at between 100 and 200 mA. This was used as a guide to optimize the discharge conditions to a first approximation without the need to acquire TOF profiles or excitation spectra.

4) The carrier gas used for the molecular beam determines the speed, spread of velocities and rotational cooling of the OD radicals, with helium providing a fast packet of radicals with a small spread of speeds but a warmer rotational energy distribution, and neon providing slower moving radicals with a larger spread of speeds, but a rotationally colder energy distribution.

5) Of the other *in situ* parameters that can be changed while the scattering experiment is running, only the length of the discharge pulse affects the rotational cooling of the radicals, with short pulses providing for colder beams regardless of the carrier gas used. The other parameters, such as discharge voltage, backing pressure and the discharge-gas pulse delay, do not affect the rotational cooling as much, though they may affect the shape of the TOF profile and the stability of the discharge, and so those were set to optimize OD number density and discharge stability

6) Of the discharge device components tested, only the faceplates with channels improved the cooling of the radicals. However, the faceplate with channel appears to only work effectively with He as the carrier gas.

7) None of the other discharge components and variations tested affected the rotational cooling of the radicals, but did affect the stability of the discharge. Optimization experiments determined that the best set-up must include a 2 mm inner hole diameter front electrode with the edges of the inner hole rounded on both sides, a conical grounding electrode with a flat edge of the tip and a nozzle diameter of 1 mm or less, and a cylindrical ceramic spacer of diameter 3 mm.

8) To obtain a stable discharge with short discharge pulse lengths, a source of electrons is needed to seed the discharge device. The Penning-type pressure gauges mounted on the experimental chamber can provide enough seeding electrons to make the short pulse discharge work, though an extra source of electrons from a hot filament, or biasing the front electrode with a positive voltage when the HV pulse is not active, may be required to stabilize certain experimental set-ups or experiments with different carrier gases.

9) A 2 mm diameter skimmer, positioned with the tip at ~40 mm away from the faceplate of the discharge device, can further help to improve the OD LIF signal intensity and rotational cooling of the radicals.

10) In order to prevent OD radicals from passing around the skimmer plate holder, and thus prevent them from scattering off the bath assembly back into the probe region, a ‘gas baffle’ was added to the skimmer plate. A baffle of 10 x 10 cm was found to be sufficient for the purpose when the skimmer is set at the optimal distance from the discharge device.

Chapter 4- Single-Point Detection Set-Up Results

4.1 Introduction

In previous experiments done by the group, OH radicals generated via the 'bulk photolysis' method were scattered off the liquid surfaces squalane, squalene, oleic acid, and PFPE, the latter used as an inert reference [10-12]. The results from these experiments, discussed in more detail in the general introduction (Chapter 1 Section 1.3.3), have been invoked by others in the context of studying reactions occurring on the surface of aerosols in the atmosphere [3, 17, 26, 54, 80, 211-216]. Although this may be entirely reasonable because those were the best values available, the interpretation might not have been secure, because they were measured at fixed collision energies, determined by the choice of precursor and photolysis wavelength, that were considerably higher than those characteristic of ambient atmospheric conditions, distributed around an average of ~ 4 kJ mol^{-1}. By contrast, the new molecular beam source implemented in this experiment allows for the speed of the incident species, and thus the collision energy with the surface, to be adjusted in a controllable fashion through the choice of carrier gas. Importantly, this approach allows access, for the first time, to lower collision energies comparable to the reaction conditions in the atmosphere. In this chapter, the molecular beam source will be used to investigate the inelastic scattering dynamics and uptake of OD radicals at the surfaces of squalane, squalene, and PFPE at two different collision energies. These radicals were detected using the single-point detection set-up, described in the experimental methods (Chapter 2 Section 2.7.1). The results presented in this chapter have been recently published in the Journal of Physical Chemistry C [217].

The key results reported and discussed in this chapter are the uptake of OD on the liquid surfaces at the two different collision energies. These results were compared with those previously obtained through the 'bulk photolysis method [10-11] at a higher collision energy, in order to uncover new information on the collision-energy dependence of the uptake of OD with a given liquid surface. New dynamical information, related to the scattering of rotationally cold incident OD off the liquid surfaces, was also uncovered from the experiments in this chapter. However, the single point detection method used to measure the LIF signal has some limitations in terms of providing a full characterization of the inelastic scattering of OD, as discussed in this chapter.

Consequentially, the chapter will primarily focus on the differences in the reactive uptake of OD at different collision energies, only mentioning the dynamical information that is relevant to the correct interpretation of the uptake measurements. The scattering dynamics will be covered in more detail using the results from the image acquisition set-up shown in Chapter 5.

In order to understand how the experimentally obtained uptake of OD is expected to change between the collision energies reported in this chapter (Section 4.3) and in previous 'bulk photolysis' experiments [10-11], and rationalize any deviation from the expected values, it is important to know what type of reactions are likely to occur at the surface, and the activation energy, E_a, (if any) needed for a reaction to occur. An excitation function, defined here as the probability of reaction occurring at a given collision energy, can then be predicted from the activation energy, based on reasonable assumptions discussed in this section. For illustrative purposes, it will be assumed below that the excitation function is described by a simple but physically realistic line-of-centres model [218] defined by the expression

$$\sigma = \sigma_{max}(1 - \frac{E_0}{E_{coll}}) \tag{4.1}$$

where σ_{max} is the asymptotic high-energy value of the reaction cross section, σ, E_0 is the threshold energy of reaction derived from the activation energies, and E_{coll} is the centre-of-mass collision energy.

Activation energies for reactions of OH radicals with a wide range of molecules have been studied extensively in the literature via temperature-dependent measurements of the rate constant of the reaction in the gas phase [219-220]. However, direct measurements of E_a for reaction with squalane and squalene are unavailable, due to the low volatility of the squalane and squalene molecules preventing them from being present in sufficient quantities in the gas phase. Therefore, for the purpose of determining the excitation function, these reaction barriers will be estimated based on the results from smaller alkane and alkene molecules comparable with squalane and squalene respectively. For squalane, it is known in the literature that the only reaction channel available at low collision energies (such as the ones available with the current

molecular beam set-up) is direct abstraction of an H atom to form H_2O and an alkyl radical [220] via the reaction equation:

$$OH + R - CH(R') - R' \rightarrow R - C^{\bullet}R' - R'' + H_2O \quad (4.2)$$

There is overwhelming evidence that this is a positively activated process for alkanes in the gas phase [219-220]. However, the quantitative variation in reactivity that might be expected obviously depends on the relationship between the collision energies spanned and the barrier heights. This is complicated by the presence of primary, secondary and tertiary sites in the squalane molecule, with significantly different bond strengths and corresponding activation energies [221-222]. More fundamentally, for all three C-H bond types the barriers are relatively low, below ~ 10 kJ mol^{-1}; Arrhenius plots are found to be strongly curved over the accessible range of temperatures for which they have been measured (typically 300 – 1200 K) for related alkane molecules in the gas phase [221-222]. Tolman's interpretation of these concave plots [223] states that the negative of the local slope of the plot can be interpreted as equal to the average energy of the molecules that react minus the average energy of all possible reactants. As such, it is not sufficient to simply equate the Arrhenius activation energy E_a measured in any particular temperature range to the threshold energy, E_0. To proceed to a reasonable estimate of E_0 for the different C-H bond types in squalane, the relationship between E_a and E_0 has been extracted for the well-studied parent molecule, ethane. There is broad agreement in the literature that the experimental value of E_a for ethane at temperatures in the vicinity of 300 K is around 8.9 kJ mol^{-1} [219-220]. Sophisticated transition-state theory calculations, incorporating other temperature-dependent factors responsible for the curvature in Arrhenius plots, have shown that the experimental rate constants can be reproduced faithfully over the full measured range (200 - 1250 K) based on a zero-point-energy-corrected barrier height of 6.7 kJ mol^{-1} [224]. In the absence of equivalent detailed information, an assumption is made here that a similar ratio between empirical, room-temperature E_a and threshold energies E_0 also applies to larger alkanes. Site-specific E_a values are available for a range of alkanes in the literature. By selecting the largest molecules for which data are available, where the abstraction takes place either exclusively or predominantly around room temperature from a single C-H bond type, suitable estimates of E_a for squalane can be obtained. The E_a values are collected in Table 4.1, along with the projected values of E_0.

Alkane	***Ea* / kJ mol^{-1} (d)**	***E*$_0$ / kJ mol^{-1}**
ethane	8.9	6.7 (e)
Large 1y (a)	7.6	5.8 (f)
Large 2y (b)	3.4	2.5 (f)
Large 3y (c)	2.1	1.6 (f)
a) based on neopentane; b) based on cyclohexane; c) based on an average of 2,3-dimethylbutane and 2,3,4-trimethyl pentane; d) From reference [220]; e) from reference [224]; f) estimated by analogy with ethane, as described in the text.		

Table 4.1: Measured Arrhenius activation energies, E_a, around 300 K for gas-phase reactions of OH with different C-H bond types in alkanes and corresponding estimated threshold energies, E_0.

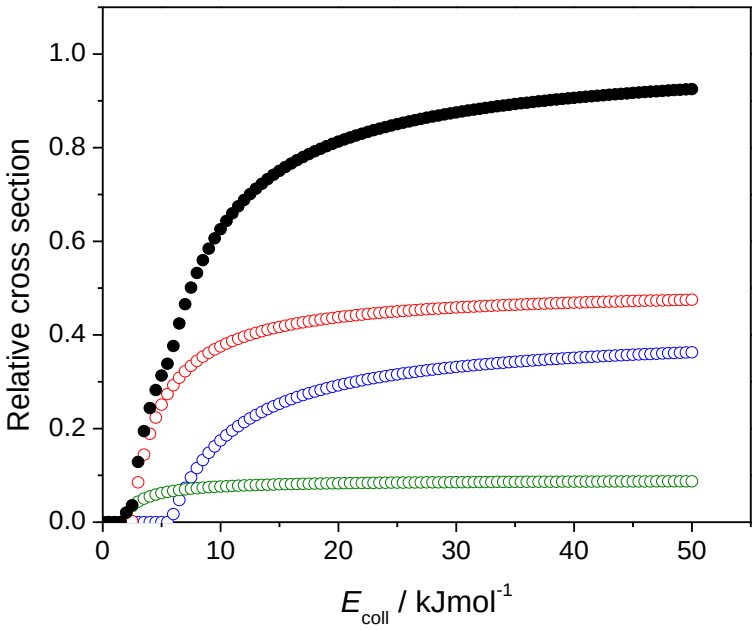

Figure 4.1: Relative reaction cross sections of H-abstraction reactions by OD radicals from primary (blue points), secondary (red), and tertiary carbons (green) and their sum (black) on the squalane surface, assuming simple line-of-centres behaviour.

From the E_0 values in Table 4.1, a plot of the relative cross section as a function of E_{coll} can be estimated for each of the C-H bonds using Equation (4.1). Previous analysis on molecular dynamic simulations done within the group have shown that the outer surface of squalane is occupied by primary, secondary and tertiary C-H sites in the ratio 0.41:0.50:0.09, which is only slightly different from their stoichiometric ratios 0.39:0.51:0.10 in the squalane molecule [95]. The excitation function derived for all three C-H sites individually, and their sum, is shown in Figure 4.1. The results predict that the uptake of OD on squalane is expected to increase dramatically over a range of 2 to 15 kJ mol^{-1}, while more moderate increases are expected when using higher collision energies.

By contrast, it is known from gas phase reactions of OH with alkenes [219] that there is a significant component of addition to the double bonds, via the reaction:

$$\begin{aligned} OH + R-CH=C(CH_3)-R'' \quad &\rightarrow \quad R-C^{\bullet}H-COH(CH_3)-R'' \\ &\text{Or} \quad R-CH(OH)-C^{\bullet}(CH_3)-R'' \end{aligned} \tag{4.3}$$

Estimates of the branching ratio between H-abstraction and addition reactions on small alkenes [225] show that H-abstraction contributes at most 8% of the loss of OH for propene and 3% for 1-butene, whereas addition reactions account for circa 71% of the OH signal lost for both molecules studied. Similar observations were also noted for the larger alkenes reported in the review by Atkinson *et al.* [219], with H-abstraction pathways contributing to less than 5-10% total loss of OH. The addition reaction is known to have a negative temperature dependence and nominally negative activation energy, which was estimated to be circa -3 kJ mol^{-1} based on the activation energies reported for the largest alkenes available in the review by Atkinson *et al.* [219]. The above consideration suggests that the uptake of OD on the squalene surface is expected to increase with decreasing collision energy.

4.2 Experimental

4.2.1 Experimental set-up

The experiments were performed using the methods outlined in Chapter 2, with the liquids described in section 2.4, and the single-point detection set-up detailed in Section 2.7.1. The probe-laser beams was set to provide ~200 μJ pulse^{-1}, using a combination of a polarizer and a $\lambda/2$ waveplate. The valve was placed to generate a molecular beam at normal angle of incidence with respect to the surface, intersected by the probe beam at right angles at a distance, *d*, of 230 ± 1 mm. The surface itself was placed at 10 ± 1 mm from the probe beam, thus the overall distance between the valve and the liquid surface was determined to be 240.0 ± 1.4 mm.

The experiments reported in this chapter were carried out prior to the comprehensive molecular beam optimization tests reported in Chapter 3, and without monitoring the current draw of the discharge device. As such, the properties of the molecular beam were optimized by monitoring the stability and reproducibility of the LIF signal over a lengthy period of time with the 'tune-up' program, and via acquisition of preliminary TOF profiles and excitation spectra. For each carrier gas used, the conditions were optimised to provide the highest OD number density and the most rotationally cold beam, by varying the voltage of the HV pulse and the backing pressure of the gas. All other *in situ* conditions were set arbitrarily based on previous conditions determined from experiments where OH was produced via photolysis (Section 2.5.3)

A high pressure of carrier gas (3 bar of He or 2 bar of Ne) was bubbled through the D_2O reservoir, creating molecular beam mixtures of ≈1% and ≈1.5 % D_2O in He and Ne, respectively. The mixture was fed to the pulsed valve, which had an aperture of 1.0 mm. The nominal pulse length of the pulsed valve was set at 500 μs. The discharge device attached to the valve was the original un-modified design provided by the Greaves group, described in section 2.5.4. The fast switch was triggered to apply an optimized voltage of -1400 V for the He-seeded beam and -1150 V for the Ne seeded beam for a duration of 10 μs, timed to fire typically 100 μs into the gas pulse. To further stabilize the discharge, a tungsten filament was placed in the 'source' part of the main chamber (see below), and a current of between 0.4 and 2 A was applied, adjusted regularly throughout the day to achieve the optimal discharge conditions.

The free-jet expansion of the beam was collimated by a 5 mm diameter conical skimmer, located at 167.0 mm from the valve nozzle and 160.5 mm from the last constraining element of the discharge device, i.e. the aperture of the front electrode. This was chosen to ensure that the molecular beam would dose a ~ 1 cm^2 area on the liquid surface. A 30 x 30 cm gas baffle (as described in section 3.6.2) was attached to the skimmer holder plate, effectively dividing the main chamber into source and scattering chambers. The position of the skimmer holder allowed the user to easily accommodate both the hot filament on the 'source' side of the main chamber, and the large gas baffle itself.

4.2.2 Monte Carlo Simulations

To aid in the interpretation of the experimental profiles obtained from the single-point detection set-up, OD TOF profiles were simulated with a variant of the LabVIEW™ Monte Carlo simulation previously developed in the McKendrick group [59].

The simulated TOF profiles were obtained by calculation of a large number of individual OD trajectories with correctly weighted Monte Carlo sampling over the experimental parameters. The LabVIEW™ program allowed the user to set parameters, such as the pulsed valve-to-surface distance, the valve-to-skimmer distance, the diameter of the skimmer, the angle of incidence with respect to the surface, length of the HV pulse, the probe beam size and shape (round beam or rectangular sheet), and the dimensions of the liquid surface to match the experiments. The trajectories of the incident OD radicals were selected by checking whether they passed through the skimmer. If the incident OD trajectories then intersected the detection volume (i.e. the fraction of the probe beam viewed by the single-point detection set-up), the simulation program would calculate the range of delays in which the OD radicals were within that volume, based on the velocity of OD in that trajectory. The intensity of the simulated TOF profile was then appropriately incremented at the relevant delays.

The velocities of the OD radicals with incident trajectories were picked at random from a distribution of speeds which was assumed to follow a sum of individual Gaussian distributions. The average speed and full width half maximum (FWHM) of each Gaussian distributions, as well as the relative weighting of each individual distribution with respect to the overall simulated profile, were varied by the user until the simulated

profile matched an experimentally obtained incident beam profile imported into the simulation program. To accurately determine the incident beam parameters, the experimental profile was obtained from the set of incident OD profiles acquired at the lowest *N* level probed.

The trajectories and velocities obtained from the simulated incident beam were then used to determine the trajectories of the scattered OD from the surface. Once an incident OD trajectory that had successfully passed through the skimmer was determined to have intersected the liquid surface, the impact point and flight time to the surface were used as the starting point for an OD recoil trajectory. The IS or TD character (see Chapter 1) of these trajectories was assigned by sampling from a binary distribution given by a user-set IS/TD ratio. TOF profiles of both the IS and TD component were then simulated separately. As with the incident beam, when the trajectories intersected the probe volume, the range of delays when OD was in the probe volume were calculated, and the intensity of the simulated profiles was incremented at the relevant delays. A representative simulation of incident and scattered OD profiles with typical experimental parameters and a 1:1 IS/TD ratio is presented in Figure 4.2.

To obtain the TD profile, the direction of the simulated TD trajectories was sampled from a cosine-weighted distribution around the surface normal, whereas the recoil speed was selected at random from a Maxwell-Boltzmann distribution characterized by a user-defined surface temperature [4, 88-90]. With regards to the IS profile, the speed and direction of the IS trajectories was determined by the program from a user-defined angular distribution of the IS trajectories, a final-to-incidence angle ratio, and an effective surface mass of the liquid. Unlike the assumed TD distribution, those parameters are unknown *a priori*, as they are dependent on the mass, angle of incidence and collision energy of the incident projectile [88-91]. There are no known results in the literature that provide those parameters for experimental conditions comparable to the ones used in the scattering experiments reported in this chapter. Therefore, only the simulated TD profiles will be used for comparison with the experimental TOF profiles shown below.

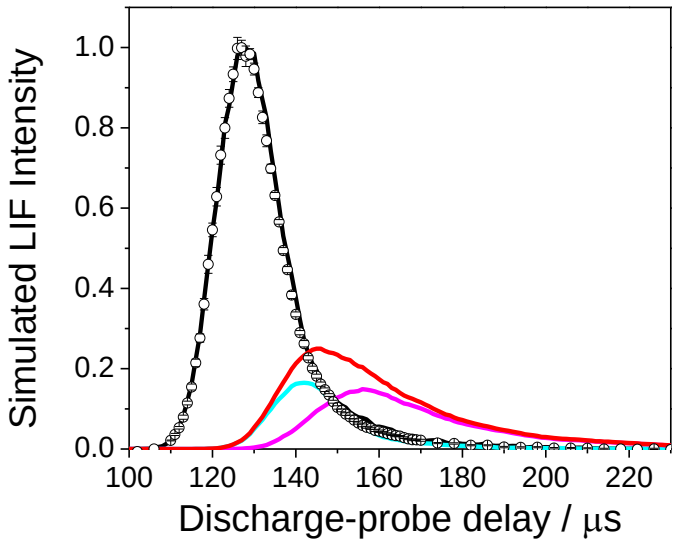

Figure 4.2: Representative Monte Carlo simulated TOF profiles. 10^7 trajectories were simulated in these profiles, with an IS/TD ratio of 0.5, a TD temperature of 300 K, and detection time step of 1 μs. The parameters of the simulated incident beam (black line) were manipulated to match an experimental TOF profile (open circles) on the $Q_1(2)$ transition. This gave a simulated scattered OD profile (red line), where the IS and TD contributions are represented by the cyan and magenta lines, respectively. For demonstrating purposes, the parameters of the simulated IS profile were arbitrarily set to match the results obtained from scattering $O(^3P)$ from squalane at high collision energies, as reported in references [4, 88-90]

4.3 Incident Beam Characterization

The first goal of the experiment was to characterize the incident beam of OD radicals, using He and Ne as the carrier gases for the molecular beam. For both sets of experiments, the liquid bath-assembly was fully retracted in the load-lock chamber.

To determine the average speed, and thus the collision energy of the incident radicals, TOF profiles were taken at the lowest rotational *N* level for each of the carrier gases used. The profiles shown in Figure 4.3 were obtained from an average of between 4 and 5 individual profiles, plotted as a function of probe-pulse delay with respect to the start of the discharge pulse. The figure illustrates the differences in the arrival time of OD when using different carrier gases, whereby the beam using the He carrier arrives

earlier, and has a narrower profile, than with Ne, as is expected. The full-width at half-maximum (FWHM) was extracted from each individual profile and averaged.

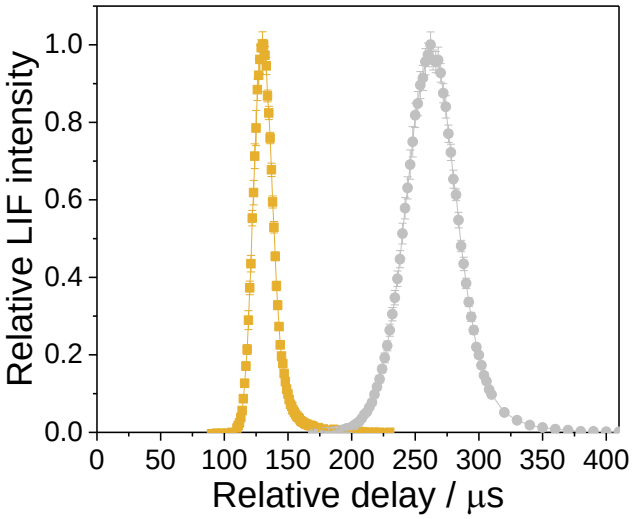

Figure 4.3: Peak-normalized TOF profiles of the OD LIF signal probed on the $Q_1(1)$ transition versus discharge-probe delay. Carrier gases used: He (orange squares) and Ne (grey circles).

To obtain the average speed of the radicals, the mean arrival time, $<t>$, was calculated for each individual profile, integrating between 110 μs and 170 μs for the He carrier profile and between 186 μs and 310 μs for the Ne carrier profile. The speed was then calculated via the equation:

$$< v > = \frac{\mathrm{d}}{(<t> - 5\ \mu s)} \tag{4.4}$$

where d is the distance from the valve nozzle to the probe beam (determined above). The factor of 5 μs accounts for the fact that the OD detected at the peak of the TOF profile will have, on average, been created half way through the high-voltage pulse. This assumes that OD is generated at a constant rate during the pulse. Finally, the average lab-frame kinetic energy $<E_k>$ is calculated via the equation:

$$< E_k > = \frac{1}{2} m < v >^2 \tag{4.5}$$

where m is the mass of OD. A summary of the properties obtained from the TOF profiles is reported in Table 4.2.

Carrier gas	**Mean arrival time / µs**	**FWHM / µs**	**$\langle v \rangle$ / m s^{-1}**	**$\langle E_k \rangle$ / kJ mol^{-1}**
He carrier	132.0 ± 0.2	17.5 ± 0.3	1811 ± 8	29.5 ± 0.3
Ne carrier	262.2 ± 0.2	45.8 ± 0.4	894 ± 3	7.20 ± 0.06

Table 4.2: Summary of properties extracted from the incident beam TOF profiles measured on the $Q_1(1)$ transition, using He and Ne as the carrier gas

For the purposes of predicting the excitation function for uptake of OD on squalane as discussed in the introduction (section 4.1), $\langle E_k \rangle$ can be related to the centre-of-mass collision energy, E_{coll} in Equation (4.1) via the expression

$$E_{coll} = \frac{m_s}{m_s + m_{OD}} \langle E_K \rangle \tag{4.6}$$

where m_{OD} is the mass of OD, and m_S is the characteristic mass of the surface. Previous gas-liquid scattering experiments and related studies at SAM surfaces have shown that the surface behaves as if it has a finite mass [2, 68, 75, 78, 88-91, 117, 125] that is significantly less than the mass of an intact liquid molecule, including squalane as a specific well-studied example [88-91]. There are no previous experiments on OH (or OD) scattering from squalane surfaces from which an accurate value of m_S can be adopted for use in Equation (4.6). However, there have been a number of studies by Minton and co-workers on O(^{3}P) atom scattering from squalane surfaces [88-91]. For the lowest lab-frame energies, $\langle E_k \rangle$ = 47 kJ mol^{-1}, for which results are available for O + squalane collisions, the group report m_S = 109 amu for inelastic scattering of O and 76 amu for reactive scattering to form OH. It is expected that OH (or OD) would be reasonably kinematically similar to scattering of O(^{3}P) from squalane. Therefore, for the purpose of obtaining an estimate value of E_{coll}, an indicative value of m_S = 100 amu was adopted. This value is likely to be an underestimate of the true value of m_S for this experiment, as the work by Minton *et al.* has shown that m_S is inversely dependent on the collision energy used. However, given that the indicative m_S used is already a factor

of 5 higher than the value of m_{OD}, a higher value of m_S is unlikely to significantly change the value of E_{coll} obtained via Equation (4.6). On this basis, for the two $\langle E_k \rangle$ values of 7.20 ± 0.06 and 29.5 ± 0.3 kJ mol^{-1} obtained for the Ne and He carrier, E_{coll} is estimated to be around 6.10 ± 0.05 and 25.0 ± 0.2 kJ mol^{-1}, respectively.

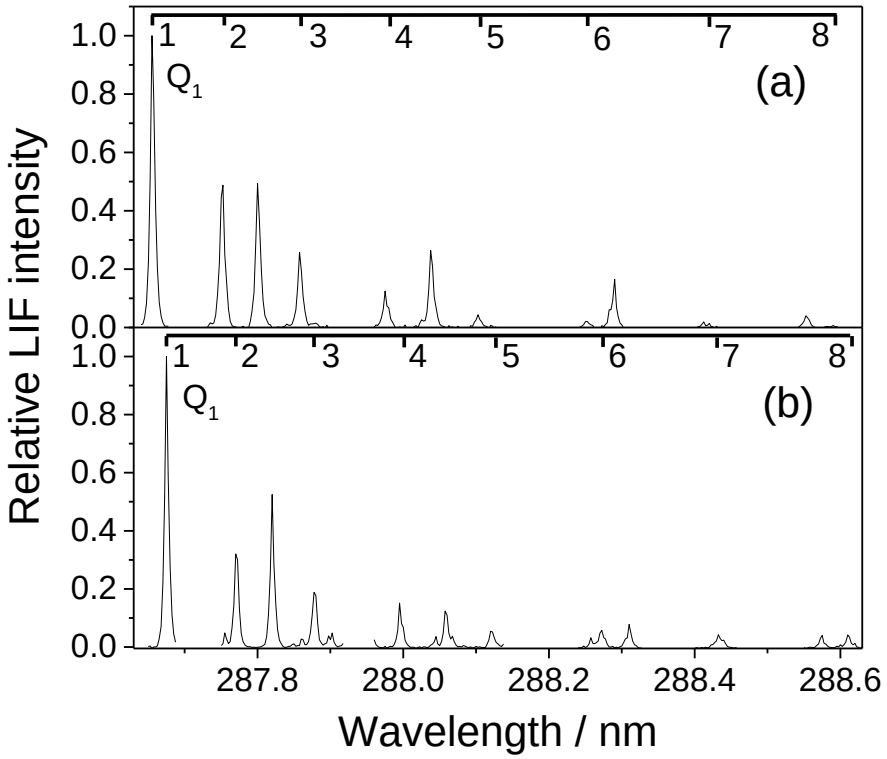

Figure 4.4: Representative LIF excitation spectra on the OD A-X (1,0) band taken at the peak of the incident OD TOF profiles obtained with the He (a) and Ne (b) seeded beam All spectra have been normalized to the intensity of the $Q_1(1)$ transition. Note that the probe laser wavelength was stepped discontinuously, capturing regions containing Q_1 branch lines, with P_1 branch lines used as reference.

The rotational energy distribution of the radicals for each incident beam was characterized via excitation spectra, taken at the delay corresponding to the peak of the respective TOF profiles. Representative spectra obtained using either He or Ne as the carrier gas are shown in Figure 4.4. An average of the populations for each of the rotational levels probed was extracted from 3-4 individual spectra obtained from each carrier gas, and shown in Figure 4.5. By inspecting the relative populations, it was observed that the majority of OD radicals populate the lowest few *N* levels for both

carriers, with almost half of the radicals populating the N = 1 level (45% with the He carrier, 48% for Ne), and more radicals populating N = 2 using He compared to Ne (28% and 18%, respectively). It was also noted that in both cases, a number of higher N levels were also populated, suggesting that the cold rotational distribution was accompanied by a secondary hotter distribution.

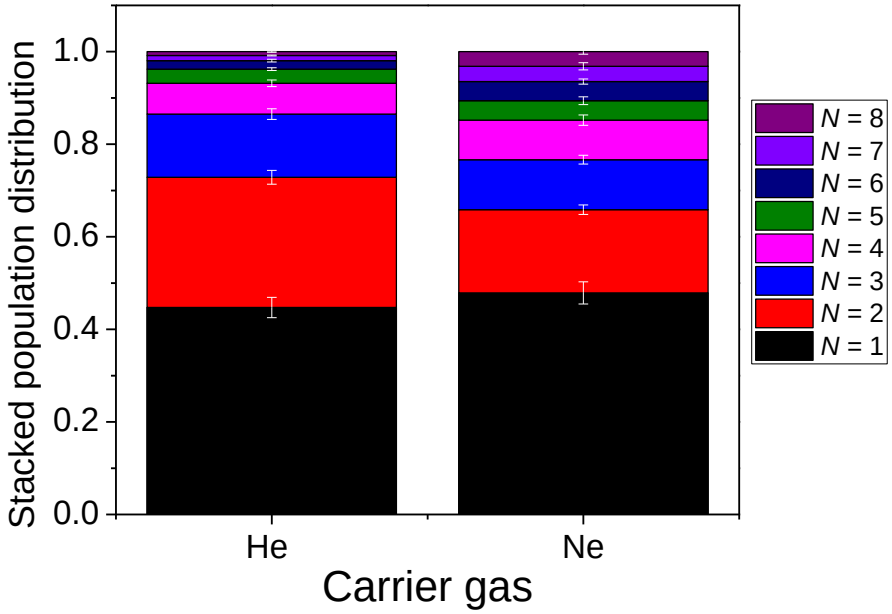

Figure 4.5: Stacked average rotational population distributions from N = 1 to N = 8 included, normalized to the sum of their populations. The populations were obtained from excitation spectra taken at the peak of the incident OD TOF profiles using He (left) and Ne (right) as the carrier gas. Error bars represent the standard error of the mean of the populations.

This was further confirmed from Boltzmann plots of these populations, obtained as described in Section 2.9.2. As shown in Figure 4.6., these plots are clearly non-linear, requiring the two-temperature model fit described in the Experimental Methods (Section 2.9.2) to parameterise the distribution. The results are reported in Table 4.3.

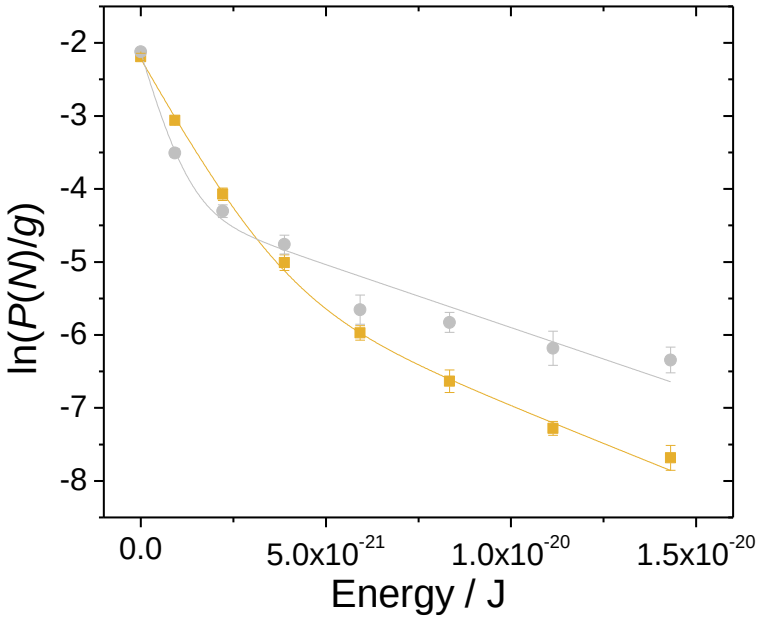

Figure 4.6: Representative Boltzmann plot for the incident OD taken at the peak of the TOF profile for the He-seeded beam (orange squares) and Ne-seeded beam (light gray circles). Populations derived from Q_1 branches. Lines represent the best fit to two temperatures.

Carrier gas	T_1 / K	T_2 / K	α (%)
He carrier	78 ± 5	171 ± 46	76 ± 4
Ne carrier	38 ± 3	203 ± 40	38 ± 3

Table 4.3: Summary of parameters extracted by applying the two-temperature fit to rotational populations derived from Q-branch excitation spectra taken at the peak of the incident beam profiles.

The low α value (fraction of the population with the lower temperature) obtained for the Ne carrier as shown in Table 4.3 would imply that the higher rotational temperature is predominant in the beam. However, a comparison of the LIF signal sizes in the excitation spectrum in Figure 4.4 (b) clearly shows that the LIF signal at $N = 1$ is higher than the signal present in all other N levels. If the α value truly represented the amount of 'cold' OD radicals in the beam, it would have been higher for the Ne carrier than for

He. This discrepancy may be due to the smaller number of points used by the two-temperature fit to determine T_1 in the Boltzmann plot for the Ne carrier shown in Figure 4.6

4.4 Results

4.4.1 TOF profiles

TOF profiles of OD radicals scattering off each of the liquid surfaces were measured systematically via the $Q_1(2)$, $Q_1(5)$ and $Q_1(8)$ transitions with the He carrier, and via $Q_1(2)$, $Q_1(5)$ and $Q_1(7)$ with the Ne carrier. These were plotted against the delay relative to the start of the discharge pulse. The transitions used for the measurements were chosen because they span, in approximately equal rotational energy increments, the range of N' levels significantly populated via collisions at the surfaces. Between 9 and 12 individual profiles, with 30 laser shots per point, were acquired for each of the lines probed, and then averaged.

A full set of profiles was acquired for the PFPE liquid alongside a set for squalane, alternating surfaces between each individual profile, while a smaller set of PFPE profiles was acquired in conjunction with the full set for squalene, with individual PFPE profiles acquired at regular intervals between squalene profiles, thus ensuring reproducibility of the results. In addition, individual profiles of the incident beam were acquired alternately between profiles with the surfaces in place. The profiles with surface in were normalised at the delay corresponding to the peak of the average incident beam profiles taken on the same day. This ensured that the profiles with surface present were consistent with the corresponding incident beam intensity. Both the average profiles with surface in and their respective incident beam profiles for the experiment with the He carrier are displayed in Figure 4.7, whereas the equivalent results using the Ne carrier are shown in Figure 4.8. All the profiles with the liquid surfaces in place (Figures 4.7 (a) and 4.8 (a)) show clearly that additional OD signal is present at later times relative to the incident beam profile; this is obviously consistent with OD that has scattered and rebounded into the probe region. The inclusion of the skimmer and the gas baffle described in section 3.6, and further elaborated on in Chapter 3 section 3.6.2, ensured that this additional OD can only come from collisions with the liquid surface.

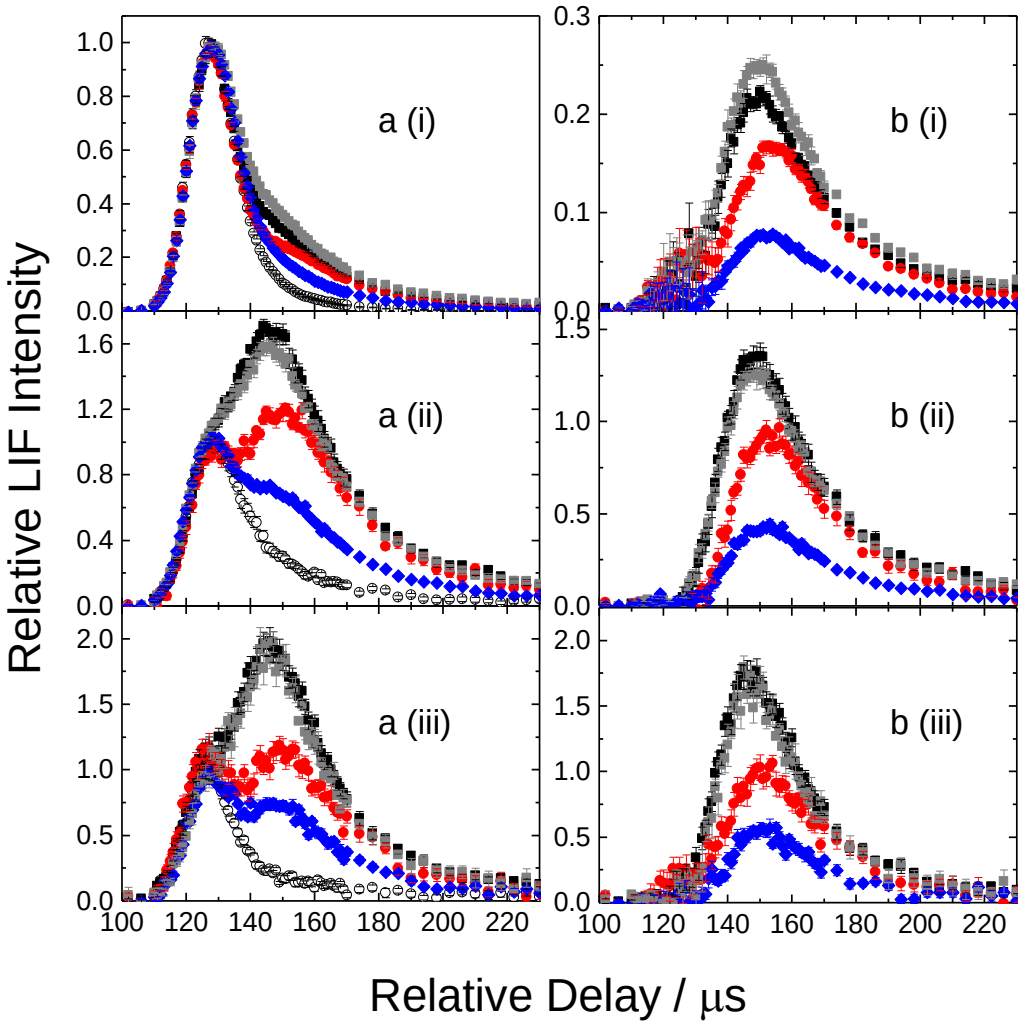

Figure 4.7: TOF profiles of the intensity of the OD A-X (1,0) LIF transition as a function of discharge-probe delay with $\langle E_k \rangle = 29.5 \pm 0.3$ kJ mol^{-1}. The incident beam with no liquid surface present is represented by open circles. The remaining profiles include scattered signals with a liquid surface at a distance of 10 ± 1 mm from the probe beam: PFPE (black squares for profile taken with squalane, grey squares for profile taken with squalene), squalane (red circles) and squalene (blue diamonds). (a) Raw profiles; (b) profiles following subtraction of the incident beam. Probe transitions: (i) $Q_1(2)$, (ii) $Q_1(5)$, (iii) $Q_1(8)$. All profiles have been normalized to the peak of the corresponding incident beam.

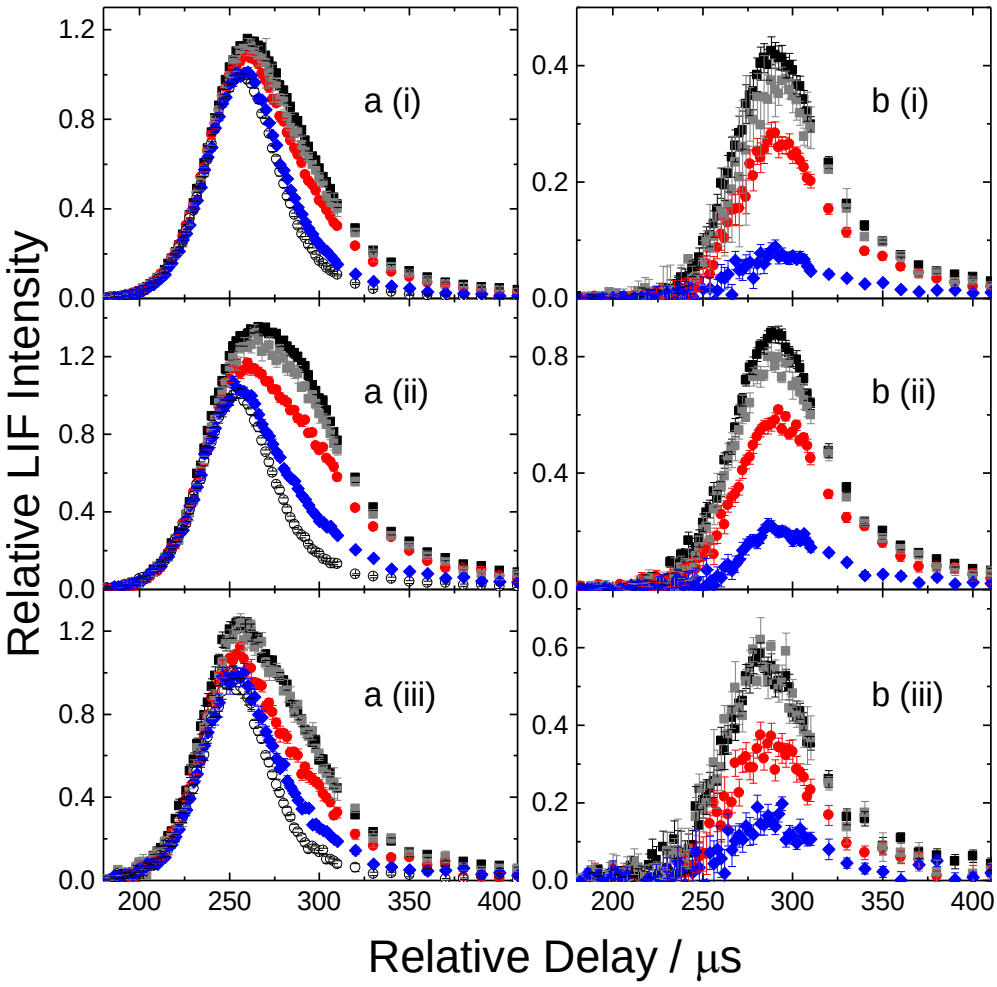

Figure 4.8: TOF profiles of the intensity of the OD A-X (1,0) LIF transition as a function of the discharge-probe delay with $\langle E_k \rangle = 7.20 \pm 0.06$ kJ mol^{-1}. The incident beam with no liquid surface present is represented by open circles. The remaining profiles include scattered signals with a liquid surface at a distance of 10 ± 1 mm from the probe beam: PFPE (black squares for profile taken with squalane, grey squares for profile taken with squalene), squalane (red circles) and squalene (blue diamonds). (a) Raw profiles; (b) profiles following subtraction of the incident beam. Probe transitions: (i) $Q_1(2)$, (ii) $Q_1(5)$, (iii) $Q_1(7)$. All profiles have been normalized to the peak of the corresponding incident beam.

To obtain the profiles of OD radicals scattered off the surface, the daily-average incident beam profile was subtracted from the profiles with the surfaces in, and the results shown in column (b) of the Figures 4.7 and 4.8. A straight subtraction of the incident beam profile from the raw profiles was found to be sufficient to give a scattered

OD profile with no systematically unphysical residuals at early delays. The slight exception was with the $Q_1(2)$ profile at the higher collision energy, where the scattered signal is the lowest proportion of the incident beam. This suggests that there is some small attenuation of the incident beam, likely due to gas-phase inelastic collisions between OD radicals in the molecular beam with mainly carrier gas projectiles that have scattered from the surface prior to the arrival of the OD packet in the detection region. These collisions cause a small fraction of the incident radicals in $N = 2$ to change rotational state, resulting in an apparent loss of incident OD signal in the TOF profile. This, in turn, may lead to an increase in signal in TOF profiles for higher N levels and at later delays. Another possible outcome is for the OD radicals to scatter with a trajectory that does not pass through the detection region. For the purpose of analysing the TOF results, the incident beam profile was scaled by an empirically determined factor, which was on average 96% of unity, and never smaller than 93%, to ensure the subtraction smoothly approached zero at early times, as physically required. This represents a small fraction of the overall TOF profile, so the effects of the attenuation of the $N = 2$ signal is likely to have a negligible effect on profiles obtained at the higher N states. A representative example of the $Q_1(2)$ scattered OD profile after subtracting the uncorrected and scaled incident beam profiles is shown in Figure 4.9.

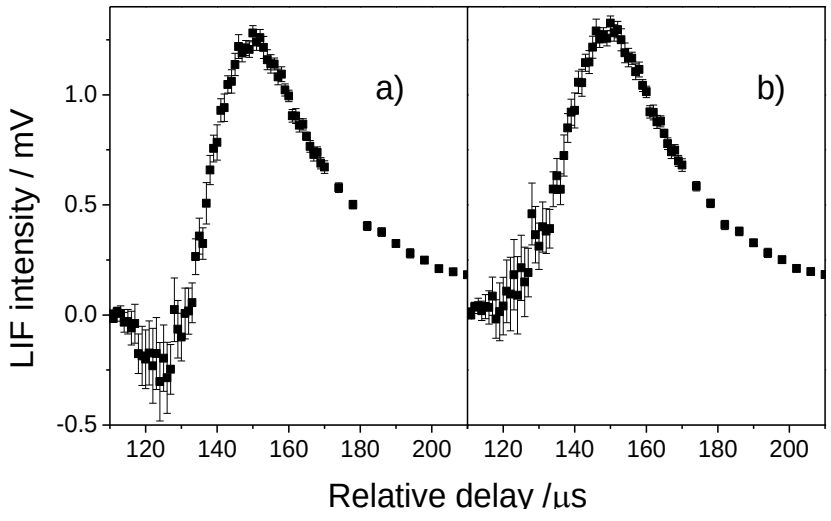

Figure 4.9: Representative TOF profiles of OD radicals probed off the $Q_1(2)$ scattered off PFPE surface, following subtraction of the incident beam contribution. In (a) the raw incident beam contribution was used for subtraction, while in (b), the incident beam was scaled in order to remove the negative signal appearing at early delays.

The most obvious feature of interest apparent in both Figure 4.7 and Figure 4.8 is the systematic variation in the relative magnitude of the scattered signal for the different liquids. The OD LIF signal is consistently larger for PFPE at either collision energy across all transitions studied, and gets progressively smaller for squalane, and then for squalene. These differences will be quantified and discussed in further detail in section 4.4.4. Other, more subtle features of interest from a dynamical perspective, were also observed via comparison of the peak-normalized scattered OD profiles from each liquid at each of the transitions probed with each other and with a Monte Carlo simulation (Section 4.2.2) of the expected profiles if all scattering occurred by a fully thermalized TD mechanism (Figure 4.10).

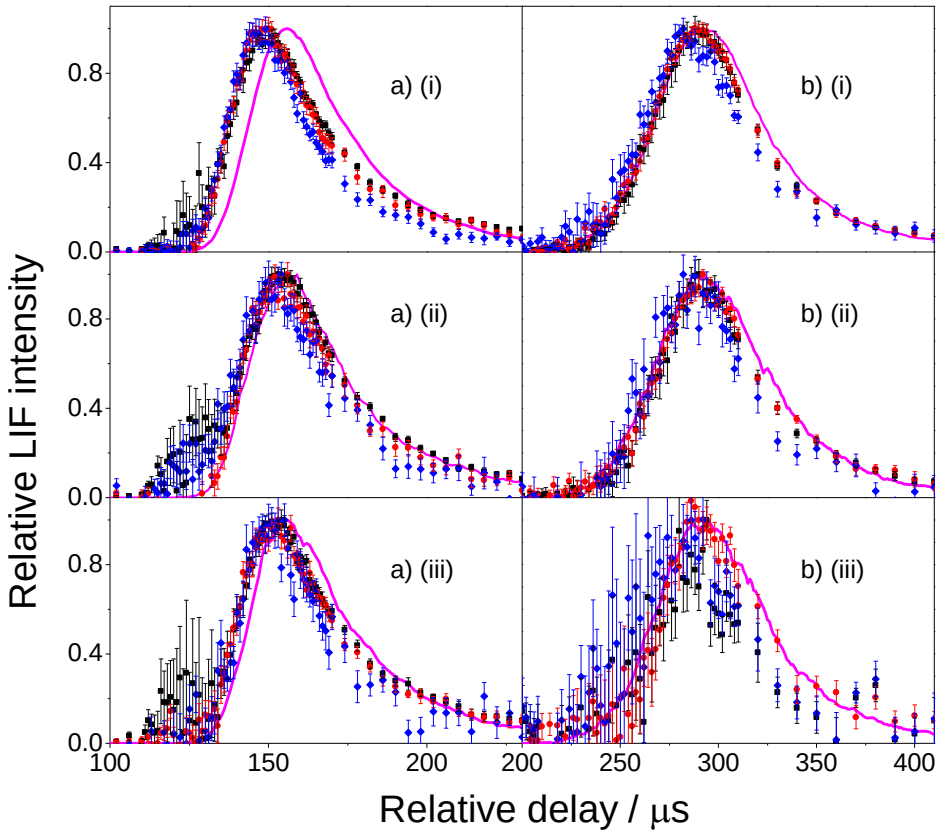

Figure 4.10: Peak normalized TOF profiles of the OD A-X (1,0) LIF signal on the discharge-probe delay, at high (a) and low (b) collision energies. Liquids: PFPE (i), squalane (ii) and squalene (i). Transitions probed are $Q_1(2)$ (black squares), $Q_1(5)$ (red circles), and $Q_1(7)$ [in (a)] or $Q_1(8)$ [in (b)] (blue diamonds). Solid lines represent a Monte-Carlo simulation of the anticipated TD profile (magenta), as described in text.

As shown in Figure 4.10 (a), there are noticeable differences in the peak arrival times between liquids for the scattered profiles obtained at higher $<E_k>$, where the peaks are always earliest from PFPE, and latest from squalane regardless of the transition probed. These differences in arrival time are not readily apparent in the profiles obtained at lower $<E_k>$ in Figure 4.10 (b). Comparison of the profiles for each liquid at each transition probed also show some subtle differences in shape between Figure 4.10 (a) and (b). At higher $<E_k>$, the profiles have relatively similar rising edges, but at longer times the profiles for $N' = 5$ and 8 decline progressively more rapidly relative to $N' = 2$. The behaviour is generally similar, although less clear-cut, at the lower $<E_k>$. The slightly more rapid rise for the $N' = 7$ data observed at that collision energy may be an artefact of its lower signal to noise. These differences provide an indication of positive correlation between translational and rotation energies of the scattered OD, which are related to the underlying scattering dynamics. Finally, a comparison of the scattered profiles with the predicted TD distribution shows that the scattered products are superthermal for collisions at higher $<E_k>$ implying a considerable proportion of IS-like scattering. At the lower $<E_k>$, the departure from the predicted TD distribution is marginal. The differences in profile shape observed for the different transitions discussed earlier suggests that it would be incorrect to interpret this result as indicating that all the radicals scattered with a TD-like mechanism, but rather as a contribution between TD scattered OD and IS scattering that happened to produce near-thermal final speeds because of the modest incident energy. Distinguishing between those two contributions, however, is not possible with the data obtained in this chapter. An attempt to distinguish the two contributions will be discussed in Chapter 5.

4.4.2 Excitation spectra

Excitation spectra were acquired at delays corresponding to the peak of each of the scattered OD profiles, as determined from Figure 4.7 (b) and Figure 4.8 (b). They were contrasted with spectra obtained from the peak of the incident beam, as determined from Figure 4.7 (a) and Figure 4.8 (a). Each spectrum was acquired as described in the experimental methods (Chapter 2, section 2.9.2) in order to obtain a full set of Q_1 branch lines for $N' = 1 - 8$. P_1 branch lines for $N' = 1 - 4$ were also acquired but were only used as an internal reference to help identify the Q_1 branch lines. Representative excitation spectra for the high $<E_k>$ are shown in Figure 4.11, whereas the equivalent spectra for the low $<E_k>$ are displayed in Figure 4.12.

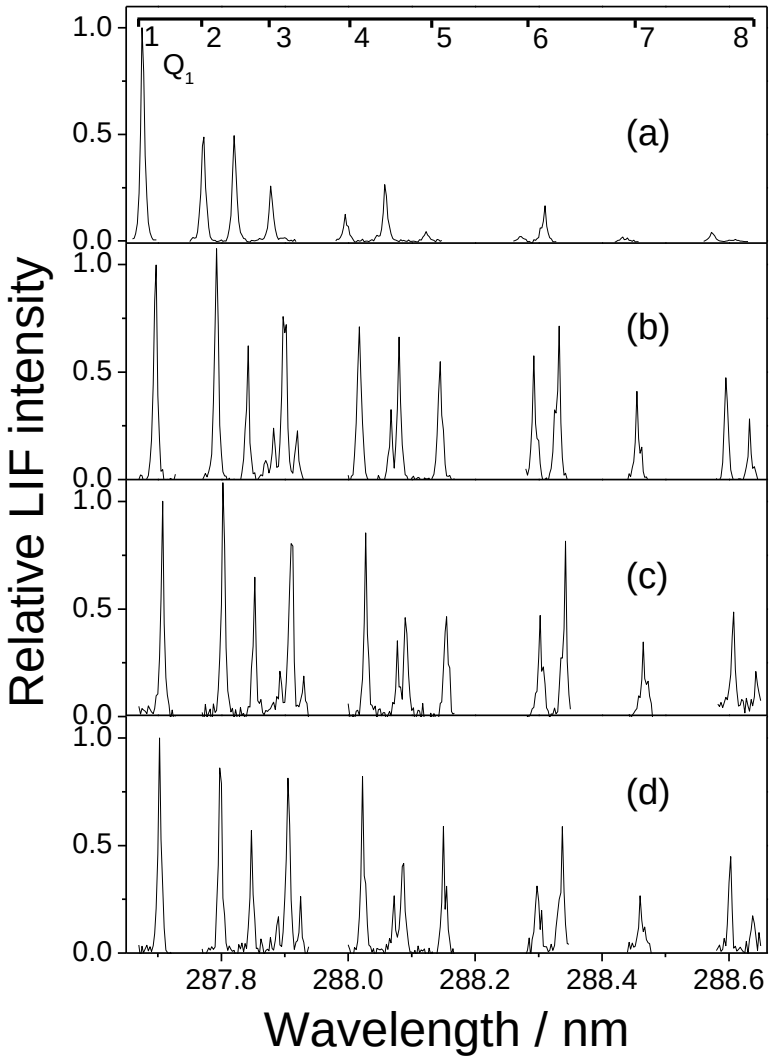

Figure 4.11: Representative LIF excitation spectra on the OD A-X (1,0) band taken at the peak of the (a) incident; and (b) – (d) scattered OD TOF profiles from the He-seeded beam at $\langle E_k \rangle$ = 29 kJ mol^{-1}. Liquids: (b) PFPE, (c) squalane, (d) squalene. All spectra have been normalized to the intensity of the $Q_1(1)$ transition. Note that the probe laser wavelength was stepped discontinuously, capturing only regions containing Q_1 branch lines.

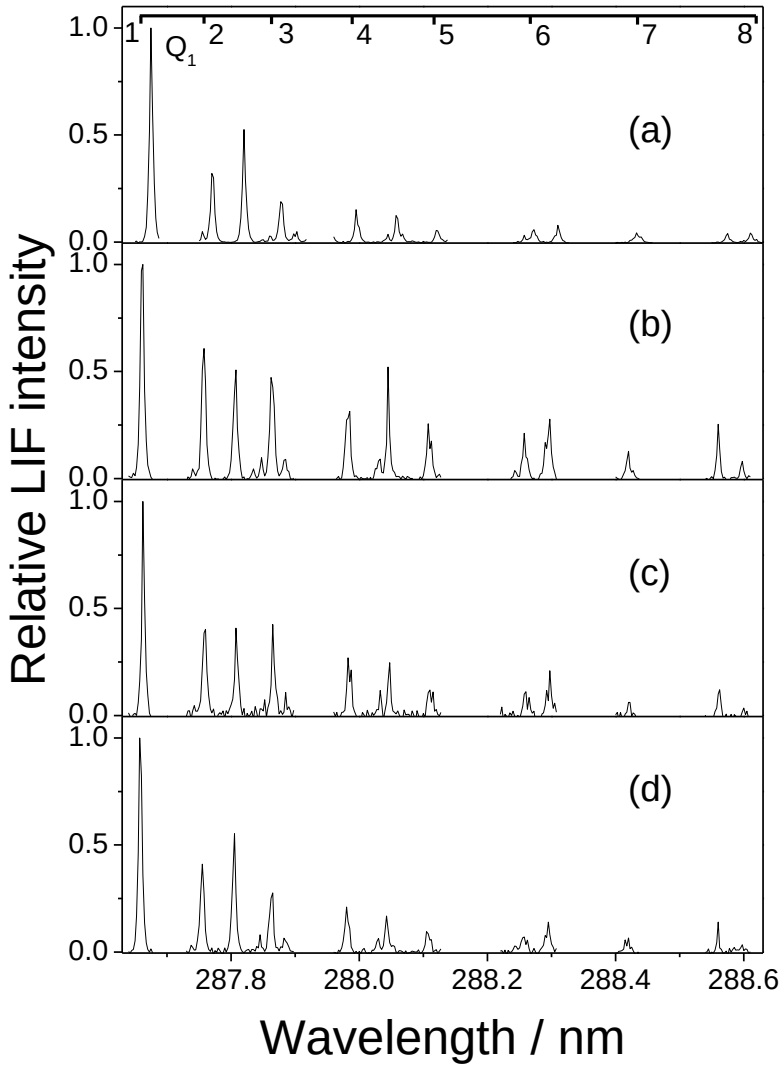

Figure 4.12: Representative LIF excitation spectra on the OD A-X (1,0) band taken at the peak of the (a) incident and (b) – (d) scattered OD TOF profiles from the Ne seeded beam at $\langle E_k \rangle$ = 7.5 kJ mol^{-1}. Liquids: (b) PFPE, (c) squalane, (d) squalene. All spectra have been normalized to the intensity of the $Q_1(1)$ transition. Note that the probe laser wavelength was stepped discontinuously, capturing only regions containing Q_1 branch lines.

The representative spectra for the scattered OD clearly show that the higher N' levels are more populated than the equivalent incident beam spectra when looking at the high $<E_k>$ results. This is perhaps not quite so readily apparent when looking at the spectra obtained at the low $<E_k>$ results, however, it is apparent from Figure 4.8 (a) that there is a significant contribution from the tail of the incident beam at the delays at which the scattered OD spectra were taken, which affects the signal size of the lower N' levels in the spectra. Figure 4.7 (a) shows a smaller, but still non-negligible, tail of the incident beam is also present at the delays for scattered OD at the higher $<E_k>$, which , if not properly removed, would likely result in the rotational temperatures extracted from the raw spectra being underestimated. To account for this factor, a suitably-scaled multiple of the incident population distribution, extracted from excitation spectra taken at the same delay but with the liquid surface absent, was subtracted from the population distributions of the scattered OD. The scaling factor was based on the observed scattered:incident OD signal ratio obtained for $N = 2$, at the same delay as when the excitation spectra were taken. Rotational-level dependent correction factors derived from the thermal calibration method (Section 2.9.2) were applied to both sets of populations before subtraction. The initial populations, the scaled incident populations and the resulting subtracted populations are shown in Figure 4.13. The subtracted populations were then plotted in Boltzmann plots (Section 2.9.2), which were generally found to be well-fit by single Boltzmann temperatures, using instrumental weighting of the uncertainties. These temperatures are reported in Table 4.4, alongside the results from the global rotational temperatures discussed in the next section.

In principle, by recording more spectra at a sufficiently closely-spaced set of delays with both the surface in and out, complete information on the internal energy distribution over the entire scattered profile could be obtained. In practice, this approach would have been impractically laborious, and would have been subject to large statistical errors due to subtraction of the incident beam contribution, particularly for squalene (Figure 4.13 (iii)) and at the lower $<E_k>$ (Figure 4.13 (b)). Because of this, the excitation spectra were only taken at the peak of the TOF profiles, to provide corroboration for the global rotational temperature results discussed in the next section.

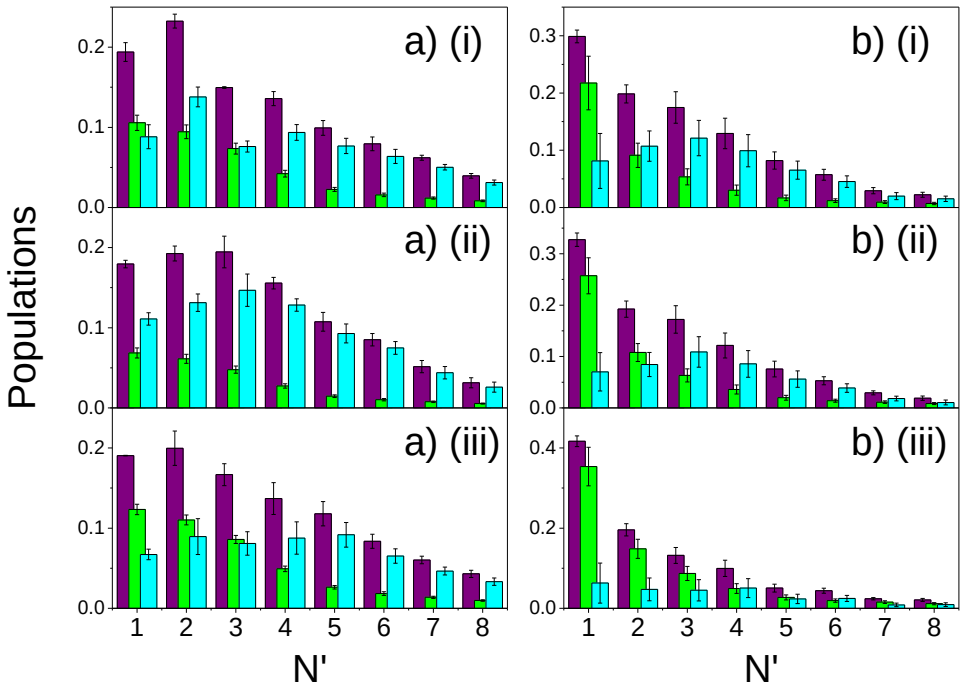

Figure 4.13: Relative population distributions extracted from the excitation spectra of the scattered OD (purple bars), scaled population distribution of the incident beam taken at the same delay (green bars), and population distribution of scattered OD profiles after subtraction of the ingoing beam (cyan bars). Carrier gases: a) He, b) Ne. Liquids: (i) PFPE, (ii) squalane and (iii) squalene.

4.4.3 Global rotational temperatures

Another method of obtaining the rotational temperature of scattered OD from a given surface is to derive what is referred to as its 'global rotational temperature', i.e. the rotational temperature integrated over the full TOF profile. This method, described in previous papers by the McKendrick group [11], consists of integrating the scattered OD profiles obtained from different rotational levels. After applying the thermal calibration correction, the integral yields were then used as points in a Boltzmann analysis (described in section 2.9.2), and a suitable Boltzmann fit was used to derive the global T_{rot}. From those temperatures, the rotational population in energy levels that were not probed directly in a set of scattering experiments can then be interpolated, providing information from N levels with overlapping transitions which would otherwise not be resolved experimentally. It also allows for the overall survival probabilities to be

correctly assessed without the need to acquire TOF profiles from all transitions where LIF signal is present, a task which is experimentally impractical.

The scattered profiles were integrated from 135 μs to 230 μs delay at high collision energy, and from 250 μs to 410 μs at low energy. The lower limits were chosen to avoid integrating over the noisy baseline region at early times, which is subject to the largest errors caused by subtraction of the incident beam. The resulting Boltzmann plots are shown in Figure 4.14 for the high collision-energy results, and Figure 4.15 for the low collision energy. There is no fundamental reason why the results of dynamical, IS-like scattering should be well-described by a single temperature, but in general, the 3-point fits were found to be reasonably linear.

The temperatures obtained from the Boltzmann fits are reported in Table 4.4, alongside the temperatures obtained from the excitation spectra. As is clear, the major influence on the rotational excitation of the scattered OD is the collision energy. All the global rotational temperatures at the higher $<E_k>$ are of order 100 K higher than thermal, whereas at the lower $<E_k>$ they are generally closer to thermal. Squalene may be something of an exception, giving the highest temperature at both collision energies; this may have a dynamical explanation, which will be discussed later in this chapter. The equivalent temperatures obtained from the excitation spectra follow a similar trend. This may be due to the fact that the excitation spectra only measure a subset of the scattered molecules, as opposed to the integral contribution over the whole profile. In addition, the peak of the profiles from different liquids occurs at different times (as shown in Figure 4.10), so the differences in temperature are likely going to be larger than if the spectra were taken at the same delay. Nevertheless, despite these detailed differences, there is generally reasonable agreement between the two sets of temperatures.

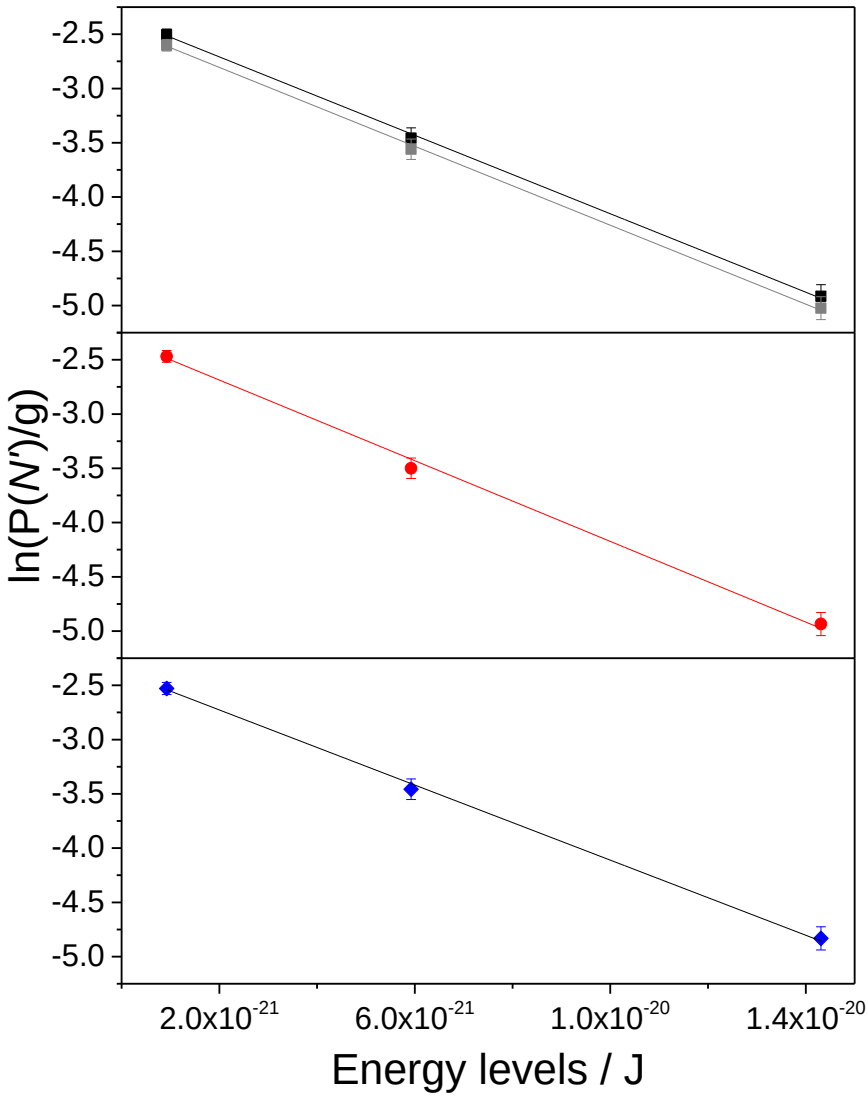

Figure 4.14: Boltzmann plot for the scattered OD using He carrier. Populations derived from the integrated TOF profiles at N' = 2, 5 and 8 on the Q_1 branch. Liquids: PFPE (black squares for profile taken with squalane, grey squares for profile taken with squalene), squalane (red circles) and squalene (blue diamonds). The two PFPE plots have been offset for clarity. Lines represent the best fit to a single temperature using instrumental weighting of the points.

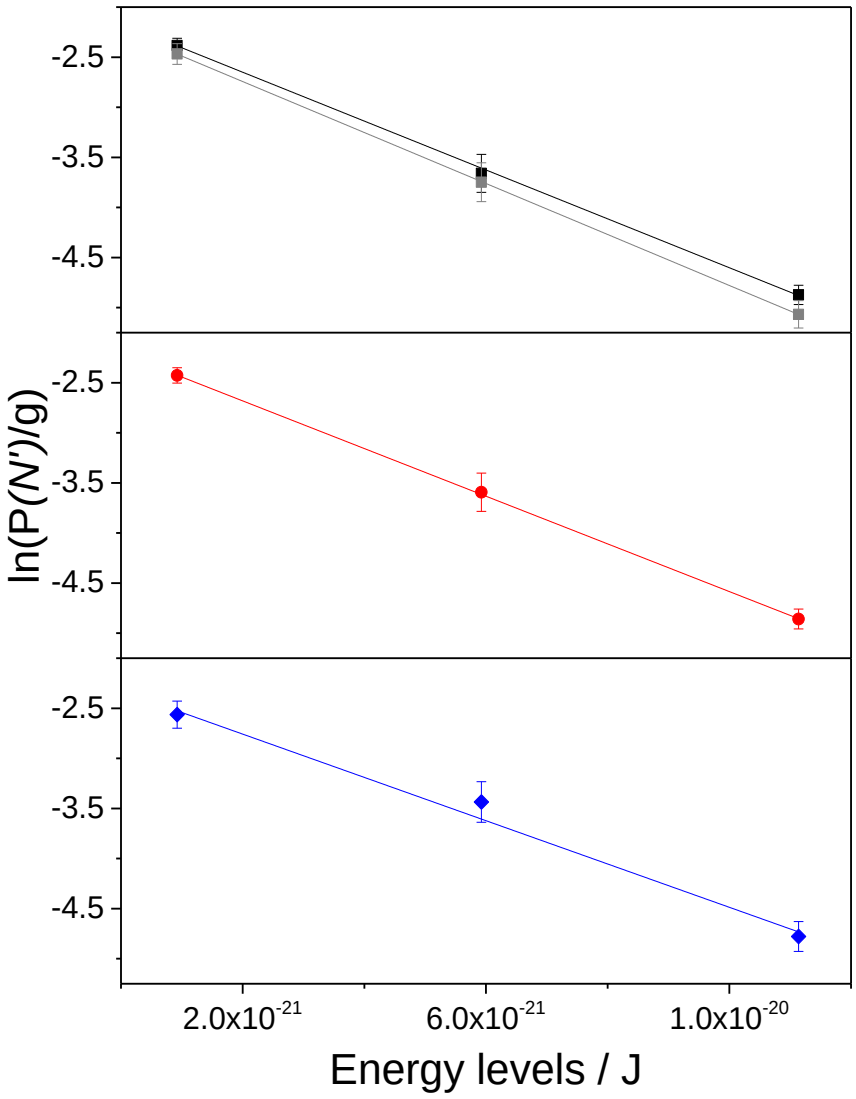

Figure 4.15: Boltzmann plot for the scattered OD using Ne carrier. Populations derived from the integrated TOF profiles at $N' = 2, 5, 7$ on the Q_1 branch. Liquids: PFPE (black squares for profile taken with squalane, grey squares for profile taken with squalene), squalane (red circles) and squalene (blue diamonds). The two PFPE plots have been offset for clarity. Lines represent the best fit to a single temperature using instrumental weighting of the points.

Liquid surface	**Excitation spectra / K**		**Global temperature / K**	
	He Carrier	Ne Carrier	He Carrier	Ne Carrier
PFPE	438±28	296±44	401±19 398±19	297±14 285±19
Squalane	354±24	297±46	390±18	304±16
Squalene	456±65	293±65	419±21	335±30

Table 4.4: Rotational Temperatures of the scattered OD radicals

4.4.4 Survival probabilities

The differences in signal magnitude between the scattered OD profiles from different liquids presented in Figure 4.7(b) and Figure 4.8(b) show that the experimental approach is capable of measuring differences in the number density of OD radicals that have survived an encounter with each of the liquid surfaces probed. The fraction of OD that survives an encounter with a given liquid surface can be quantified in terms of a survival probability, σ, defined as the ratio of the integrated product density from a potentially reactive liquid, $D(N')_{\mathrm{liq}}$, to that from PFPE, $D(N')_{\mathrm{PFPE}}$, in a specific final rotational state, N'. For the integrated densities to properly represent the total populations across all final rotational levels, they must be adjusted for the relative fraction of the total rotational populations, $p(N')_{\mathrm{liq}}$ and $p(N')_{\mathrm{PFPE}}$, that resides in the level for which the profiles were measured. The survival probability is thus calculated via the equation

$$\sigma = \frac{\int_{t_{min}}^{t_{max}} D(N\prime)_{liq}\, dt}{\int_{t_{min}}^{t_{max}} D(N\prime)_{PFPE} dt} \frac{p(N\prime)_{PFPE}}{p(N\prime)_{liq}} \tag{4.7}$$

In principle, the overall survival probabilities derived from each of the observed N' product levels would be the same for a given reactive liquid. This relies on the relative integral populations being described perfectly by the fitted global rotational temperature T_{rot}. In practice, the finite scatter around the best-fit line in the Boltzmann analysis may result in slight differences in the survival probabilities. This is evident in the survival probabilities for each of the N' levels probed, reported in Table 4.5 below.

Ne Carrier $\langle E_k \rangle$ = **7.20 ± 0.06 kJ mol^{-1}**	**Liquid surface**	**$Q_1(2)$ transition**	**$Q_1(5)$ transition**	**$Q_1(7)$ transition**
	PFPE (a)	1.00	1.00	1.00
	Squalane	0.61±0.04	0.67±0.17	0.61±0.09
	Squalene	0.19±0.02	0.24±0.06	0.19±0.03
He Carrier $\langle E_k \rangle$ = **29.5 ± 0.3 kJ mol^{-1}**	**Liquid surface**	**$Q_1(2)$ transition**	**$Q_1(5)$ transition**	**$Q_1(8)$ transition**
	PFPE (a)	1.00	1.00	1.00
	Squalane	0.68±0.04	0.66±0.08	0.70±0.10
	Squalene	0.32±0.02	0.31±0.04	0.31±0.04
a) A survival probability of unity is assumed for PFPE.				

Table 4.5: Survival probabilities of OD from each liquid surface at each of the transitions probed.

To take due account of this, the average of the individual survival probabilities was taken, propagating individual statistical uncertainties in the results for each N' into the final uncertainty, and reported in Table 4.6. Also included in the table for comparisons are the values previously obtained using the 'bulk photolysis' method [11], which produced OH radicals with higher translational energies than those available using the molecular beam source. The breaking or even extension of the existing O-H/D bond does not correspond to the reaction coordinate for either H-abstraction or OH-addition reactions, as discussed below, and so isotopic effects are not expected to make a significant impact on the survival probability, allowing both sets of results to be compared. In both this experiment and the previous 'bulk photolysis' experiments, the relative survival probabilities between squalane and squalene are statistically better determined than what might be immediately apparent from Table 4.6, as the uncertainties quoted depend on the statistical fluctuations in the signals from each of the reactive liquids and in the PFPE profiles with which they are compared.

Liquid surface	**Ne Carrier** $\langle E_k \rangle$ **= 7.20 ± 0.06 kJ mol^{-1}**	**He Carrier** $\langle E_k \rangle$ **= 29.5 ± 0.3 kJ mol^{-1}**	**Bulk photolysis (c)** $\langle E_k \rangle$ **= 54 kJ mol^{-1}**
PFPE (a)	1.00	1.00	1.00
Squalane	0.63 ± 0.06 (b)	0.68 ± 0.04 (b)	0.70 ± 0.08 (b)
Squalene	0.21 ± 0.02 (b)	0.31 ± 0.02 (b)	0.61 ± 0.07 (b)
a) A survival probability of unity is assumed for PFPE; b) 1σ errors reflect the compounded effect of relative uncertainties in the magnitude of all contributing TOF profiles; c) From reference [11].			

Table 4.6: Average survival probabilities of OD from each liquid surface.

4.5 Discussion

The discussion of these results will mainly focus on the collision-energy dependence of the OD survival probabilities on different liquid surfaces, covering the effect on each of the reactive liquids in turn. To aid this discussion, the survival probabilities will be related to a reaction uptake coefficient γ for each liquid surface at each collision energy, which is useful in order to discuss the reactivity of the radicals with the surface. The equation used to convert survival probabilities into uptake coefficients, and the underlying assumptions that allow the correct interpretation of these results, will be discussed below. Some interesting information of the dynamics of scattering was also observed in the experiment, and will be discussed briefly below.

4.5.1 Dynamical properties

Both the scattered OD profiles from Figure 4.8 and the rotational temperatures reported in Table 4.4 show unambiguously that OD scattered off surfaces at the higher collision energy $\langle E_k \rangle$ = 29.5 kJ mol^{-1} have superthermal translational energies and rotational distributions, the latter of which are reasonably well described as Boltzmann temperatures. There are also noticeable differences in the arrival time of OD after scattering from each liquid, as well as more subtle differences in the TOF profiles from each N' level probed. Both differences imply that a significant amount of OD scatters off all the surfaces via an IS mechanism. This is broadly in agreement with previous

measurements using the 'bulk photolysis' source of OH with higher collision energies [10-12]. The more efficient conversion of kinetic to rotational energy for PFPE than for squalane is consistent with well-established differences in the stiffness of these two surfaces with a range of gas-phase projectiles [4, 8, 57, 59, 64, 66, 88, 125, 129, 136]. The predominance of single-bounce, IS-type trajectories with some conversion of translational to rotational energy is also consistent with the QCT predictions by Troya *et al.* [64-65, 226], which simulates OH scattered off a fluorinated SAM surface at the somewhat higher collision energy of our earlier experiments, assuming the SAM surface is a reasonable model for PFPE. The somewhat higher rotational temperature for squalene has also been seen in the previous 'bulk photolysis' experiments within the group [11-12]. These have previously been explained as potentially resulting from the survival of hotter, impulsively scattered molecules, while the slower, thermally accommodated molecules are more likely to react with the double-bonds. This interpretation will be discussed further below in terms of the collision-energy dependence of this survival probability, with the additional context provided by the new measurements.

In terms of the results obtained using the modestly superthermal collision energy of $\langle E_k \rangle$ = 7.20 kJ mol^{-1}, the TOF profiles appear to quite closely match the simulated TD profile, and the scattered OD rotational temperatures were also found to be close to thermal. However, residual subtle differences in the scattered OD profiles as a function of N were also observed at these lower collision energies. These differences are more consistent with molecules scattering with an IS mechanism, which suggests that IS scattered radicals, produced with near-thermal final speeds due to the modest incident energy, are also present in the scattered OD profiles. On the basis of the measurements acquired for this chapter, the two contributions could not be distinguished unambiguously; therefore no further dynamical information can be obtained at this stage.

4.5.2 Survival probability and uptake coefficient: validity of the underlying assumptions

As reported in the general introduction (Chapter 1, section 1.3), many other groups have studied the reactivity of OH on a variety of surfaces, by measuring the loss of OH directly [10-12, 41, 53, 227-228], or by measuring a change in the concentration of a

species present at the surface [21, 24, 49-50, 54, 81, 229-232]. This reactivity is usually quantified by the uptake coefficient, γ, defined as the probability of reaction per collision with the surface. The experimental set-up described in this thesis does not measure the reactivity of OD directly; it can only measure the loss of radicals from the surface via the survival probabilities. However, the survival probability can be assumed to simply be the complement of the sticking coefficient, defined by Houle *et al.* [26] as being the fraction of incident molecules that are not elastically or inelastically scattered off the surface, and which do not desorb without reaction. The equation to convert survival probabilities to sticking coefficients is:

$$S = 1 - \sigma \tag{4.8}$$

The sticking probabilities of OD on squalane and squalene derived from the survival probabilities of Table 4.6 are shown in Figure 4.16

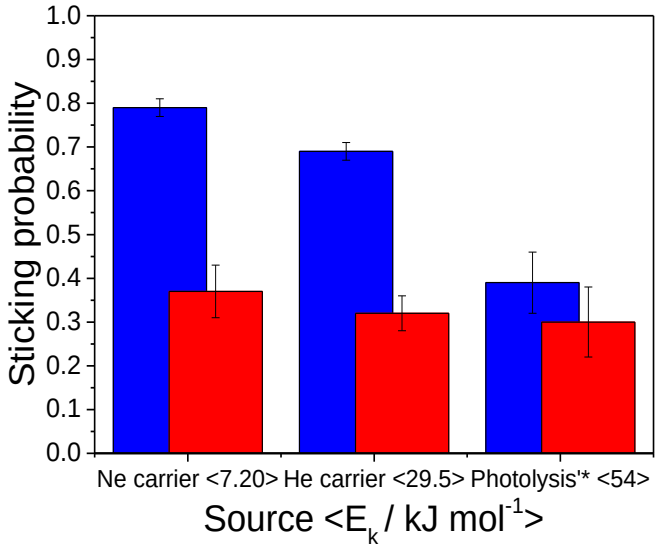

Figure 4.16: Sticking coefficients *S* for OD at the surfaces of squalane (red) and squalene (blue), in order of increasing collision energy. * From reference [11]

As discussed at length in the atmospheric chemistry literature, and widely reported from other experimental techniques, the sticking coefficient is related to, but not necessarily the same as, the reactive uptake coefficient [21, 25-26]. For the sticking coefficients to exclusively represent reactivity of OD with the surface, it is assumed that a) loss of OD

at squalane or squalene is exclusively due to reaction with fresh molecules forming the liquid surface, and b) no OD molecules are lost at the PFPE surface through any other processes. The following sections will discuss in detail the validity of both assumptions in our experiment.

4.5.3 Assumption 1: Is OD lost exclusively due to reaction with the surface?

For this first assumption to be valid, a) an incident OD radical must be able to dose a reaction site on the organic surface (where a 'site' is assumed to correspond to a carbon atom and its associated H atoms), b) the OD radical must react exclusively with the molecules of the liquid surface, and not with species from the molecular beam that have adsorbed on the surface, and c) the reaction site must not have been previously modified via reaction with other species present in the molecular beam, including OD itself. Furthermore, d) the scattered OD radicals detected must have exclusively come from the incident molecular beam. The latter point has been discussed in more detail in Chapter 2 Section 2.5.5 of this thesis. This section will therefore focus on discussing the validity of points a) through c). In order to test each of these points, it is important to establish how many reaction sites are available on the organic surface, the likely dosage of each species in the molecular beam onto the surface prior to discharge pulse and throughout the discharge pulse itself, and how each species is likely to affect the surface. Knowing the rate of desorption of the dosing species assuming all molecules stick to the surface will also be useful to address points a) and b) above, whereas to address point c), the amount of time required for a molecule of the organic liquid to self-diffuse into the liquid itself, and thus expose new molecules to the molecular beam, will need to be known. Each of these points will be discussed separately in this section. For the purpose of testing this assumption, squalane will be used to determine the parameters of the liquid surface, though the conclusions derived from this test are likely to apply to squalene as well, due to its similarities to the structure of squalane.

In order to test the assumptions outlined above, the number of reactive sites needs to be known. There are several methods by which the number of sites per unit area on the squalane surface can be estimated. A lower limit on the area occupied by each site can be obtained from the average bond distance between carbon atoms, known to be 1.54 Å. By assuming that the area per group is obtained from a corresponding circle centred on the C atom with radius 0.77 Å, the area per site was determined to be 1.9 $Å^2$. The

method, however, neglects the fact that some of the separations between exposed groups are between non-bonded rather than bonded groups. At the other extreme, it can be assumed that all the distances are non-bonded. An unweighted average of the van der Waals radiuses for non-bonded united atoms was determined to be 3.85 Å from molecular dynamics simulations done previously within the group [95]. The location of the minimum of the van der Waals potential, r_m, was determined to be 4.32 Å, from which the average area occupied per group (once again assuming the area is a circle centred on the carbon atom with r_m as its diameter) was determined to be 14.7 $Å^2$. This method, however, is likely to be an overestimate. A more realistic compromise between the two methods can be determined from the simulated bulk density of squalane, ρ, expressed in united atoms (assumed to be the same as the 'sites' at the surface) per unit volume. This was determined [95] to be 33 united atoms nm^{-3}, which gives an area per site of 9.7 $Å^2$. For the purpose of testing the assumptions discussed in this section, the area per site is thus taken to be 10 $Å^2$, equivalent to an areal density of 0.1 $Å^2$, or 1×10^{15} cm^{-2}.

The number of molecules dosing the surface per unit area, d, can be determined as a product of the flux of molecules in the molecular beam, f, and the relevant amount of time t, assuming the flux is constant over that period. The flux is, in turn, the product of the peak number density n and the speed of the radicals, hereby assumed to be the average speed $<v>$. Therefore, the overall equation for calculating the dosage can be written as

$$d = n\, t < v > \tag{4.9}$$

The peak number density was not measured in this experiment, so a reasonable value was estimated from comparable results in the literature. In a recent study, Yan *et al.* have characterised a sequence of commercially available molecular-beam valves to compare with the newly developed Nijmegen valve presented in their work [233]. The commercially available valves studied included a General Valve model which is essentially identical to the one used as the molecular beam source in the experiments reported in this thesis (Chapter 2 Section 2.5.2). The beam intensities of the valves were measured via a fast ionization gauge. The results obtained by Yan and co-workers suggests that, for a molecular beam of pure helium with backing pressure 3 bar, the ratio of peak particles numbers between a General valve and a Nijmegen valve is 1/4.5, from

which the beam intensity (in terms of number of molecules per unit volume) for a General valve, measured at a distance equivalent to the distance between the valve and the surface in the experimental set-up, is estimated to be 1.5 x 10^{14} molecules cm^{-3}. This compares well with the typical range of 10^{13}-10^{14} molecules cm^{-3} also quoted by Yan *et al.* As further corroboration to these results, a flux per unit angle, B = 2 x 10^{22} molecules s^{-1} sr^{-1} , was estimated for a beam of pure He at 3 bar backing pressure and a gas temperature of 295 K in the stagnation state using the prescription of Scoles [85]. When combined with the measured beam speed for He (~1800 m s^{-1}, Section 4.3), and the known distance from the source to the intersection with the probe beam (23 cm), the predicted number density was determined to be 2.2 x 10^{14} molecules cm^{-3}. This value is in very good agreement, given the levels of approximation, with the results based on the Yan *et al.* characterization. For the illustrative purposes of this section, the beam intensity determined based on the Yan *et al.* characterization will be used below.

The delay between the start of the gas pulse and the HV pulse is typically ~100 μs. Throughout this period, the surface will be dosed by the stable species in the beam, which include the carrier gas (He or Ne) and D_2O, present at a dilution of ~1% (Section 2.5.6). Assuming that the beam has been on at peak density for that duration, the resulting dosage of molecules on the surface using He as the carrier gas is calculated to be ~3 x 10^{15} molecules cm^{-2}. When compared to the number of sites available, this would suggest that each site is dosed by ~3 atoms or molecules. The number of sites dosed by D_2O will be ~3%. The equivalent values for the Ne carrier are likely to be lower by a factor of ~2 based on the differences in speed between the two carrier gases, assuming that there are no differences in the peak density between carrier gases. These numbers are also likely to be an overestimate, as both previous work in the literature [234], and the earlier characterisation of the OD density at different delays with respect to the opening of the valve done in chapter 3 (section 3.3.5), suggest that the beam has only just reached peak density at that gas-discharge delay. Even so, the results suggests that if the lifetime of all those molecules stuck to the surface were to be sufficiently long, the OD radicals would be far more likely to scatter off the carrier gas or undissociated D_2O than the liquid surface itself, regardless of the carrier gas used.

The rate of thermal desorption is commonly assumed to follow Arrhenius behaviour, via the equation

$$k = Ae^{\left(\frac{-E_a}{RT}\right)} \qquad (4.10)$$

where A is assumed to be roughly 10^{13} s^{-1}, a fairly typical value for a simple unimolecular reaction which is also of the same order of magnitude as a vibrational frequency [118]. As discussed by Nathanson and co-workers, E_a would correspond to the binding energy between the gas species and the liquid surface [118]. He and Ne will have very low binding energies (< 5 kJ mol^{-1}) and hence desorption rates of > 10^{12} s^{-1}, or lifetimes of < 1 ps. As they further suggest, the solvation enthalpies provide a reasonable approximation to the gas-liquid surface binding energies in the absence of experimental data. For D_2O on the squalane surface, Nathanson and co-workers estimated E_a to be -17 kJ mol^{-1}, based on the known result of the solvation enthalphy of H_2O on hexane [235]. This gives an estimated rate constant for desorption at room temperature of ~10^{10} s^{-1}, or a lifetime of ~100 ps. In a later study [147], Nathanson and co-workers tried to determine the residence time of HCl on cold salty water, however, they could not detect a measurable delay for the desorption of HCl, and so they concluded that the residence time was less than 1 μs. Similar results were also observed for the desorption of D_2O from a nopinone film conducted by Johansson *et al.* [236]. To confirm the results for HCl, Nathanson and co-workers estimated the lifetime of HCl on the surface from the rate constant obtained via Equation (4.10) using the desorption energy of HCl from ice of 28 kJ mol^{-1} [237], and revising their estimate A factor to 2 x 10^{14} s^{-1}. From those values, the lifetime was determined to be ~100 ps. Since neither HCl nor D_2O stick on water or more polar surfaces for more than 1 μs, it can be safe to assume that H_2O and D_2O stick for an even shorter time on squalane, which is consistent with the 100 ps estimate above.

The results described above indicate that the steady-state coverage of the surface by the molecules in the molecular beam is negligible, thus satisfying assumption a) described at the start of this section. Any remaining realistic possibilities responsible for any secondary chemistry must therefore result from the reactive species formed during the discharge. Metastable helium atoms are known to form in electric discharge sources [238], and it would not be unreasonable to suggest the process could also form

metastable neon atoms, both of which may contribute to modifying the liquid surface. For the He carrier, the total dose of molecules on the surface for a discharge pulse length of 10 μs, assuming the beam has been on at peak density for that duration, is estimated to be ~3 x 10^{14} molecules cm^{-2}. Taken literally, this would suggest that up to ~30% of the sites dosed by the carrier gas could have reacted with metastable He. However, previous independent work has shown that the production efficiency of metastable He in an electric discharge is in the range of 10^{-5}-10^{-3}%, assuming 100% ionization probability [238-240]. If true for the current experimental set-up, this would suggest that only ~10^{-3} % of available sites will be dosed by metastable He at most. From this result it is concluded that any effect metastable He or Ne atoms have on the liquid surface will be negligible, even ignoring the diffusion of molecules away from the liquid surfaces discussed below. The more plausible candidates for reaction with the surface is the intended OD projectile, or other fragments formed from the dissociation of D_2O, which can produce a number of positive ions, negative ions, and neutral products involving D, O, D_2 or OD [241]. The efficiency of the dissociation of D_2O under the experimental conditions discussed in this chapter is not known accurately. though previous related studies would suggest that the efficiency could by anywhere within a range of 10-100% [177]. As established in section 4.2, the amount of D_2O present in the molecular beam is estimated to be ~1% in the He carrier at 3 bar of backing pressure. Therefore, assuming the dissociation process caused by the discharge is 100% efficient, the OD radicals would dose only ~0.3% of the available sites on the surface. This value is sufficiently low to suggest that reactions of OD with other incident projectiles adsorbed on the surface, or with a site on the surface that has already reacted with another projectile, are negligible, thus satisfying conditions b) and c) described at the start of this section. This assumes, though, that the molecules in the liquid stay on the surface on a timescale comparable to that of the duration of the gas pulse. Whether this is true can be determined from the standard, one-dimensions equation for diffusion of molecules from the surface into the bulk [242], expressed via the equation:

$$< z > = 2\,(D\,\tau\,/\,\pi\,)^{1/2} \qquad (4.11)$$

where $<z>$ is the average distance a molecule diffuses in the normal direction in time τ and D is the bulk diffusion coefficient. The work by Harris *et al.* [243] determined that D for the self-diffusion of squalane is 28.75 x 10^{-12} m^2 s^{-1} at 25.04 °C. Molecular

dynamic simulations done previously by the McKendrick group [95] give an average end-to-end distance for squalane molecules, and hence the thickness of a molecular layer, of 18 Å. Assuming that the radical products of squalane produced in reaction with OD have similar sizes and mobility, the time taken for one molecule of squalane to diffuse by one molecular layer into the bulk is ~90 ns, which is shorter than the duration of the discharge pulse by a factor of ~100. Put the other way, on average, the distance a molecule of squalane would have diffused away from the surface within a HV pulse length of ~10 μs is ~200 Å This indicates that the primary reaction products of OD with squalane do not remain on the surface for a sufficiently long time to be available for secondary reactions with OD. Together with all the other aspects explored in this section, it can be safely assumed that OD is lost exclusively due to primary reaction with the surface.

4.5.4 Assumption 2: Do all OD radicals scatter off PFPE?

PFPE has been used both here and previously as an inert reference surface, due to the absence of any obvious exothermic reactions of OH or OD radicals with PFPE molecules. Though the OD radicals cannot react with the surface at the collision energies used, it is possible for them to be lost via other processes that trap the radicals within the liquid on a timescale larger than the one used for data acquisition. To test the assumption that all OD scatters off the PFPE surface, the ratio of the experimentally obtained incident and scattered OD profiles was compared with simulated TOF profiles obtained via Monte Carlo simulation program (Section 4.2.2). The simulation program assumes that all incident OD scatters of the liquid surface. Therefore, if the ratio obtained from the simulations overestimates the ratio obtained from the experimental profiles, it would provide a clear indication that OD is lost at the PFPE surface by processes other than via reaction.

The simulated scattered OD profile was generated using an experimental incident beam profile to determine the parameters of the simulated incident OD. Because the majority of the scattered OD derives from molecules that were in the lowest rotational levels in the incident beam, the experimental profile used to set the simulated incident beam parameters was taken from the results at the $N' = 2$ rotational level. As for the scattered OD profile, the program was set to assume that all OD scattered via a TD mechanism. The relative magnitudes of the predicted incident and scattered profiles were then

adjusted for the measured relative fractions of the population in $N' = 2$ in the incident and scattered rotational distributions for PFPE, using the data reported in sections 4.3 and 4.4.3, respectively. These suitably weighted simulated profiles were then normalized to the peak of the incident beam profile and plotted alongside the equivalent experimental results in Figure 4.17.

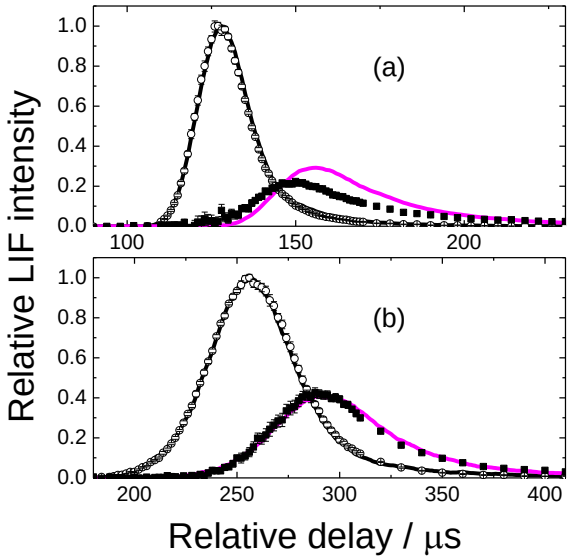

Figure 4.17: TOF profiles of the OD LIF signal on the $Q_1(2)$ transition versus discharge-probe delay, with (a) He carrier; and (b) Ne carrier. Liquids: PFPE (black squares). The incident beam with no surface present is represented by open circles. Solid lines are the simulations of the incident beam (black) and the predicted TD-scattered OD (magenta), weighted by the experimental ratio of incident-to-scattered populations in $N = 2$ for PFPE.

As is clear from Figure 4.17 (b), the simulated scattered profile almost perfectly matches the experimental observation at the lower collision energy. The predicted relative magnitude of the peak scattered signal is within 5% of the experimental result. The shape of the simulated profile is also very similar to the observation, reflecting the marginal deviation of the observed distribution from a pure TD distribution, as discussed above. This therefore provides persuasive evidence upholding the assumption that all incident OD scatters off PFPE, at least at the lower collision energy. Figure 4.17 (a) shows that there are more significant differences between the simulated and

observed scattering at the higher collision energy, with the simulation over-predicting the observed peak signal by ~24%.

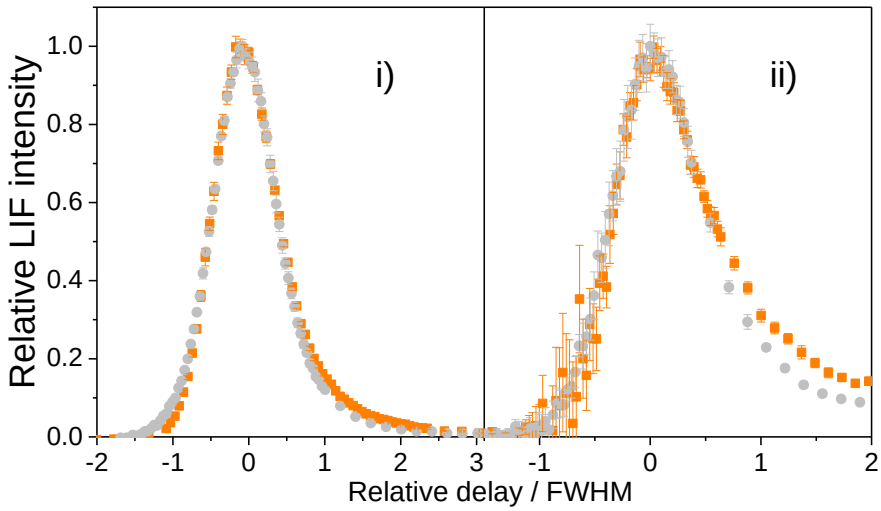

Figure 4.18: TOF profiles of the incident OD (i) and scattered OD off the PFPE surface (ii), with He carrier (orange squares) and Ne carrier (grey circles), taken on the $Q_1(2)$ transition. Profiles have been normalized to the peak of their LIF signal size and to the FWHM of their respective profiles.

In principle, the difference between the experimental and simulated scattered OD profile for the higher collision energy may be due to the presence of a significant IS-like superthermal speed distribution in the experimental results. This would shift the experimental TOF profile to shorter delays, and thus decrease the number density for the given flux. The effect of the radicals scattering with IS-like speed distributions could be accounted for via a density-flux conversion of the profile. In practice, the speed and angular distribution of the scattered OD via an IS mechanism would need to be specified in the simulation in order to perform a rigorous density-flux transformation. Unlike the assumed TD distribution, those parameters are unknown *a priori*. However, approximate density-flux corrections can be attempted, provided that the reduced incident and scattered OD profiles from both collision energies have a similar area. The reduced TOF profiles were obtained by scaling the amplitude to the peak of the profile, and the width to the FWHM, and were plotted in Figure 4.18. As demonstrated in the figure, the reduced profiles appear to overlap almost exactly. Therefore an approximate

density-flux calculation can be carried out by assuming the OD flux is the area of the TOF profile obtained as the product of the profile height, d_{peak}, and width, d_{FWHM}.

For either He or Ne carrier, the total incident flux is assumed to be the product of d_{peak} and d_{FWHM}, of the incident density profile, divided by the fraction of the incident population, $P(N)$, known to be in the observed $N = 2$ level, weighted by the measured mean speed, $\langle v \rangle$, of the incident beam:

$$f_{inc} \propto \left(\frac{d_{peak}\, d_{FWHM}}{P(N=2)}\right) < v > \tag{4.11}$$

The corresponding scattered fluxes, f_{sc}, are assumed to be analogously approximately proportional to the corresponding peak height and width of the scattered density profiles (indicated by primes), divided by the measured fraction of the scattered population in this level, scaled by an approximate mean speed relative to that of the predicted TD distribution; for these purposes, this relative speed is taken to be inversely proportional to a ratio of time intervals:

$$f_{sc} \propto \left(\frac{d'_{peak}\, d'_{FWHM}}{P(N'=2)}\right) \frac{(t_{TD}-(t_{inc}+t_{trans}))}{(t_{sc}-(t_{inc}+t_{trans}))} \tag{4.12}$$

where t_{inc} and t_{sc} are the experimentally determined peak times of the incident and scattered profiles, respectively; t_{TD} is the predicted peak time of the simulated TD distribution; and t_{trans} is the known in-going transit time from the centre of the probe-beam axis to the liquid surface at the known mean speed of the corresponding incident beam. The incident and scattered fluxes, and the ratio between the two, for a given carrier gas are reported in Table 4.7. The calculations were performed for the two independent sets of PFPE data taken alongside the squalane and squalane measurements, respectively, as described in section 4.4.1.

The ratio between these scattered and incident fluxes, $f_{\text{sc}} / f_{\text{inc}}$ for a given carrier gas contains arbitrary scaling factors, but it is the ratio of these ratios for the two carrier gases, $(f_{\text{sc}} / f_{\text{inc}})_{\text{He}} / (f_{\text{sc}} / f_{\text{inc}})_{\text{Ne}}$, which is of interest. This ratio of ratios was determined to be 1.05 ± 0.10 and 1.17 ± 0.13 for the two independent sets of PFPE data. When considered alongside the near perfect prediction of the incident-to-scattered ratio of

signals for the TD-like distribution at the lower collision energy from Figure 4.17 (b), these values of $(f_{sc} / f_{inc})_{He}$ / $(f_{sc} / f_{inc})_{Ne}$ close to unity offer reassurance that the under-prediction of the magnitude of the scattered profile in Figure 4.17 (a) is satisfactorily accounted for by flux-density effects. The simulations and approximate density-flux conversions have therefore shown that there is no strong evidence of an OD loss mechanism at the PFPE surface at either collision energy. Combined with the lack of evidence for other OD loss mechanisms provided above, it is concluded that the uptake coefficients derived from the survival probabilities via Equation (4.8) correctly represent loss of OD via single reactions with the molecules of the liquid surface.

Carrier gas	**Surface**	f_{inc} **(a)**	f_{sc} **(b)**	f_{sc}/f_{inc}
Helium	PFPE 1	0.98 ± 0.03	0.99 ± 0.09	1.01 ± 0.10
	PFPE 2	1.02 ± 0.04	1.01 ± 0.09	0.99 ± 0.09
Neon	PFPE 1	2.08 ± 0.04	2.20 ± 0.09	1.06 ± 0.05
	PFPE 2	2.09 ± 0.06	1.91 ± 0.12	0.92 ± 0.06
a) Values in column scaled to the average PFPE value for He of $(119 \pm 3) \times 10^{-3}$ m b) Values in column scaled to the average PFPE value for He of $(58 \pm 4) \times 10^{-6}$				

Table 4.7: Table of approximate density flux conversion results for each step of the calculations, as described above

4.5.5 Uptake on squalene surfaces

From Table 4.6 it is observed that the survival probabilities are in the sequence PFPE > squalane > squalene at both of the collision energies studied in this experiment, and at the higher collision energy studied via the 'bulk photolysis' experiment [11]. Although the qualitative sequence remains the same, the magnitude of the survival probability from each of the reactive liquids shows some clear differences between the two liquids, which will be discussed in turn.

When considering results for squalene, it is noted that there is a clear *increase* in the survival probability when increasing $<E_k>$ from 7.20 kJ mol^{-1} to 29.5 kJ mol^{-1}, and a further, more dramatic increase when compared to the results from the photolytically generated OH at $<E_k>$ = 54 kJ mol^{-1}. This suggests that the higher uptake on squalene than on squalane at lower collision energies is not simply the result of the lower activation energies to be expected for H-abstraction from the allylic C-H bonds in squalene [74]. Rather, it strongly reinforces the conclusion reached previously by the group [11] that the higher uptake on squalene than on squalane at the higher translational energy was due to the existence of the extra channel of addition at the double-bond sites, to generate a transient hydroxyalkyl radical. The higher rotational temperatures obtained from the radicals scattered off squalene suggested that the slower moving radicals more likely to be thermally accommodated on the surface were more likely to react than the faster, IS-type scattered molecules. As the fraction of expected TD-like scattering is expected to increase at lower collision energies, the loss of OD via addition reaction is also expected to increase, and such behaviour is indeed observed in the results obtained. This explanation is consistent with analogous reactions of OH with alkenes in the gas phase, where the negatively activated addition mechanism is found to dominate for larger alkenes [219], as discussed in the introduction to this chapter. In conclusion, the results here provide the first direct evidence that the uptake of OH (or OD) at the squalene surface is negatively activated.

4.5.6 Uptake on squalane surfaces

From the characterization of the properties of the incident beams discussed in section 4.3, the centre-of-mass collision energies for the Ne and He carrier were estimated to be 6.10 ± 0.05 and 25.0 ± 0.2 kJ mol^{-1}, respectively. A comparison of those values with the estimated E_0 for different C-H bonds in table Table 4.1 reveals that the lower E_{coll} only modestly exceeds the estimated E_0 values for secondary and tertiary C-H bonds but is barely above threshold for primary C-H bonds. Molecular dynamics simulations done for squalane [95] show that the primary C-H sites are expected to occupy circa 41% of the surface. Therefore, at the lower collision energy, almost two fifths of the exposed squalane should be unreactive to OD. Further investigation of the excitation function shown in Figure 4.1 shows that these sites, as well as the sites of the secondary and tertiary C-H bonds should become substantially more reactive at the higher E_{coll}. A comparison of the relative cross sections for the sum of the excitation function of all

three C-H bonds suggest that an increase of the collision energy between Ne and He carrier experiments would lead to an expected increase in the uptake of OD (and corresponding decrease in the survival probability) by more than a factor of 2.

Surprisingly, no such decrease is observed in the measured survival probabilities as a function of collision energy in Table 4.6. Instead, the survival coefficients are essentially the same at around 65% for both collision energies, and even for the higher collision energy accessed via the 'bulk photolysis' experiments [10-11], within experimental uncertainty. There are undoubtedly some detailed differences in incident angular distributions and possibly in the sampling of the product angular distributions between the current set-up and the previous photolytic experiments that affect the measurement of the survival probability. Some caution should also be exercised when comparing experiments with different incident rotational distributions; these vary subtly between the He and Ne carriers, as characterized in section 4.3, but more significantly in the photolytic experiments. Any rotational-level dependence of the uptake coefficients could therefore, in principle, independently affect the overall uptake. Nevertheless, regardless of the possible influence of these effects, the result in the photolytic experiments continues the essentially flat trend of the lower two collision energies, and so an alternative explanation to account for this trend must be sought.

One interesting possibility is that the expected reduced reactivity in direct, IS-like trajectories at lower $\langle E_k \rangle$ is compensated by an increase in the proportion that undergo TD-like accommodation at the squalane surface. If these accommodated molecules are able to migrate until they encounter a more reactive secondary or especially tertiary C-H site, then their reaction probability would be enhanced. This explanation would be consistent with the dynamical results from this experiment, suggesting that those molecules that do escape the squalane surface retain some of the characteristics of IS trajectories even at lower collision energies, including a positive correlation between translational and rotational energies. The effect would be even more amplified in reaction at the *squalene* surface at the higher collision energies, where OH molecules which have been accommodated at the surface have a strongly enhanced probability of undergoing an addition reaction at a double-bond site. Although the differences are modest relative to the experimental uncertainties, it is interesting that the observed OD or OH rotational temperatures (reported in Table 4.4) from scattering from squalene at $\langle E_k \rangle$ = 29.5 kJ mol^{-1} or previously of 54 kJ mol^{-1} are consistently higher than those

from squalane and similar to those from PFPE, despite its known 'stiffer' surface. This would be compatible with only the most direct, impulsively scattered OH molecules escaping from squalene, whereas this constraint is weaker in squalane.

These results show that, even for surfaces of a known composition, both the absolute values and the temperature dependence of OH uptake may not simply reflect the behaviour that would be expected based on extrapolation from the corresponding gas-phase reactions. In the case of squalane, the uptake coefficient remains almost constant (at a value of ~0.35) as the collision energy is reduced to more nearly thermal collision energies. Though the explanation for this result may be as yet unknown, it at least provide some reassurance to groups invoking the previous uptake on squalane results in an atmospheric context [3, 17, 26, 54, 80, 211-216] that their conclusions are unlikely to be affected. The uptake coefficients for both squalane and squalene have also demonstrated that the collision-energy dependence is strongly affected by the chemical nature of the surface. This implies that the corresponding temperature dependence of uptake in the atmosphere is almost certainly a non-trivial function of the initial and evolving composition of the aerosol surface during ageing, which has potentially important consequences for the understanding and modelling of such reactions.

4.6 Summary Points

1) OD radicals, generated from the new molecular beam and electric discharge source, were scattered from the surfaces of squalane, squalene and PFPE. The radicals were then detected by LIF using the single-point detection set-up described in section 2.7.1

2) Helium and neon were chosen as the carrier gases for the molecular beam. From a detailed characterization of the radicals in the incident beam, it was determined that $\langle v \rangle$ = 1811 ± 8 m s^{-1}, $\langle E_k \rangle$ = 29.5 ± 0.3 kJ mol^{-1} and that OD radicals were populating 45% of N = 1 and 28% of N = 2 when using the He carrier, whereas for the Ne carrier it was determined that $\langle v \rangle$ = 894 ± 8 m s^{-1}, $\langle E_k \rangle$ = 7.20 ± 0.06 kJ mol^{-1}, and that the relative populations in N = 1 and N = 2 were 48% and 18%, respectively.

3) At the higher collision energy, the OD radicals scattered off the liquid surfaces have clear superthermal translational energies and rotational distributions, indicating the presence of a significant component of IS-like scattering. There is also some evidence of IS-like scattering present from scattering at the lower collision energy, however, its contribution with respect to the TD scattered molecules could not be unambiguously distinguished with the current data.

4) The experimental set-up obtains direct measurements of the survival probability of OD off a liquid surface. This can be related to uptake coefficient values corresponding to single reactions of OD with the surface, provided that no other OD loss mechanisms are present, and that all OD detected scatters off the inert PFPE surface. Both assumptions were found to be valid within the context of this experimental set-up.

5) For squalene, the results show that addition reactions at the vinyl sites on the surface predominate, and that such reactions are negatively activated, with the uptake coefficient decreasing with increasing collision energy.

6) Surprisingly, the results for squalane show that the uptake coefficient is 0.35 regardless of the collision energy used, within statistical uncertainties. A possible explanation for those results suggests that the expected reduction in OD reactivity from IS-type scattered molecules off primary C-H sites at lower $<E_k>$ is compensated by thermally accommodated radicals migrating on the surface until they encounter a more reactive secondary or tertiary C-H bond.

Chapter 5 – Image Acquisition Set-Up Results

5.1 Introduction

The angular distribution with which the incident atomic or molecular projectiles scatter off a given liquid surface provides additional information on the scattering dynamics of the projectiles and the properties of the surface [4]. Scattering experiments conducted by both Nathanson and co-workers [1-2, 4, 92, 116-120] and Minton and co-workers [68, 78, 88-91] have shown that projectiles scattered off the surface with an IS mechanism have a narrow and directed angular distribution correlated to the incident angle, whereas with a TD mechanism, the scattered species leaves the surface with a $cos(\theta)$ angular distribution centred around the surface normal. The dynamical information can also provide further insights on the properties of the liquid surface, such as its structure and surface fluctuations at a molecular level (surface *roughness*) and its efficiency at transferring momentum from the projectiles (surface *stiffness*). As such, the scattering angle distribution of OD can help interpret the dynamical information obtained from the single-point detection results discussed in the previous chapter (Section 4.5.1), and in particular might help distinguish unambiguously between IS and TD scattering when using moderately superthermal collision energies from OD seeded in Ne. However, conventional spectroscopic techniques and associated detection set-ups are not capable of spatially resolving the distribution of molecules around the surface before and after scattering events. One way to get around this limitation would be to obtain sequential individual single-point detection measurements at various points along the axis of the probe beam by translating the liquid light guide and PMT, as has been recently reported by Nesbitt *et al.* [244]. This approach, however, does not provide the spatial resolution to determine the exact angular distribution and speed of the scattered species along each final scattering angle, due to the large probe volume (13 mm^3) observed by the detector, and the absence of measurements on the size of the target area hit by the incident beam. It could, in principle, provide temporal resolution through pointwise measurements along a given angle, provided that a short gas pulse is used. Mass spectrometry detection methods, such as those used by Nathanson and co-workers [1-2, 4, 92, 116-120] and Minton and co-workers [68, 78, 88-91] do offer the spatial and temporal resolution to determine the speed of the scattered radicals at a range of final scattering angles. However, as discussed previously in Chapter 1, Section 1.4.1, MS detection methods do not provide the internal energy distribution of the

scattered projectiles that spectroscopic methods provide. There are also practical limitations in positioning the mass spectrometer with respect to the pulsed valve of the molecular beam that prevent it from detecting molecules that are scattered 'backwards' towards the molecular beam source. More recently, Hadden *et al.* [245] have demonstrated that the angular-resolved speeds of a species scattered off a solid surface and probed on different internal states can be obtained from a suitably modified velocity-map imaging (VMI) detection set-up, in which the surface is inserted on a 'stick' within the ion-optics set-up, with a voltage applied on electrodes attached to the stick in order to stabilize the electric field generated by the ion-optics stack. This method, however, has yet to be proved to work for liquid surfaces.

In this chapter, the new image-acquisition detection set up (Section 2.7.2) will be used to probe the spatial distribution of the OD radicals in the molecular beam and scattered off the surfaces, using planar-LIF (pLIF). Planar-LIF is a variation of the conventional LIF technique, which consists of expanding the probe laser beam in one direction to form a sheet, and then imaging the fluorescence from the probed species onto an appropriate detector. Depending on the species being detected, the wavelengths and intensities of the emission involved, and the distance between the plane of detection and the camera, the detection set-up may simply involve a set of lenses to image the fluorescence directly onto a camera. For relatively weak signals associated with low number densities (such as OD radicals detected in the experimental set-up described in this thesis), an image intensifier is used to amplify the fluorescence light and to convert it from e.g. UV light to a visible image, allowing it to be captured by the camera. The image intensifier can either be incorporated into the camera itself [87, 246], or used as a separate unit coupled with a standard, relatively inexpensive camera [247].

Planar-LIF was developed independently in 1982 by Dyer and Crosley [183], and by Kychakoff *et al.* [184], and has commonly been used to study gaseous species resulting from combustion processes in flames, turbine combustion, internal combustion engines, and propellants [248-251]. Other areas in which this technique has been applied are in studies of flow visualization of liquids and soot particles [252-254], and monitoring fuel mixing in combustion systems [255]. There has also been a limited number of studies where pLIF has been used to look at catalytic reactions occurring at the gas-solid surface interface [246]. These reactions were studied by flowing a high pressure gas-mixture containing the reagents over the solid surface used by the catalyst.

Examples of such work include the studies on the formation and distribution of OH from H_2 oxidation processes on a Pd catalyst [256-260] or desorption of OH from catalytic water formation [261] conducted in the 1990s, and the more recent work reported and reviewed by Lundgren and co-workers [87, 246, 251] on catalytic CO oxidation on Pd model catalysts; hydgrogen-assisted NH_3 oxidation above an Ag/Al_2O_3 powder catalyst; and catalytic reduction of NO by hydrogen to ammonia over a Pt/Al_2O_3 catalysts.

Planar-LIF was chosen as the new method to detect OD radicals as it provides a number of improvements over the LIF detection method used by Nesbitt and co-workers [244] or the MS detection methods used by Nathanson *et al.* [1-2, 4, 92, 116-120] and Minton *et al.* [68, 78, 88-91]. One key improvement is that pLIF allows the user to probe a wide range of final scattering angles in a single measurement without having to move the detector, and thus without the need to maintain the conditions constant between measurements, or without having to normalize these differences as part of the data analysis. Planar-LIF also allows the user to probe 'back'-scattered radicals, i.e. OD radicals scattered in the same direction as the incident radicals. This method could, in principle, provide both spatial and temporal resolutions to determine the speed and angular distributions of the scattered radicals by taking a sequence of images at different discharge-probe delays. To our current knowledge as of writing, there are no examples in the literature of the pLIF technique being used to study gas-surface scattering experiments using projectiles from a molecular beam source. The results reported in this chapter will thus be the first time in which the technique has been applied to study gas-liquid surface scattering experiments. As such, the analysis of the results is still ongoing. The discussion of the results will be limited to the preliminary analysis obtained using the custom LabVIEW™ programs available at the time of writing. Suggestions for future developments of the analysis programs will be outlined in Chapter 6.

Previous gas-liquid experiments reported in the literature (discussed in Chapter 1 and above) and the dynamical information from our own results using the single-point detection set-up (Chapter 4) can provide hints as to the angular distribution of the scattered products that might be observed using the new image acquisition set-up. One of the more recent results reported by Nesbitt *et al.* [244] describes the angle-resolved inelastic scattering of NO off the surfaces of PFPE, squalane and the ionic liquid

[bmim][Tf_2N]. The molecules were scattered off the surface at 45° incidence with respect to the surface normal, with collision energies of 11 kJ mol^{-1} and 84 kJ mol^{-1}, which are somewhat higher, but spanning the same low and high collision energies reported in our own experiment (Section 4.3). NO was then probed via LIF while translating the PMT and associated optics to collect fluorescence from a small volume located at different points along the probe beam axis, corresponding to a range of 'front' and 'back' final scattering angles with respect to the surface normal. A representative set of those results is shown in Figure 5.1 below.

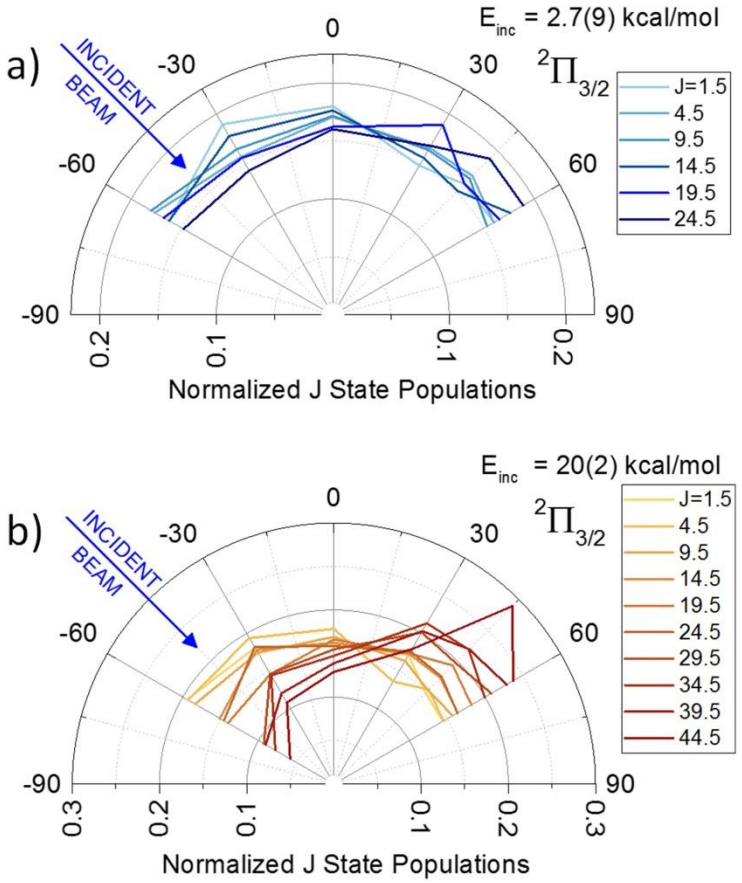

Figure 5.1: Representative polar plots of NO($^2\Pi_{3/2}$) rotational distributions scattered off a liquid surface as a function of final scattering angle θ_s. (a) At low E_{inc} conditions (2.7 kcal mol^{-1}, or 11 kJ mol^{-1}) with NO thermally desorbing from the surface, the NO rotational distributions are relatively insensitive to θ_s. (b) At high E_{inc} (20 kcal mol^{-1}, or 84 kJ mol^{-1}), however, the rotational distributions evolve considerably with increasing θ_s, with a greater propensity for high J state populations scattered in the forward direction. Figure and caption text adapted from reference [244]

From the results obtained from those scattering experiments, Nesbitt and co-workers were able to determine that at the lower collision energy, NO was scattering with a broad, *cos(θ)* angular distribution and a rotational temperature independent of the angle probed from all of the three liquids. The authors suggest that this is consistent with all incident NO being thermally accommodated on the surfaces. At the higher collision energy, the authors found that NO was more likely to scatter in the 'forward' direction and angles close to the specular angle (Figure 5.1), with ≈3-4 fold hotter rotational temperatures than those obtained from TD-scattering trajectories, strongly suggesting that a significant component of scattered NO does so with an IS-like mechanism.

The forward-directed distribution becomes much more predominant at the higher collision energies (451-472 kJ mol^{-1} in the c.m. frame) accessed via the laser-detonation method of generating O-atoms used by Minton *et al.* [68, 78, 88-91]. As shown in Figure 5.2 below, Minton and co-workers found that O-atoms inelastically scatter off the liquid surface with a strong 'forward' angular distribution. Even its primary reaction product OH, from reactions with squalane and other organic and ionic liquids, has a similar strong preference towards 'forward' scattering in the same direction, whereas H_2O, formed upon further reaction with the surface, escapes from the liquid with more TD-like trajectories. These results are well described by a kinematic analysis using the soft-sphere model (Equation 1.5) where the species are scattered off a smooth surface, as discussed in Chapter 1, Sections 1.4.2 and 1.4.3. One of the aims of the scattering experiments in this chapter is to determine whether the OD radicals scatter with a strong, directed angular distribution seen at much higher collision energies than those accessible by our current set-up (29.5 kJ mol^{-1} and 7.20 kJ mol^{-1} for the He and Ne carrier, respectively), or whether the projectiles scatter with a broad angular distribution as observed by Nesbitt *et al.* [244], and in the latter case, whether evidence of projectiles scattered with IS-like trajectories in a particular direction can be observed within the broad angular distribution of the scattered species, as seen in Figure 5.1 at the higher collision energy.

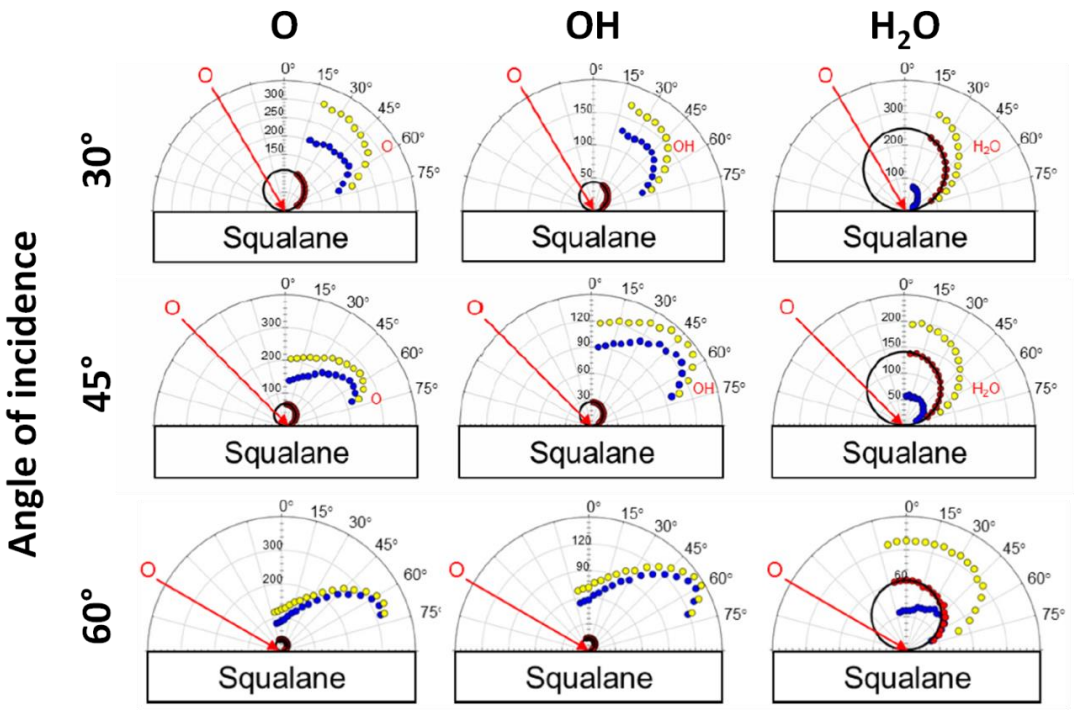

Figure 5.2: Flux angular distribution of scattered O, OH and H_2O off a squalane surface. O atoms impact the surface at 30°, 45° and 60° angle of incidence, with a collision energy of 486 kJ mol^{-1}. Total signal size is represented in yellow circles. Red circles represent the TD component, obtained via a Maxwell-Boltzmann fit of the slow component in TOF profiles. The TD component is well described by a cosine distribution about the surface normal, shown as black lines. Blue circles represent the IS component, derived from subtraction of the TD component from the data. Figure and caption adapted from reference [78]

5.2 Experimental

The experiments in this chapter were performed using the methods outlined in Chapter 2, with the liquids described in Section 2.4, and the image acquisition set-up detailed in Section 2.7.2, expanded in further detail below. Both carrier gases used for this experiment (He and Ne) were bubbled through the D_2O reservoir at a high pressure of 3 bar, in both cases creating mixtures of ≈1% D_2O in the carrier gas. The mixture was fed to the pulsed valve, with an aperture of 1.0 mm. The nominal pulse length of the valve was set at 350 μs. The valve was placed at a distance of 180.5 ± 1.0 mm from the focus point of the molecular beam ports, where the liquid surfaces was placed. Experiments were taken with the pulsed valve placed at normal incidence and at 45° with respect to the surface normal, switching between the two positions after acquiring a full set of data

from each liquid surface using a given carrier gas. The free-jet expansion of the beam was collimated by a 2 mm diameter conical skimmer. A 10 x 10 cm gas baffle (as defined in Section 3.6.2) was attached to the skimmer holder plate.

The discharge device attached to the valve was an optimized variant of the Greaves device design, using design 3 for the grounding electrode (Figure 3.29), the front electrode with the 2 mm diameter hole, and the 3 mm diameter cylindrical spacer. A faceplate with a 12 mm channel was used for scattering experiments with the He carrier, whereas a faceplate with no channel was used for experiments with Ne. Based on the findings on the optimal skimmer position with respect to the last constraining element of the discharge device (Chapter 3 Section 3.6.1), the skimmer was placed at 67 mm from the valve when the 12 mm channel faceplate was used, and at 50 mm from the valve when the no-channel front plate was used. From those values, the diameter of the dosed area on the liquid surface hit by the incident OD radicals at normal incidence can be estimated via trigonometry. These were determined to be ~ 5 mm for the data acquired with the He carrier, and ~ 7 mm for the data acquired with the Ne carrier. The fast switch was triggered to apply an optimized voltage of -1700 V for the He-seeded beam and -620 V for the Ne seeded beam for a duration of 10 μs, timed to fire typically 100 μs into the gas pulse, as established by monitoring the density of OD generated while ensuring the stability of the supplied-current waveform. Due to concerns about the light produced by the hot filament in the chamber, the discharge was stabilized solely by supplying a voltage of +230 V to the front electrode from the Fluke power supply when the fast switch was in its passive state.

The probe beam was expanded in the plane of the molecular beam via a concave lens (ThorLabs LK4166-UV), and collimated with a convex lens (CVI Melles Griot RCX-40.0-30.0-101.7-UV-248-355) to form a 2D sheet ≈30 mm wide and ≈ 4 mm thick. An iris placed after the set of lenses was used to adjust the width of the sheet. The centre of the probe sheet was placed at ≈20 mm from the surface, ensuring that the distance between the surface and the edge of the sheet was ≈5mm. The polarizer and the λ/2 waveplate were removed from the laser beam path to provide a probe beam energy of ~700 μJ pulse^{-1} for the scattering experiments with the He carrier, and ~600 μJ pulse^{-1} with the Ne carrier, prior to expanding the cylindrical probe beam into a sheet. The distribution of power from the probe beam across the width of the sheet was measured by probing different sections of the sheet using a power meter (Gentec-e

ED-100A UV) with a 4 mm diameter sensor. A representative set of measurements is shown in Figure 5.3. The measurements show that the probe beam power is not evenly distributed across the width of the sheet, but may have 'hot spots'. The power distribution of the sheet is dependent on the profile of the beam as it exits the dye laser. The vertical position of the beam spot in the dye laser can be optimised by adjusting the internal optic components, however, the horizontal position of the beam spot cannot be easily optimized, resulting in the power distribution shown in Figure 5.3 (a). Therefore, the probe beam profile was rotated by 90° with the use of mirrors in a periscope set-up, providing a more even power distribution as shown in Figure 5.3 (b).

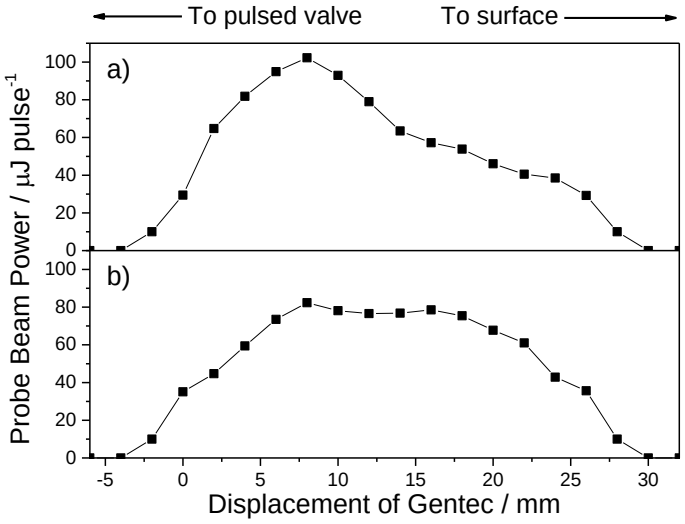

Figure 5.3: Power of the probe sheet at different points measured by scanning the Gentec power meter across the sheet. a) Power measured with the probe beam spot in 'vertical' configuration before expansion, b) power measured with the probe beam spot in 'horizontal' configuration. Each point represents the power of a section of the laser sheet hitting a power meter with a 4 mm diameter sensor. The X axis represent the translation distance of the power meter with respect to the edge of the probe sheet closest to the pulsed valve, where 0 is set as the first point where the probe sheet hits the entire sensor of the power meter when placed at the edge of the sheet.

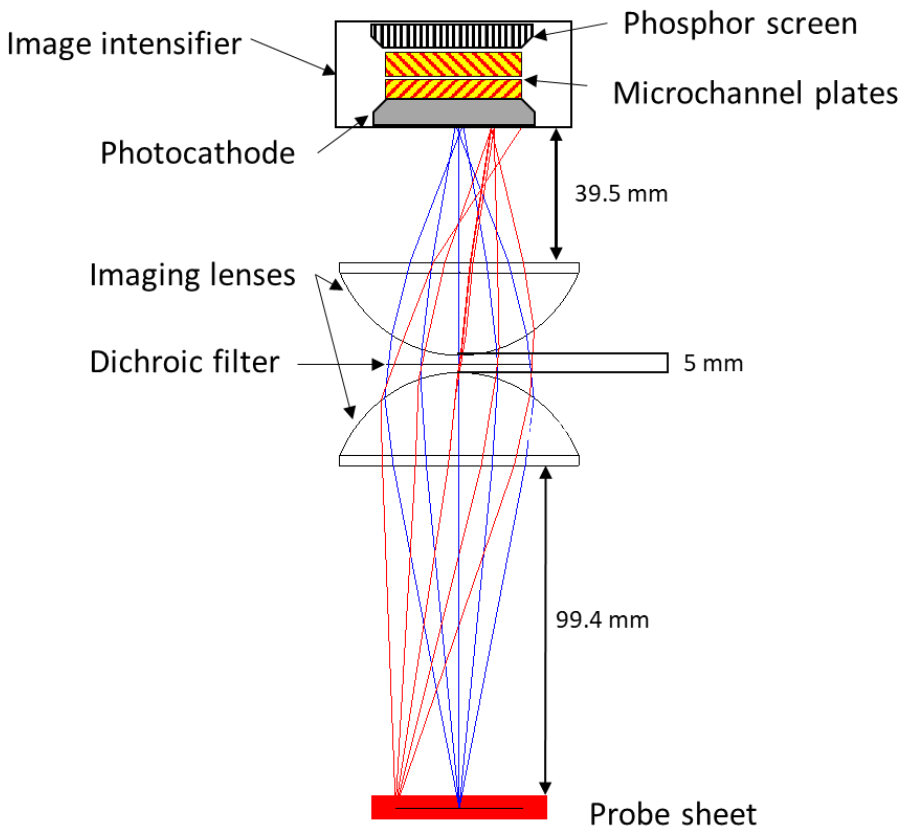

Figure 5.4: Schematic of the components in the optics stack, with distances between components. The position of the camera and the supporting components in the vacuum chamber are omitted for clarity. Blue and red lines are adapted from the optical ray-trace analysis performed by Dr. David Lee and Prof. Alan Greenaway, from reference [185, 262]

The detection set-up consists of an image intensifier (Photek, MCP240/Q/S20/P43/GL, described in further detail in Chapter 2 Section 2.7.2), two fused silica lenses (Thorlabs La4384), and a dichroic optical filter centered at λ = 317 nm with FWHM = 8 nm (Laser Components). These components were arranged as shown in Figure 5.4. The optimal distances between the components were determined via an analysis of the custom made fused silica lenses and tested on the bench by previous students in the McKendrick group [185], in collaboration with Dr. David Lee and Prof. Alan Greenaway [262]. The analysis determined that for an image focal plane of 40 x 40 mm, the optimal distance between the probe sheet and the lenses was 99.4 mm, the gap between the lenses was 5 mm, and the distance between the lenses and the image intensifier was 39.5 mm. This provided a magnification of the probe sheet plane of 0.5, for a wavelength of 310 nm. The optics stack was mounted onto supporting rods to a

flange, in line with a port that was offset from the focus point of the molecular beams. The distance between the image intensifier on the optics stack and the port was determined to be 123.3 mm. A CCD camera (Basler Scout FireWire Camera, scA780-54fm) was placed outside the vacuum chamber on a supporting structure insulated from the main chamber, in order to ensure that the placement of the camera remains fixed and consistent between measurements. The camera was placed as close as possible to the port to maximise the area of the camera's detector element occupied by the image intensifier's phosphor screen. The exposure time of the camera was set at 1.5 ms, triggered 55.7 μs before the gating unit of the image intensifier's power supply.

As with the acquisition of TOF profiles (Section 2.9.1), the probe laser wavelength was tuned to a given transition with the LabVIEW™ tune-up software prior to the acquisition of the images. This was done by varying the wavelength of the laser and the discharge-probe beam delay to find the maximum light level produced by the phosphor screen of the image intensifier, as detected by the photodiode placed next to camera. To determine the signal size from the waveform trace produced by the photodiode, the light from the phosphor screen was collected by the tune-up software in a circa 150 μs gate after the probe pulse, whereas the electronic baseline was recorded via a shorter gate (typically 50 μs) before the probe pulse. The image acquisition and the 'tune-up' functionalities were integrated into a single LabVIEW™ program. This allowed the user to monitor the signal from the image intensifier and re-tune the laser wavelength accordingly after each image or sequence of images acquired.

5.3 Image Acquisition and Analysis

This chapter will present a preliminary analysis of the results acquired with this detection set-up. The data manipulation and analysis programs used, and their limitations, will be described in this section. This continues to be an area of active development at the time of writing this thesis; some discussion of how it could be further improved is given in Chapter 6.

5.3.1 Acquiring the sequence of images

The primary outputs acquired for this set of scattering experiments were the sequences of summed images, as described in Section 2.9.3 of the Experimental Methods chapter.

These sequences consist of 21 summed images acquired over a range of discharge-probe delays, as specified in the results section. Between 3 and 5 sequences of images were acquired for PFPE and for squalane for each rotational level probed, alternating surfaces between each individual sequence. This was then repeated for PFPE and squalene. The sequences for PFPE were acquired to provide an internal reference to compare with the squalane and squalene sets, thus ensuring reproducibility of the results. Individual sequences of the incident beam were acquired between alternating liquid surfaces. For each set of scattering experiments, the pixel intensities of images at a given discharge-probe delay in each sequence were then averaged. For each average sequence of images with the surface in, another sequence of images was obtained by subtracting the pixel intensity of the incident beam sequence of images at a given pixel position from the corresponding images from the sequence with the surface in; this is analogous to how the ingoing beam contribution was subtracted from the TOF profiles with the surface in, as described in Section 4.4.1 in the previous chapter. For low rotational levels, this resulted in subtracted images containing pixels with negative intensity, which is likely due to the slight attenuation of the incident beam observed in the results from the single-point detection set-up (Section 4.4.1). Due to constraints of time available, this preliminary analysis was conducted solely on the sequences obtained from a straight subtraction of the incident beam contribution, and no attempt was made to account for the incident beam attenuation.

5.3.2 Locating the liquid surface in the image

Throughout the acquisition of the sequences of images, additional features were detected on the phosphor screen outside of the area probed by the probe beam (discussed in Section 5.3.3). These were identified as arising from the image intensifier amplifying probe beam laser light that had scattered from the wheel, and from the supporting rods to which the skimmer plate holder is attached to. A representative image of these features is shown Figure 5.5. These features allow the user to obtain a rough estimate of the position of the surface in the raw images with respect to the edge of the sheet. If the distance between the rods and the skimmer is known accurately, these features could be used, in principle, to estimate independently the pixel-to-real space conversion factor, which will, in turn, allow the user to determine the speed of the OD radicals at a given final scattering angle. However, the signal from the scattered light is usually very low compared to the OD LIF signal detected by the image

intensifier. It is also not clear from the image whether the scattered light features emerge from the same plane of the probe sheet. One way to address this issue would be to coat the wheel and the rods with some substance that produced fluorescence when exposed to scattered UV light from the probe beam. Alternatively, an object of known dimensions could be introduced in the main chamber in the same plane as the probe sheet, in order to obtain an image of the laser light that scatters off the object. Due to time constraints, neither of the two approaches were attempted at the time of writing this thesis, and so the features were used only to estimate the position of the wheel in the raw images acquired. The pixel-to-real space conversion factor will be estimated via an indirect method discussed in Section 5.3.6.

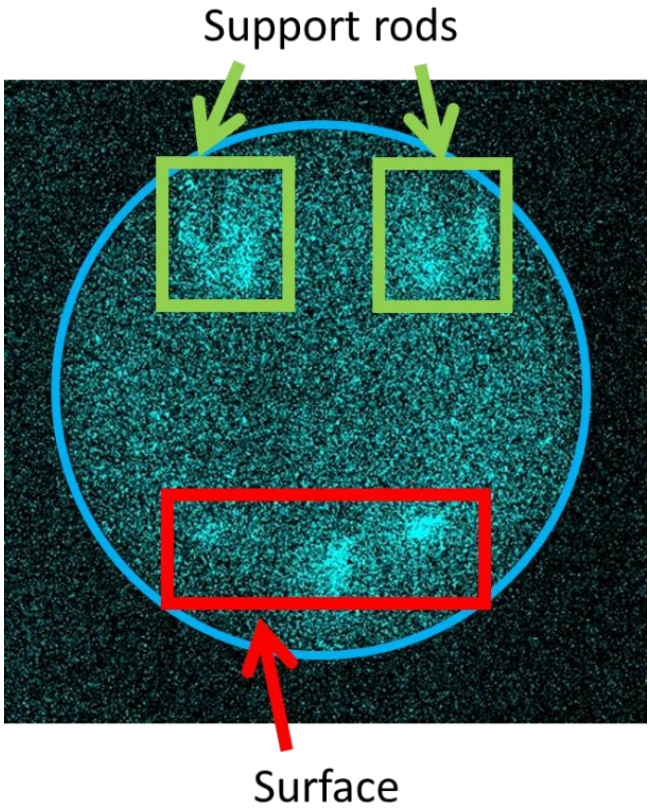

Figure 5.5: Representative image signal emerging from probe laser light scattering off the wheel where the liquid surface is generated (red box), and the supporting rods to which the skimmer plate holder is attached. The image was acquired with no OD LIF signal present. The image intensifier voltage was set at 1500 V. Positive pixel intensity is shown in cyan. Blue circle represents the area where the phosphor screen is located in the image.

5.3.3 Instrument Function correction

To account for changes in the intensity of the signal size due to the distribution of probe beam power (Figure 5.3) and the collection efficiency of the optics stack, etc, at different points across the sheet, 'instrument function' summed images were taken prior to acquiring the scattering data. The images were taken at a delay of circa 1 ms from the start of the discharge, with the discharge conditions set to strike over the entire gas pulse. The OD detected at that delay was assumed to be uniformly distributed in the vacuum chamber, therefore the images acquired were assumed to represent the detection sensitivity of the image intensifier for a given power distribution in the probe sheet (this assumption will be tested and discussed in Section 5.3.6 below). A set of three images was acquired for each of the rotational levels probed, and averaged. A sample instrument function image is shown in Figure 5.6.

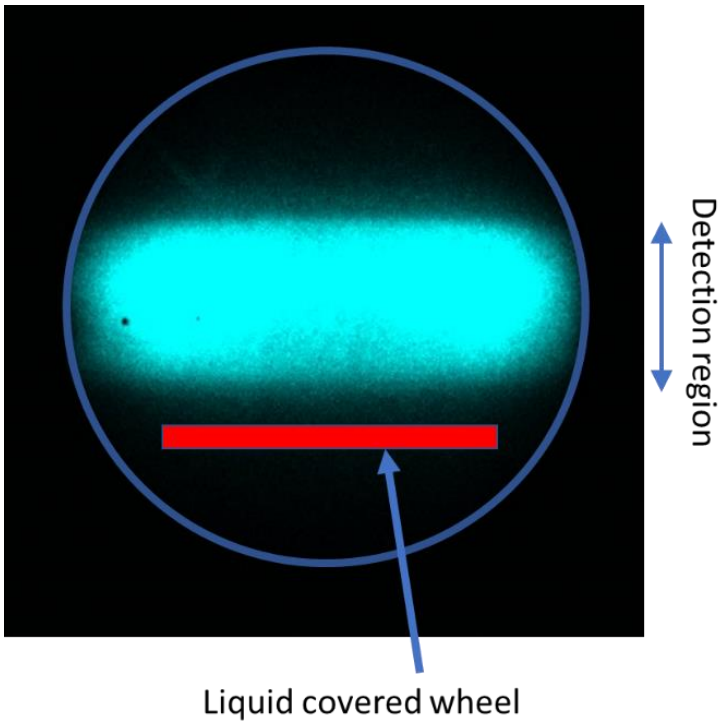

Figure 5.6: Representative image of the instrument function for a uniform distribution of OD at long (1 ms) delays, as described in text. Image was acquired on the $Q_1(1)$ transition, with the image intensifier voltage set at 1400 V. Positive pixel intensity is shown in cyan. Blue circle represents the area where the phosphor screen is located in the image. Red line represents the position of the liquid covered wheel, estimated as described in Section 5.3.6.

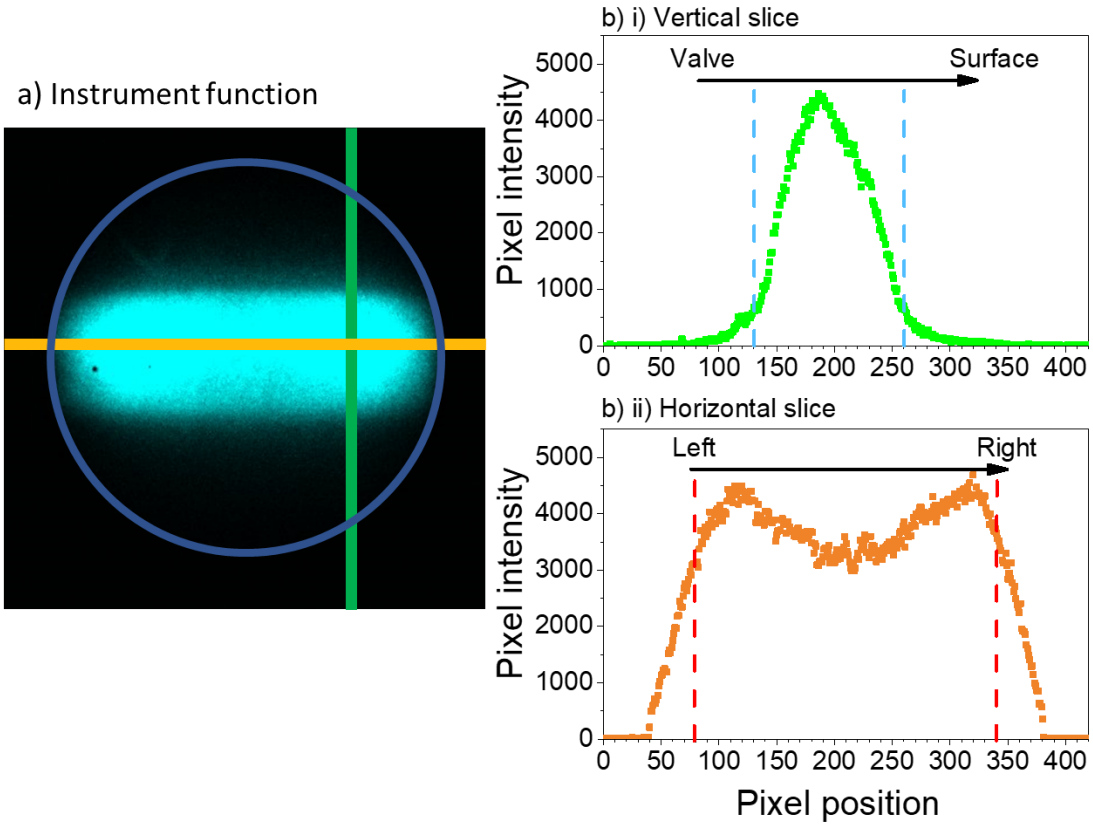

Figure 5.7: a) Image of the instrument function acquired on the $Q_1(1)$ transition with the image intensifier voltage set at 1400 V. Positive pixel intensity is shown in cyan. Blue circle represents the area where the phosphor screen is located. b) One pixel-wide vertical (i) and horizontal (ii) slices of the instrument function acquired in the positions shown by the green (vertical) and orange (horizontal) lines in the image (a). Dashed blue lines in the vertical slice indicate estimated edges of the area detected by the probe sheet. Dashed red lines in the horizontal slice indicate region being analysed in the horizontal slices shown in subsequent images.

A custom LabVIEW™ program was then used to extract the pixel intensities lying on a given horizontal or vertical 1-pixel wide slice of the instrument function image, the results of which are shown in Figure 5.7. The OD signal along the vertical slice was found to be similar to the power distribution of the beam measured via the power meter. The vertical slicing of the instrument function could, in principle, also be used to estimate the conversion factor between pixels in the image and the distances in the plane of detection, provided that the width of the OD LIF signal detected in the instrument function corresponds exactly with the physical width of the probe sheet in the centre of

the chamber. This will be discussed in further detail in Section 5.3.7 below. Throughout the following sections the distance travelled by OD (either incident or scattered) detected by the probe sheet over time will be measured from the edge of the probe sheet closest to the surface, determined from the instrument function to be at 255 pixels from the top of the images acquired.

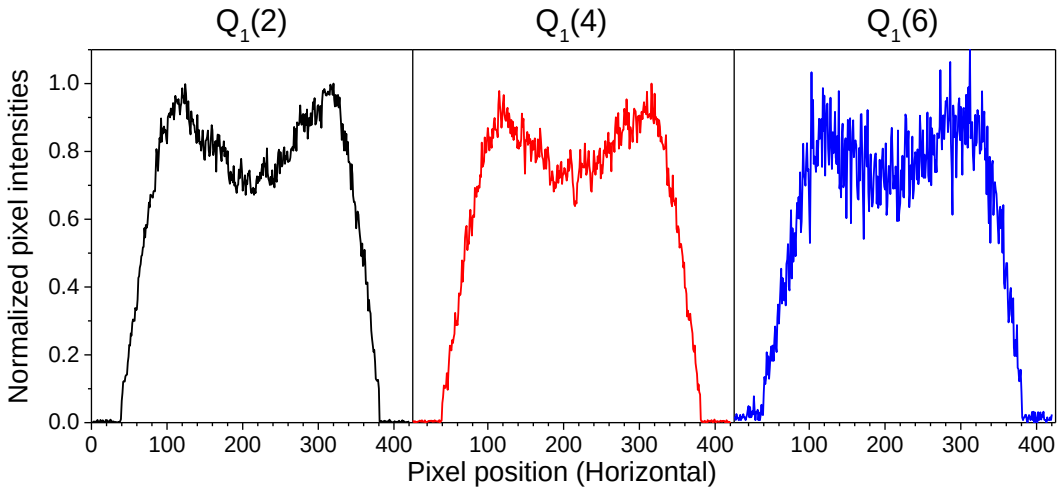

Figure 5.8: Peak-normalized horizontal slices of the instrument functions taken on the $Q_1(2)$ (left), $Q_1(4)$ (centre), and $Q_1(6)$ transition (right) with the image intensifier set at 1400 V, extracted at the position in the image indicated by the orange line in Figure 5.7 (a)). The instrument function from the $Q_1(6)$ transition was scaled so that the peaks at around 105 and 315 pixels matched the peak of the other instrument functions.

Interestingly, the horizontal slice of the instrument function image shows two peaks in the pixel intensities, centred at ≈105 and 315 pixel position in the image, and corresponding to opposite ends of the phosphor screen. They also feature a central dip in the signal size in the centre of the detection region. Equivalent slices were obtained from the instrument functions of the N = 2, 4 and 6 levels (Figure 5.8), and compared with the horizontal slice at N = 1 from Figure 5.7 (b) (ii). A comparison between the slices shows that the dip in pixel intensities appears to be essentially the same across the rotational levels probed, with the reduction in signal estimated to be at most ≈25%. As of writing, it has yet to be determined whether this feature is an intrinsic feature of how the OD fluorescence light is transmitted through the lenses in the optic stack, or whether

the signal transmission is inhibited by e.g. a coating of liquid that has evaporated from the baths and preferentially covered the centre portions of the imaging lenses, etc...

5.3.4 Analysing the images: Slices from image sections

To obtain a preliminary estimate of the angular distribution and speeds of OD radicals scattered off the liquid surfaces, the sequences of images from the scattering experiments were analysed via two different methods, each with its associated custom LabVIEW™ program, as described in this and the following section. Information on the angular distribution of the scattered species was obtained by defining horizontal sections of the images parallel to the liquid surface and within the detection region (determined by the instrument function), extracted at selected discharge-probe delays. The 'image sections' were represented by a single horizontal slice, resulting from an average of all the horizontal slices contained within the defined section. Each image section was set to be 30 pixels wide, and placed at distances of 0, 30, and 70 pixels from the edge of the probe sheet closest to the surface, defined as being at 255 pixels from the top of the images acquired, as shown in Figure 5.9. Any background noise in the slices was removed by subtracting from each slice the average pixel intensity derived from a slice obtained at a discharge-probe delay where no OD LIF signal is present, i.e. at the earliest delay available in the sequence. Prior to averaging the horizontal slices, the pixel intensities in each image section were corrected for the detection sensitivity at a given pixel by applying the correction factor extracted from the corresponding instrument function (discussed above), via the equation:

$$Pix_{CORR} = \frac{Pix_{Raw}}{Pix_{Inst}} \tag{5.1}$$

where Pix_{Raw} is the pixel intensity from the raw data, and Pix_{Inst} is the peak-normalized value of the corresponding pixel in the instrument function. To avoid up-weighting the pixel intensities outside of the region probed by the sheet, the analysis of the slices was restricted between pixel positions 80 and 340, as shown in Figure 5.7 b) ii). A cubic-spline fit was then applied to the slices, with a balance parameter of 0.0005, as shown in Figure 5.9. As of writing, the analysis has been conducted on the average sequence of images without attempting to extract the statistical uncertainty in each point.

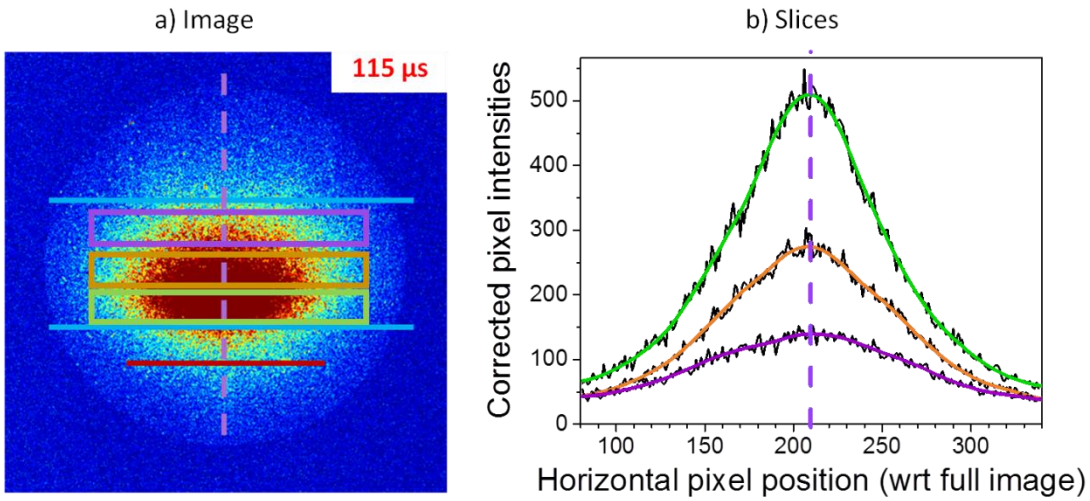

Figure 5.9: a) False-colour image of OD LIF signal scattered off the PFPE surface at normal incidence at the discharge-probe delay of 115 µs, using the He carrier, and probing the $Q_1(6)$ transition. Strong, positive pixel intensity is indicated in red, whereas signal intensity close to 0 is indicated in blue. Cyan lines show the detection region of the probe sheet. Red line indicates position of the surface, estimated as described in Section 5.3.2. Dashed purple line indicates the axis normal to the surface, centred at the focus point of the incident beams. b) Slices obtained from the image sections shown in a). Black lines represent data from image corrected by the instrument function, coloured lines represent cubic spline fit to data from the corresponding image sections in the image.

5.3.5 Analysing the images: TOF profiles

To determine the speeds of both incident and scattered OD radicals, TOF profiles were obtained using the second analysis program by integrating the pixel intensities from an image within a user-defined Region of Interest (RoI) and plotting them as a function of the discharge-probe delay. As with the slices from image section analysis described in the previous section, the pixel intensities within the RoI were corrected for the detection sensitivity prior to integration, by applying the instrument function correction factor using Equation (5.1). The background noise in the profiles was removed by subtracting the pixel intensity obtained at a discharge-probe delay where no OD LIF signal is present, i.e. at the earliest delay available in the TOF profile. The scattered OD profiles were then obtained via a straight subtraction of the incident OD contribution from the profiles with surface in, as described in Chapter 2 Section 2.9.1.

For the purpose of the preliminary analysis conducted for this thesis, two sets of TOF profiles were obtained from RoIs placed at 0, 30, and 70 pixels from the edge of the probe sheet closest to the surface. The first set of profiles were obtained by integrating the same RoIs defined by the image sections shown in Figure 5.9. As discussed in Section 5.3.7, the area defined by the image sections, and especially the one defined by the section nearest to the surface, act as a good mimic to the area in real space detected by the single-point detection set-up.

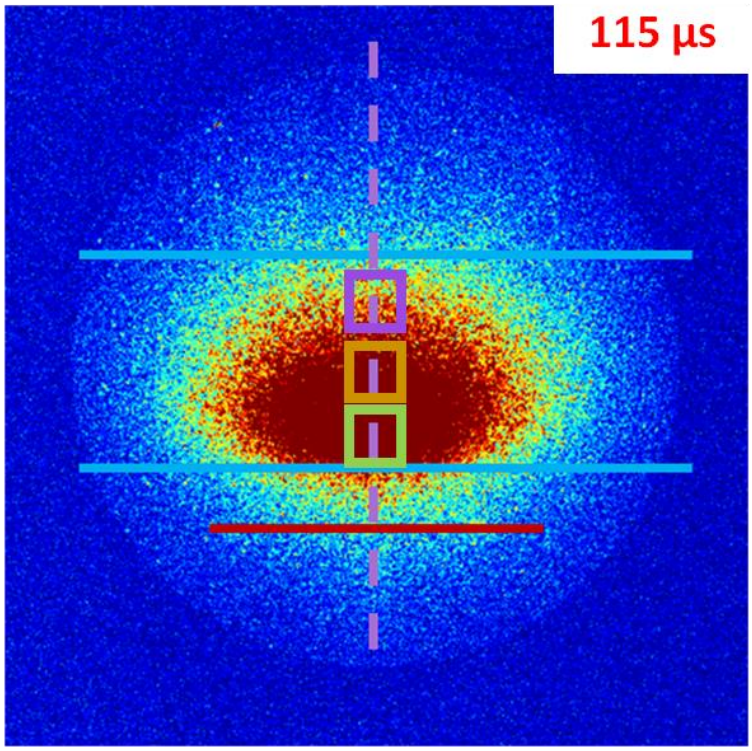

Figure 5.10: False-colour image of OD LIF signal scattered off the PFPE surface at normal incidence at the discharge-probe delay of 115 µs, using the He carrier, and probing the $Q_1(6)$ transition. Strong, positive pixel intensity is indicated in red, whereas signal intensity close to 0 is indicated in blue. Cyan lines show the detection region of the probe sheet. Red line indicates position of the surface, estimated as described in Section 5.3.2. Dashed purple line indicates the axis normal to the surface, centred at the focus point of the incident beams. 30 x 30 pixel RoI are defined by the coloured boxes.

The second set of profiles were obtained by integrating smaller regions of interest within the detection region. Analysing the TOF profiles obtained from a smaller RoI allows the user to obtain information on OD scattered on a narrower range of final

scattering angles, compared to than the larger image section RoI. These regions could also, in principle, be placed along any given final scattering angle with respect to the surface. Due to time constraints, this proof-of-concept analysis was restricted to probing only OD scattered at normal angle of incidence, centred at the focus point of the incident beams, using regions of 30 x 30 pixels as shown in Figure 5.10. A representative set of incident and scattered OD TOF profiles is shown in Figure 5.11.

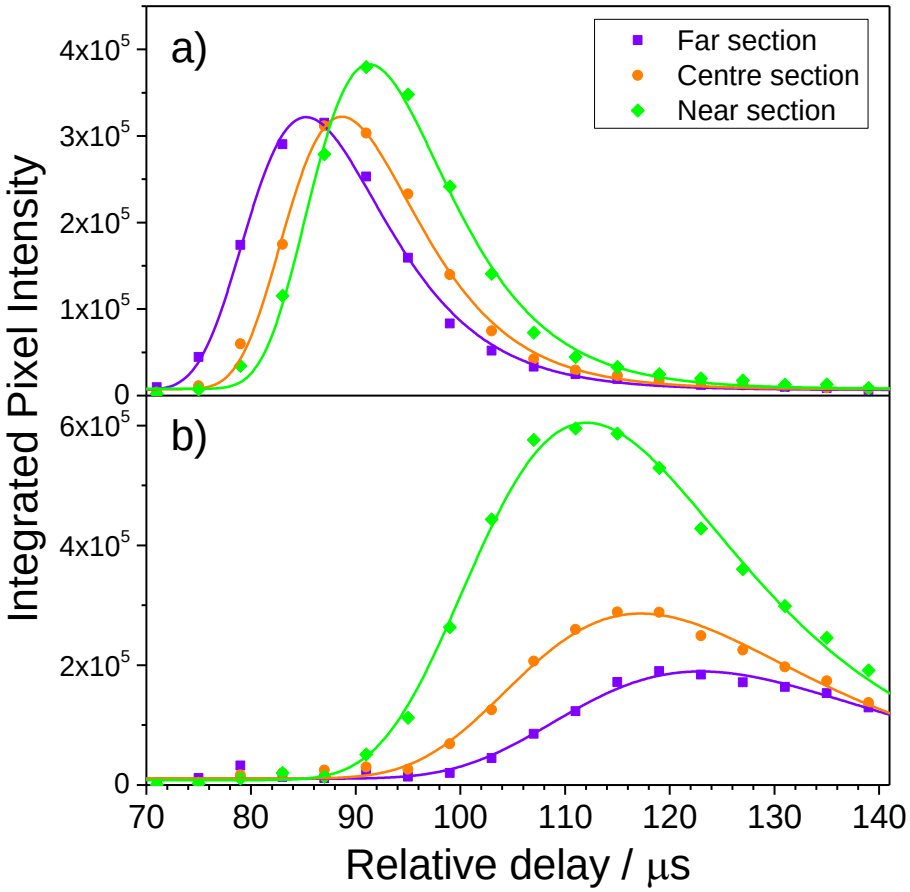

Figure 5.11: Representative TOF profiles of the intensity of incident (a) and scattered (b) OD LIF signal as a function of the discharge-probe delay, from the RoI shown in Figure 5.10, with associated Gumbel probability density function fits. Both profiles were obtained by probing OD scattered off PFPE at normal incidence with respect to the surface on the $Q_1(6)$ transition.

Unlike the TOF profiles shown in Chapter 4, the sequences of images from which the TOF profiles were derived from were obtained from a smaller set of discharge-probe delays, with larger steps between delays probed (4 μs steps when using the He carrier, 10 μs when using Ne). As such, the peaks of the raw TOF profiles are not well defined compared to those shown in Figures 4.7 and 4.8. To address this issue, the peak arrival time of the TOF profiles was obtained by fitting each profile to a Gumbel probability distribution (also known as the General Extreme Value distribution Type-I), expressed in the form of the equation:

$$y = y_0 + A \exp\left[-exp\left[-\left(\frac{x-x_c}{w}\right)\right] - \left(\frac{x-x_c}{w}\right) + 1\right] \tag{5.2}$$

where y_0 is the offset of the baseline of the fitted curve on the y-axis; A is the amplitude of the fitted curve, corresponding to the y-axis coordinate of the peak of the curve; x_c is the location parameter, corresponding to the x-axis coordinate of the peak of the curve; and w is the statistical dispersion of the probability distribution. Of the readily available non-linear curve fitting functions by the programs used for analysis of the data, the Gumbel probability distribution provided a good empirical fit going smoothly through the TOF profiles, as shown in Figure 5.11. The peak arrival time of the TOF profile was assumed to be the location parameter x_c of the fitted curve.

The peak arrival times were extracted from each TOF profiles, and plotted as a function of the average distance of the RoI with respect to the edge of the surface (Figure 5.12). For a given point, the error on the peak arrival time was derived from the Gumbel probability function, whereas the error in the distance was set at 15 pixels, i.e. half the length of the RoI used. From these plots, the speed of the OD radicals travelling through the RoI (in pixels per unit time) were obtained from the slope of a linear fit through the points, whereby negative slopes indicate the velocity of OD projectiles travelling towards the surface, and positive slopes indicate the velocity of OD travelling away from the surface. The speeds were then converted in standard SI units using the conversion factor discussed in Section 5.3.7.

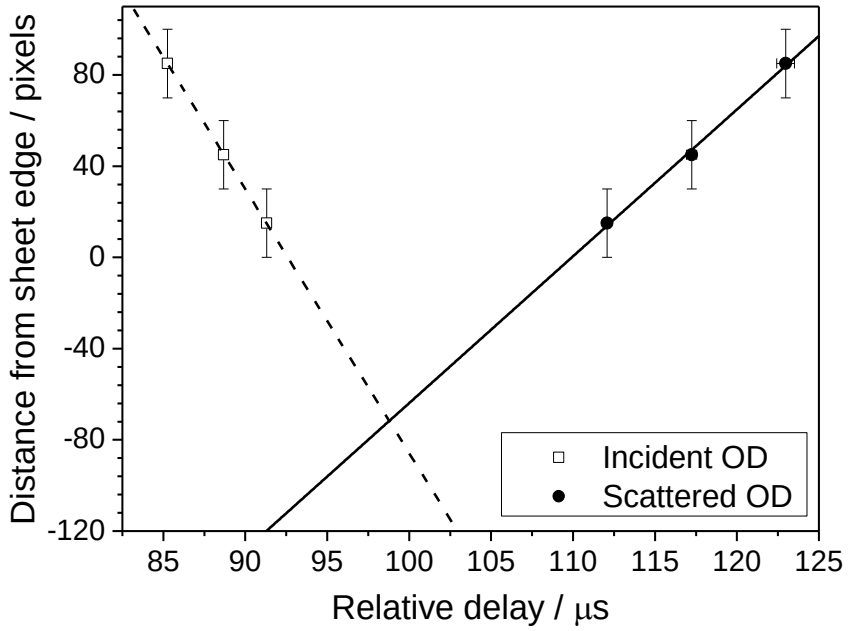

Figure 5.12: Representative plots of peak arrival times (from TOF profiles in Figure 5.11) over distance from the edge of the sheet closest to the surface (in pixels), with associated linear fits to each set of points, representing the speeds of the radicals probed. Data shown are from incident OD (dashed line, empty circles), and scattered OD from PFPE, both probed on the final scattering angle normal to the surface, centred at the focus points of the molecular beams, on the $Q_1(6)$ transition using He as the carrier gas.

5.3.6 Testing the effectiveness of the Instrument Function

To test whether the instrument function correction accounts for the power distribution of the probe beam, slices of the incident beam packet were obtained at selected delays, corresponding to the peak arrival time of the incident OD packet in the corresponding TOF profiles obtained by integrating the pixel intensities within the three image sections shown in Figure 5.9. It is assumed that the number density of OD in the incident beam is the same across all the image sections from which the slices were extracted when probed at the corresponding peak arrival times for each section.

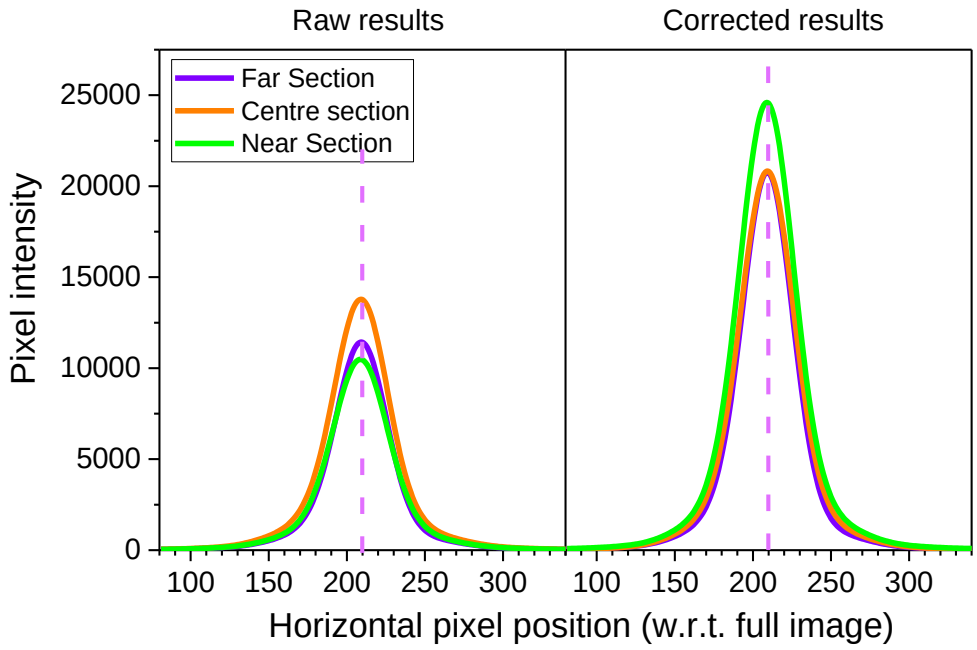

Figure 5.13: Representative slices of image sections (shown in Figure 5.9 (a)) from images of the incident OD at the corresponding peak arrival times for each image section. The OD packet in the He is travelling at normal incidence with respect to the surface, and probed on the $Q_1(2)$ transition. Dashed purple line indicates the axis normal to the surface, centred at the focus point of the incident beams. a) Slices fitted to the raw data with background signal removed, b) slices fitted to the data after applying the instrument function correction.

A representative set of results, comparing the slices from the data before and after applying the instrument function, is shown in Figure 5.13. The uncorrected slices from Figure 5.13 (a) show clear differences in the peaks of the signal size, with the signal being highest in the central image section, followed by the far image section, and being lowest in the near image section. The order of the signal size from each image section is consistent with the power distribution of the probe sheet extrapolated from the instrument function shown in Figure 5.7 (b) (i). Differences between slices were also observed when the instrument function correction was applied to the data (Figure 5.13 (b)). However, several of the slices analysed across different rotational levels and different angles of incidence (Figure 5.14) were found to overlap almost exactly, indicating that the instrument function correction does, in principle, correct the raw data by the distribution of the probe beam power across the sheet.

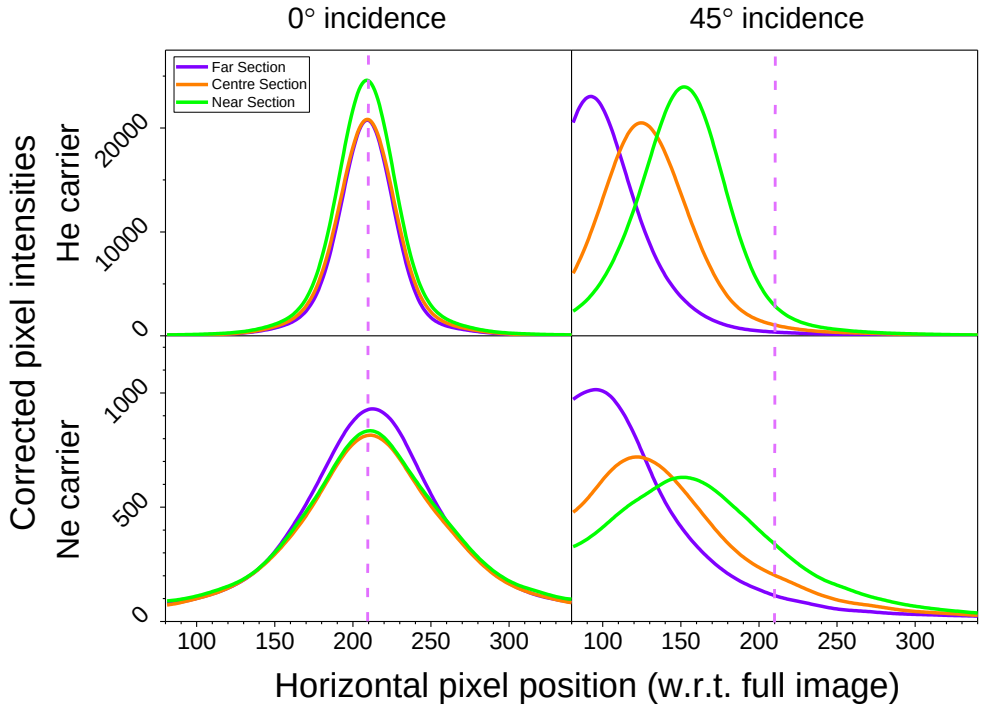

Figure 5.14: Representative slices of image sections (as shown in Figure 5.9(a)) from images of the incident OD at the corresponding peak arrival times for each image section, probed on the $Q_1(2)$ transition. The slices were acquired for normal incidence (left) and 45° incidence (right) using He (top) and Ne (bottom) as the carrier gases. The instrument function correction was applied to the images prior to acquisition of the slices from each image section. Dashed purple line indicates the axis normal to the surface, centred at the focus point of the incident beams.

The standard deviation of the integrated pixel intensities from each section, and from the corresponding TOF profiles, across multiple measurements was found to be ~12 ± 5 %, which is in good agreement with the shot-to-shot variation of the probe beam power. This suggests that that the instrument function correction does not systematically over- or under-correct the pixel intensities beyond the variation in the LIF intensity expected from the experimental set-up. However, larger discrepancies in the size of the slices have been observed for OD arriving at 45° to the surface normal. There are several factors that contribute to these discrepancies above and beyond the shot-to-shot variation of the probe beam power. One such factor is that the OD packet is travelling across the left peak of the instrument function (Figure 5.7 (b) (i)) and thus the pixels where OD LIF signal is detected are being subjected to different correction factors between the slices, compared to the normal incidence results where the OD

signal is cylindrically symmetric with respect to the axis normal to the surface, centred around the focus point of the beams. The other factor to consider is that the molecular beam is travelling diagonally across the image sections probed. This results in the distance that the OD projectiles travel between sheet edges being longer by a factor of $\sqrt{2}$ than the distance travelled by OD at normal incidence, and thus it would take longer for the OD projectiles to travel across the sheet. The TOF profiles in Figure 5.11 show that the peak LIF signal from the raw profiles does not always correspond to the most likely peak of the profile obtained from the Gumbel distribution function fitted to the profile, and the difference between raw and fitted peak arrival times is likely to be larger when looking at the results from 45° incidence. Finally, it is also possible for the OD packet to diverge transversely as it travels towards the liquid surfaces, resulting in an apparent decrease of the OD LIF signal across the image sections, and an increase in the FWHM of the profiles. This appears to be the case with the results obtained with the Ne carrier from 45° incidence shown in Figure 5.14. The integrated pixel intensities of the slices should, in principle, remain the same within the ~12% variation in signal size expected above, provided each slice captures the full width of the packet, which may not be the case for the examples shown in Figure 5.14. Further analysis of the instrument function will be required in later studies to ensure all those factors have been fully accounted for.

5.3.7 Estimating the pixel-to-real space conversion factor

The analysis of the TOF profiles described in Section 5.3.5, allows the user to determine the speeds of the OD radicals in pixels per unit time. To express those speeds in standard SI units, the pixel-to-real space conversion factor of the image acquisition set-up needs to be determined.

A preliminary pixel-to-real space conversion factor was estimated by assuming that the distance between the edges of the detection region defined by the instrument function is equivalent to the full width of the probe sheet, measured to be ~30 mm. The vertical slices of the instrument function images (Figure 5.7 (b) (i)) suggest that the distance between the edges of the sheets is ≈130 pixels. This would give a conversion factor of ~0.23 mm pixel^{-1}, or ~2.3 x 10^{-4} m pixel^{-1}. To test the validity of the conversion factor, TOF profiles were obtained from sequences of images of incident OD at normal incidence to the surface and probed on the $Q_1(1)$ transition, integrating the 30 x 30

pixels RoI (Figure 5.10) as described in Section 5.3.5. The sequences of images used for this analysis were acquired on the same day prior to and after the acquisition of OD LIF signal on the $Q_1(6)$ transition, which the rest of the TOF data analysis will be focused on (Section 5.4.2). This provided a set of 2 independent measurements for both He and Ne carrier gases, each on two different days, providing a total of 4 measurements obtained on the $Q_1(1)$ transition for each carrier gas. For each carrier gas, the speeds of incident OD were derived for each individual set of profiles. The average speeds of OD seeded in each of the carrier gases used were then converted to standard SI units using the conversion factor estimated above and compared with the experimental speeds obtained from the single-point detection set-up (Chapter 4 Section 4.3). The results are shown Table 5.1.

Carrier gas	**Incident speeds** (a) / 10^6 pixels s^{-1}	**Converted speeds** (b)/ m s^{-1}	**Reference speeds** (c)/ m s^{-1}
Helium	11.5 ± 3.9	2634 ± 896	1811 ± 8
Neon	5.4 ± 1.9	1241 ± 430	894 ± 3
a) Errors are derived by propagating the errors from individual linear fits; b) Using a conversion factor of 2.3 x 10^{-4} m $pixel^{-1}$; c) From Chapter 4 Section 4.3			

Table 5.1: Table of experimental and converted speeds of incident OD radicals arriving at normal incidence to the surface and probed on the $Q_1(1)$ transition

As can be seen from Table 5.1 above, the converted speeds of incident OD radicals are significantly higher than the experimental incident speeds obtained in the previous chapter. Although the converted speeds are reassuringly within error of the speeds determined via the single-point detection set-up, using the conversion factor derived from the instrument function will result in the speeds derived from the sequences of images to be overestimated by a factor of ~1.4. This suggest that the width of the detection region in real space as defined by the instrument function does not correspond to the physical width of the probe sheet observed by blocking it with a card or piece of white paper. The source of this discrepancy is possibly caused by the presence of Amplified Spontaneous Emission (ASE) in the probe beam profile as it emerges from the dye laser, which is expanded alongside the pure laser emission. The bandwidth of the ASE areas is much broader than the true laser emission in the probe beam profile.

As such, most of the light in the ASE areas will not be resonant with the wavelength of the OD transition probed, and thus won't be absorbed by the radical. This issue becomes much more apparent when the beam is expanded into the probe sheet, resulting in low, if not absent, LIF yield in the ASE areas of the expanded laser sheet profile, which in turn leads to the sheet probing a smaller detection region than otherwise assumed. In principle, it would be possible to discriminate the area of the probe sheet consisting primarily of pure laser emission light from the areas consisting primarily of ASE light, by measuring the probe sheet power passing through a small pinhole onto a sensitive power meter, and scanning both across the probe sheet, similar to how the probe laser power across the sheet was estimated in Section 5.2. Due to time constraints, this approach was not attempted.

The second method used to estimate the pixel-to-real space conversion factor was to assume that the incident OD speeds in pixels s^{-1} shown in Table 5.1 are equivalent to the incident OD speeds determined with the single-point detection measurements (Chapter 4 Section 4.3). These speeds have been measured over a long time-of-flight period with a well-defined start time, and as such they are very well determined. They are also in good agreement with the thermodynamic predictions for each carrier gas (Table 3.1). The conversion factor can then be obtained from the ratio of the speeds. This was determined to be $(1.58 \pm 0.02) \times 10^{-4}$ m pixel^{-1} when using He as the carrier gas, and $(1.66 \pm 0.02) \times 10^{-4}$ m pixel^{-1} when using the Ne carrier. The two conversion factors were found to be in good agreement with each other, suggesting that this indirect approach provides a more reasonable estimate of the pixel-to-real space conversion factor. As such, these conversion factors will be used with data obtained with the corresponding carrier gas throughout this chapter. Further analysis of the instrument function will be required to confirm the validity of the indirect approach used above.

5.4 Results

5.4.1 Sequences of summed images

The sequences of summed images of OD radicals scattering off each liquid surface were measured systematically via the $Q_1(2)$, $Q_1(4)$, $Q_1(6)$ and $Q_1(8)$ transitions with the He carrier, and via $Q_1(2)$, $Q_1(4)$, $Q_1(6)$ with the Ne carrier. Each summed image in the sequences was the result of summing 500 individual images per discharge-probe delay, and a pixel intensity threshold of 12 was applied to remove as much of the camera noise from the image as possible, as described in section 2.9.3. For the He carrier, 3 individual sequences of images were acquired for each of the lines probed, whereas for the Ne carrier, 5 individual sequences of images were acquired, to compensate for the lower signal size and for issues with the discharge stability. Each sequence was made up of 21 individual summed images, acquired between the discharge-probe delays of 63 μs and 143 μs in delay steps of 4 μs for He and between 118 μs and 318 μs in delay steps of 10 μs for Ne. A full set of images was acquired for PFPE alongside a set of either squalane or squalene, alternating surfaces between each individual sequence, and acquiring incident beam sequences when switching between the liquids on the same day. The sequences of images for each liquid surface and for the incident beam were then averaged, as described in the previous section.

A selection of images from the sequences with surface in, probed on the $Q_1(6)$ transition, is shown in the following pages. Figure 5.15 and Figure 5.16 show the OD seeded in He scattered off the liquid surfaces at normal incidence and 45° respectively, whereas Figure 5.17 and Figure 5.18 show the equivalent scattering experiments with the Ne carrier. The images shown in the figures were obtained from the raw data without applying the instrument function correction. This was largely due to the fact that, when applied to the image, the instrument function correction would increase the pixel intensities in regions outside or at the edge of the detection region, thereby distorting the false-colour mapping applied to the image. Furthermore, the incident beam contribution has not been subtracted from the sequences, as shown in the images taken for the first two discharge-probe delays. The results obtained from probing the $Q_1(6)$ transition were chosen to be displayed in the figures, as both the incident and scattered OD could be observed without changing the false-colour mapping settings between the images. This provides a rough indication of the LIF signal of the scattered radicals in the image compared to the incident beam signal.

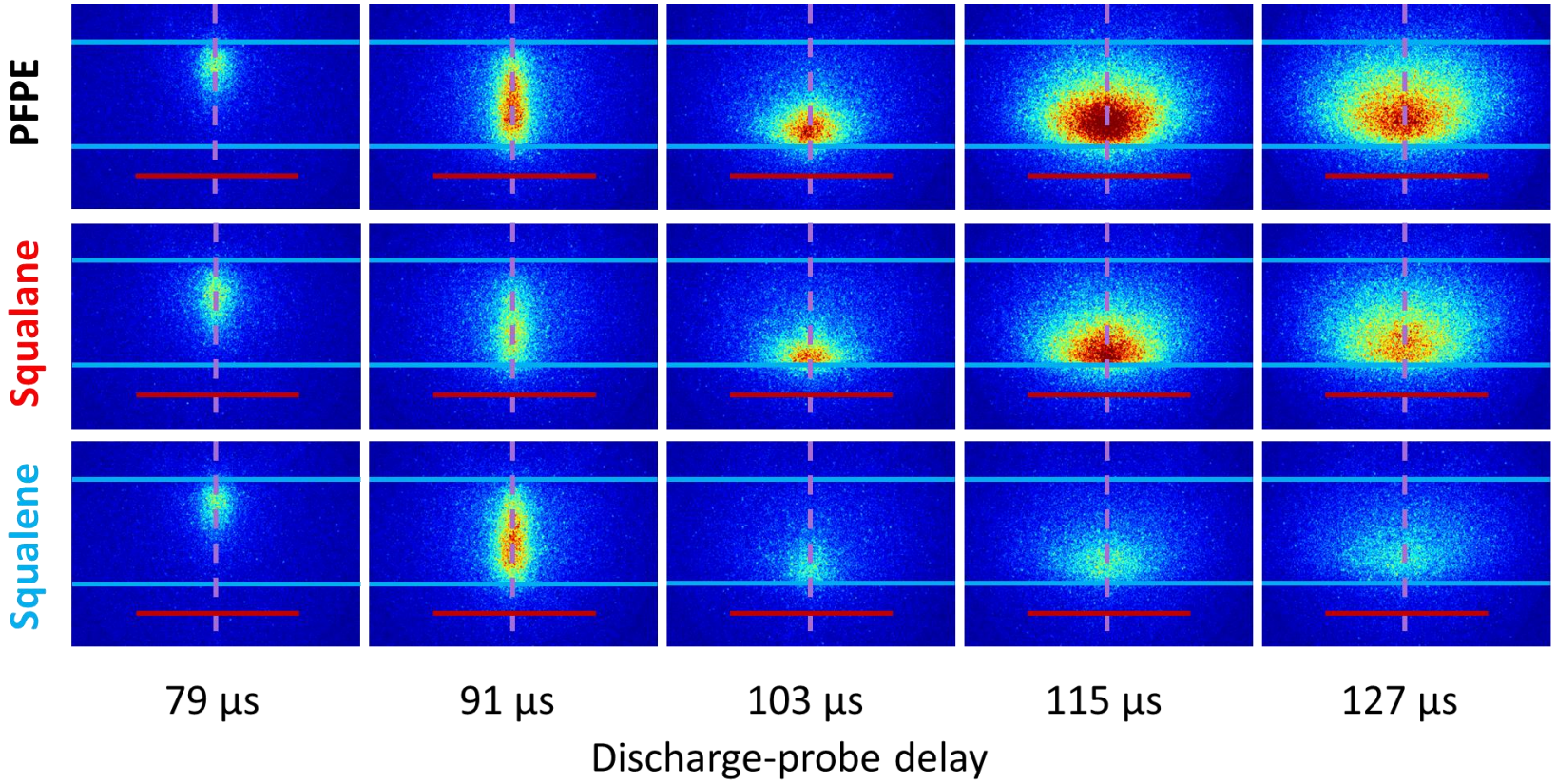

Figure 5.15: False-colour images of OD LIF signal scattered off PFPE, squalane and squalane surfaces at normal incidence at selected discharge-probe delays, using the He carrier, and probing the $Q_1(6)$ transition. The instrument function correction has not been applied to these images. Strong, positive pixel intensity is indicated in red, whereas signal intensity close to 0 is indicated in blue. Cyan lines show the detection region of the probe sheet. Red line indicates position of the surface. Dashed purple line indicates the axis normal to the surface, centred at the focus point of the incident beams.

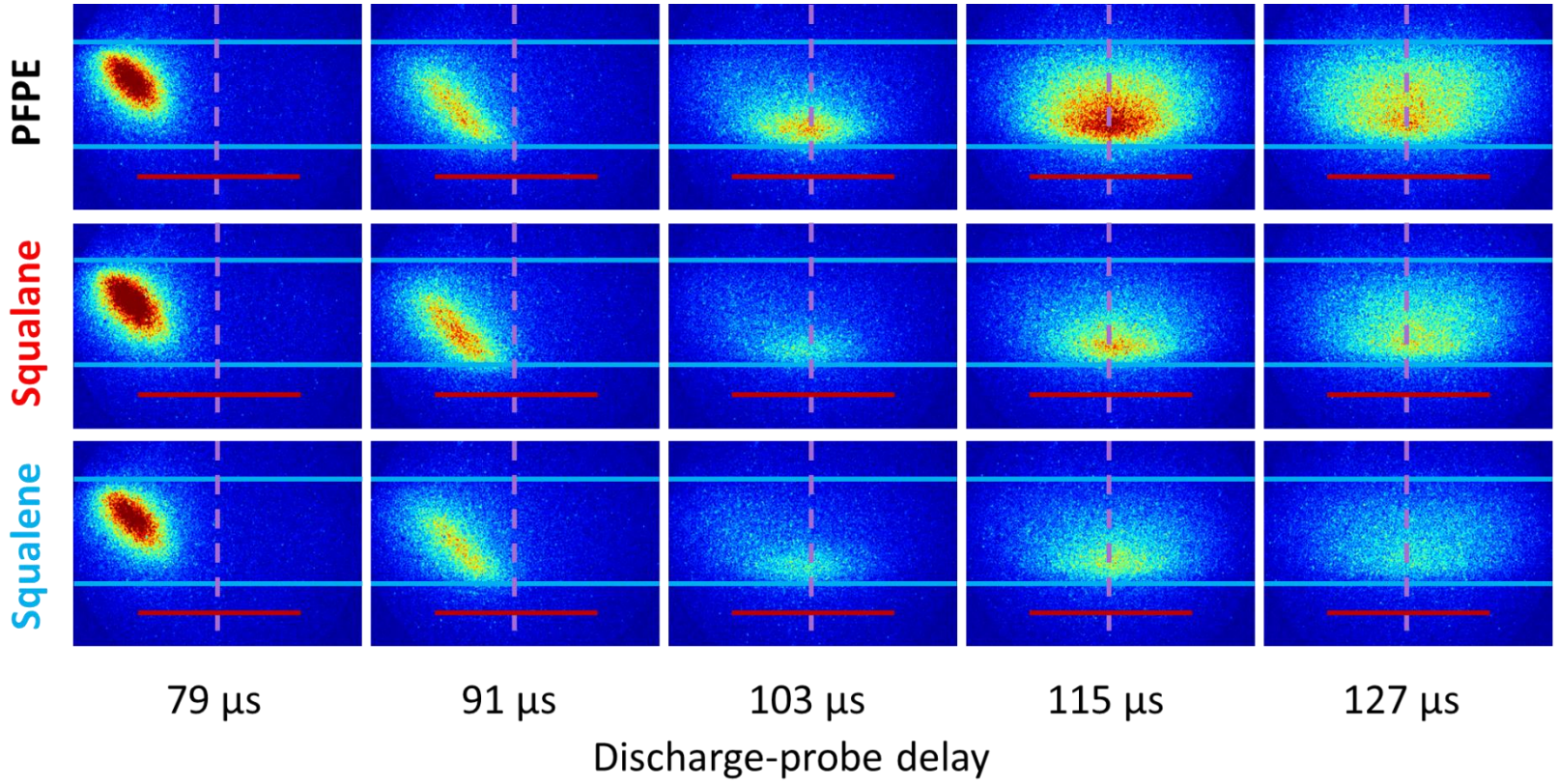

Figure 5.16: False-colour images of OD LIF signal scattered off PFPE, squalane and squalane surfaces at 45° incidence at selected discharge-probe delays, using the He carrier, and probing the $Q_1(6)$ transition. The instrument function correction has not been applied to these images. Strong, positive pixel intensity is indicated in red, whereas signal intensity close to 0 is indicated in blue. Cyan lines show the detection region of the probe sheet. Red line indicates position of the surface. Dashed purple line indicates the axis normal to the surface, centred at the focus point of the incident beams.

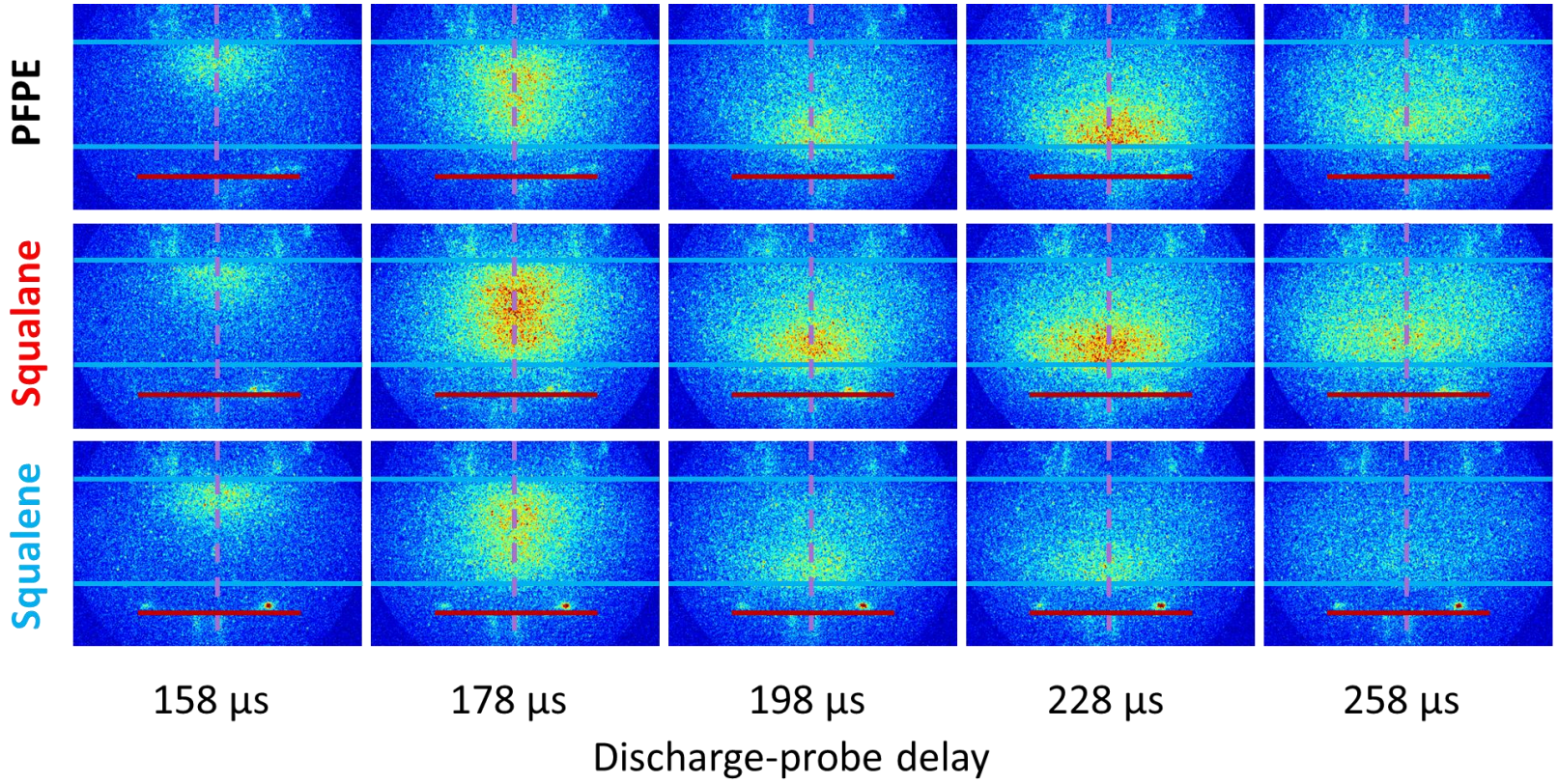

Figure 5.17: False-colour images of OD LIF signal scattered off PFPE, squalane and squalane surfaces at normal incidence at selected discharge-probe delays, using the Ne carrier, and probing the $Q_1(6)$ transition. The instrument function correction has not been applied to these images. Strong, positive pixel intensity is indicated in red, whereas signal intensity close to 0 is indicated in blue. Cyan lines show the detection region of the probe sheet. Red line indicates position of the surface. Dashed purple line indicates the axis normal to the surface, centred at the focus point of the incident beams.

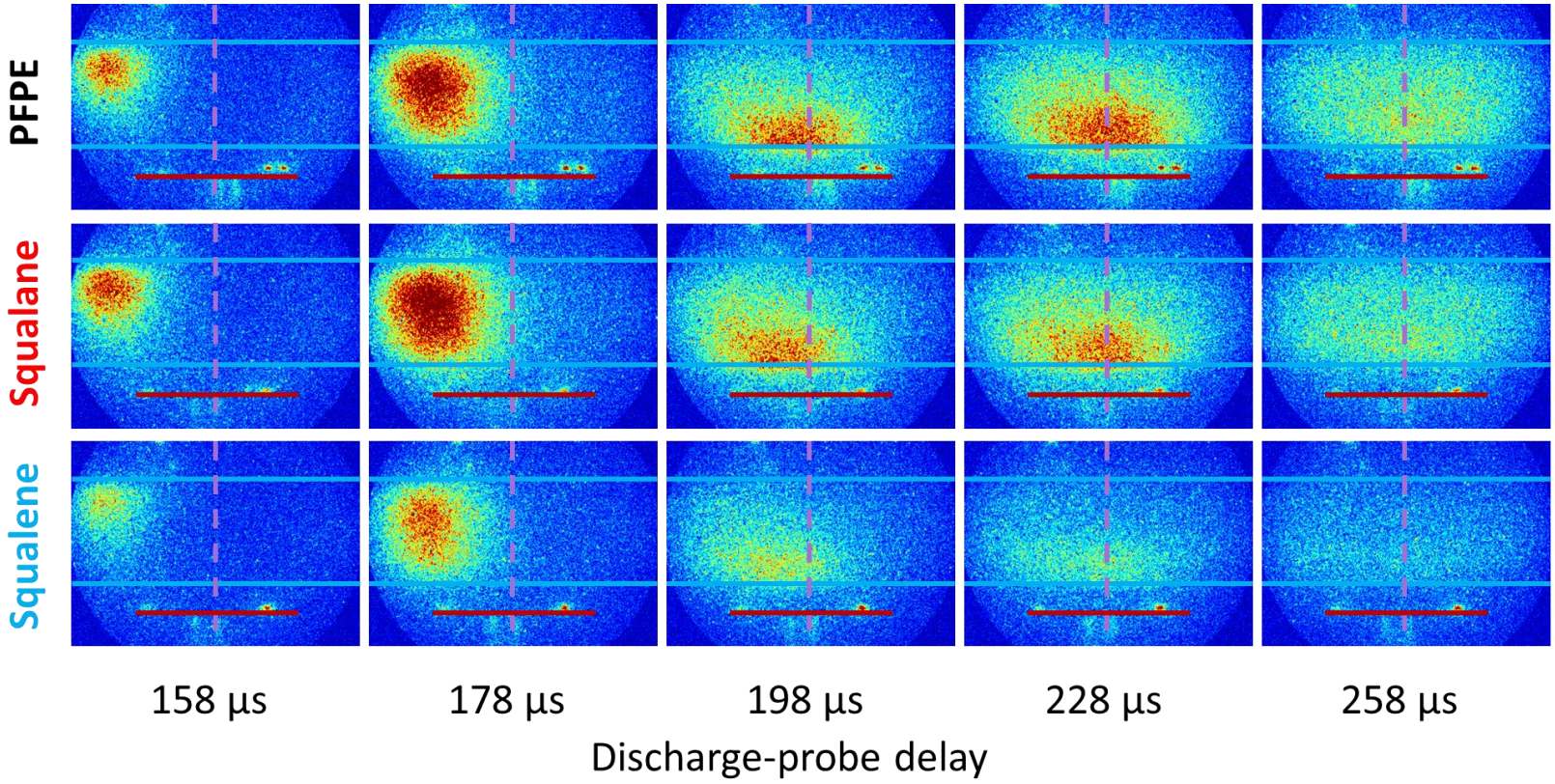

Figure 5.18: False-colour images of OD LIF signal scattered off PFPE, squalane and squalane surfaces at 45° incidence at selected discharge-probe delays, using the Ne carrier, and probing the $Q_1(6)$ transition. The instrument function correction has not been applied to these images. Strong, positive pixel intensity is indicated in red, whereas signal intensity close to 0 is indicated in blue. Cyan lines show the detection region of the probe sheet. Red line indicates position of the surface. Dashed purple line indicates the axis normal to the surface, centred at the focus point of the incident beams.

From the sets of images taken at early delays, it is immediately apparent that the incident packet of OD is travelling towards the surface from different angles of incidence, as expected. The images also appear to show noticeable differences in the spatial width of the OD packet as it travels through the detection region, with the He carrier results showing a narrower pencil-like distribution of the radicals, whereas the Ne carrier results show a significantly wider packet. These differences will be analysed in further detail in Section 5.4.3 below. When looking at later delays, it is also clear from all the figures that the OD detected is travelling away from the surface. However, unlike the incident beam, OD does not appear to scatter preferentially in any specific direction, but instead scatters across a broad range of angles.

In Figure 5.15 and Figure 5.17, the distribution of signal intensity appears to be symmetric with respect to the surface normal. This is an expected result from scattering the incoming projectiles at normal incidence to the surface, as the specular angle will be in the same direction as the angle of incidence. With regards to the scattered OD radicals from 45° incidence, previous results in the literature (described in Section 5.1) suggest that impulsively scattered OD radicals are expected to have a noticeable preference towards scattering in a 'forward' direction close to the specular angle. This should be more evident at the higher rotational levels probed. Such a preference towards specular scattering is, however, not immediately apparent from the scattered OD signal at the later delays shown in Figure 5.16 and Figure 5.18, as there is a significant amount of signal scattered at angles back towards the direction of the incident beam. Careful scrutiny of the images in Figure 5.16 shows slightly more signal intensity on the right of the surface normal than on the left when OD is scattered off squalane and squalene, suggesting that there is a modest preference towards forward scattering at the higher collision energies. The scattered OD distribution from PFPE appears to be symmetric with respect to the surface normal, which suggests that OD scatters with a slightly different angular distribution from PFPE than the organic surfaces. At low collision energies, OD scatters with a broad angular distribution that appears to be symmetric with respect to the surface normal regardless of the liquid surface used.

As noted above, the instrument function correction was not applied to the images shown from Figure 5.15 to Figure 5.18 above. The dip in detection sensitivity in the middle of the detection region and the power distribution across the probe sheet are likely to have distorted the OD LIF signal captured by the raw images, making it difficult to identify definitively any strong, directed scattering of OD from the images alone. Therefore, a more detailed analysis of the scattered OD was carried out below by obtaining TOF profiles as described in Section 5.3.5, and horizontal slices from image sections corrected by the appropriate instrument function, as described in Section 5.3.4.

5.4.2 TOF profiles analysis

A comparison of the signal intensity of the scattered OD radicals in the images shown in Figures 5.15 to 5.18 suggest that there is an unmistakable systematic variation in the relative magnitude of the scattered signal for the different liquids. The signal is consistently larger for PFPE at both collision energies and either angle of incidence, and gets progressively smaller for squalane, and then for squalene. This was, of course, expected on the basis of the results presented in Chapter 4. To confirm that the apparent trend here was not simply an artefact of the colour mapping chosen from the images, a preliminary set of TOF profiles were extracted for each of the sequences of images. These were obtained by integrating the pixel intensities from the RoI defined by the image section nearest to the surface (green rectangle, as shown in Figure 5.9 (a)). This was chosen as the relative position of the RoI with respect to the surface, and the width (30 pixels, corresponding to ~4.8 mm in real space) and length of the section, provide the closest available approximation to the detection region probed by the single-point detection set-up. The integrated pixel intensities were then plotted as a function of their discharge-probe delay, as outlined in Section 5.3.5. The profiles were peak-normalized to the integrated pixel intensity at a delay corresponding to the peak of the incident beam, and shown in Figure 5.19.

Although the TOF profiles shown in Figure 5.19 are not directly comparable with the with profiles obtained from the single-point detection set of experiments shown in Figures 4.7 and 4.8, a quick comparison between the two sets shows that they both follow the same qualitative trends in the magnitude of scattered OD signal, further supporting the conclusions derived in the previous chapter. However, unlike the data obtained in Chapter 4, the profiles with the PFPE surface in were found to not be

entirely reproducible between the sets acquired alongside the two organic liquids under all experimental conditions probed, as evidenced by the difference in the profiles shown for the results with the He carrier in Figure 5.19. As of writing, it has not been determined whether this difference between the scattered OD profiles from PFPE are within error of each other, or whether there have emerged as a result of differences in the position of the liquid surface between set of experiments.

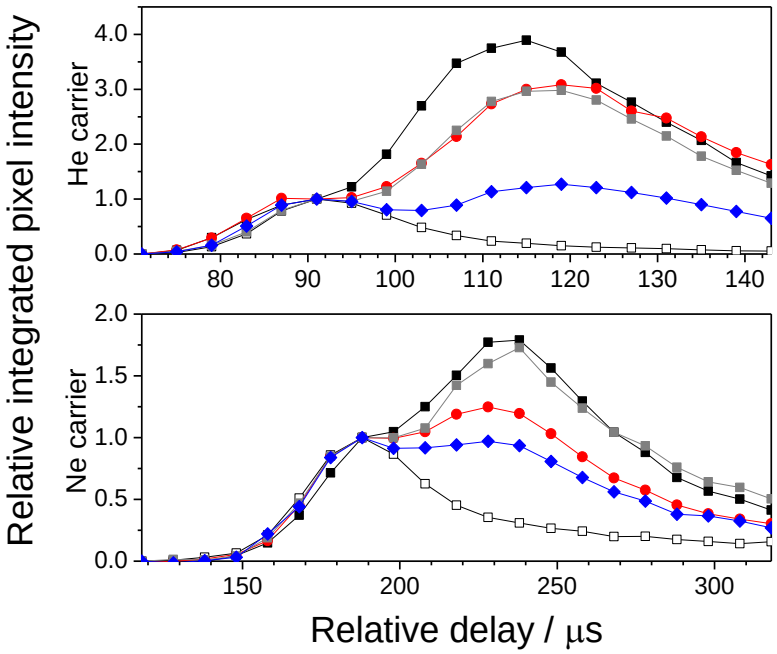

Figure 5.19: Representative TOF profiles of the OD A-X (1,0) $Q_1(6)$ LIF transition as a function of discharge-probe delay for the He (top) and Ne (bottom) carrier, scattered off the surfaces at normal incidence. Each point is obtained by integrating the pixel intensities of the near image section (green rectangle, Figure 5.9 (a)). The incident beam with no liquid surface present is represented by open circles. The remaining profiles include scattered signals with a liquid surface present: PFPE (black squares and grey squares, taken in parallel with the squalane and squalene data, respectively), squalane (red circles) and squalene (blue diamonds). All profiles have been normalized to the integrated pixel intensities at 87 μs (He) and at 178 μs (Ne).

To establish whether the radicals scatter off the surface with IS or TD-like trajectories, the speeds of scattered OD radicals were obtained using the proof-of-concept method described in Section 5.3.5, with RoIs of 30 x 30 pixels as shown in Figure 5.10. Due to

time constraints, the analysis was restricted to studying OD radicals, which were scattered off the surfaces from normal incidence, and probed on the normal incidence final scattering angle with respect to the focus point of the molecular beams. Furthermore, the analysis was limited to studying OD radicals on the $Q_1(6)$ transition, which is the highest common transition probed with the two carrier gases. The choice of analysing the results at the higher N level was motivated by two reasons. The first was that the OD radicals scattering with IS-like trajectories are more likely to populate the higher rotational levels, as observed previously in the literature [10-12] and in the results obtained in Chapter 4. As for the second reason, a preliminary attempt at obtaining the scattered OD profiles at the lower N levels from a straight subtraction of the incident beam contribution from the profiles with surface in resulted in large subtraction errors appearing in the profile. These subtraction errors are consistent with an attenuation of the incident OD LIF signal when the surface is present in the main chamber, as previously observed with the single-point detection set-up (Chapter 4, Section 4.4.1) for the $N = 2$ level. Due to time constraints, the statistical uncertainty in the raw TOF profiles was not determined. This made it difficult to establish the correction factor required to adjust the incident OD profile to remove the subtraction errors from the scattered OD profiles, as done in the previous chapter. As such, the TOF profiles analysis was not attempted at the lower N levels.

From the TOF profiles obtained by integrating the 30 x 30 pixel RoIs, the peak arrival time was obtained and plotted against the average distance of the RoI from the edge of the sheet. The speeds of OD off the liquid surfaces were then derived from the slope of a fitted straight line through the points (Figure 5.20), and expressed in standard SI units in Table 5.2 after applying the appropriate conversion factor determined in Section 5.3.7. For the purposes of comparison, the most probable Maxwell-Boltzmann speed of OD radicals with TD-like trajectories was estimated using the prescriptions of Atkins [263], via the equation:

$$c^* = \sqrt{\frac{2RT}{M}} \tag{5.3}$$

where c^* is the most probable Maxwell-Boltzmann speed, R is the gas constant, T is the temperature of the liquid surface, and M is the weight of the gas phase species, in this case OD radicals. Assuming the temperature of the surface is the same as the

temperature of the laboratory at 295 K, the most probable speed was determined to be 522 m s^{-1}. A plot of the distance travelled over time at the most probable TD speed was included in Figure 5.20.

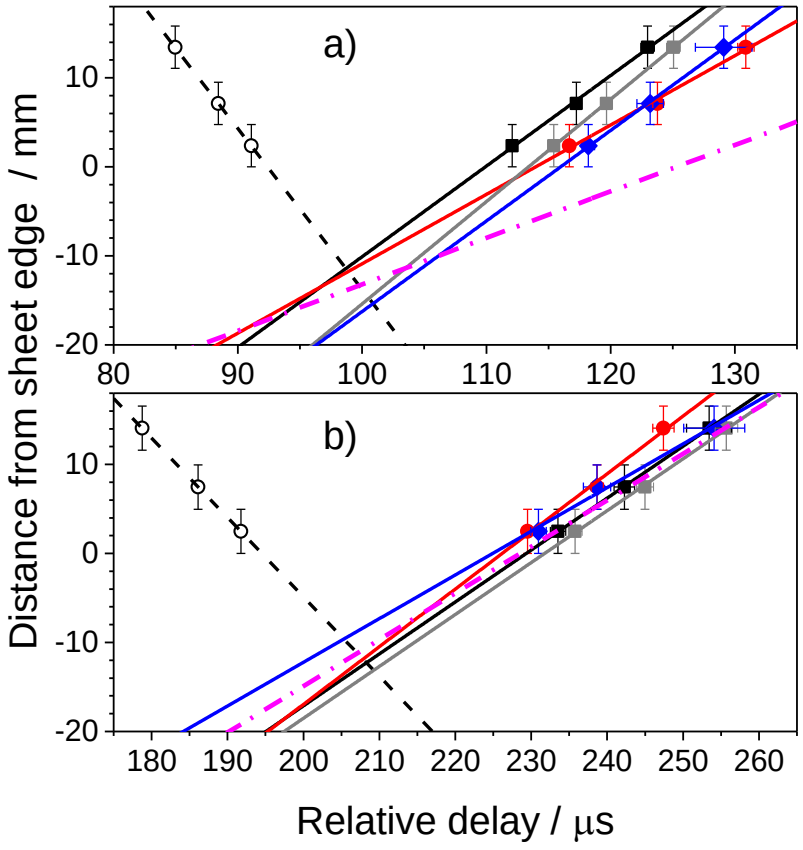

Figure 5.20: Plots of peak arrival times over distance from the edge of the sheet, derived as described in the text, with associated linear fit to each set of points, indicating the speeds of the radicals probed. Data shown are: incident OD acquired on the $Q_1(1)$ transition (dashed black line), and the scattered OD acquired on the $Q_1(6)$ transition, from PFPE (Black line acquired with squalane, Grey line acquired with squalene), squalane (red line), and squalene (blue line). All data was obtained on the normal incidence final scattering angle with respect to the focus points of the molecular beam. Dot-Dashed magenta line represents most probable speed of TD projectiles, centred at the average delay at which all four scattered OD lines intersect the incident OD line.

Liquid surface	**He carrier (a) / m s^{-1}**	**Ne carrier (a) / m s^{-1}**
PFPE	1018 ± 55	583 ± 9
Squalane	779 ± 64	648 ± 64
PFPE 2	1149 ± 25	583 ± 23
Squalene	1017 ± 37	491 ± 53
TD speed (b)	522	522
a) Errors are propagated from the errors in the linear fit; b) Reference speed of OD scattered with TD-like trajectories, derived from the most probable Maxwell-Boltzmann speed calculated via Equation (5.3)		

Table 5.2: Table of OD speeds scattered off the liquid surfaces, derived from the slopes of the linear fits shown in Figure 5.20 and converted to standard SI units using the pixel-to-real space conversion factor determined in Section 5.3.7

Considering first the results obtained using the He carrier, both Figure 5.20 and Table 5.2 show that the speeds of scattered OD off all liquid surfaces is significantly higher than the predicted speed for TD projectiles, indicating that a significant proportion of OD radicals is scattering via an IS-like mechanism. Further confirming this suggestion are the differences in the speeds of OD when scattered off different liquid surfaces, which is lowest for squalane and highest for PFPE, with squalene assuming a value close to that of PFPE. These differences are consistent with the subtle differences in the TOF profiles noticed from the single-point detection results, as described in Chapter 4, Section 4.5.1. As for the results obtained using the Ne carrier, the speeds appear to be slightly higher than, yet still close to the estimated speed of the TD projectiles. This indicates that the mechanism with which OD scatter of the liquid surfaces at the low collision energy cannot easily be determined on the basis of the speeds obtained from this proof-of-concept analysis alone, requiring further analysis of the angular distribution of the scattered radicals described in the following sections.

Additional information related to the reproducibility of the measurements may also be obtained by assuming that the point at which the lines fitted to the incident and scattered OD data in Figure 5.20 intersect represent the position and the delay at which the incident radicals arrive at the liquid interface. From the figure, the average position

where the lines intersect was determined to be ~ -12 mm, indicating that the surface is located at ~12 mm from the edge of the detection region, as defined by the instrument function. As for the average delay at which OD arrives at the surface, this was determined to be ~ 100 μs for the data with the He carrier, and 207 μs for the data with Ne. The arrival time for the He data is consistent with the predicted arrival time of 100 μs, obtained by assuming the incident OD travels the valve-to-surface distance of 180.5 ± 1.0 mm (Section 5.2) at the average speed determined in Chapter 4 Section 4.3. As for the Ne results, the experimental arrival time differs from the predicted arrival time of 202 μs by 5 μs, suggesting that the incident OD has travelled an additional ~ 4.5 mm to reach the surface. These results suggest that a) the width of the detection region in real space is not the same as the apparent width of the probe sheet measured outside the chamber, corroborating the observations described in Section 5.3.7, and b) the liquid surface was not placed consistently at the focal point of the molecular beams between measurements. The latter point would also explain the fact that the fitted lines from different liquid surfaces shown in Figure 5.20 intersect the incident OD at different points, as well as the differences in the magnitude of scattered OD signal from the two sets of PFPE data shown in Figure 5.19. It is also possible that the pixel-to-real space conversion factor obtained for the Ne carrier is being overestimated, which could be due to the fact that incident OD radicals seeded in Ne are travelling slower than expected from the incident beam characterization in Chapter 4. Further analysis of the results will be required to determine the extent of the variation in the position of the surface between data acquisition sets, and thus the effect it has on the angular distribution of the scattered radicals.

5.4.3 Slices from image sections: incident OD

In the following sections, the incident and scattered OD LIF signal will be analysed using the slices parallel to the liquid surface, obtained at selected discharge-probe delays from the image sections (Figure 5.9 (a)), as described in section 5.3.4. The analysis of the incident OD data will be discussed in this section, whereas the scattered OD results will be discussed in the next section.

The angular resolution of the OD projectiles that scatter off a given liquid surface is dependent on the dosed area on the surface which can act as starting points for the OD scattered trajectories. The dosed area can be determined from the width and the shape

of the incident OD packet at the point the packet hits the surface. If the dosed area is sufficiently narrow, then in principle the angular distribution of IS and TD-like trajectories could be predicted via a simple theoretical model that assumes all scattered OD trajectories emerge from a single point on the surface. The larger the target area on the surface, the more 'blurred' the angular distribution of IS and TD-like trajectories will be. Further complicating the issue is the fact that, at normal incidence, the target area of the surface will be circular and cylindrically symmetric, whereas at 45° incidence, the area will have an elliptical shape, with the major axis being larger than the diameter of the dosage area at normal incidence by a factor of $\sqrt{2}$.

The target area hit by the incident OD radicals could be estimated by obtaining the FWHM from slices of the incident beam from different carrier gases arriving at normal incidence to the surface, at the delay corresponding to the peak of the TOF profiles taken from the image sections (as done in Figure 5.14), and then plotting them as a function of their distance from the edge of the sheet (Figure 5.21). The rate of expansion of the FWHM and the FWHM of the beam at the edge of the sheet closest to the surface can be obtained from the slope and the intercept of a linear fit through those plots, respectively. Those parameters can then be used to estimate the FWHM of the beam at the liquid surface, assumed to be at 12 mm from the edge of the sheet based on the TOF profile analysis described in the previous section. For the purpose of this discussion, this analysis will be restricted to incident OD arriving at normal incidence, though similar arguments will apply to the data from 45° incidence after accounting for the larger target area.

The linear fit parameters, and the estimated FWHM of the incident OD packet at the surface, are shown in Table 5.3 below. The table shows that the predicted FHWM of the incident OD packet arriving at normal incidence to the surface is 7.1 ± 0.1 mm for the He carrier and 16.7 ± 0.2 mm for the Ne carrier. Both values are larger than the diameter of the dosage area on the surface estimated in Section 5.2 (~ 5 mm for the He carrier, and ~ 7 mm for Ne), with the FWHM of OD seeded in Ne being larger by more than a factor of 2. Interestingly, the rate of expansion of the FWHM of the beam over distance from the two sets of data appear to be the same within error. This suggests that the different widths of the incident OD packet may be due to OD having different transversal speeds in the packet that are dependent on the carrier gas used.

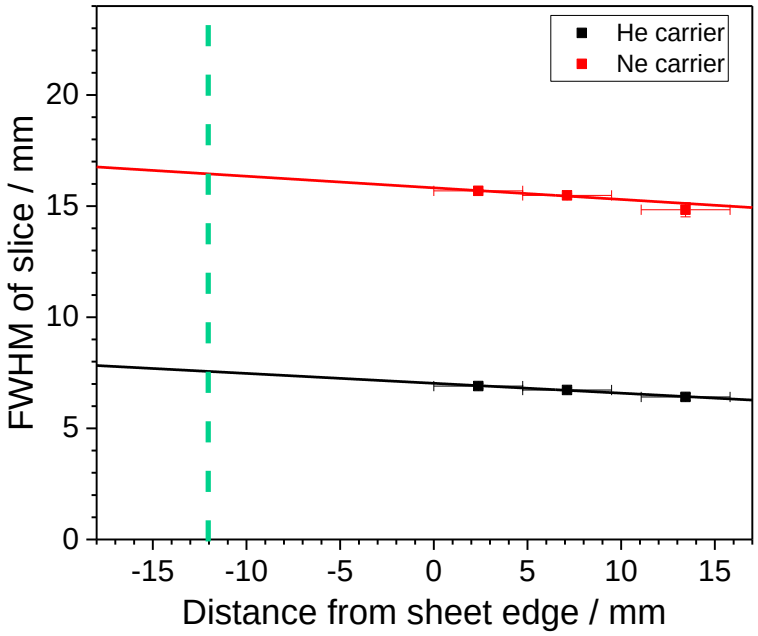

Figure 5.21: Plot of FWHM of the slices from image sections over distance from the edge of the sheet, where the distance increases away from the liquid surface. Plots include the linear fit to the FWHM for each set. The FWHM data were extracted from slices taken on the $Q_1(2)$ transition for incident OD at normal incidence with respect to the surface, at the delays corresponding to the peak of the TOF profile obtained from each image sections, using He (black) and Ne (red) as the carrier gas. Green dashed line indicates the position of the surface, assumed to be at -12 mm with respect to the edge of the sheet as described in the text.

Carrier gas	Slope (a)	Intercept (a) / mm	FWHM at surface / mm
Helium (b)	-0.044 ± 0.005	7.0 ± 0.1	7.1 ± 0.1
Neon (c)	-0.052 ± 0.017	16.6 ± 0.2	16.7 ± 0.2
a) Errors are derived by propagating the errors from individual linear fits, using an instrumental weighting of errors in the data; b) Using a conversion factor of (1.58 ± 0.02) x 10^{-4} m $pixel^{-1}$; c) Using a conversion factor of (1.66 ± 0.02) x 10^{-4} m $pixel^{-1}$			

Table 5.3: Table of parameters of the linear fit to the data shown in Figure 5.21, and predicted FWHM of the incident OD packet at the surface

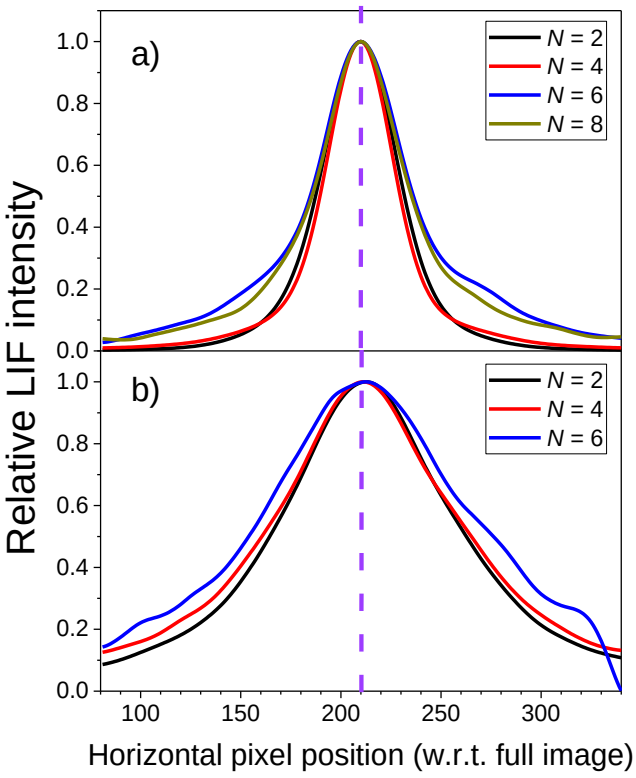

Figure 5.22: Representative slices obtained from the central image sections (Figure 5.9 (a), orange rectangle) from images of the incident OD arriving at normal incidence to the surface, taken at 87 μs with the He carrier (a) and at 178 μs with the Ne carrier (b). Slices were probed on N = 2, 4, 6, and 8 for He, and N = 2, 4, and 6 for Ne, as indicated in the figure legends. The instrument function correction was applied to the images prior to acquisition of the slices from each image section. Dashed purple line indicates the axis normal to the surface, centred at the focus point of the incident beams.

The above estimate of the FWHM of the OD packet on the surface assumes that the beam is well collimated at all rotational levels probed. To test this assumption, representative slices obtained from the central image section of the image (Figure 5.9, orange rectangle) at all rotational levels probed were peak normalized and plotted in Figure 5.22. The figure shows that there are small differences in the width of the slices as a function of N level, with a noticeable difference emerging between N = 4 and N = 6 for both carrier gases, indicating that the radicals at higher rotational levels has a slightly faster transversal speed. However, while the differences affect the entire slice when using the Ne carrier, the slices obtained with the He carrier show that the core part

of the incident OD packet has a similar width at all rotational levels probed. This may be explained, in part, by the higher transversal speed of OD at the higher rotational levels. Another possibility is that the extra OD signal around the core packet is a result of the attenuation of the beam at low rotational levels when the surface is present in the main chamber (discussed in the previous section and in Chapter 4), resulting in gas-phase collisions leading to an increase of the rotational temperature of incident OD. In any case, these differences are unlikely to have a major effect on the scattered OD signal detected, as the vast majority of scattered OD signal detected at the higher N levels will have emerged from energy transfers from incident OD at the lowest rotational levels after collisions with the surface.

5.4.4 Slices of image sections: Scattered OD

In this sections, the analysis will focus on the slices obtained at delays where the scattered OD from the liquid surfaces are present. In these slices, the ingoing beam contribution was subtracted from the corresponding sequence of images with the surface in, as described in section 5.3. Due to time constraints, the analysis will be restricted to the data acquired on the N = 2 and 6 levels of the Q_1 branch, chosen as representative of OD scattering at a low and high rotational level from the surface. Although data were acquired for N = 8 at the higher collision energies, data from N = 6 were chosen to provide a direct comparison with those obtained at the lower collision energy. The instrument function correction of the corresponding N level probed was applied to the raw data prior to extraction of the slices.

As discussed in the previous section, the angular resolution of scattered OD from a given surface will be determined by how well collimated the incident beam is prior to hitting the surface. This can be determined by comparing the FWHM of the incident and scattered OD slices obtained from different image sections. A visual representation of the differences between the two sets of slices is shown in Figure 5.23.

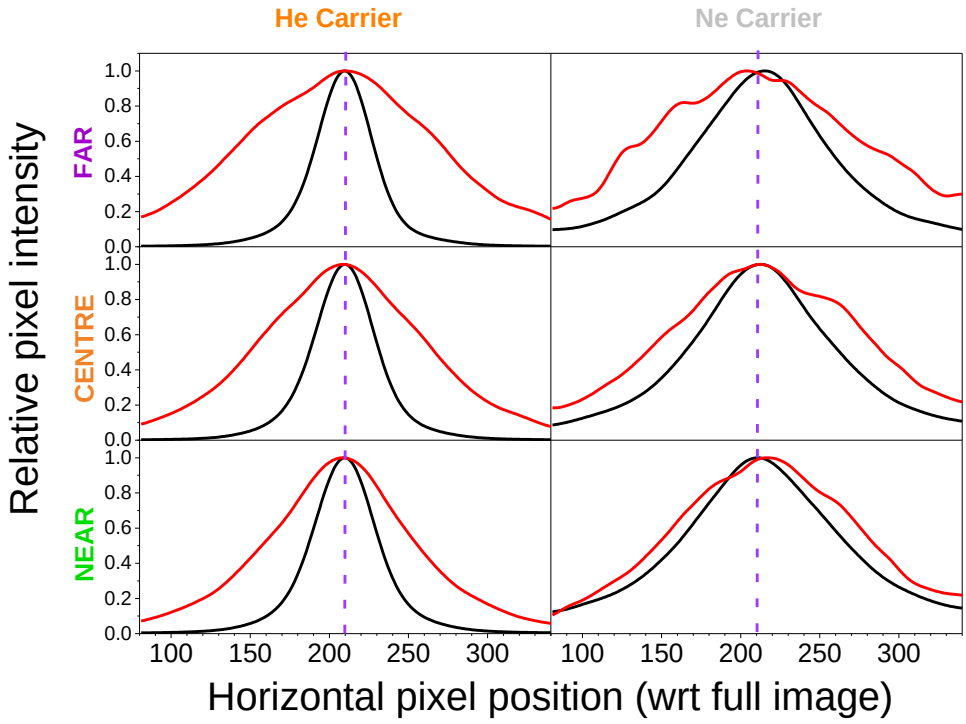

Figure 5.23: Representative peak normalized slices of OD LIF signal comparing the incident OD (black) and OD scattered off PFPE (red), using He (left) and Ne (right) as the carrier gas, extracted from the image sections shown in Figure 5.9 (a). Incident OD slices were acquired on the $Q_1(2)$ transition at 87 µs (He) and 178 µs (Ne) delay, whereas scattered OD slices were acquired on the $Q_1(6)$ transition at 115 µs (He) and 228 µs (Ne) delay, after subtracting the incident beam contribution. The pixel intensities in the slices have been corrected for the corresponding instrument function, after subtraction of the background noise. Dashed purple line indicates the axis normal to the surface, centred at the focus point of the incident beams.

From a quick comparison of the slices presented in Figure 5.23, it is clear that the distribution of scattered OD is generally broad, regardless of the distance from the sheet edge. It is also apparent that there are noticeable differences in the FWHM of the incident and scattered OD slices and that the difference in the distribution of OD between slices increases as a function of the distance from the edge of the sheet. This is especially noticeable in the results obtained at the higher collision energy and would suggest that any differences in the slices obtained from normal incidence and 45° incidence will likely be a result of dynamical effects influencing the scattered OD, after accounting for the differences in the dosage area of the surface. This will be discussed

later in this section. While there are differences in the FWHM between the slices obtained at the lower collision energy, these are considerably smaller than the results from the higher collision energy, with the slices probed closer to the surface almost overlapping. This indicates that the angular distribution of scattered OD from the liquid surfaces using the Ne carrier will be significantly less well resolved than the results obtained with the He carrier, and that any dynamical differences in the scattered trajectories, if present, would not be easily distinguished from the changes in size of the dosage area between normal and 45° incidence.

For the rest of this section, the analysis of the slices will primarily focus on the peak normalized scattered OD slices obtained from each image section, angle of incidence, and liquid surface studied. The slices were obtained at the delays of 115 and 127 μs at the high collision energy, and at 228 and 258 μs at the low collision energy, for each of the liquids probed. With regards to the PFPE results, only the first set of data obtained chronologically for each of the conditions probed is shown. The rotational levels probed were N = 2 (Figures 5.24, 5.26 and 5.28 for PFPE, squalane, and squalene, respectively), and N = 6 (Figures 5.25, 5.27 and 5.29, also for PFPE, squalane, and squalene, respectively).

The most obvious feature of interest from the slices shown in all figures between Figure 5.24 and Figure 5.29 below is that they confirm that the distribution of OD signal is broad regardless of the carrier gas used, the angle of incidence, the liquid surface, or the rotational level probed. The sole exception is in Figure 5.19, showing the results of OD scattered off squalane at the higher collision energy and probed on N = 2, which is considerably narrower than other scattered OD slices. However, this is likely a result of the scattered OD signal appearing at later delays than expected due to the surface not being placed at the focus point of the molecular beams during the data acquisition, as discussed in Section 5.4.2.

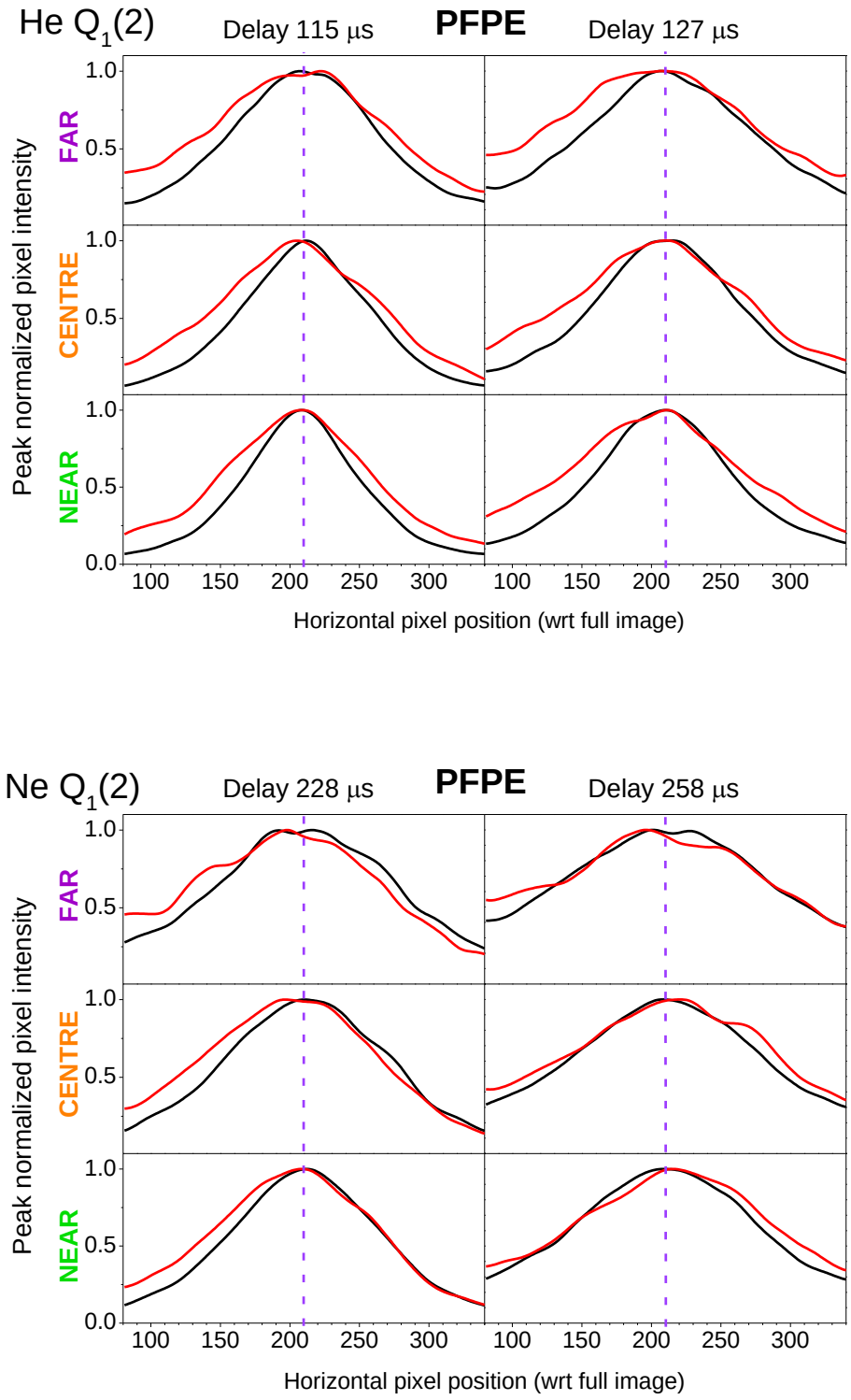

Figure 5.24: Peak normalized horizontal slices of OD LIF signal scattered off PFPE using He (top set) and Ne (bottom set) as the carrier gas, probed at the $N = 2$ level at selected delays. The pixel intensities in the slices have been corrected for the corresponding instrument function. OD was scattered from the surface at Normal incidence (black line) and at 45° (Red line). Dashed purple line indicates the axis normal to the surface, centred at the focus point of the incident beams.

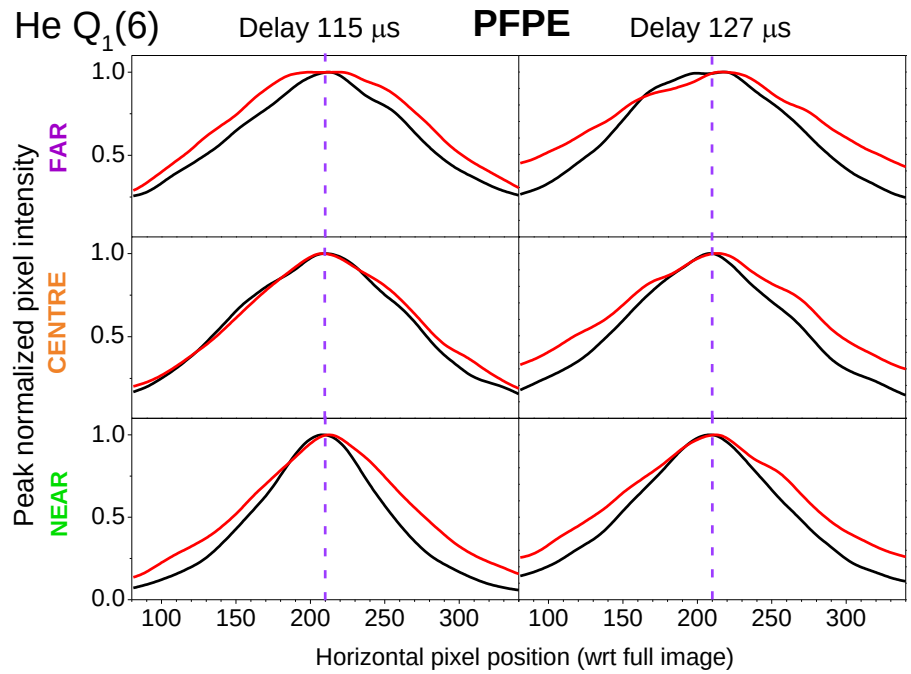

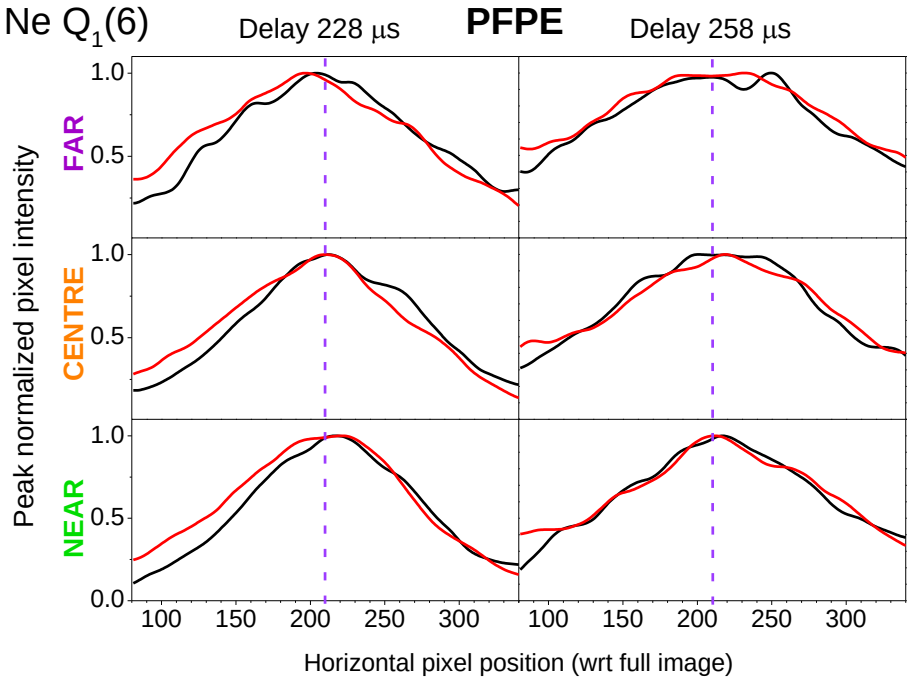

Figure 5.25: Peak normalized horizontal slices of OD LIF signal scattered off PFPE using He (top set) and Ne (bottom set) as the carrier gas, probed at the $N = 6$ level at selected delays. The pixel intensities in the slices have been corrected for the corresponding instrument function. OD was scattered from the surface at Normal incidence (black line) and at 45° (Red line). Dashed purple line indicates the axis normal to the surface, centred at the focus point of the incident beams.

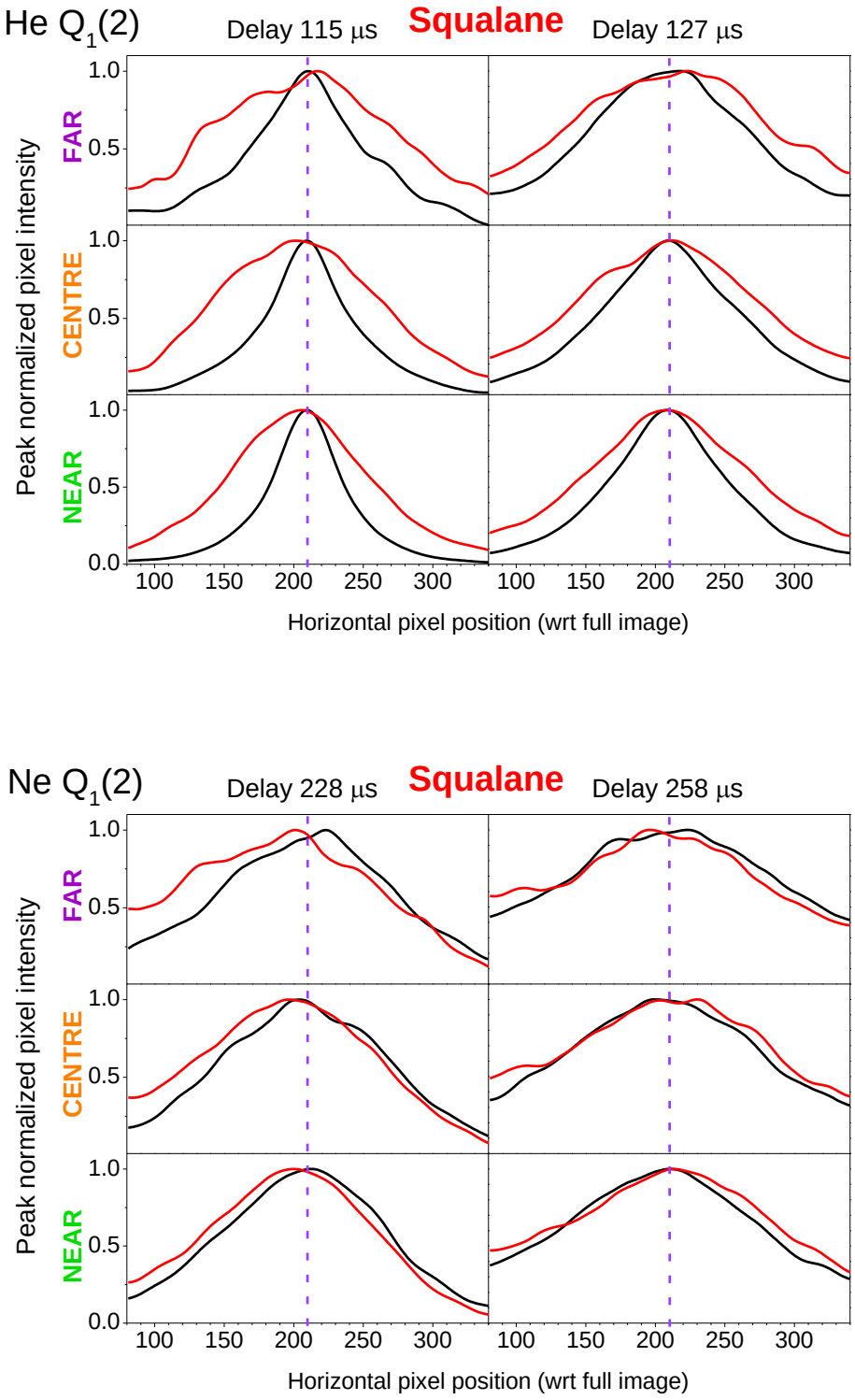

Figure 5.26: Peak normalized horizontal slices of OD LIF signal scattered off squalane using He (top set) and Ne (bottom set) as the carrier gas, probed at the $N = 2$ level at selected delays. The pixel intensities in the slices have been corrected for the corresponding instrument function. OD was scattered from the surface at Normal incidence (black line) and at 45° (Red line). Dashed purple line indicates the axis normal to the surface, centred at the focus point of the incident beams.

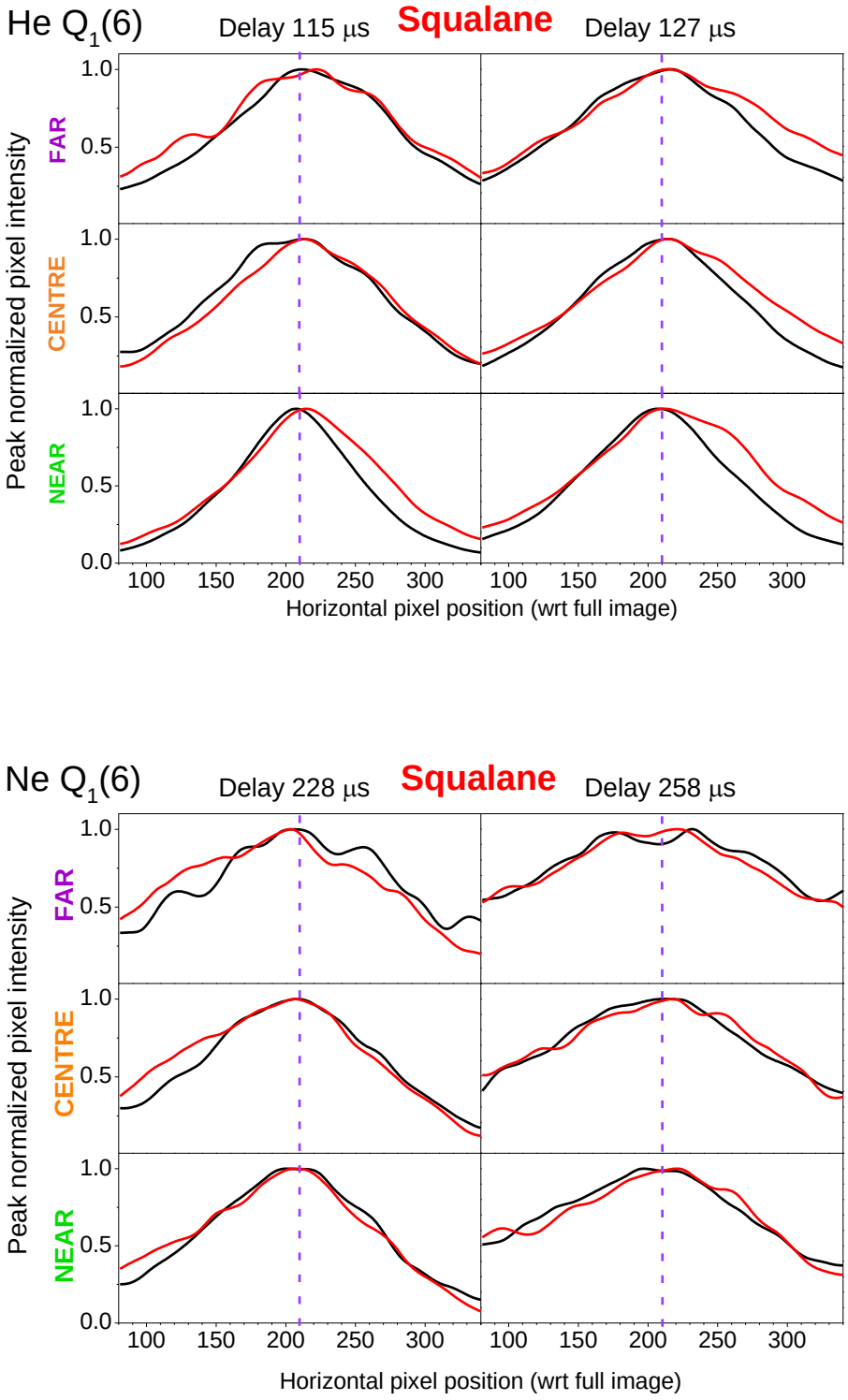

Figure 5.27: Peak normalized horizontal slices of OD LIF signal scattered off squalane using He (top set) and Ne (bottom set) as the carrier gas, probed at the $N = 6$ level at selected delays. The pixel intensities in the slices have been corrected for the corresponding instrument function. OD was scattered from the surface at Normal incidence (black line) and at 45° (Red line). Dashed purple line indicates the axis normal to the surface, centred at the focus point of the incident beams.

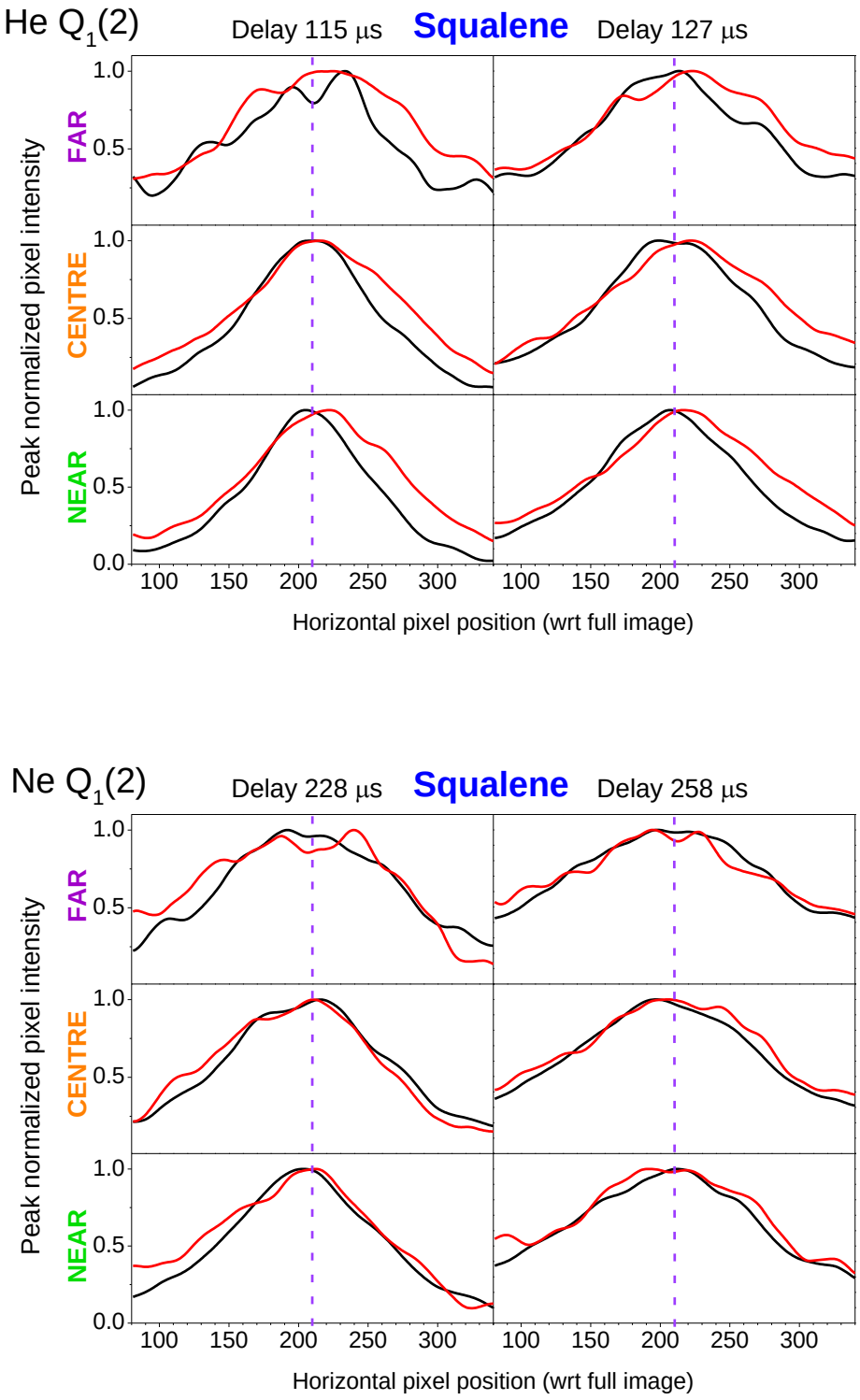

Figure 5.28: Peak normalized horizontal slices of OD LIF signal scattered off squalene using He (top set) and Ne (bottom set) as the carrier gas, probed at the $N = 2$ level at selected delays. The pixel intensities in the slices have been corrected for the corresponding instrument function. OD was scattered from the surface at Normal incidence (black line) and at 45° (Red line). Dashed purple line indicates the axis normal to the surface, centred at the focus point of the incident beams.

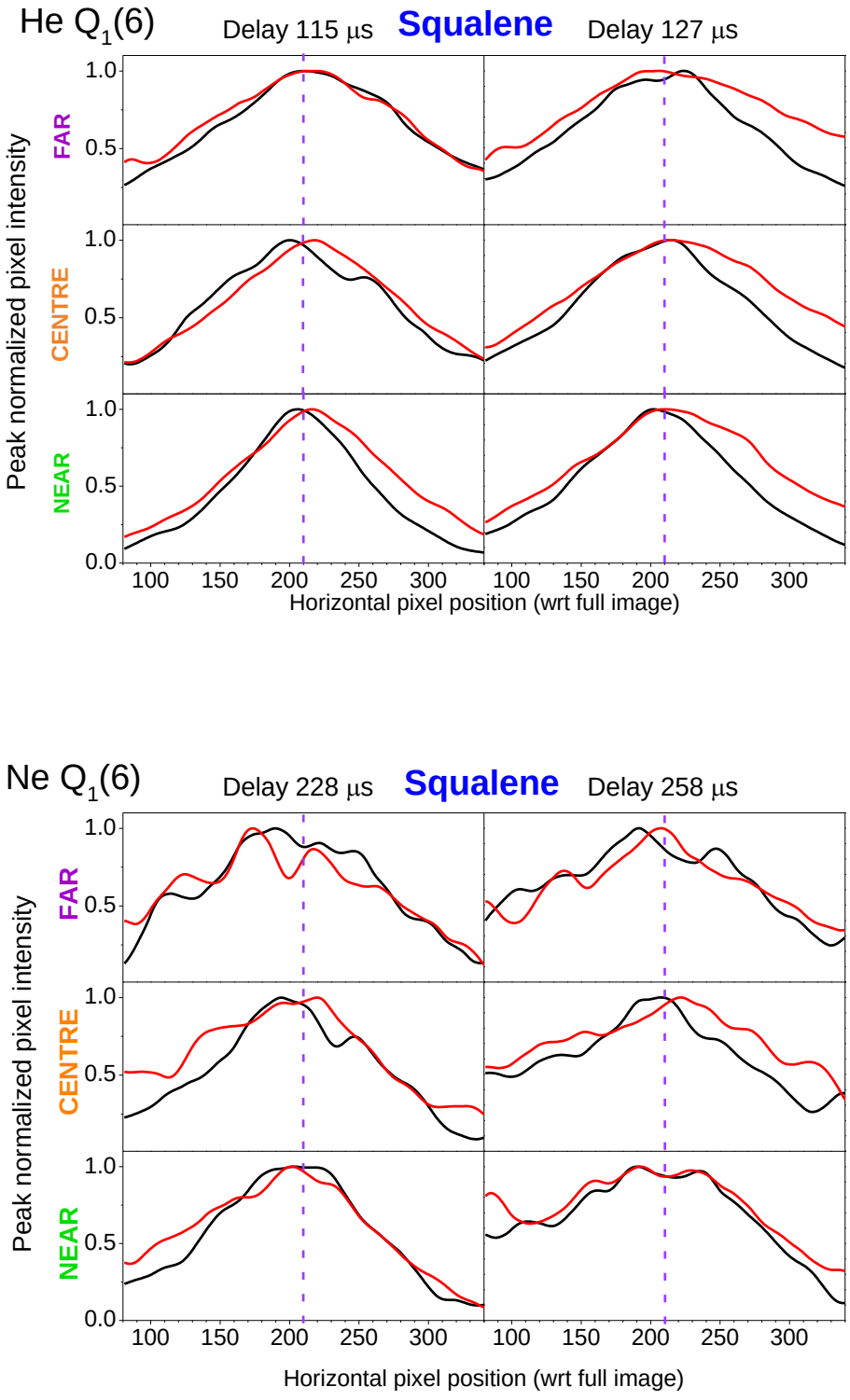

Figure 5.29: Peak normalized horizontal slices of OD LIF signal scattered off squalene using He (top set) and Ne (bottom set) as the carrier gas, probed at the $N = 6$ level at selected delays. The pixel intensities in the slices have been corrected for the corresponding instrument function. OD was scattered from the surface at Normal incidence (black line) and at 45° (Red line). Dashed purple line indicates the axis normal to the surface, centred at the focus point of the incident beams.

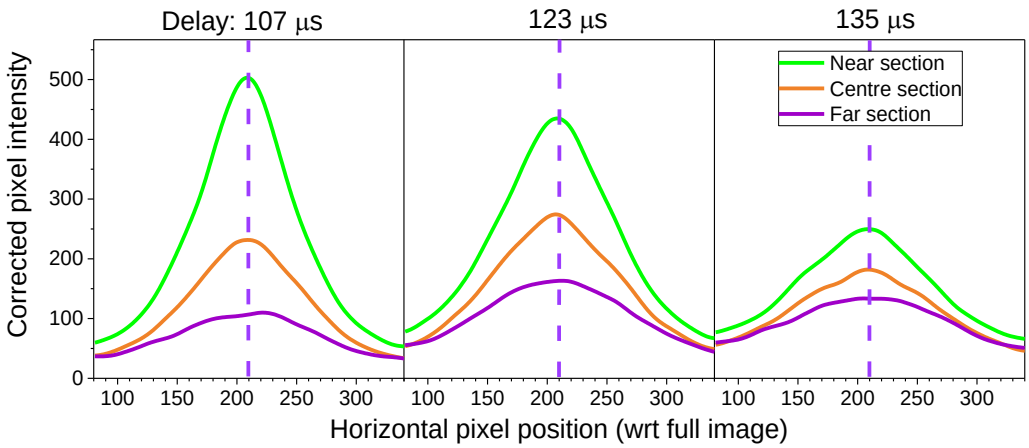

Figure 5.30: Representative slices of image sections (as shown in Figure 5.9 (a)) from images of scattered OD (after subtraction of the incident beam contribution) from normal incidence off the PFPE surface at selected discharge-probe delays. OD was probed on the $Q_1(6)$ transition. The pixel intensities in the slices have been corrected for the corresponding instrument function. Dashed purple line indicates the axis normal to the surface, centred at the focus point of the incident beams.

The fact that OD scatters off the liquid surfaces with a wide range of scattering angles in the plane of detection regardless of the conditions probed also indicated that a significant proportion of the radicals will be scattering outside of the plane of detection. As a result, the peak signal intensity in the slices will always be in the data obtained from the image section nearest to the surface and becomes progressively lower when looking at image sections further away from the surface. Furthermore, this decrease in the OD signal as a function of distance from the surface will be retained even at later delays in the corresponding sequence, with the signal in the far and centre image sections never reaching the same peak in signal size from image sections closer to the surface. This was indeed proven to be the case under all conditions probed, as demonstrated in the representative slices shown in Figure 5.30. As the scattered OD from normal angle of incidence is expected to be cylindrically symmetric with respect to the dosage area on the surface, it would be possible, in principle, to determine how rapidly the OD spreads out of the plane of detection, and thus predict by how much the OD LIF signal is expected to fall over distance, via appropriate theoretical models that take into account of the IS and TD-like trajectories of the scattered projectiles. As of writing, the theoretical modelling for the image acquisition results is not yet available,

and so the predicted decrease in scattered OD density as a function of distance from the surface was not attempted.

It is also apparent from all the slices in the figures between Figure 5.24 and Figure 5.29 that the overall peak of the slices is always centred around the axis normal to the surface, after accounting for errors in the cubic spline fit due to the low signal present. If the OD radicals were scattering with strongly directed IS-like trajectories, then there would be a sequential movement of the peak of the slice towards a preferred direction as a function of distance from the surface and discharge-probe delay. The fact that this is not apparent in any of the scattered OD slices shown in the figures above points towards the conclusion that the angular distribution of the scattered radicals is not strongly directed towards any final scattering angle. Nevertheless, there are small but noticeable differences between the slices taken from normal and 45° incidence that point towards some of the radicals being scattered preferentially towards a given direction. These differences are more noticeable in the results obtained from the He carrier, and especially when OD is scattered off either squalane or squalene, where there appears to be more OD LIF signal on the right of the normal axis of incidence than the left when OD is scattered at 45° incidence compared to the normal incidence results, which are symmetric along the normal axis of incidence. This would suggest that some of the OD radicals are being preferentially scattered in the same 'forward' direction as that of the specular angle with respect to the angle of incidence. Another systematic difference between the slices was observed in the data obtained when OD was scattered at 45° incidence using the He carrier and probed at the lower rotational level, and similarly when using the Ne carrier at either rotational level probed. In these slices, there appears to be more OD signal on the left of the normal axis of incidence at the earlier delays probed, which is consistent with the radicals beings scattered 'backwards' towards the source of the molecular beam. The preference towards 'back'-scattering then disappears when the radicals are probed at a later discharge-probe delay. These results are surprising, and without precedent in any of the gas-liquid scattering experiments reported in the literature. One possible explanation for these results may be ascribed to gas-phase collisions of the scattered radicals with the carrier gas atoms from earlier in the gas pulse that have scattered off the liquid surface prior to the arrival of the OD radicals, causing energy transfers that result in more OD radicals populating the *N* level probed. Further analysis, using a more refined method and suitably upgraded custom analysis program, will be required to determine whether the 'back'-scattered OD

resulted from gas-phase collisions, or from a dynamical effect of scattering off the liquid surface.

To determine whether there are any systematic differences in the scattered OD probed as a function of the different parameters presented throughout this section, the FWHM of the slices shown between Figure 5.24 and Figure 5.29 were measured by assuming the base of the slice starts at 0 pixel intensity. The FWHM values were then plotted as a function of the average distance of the image section from the edge of the sheet. Any systematic differences in the scattered OD between the conditions probed could then be determined, in principle, from a linear fit to the data points. The rate at which the FWHM expands as a function of the distance from the surface, and the size of the FWHM under the wide range of conditions probed can then be determined from a linear fit through the plotted data point. Differences in the scattered OD distribution resulting from a dynamical effect inherent from scattering off a liquid surface would be apparent from differences in the slope of the linear fit through the data points, whereas differences caused by a changed in the geometry of the dosed area can be determined from the relative differences in the intercept of the profiles. For the purposes of this discussion, only a qualitative comparison of the results will be made. The following images will show the differences in the FWHM of the profiles as a function of the rotational level probed (Figure 5.31), the angle of incidence (Figures 5.32 and 5.33), the liquids used (Figure 5.34), and the discharge-probe delay (Figures 5.31 to 5.33 only).

Comparing at first the differences between the scattered OD distribution as a function of *N* level probed (Figure 5.31), the analysis shows that almost all of the fitted lines, barring at most one exception in each set of data, appear to be parallel with respect to the same set of PFPE data analysed, and in most cases also between sets of PFPE data, with little difference between the delays probed. The results suggest that, at either of the collision energies probed, there is no reproducible systematic difference in the rate of expansion of scattered OD radical from different rotational levels. There are, however, systematic differences in the FWHM between rotational levels, with the FWHM from slices acquired at lower rotational levels being consistently smaller than the FHWM from slices acquired at the higher rotational levels from the same set of PFPE data. These differences are consistent with the small differences in size between the FWHM of incident OD taken at the same rotational levels (Figure 5.22), suggesting that the differences are due to changes in the size of the dosed area on the surface.

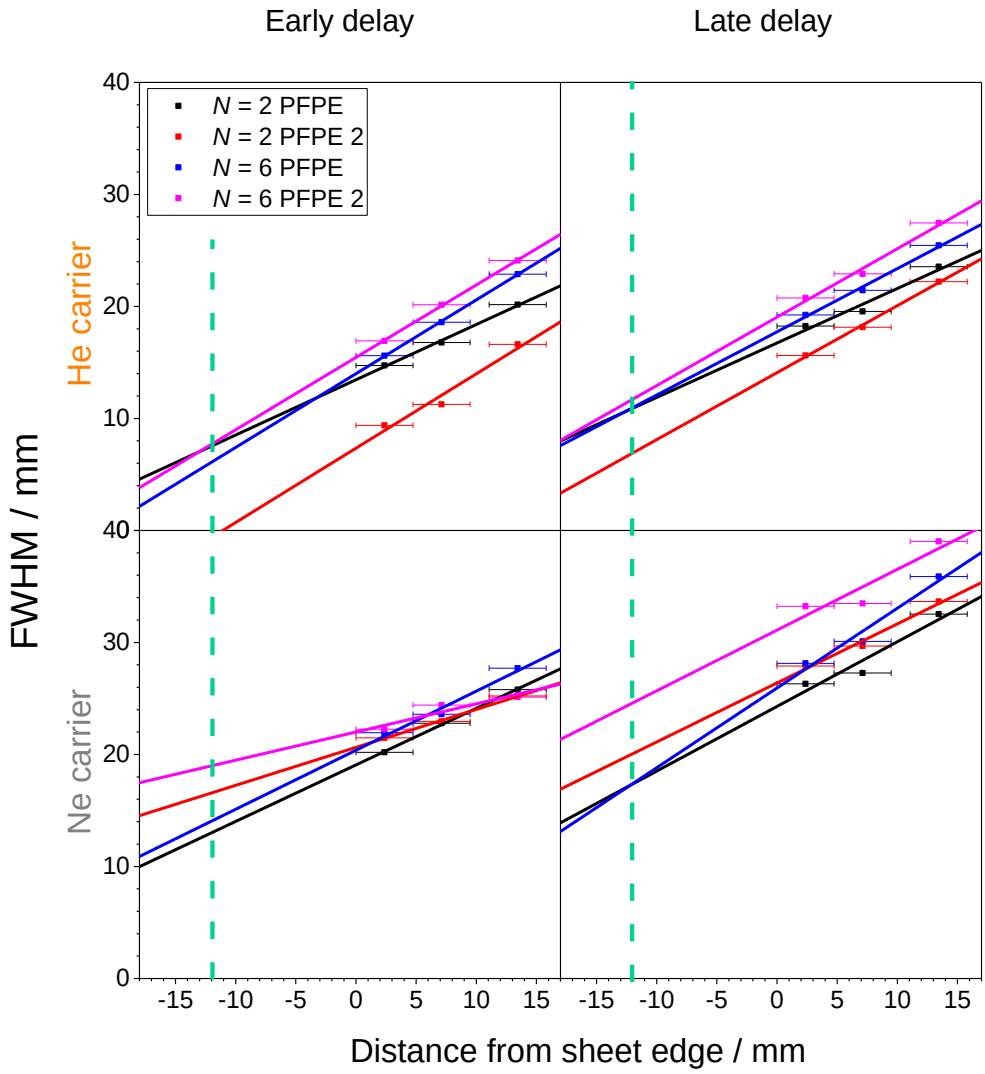

Figure 5.31: Representative plot of FWHM over distance from the edge of the sheet, where the distance increases away from the liquid surface, obtained from slices of image sections shown in Figure 5.24 and Figure 5.25. Plots include the linear fit to the FWHM for each set. The FWHM were extracted from slices taken from the two data sets of OD scattered from PFPE at normal incidence with respect to the surface, using He (top) and Ne (bottom) as the carrier gas, and probed on the $Q_1(2)$ (black and red) and $Q_1(6)$ transition (blue and magenta) at selected discharge-probe delays as described in the captions of Figure 5.24 and Figure 5.25. Green dashed line indicates the position of the surface, assumed to be at -12 mm with respect to the edge of the sheet.

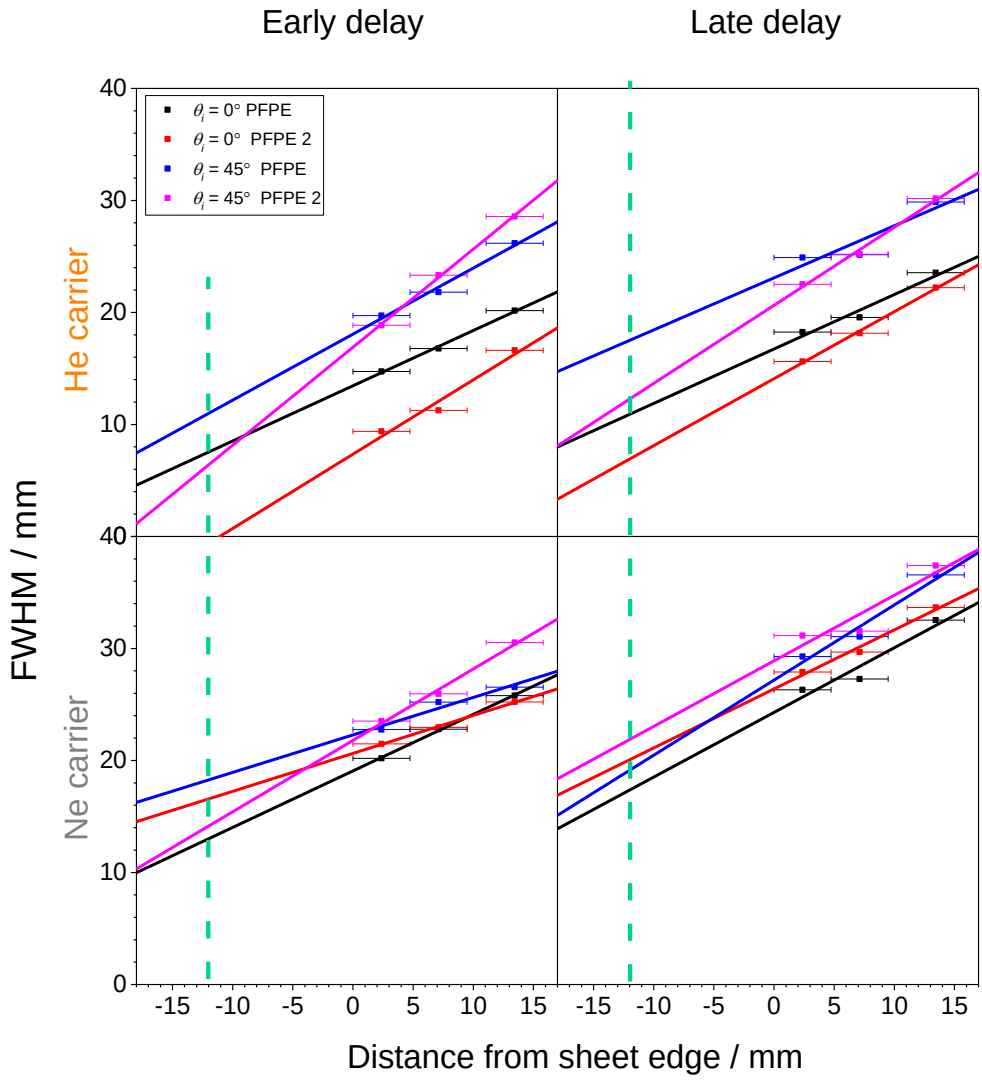

Figure 5.32: Representative plot of FWHM over distance from the edge of the sheet, where the distance increases away from the liquid surface, obtained from slices of image sections shown in Figure 5.24 and Figure 5.25. Plots include the linear fit to the FWHM for each set. The FWHM were extracted from slices taken from the two data sets of OD scattered from PFPE at normal incidence (black and red) and at 45° incidence (blue and magenta) with respect to the surface, using He (top) and Ne (bottom) as the carrier gas, and probed on the $Q_1(2)$ transition at selected discharge-probe delays as described in the captions of Figure 5.24 and Figure 5.25. Green dashed line indicates the position of the surface, assumed to be at -12 mm with respect to the edge of the sheet.

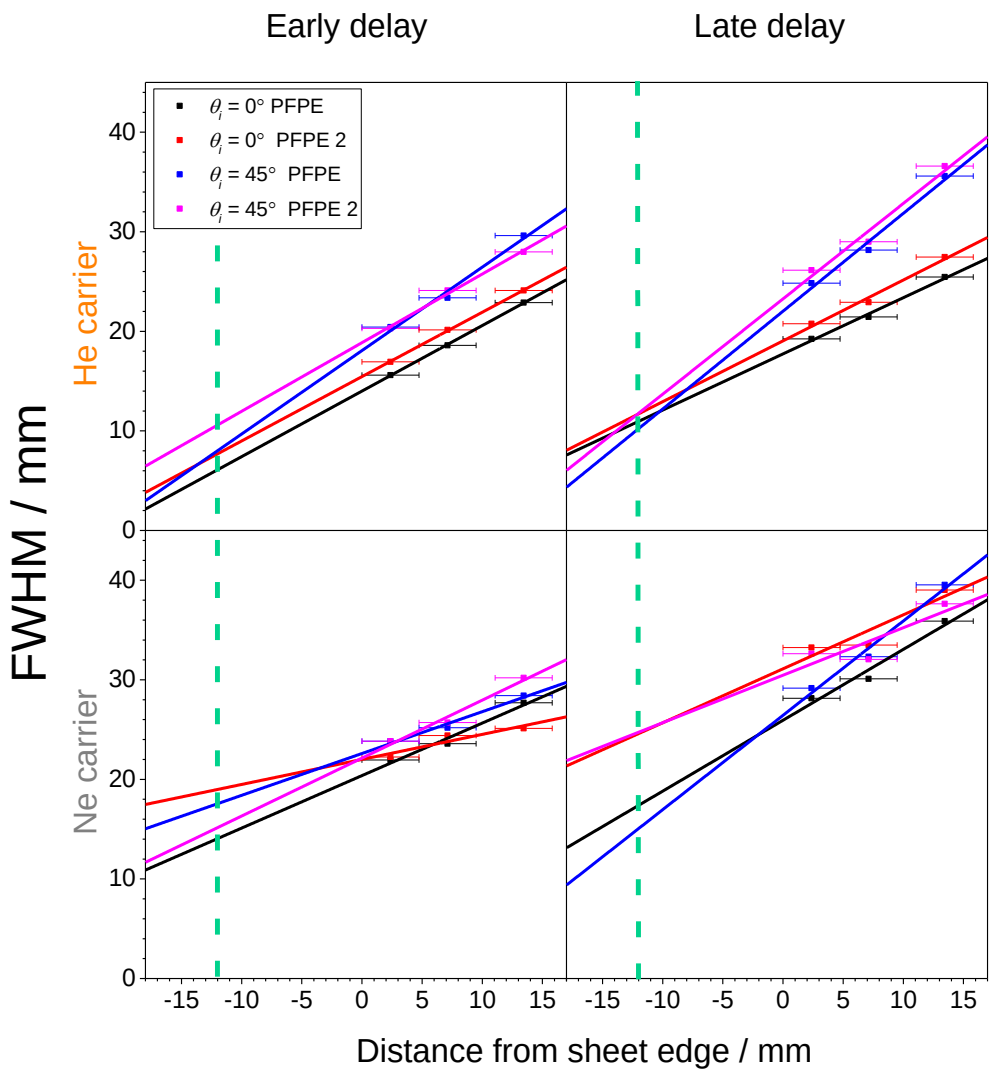

Figure 5.33: Representative plot of FWHM over distance from the edge of the sheet, where the distance increases away from the liquid surface, obtained from slices of image sections shown in Figure 5.24 and Figure 5.25. Plots include the linear fit to the FWHM for each set. The FWHM were extracted from slices taken from the two data sets of OD scattered from PFPE at normal incidence (black and red) and at 45° incidence (blue and magenta) with respect to the surface, using He (top) and Ne (bottom) as the carrier gas, and probed on the $Q_1(6)$ transition at selected discharge-probe delays as described in the captions of Figures 5.24 and 5.25. Green dashed line indicates the position of the surface, assumed to be at -12 mm with respect to the edge of the sheet.

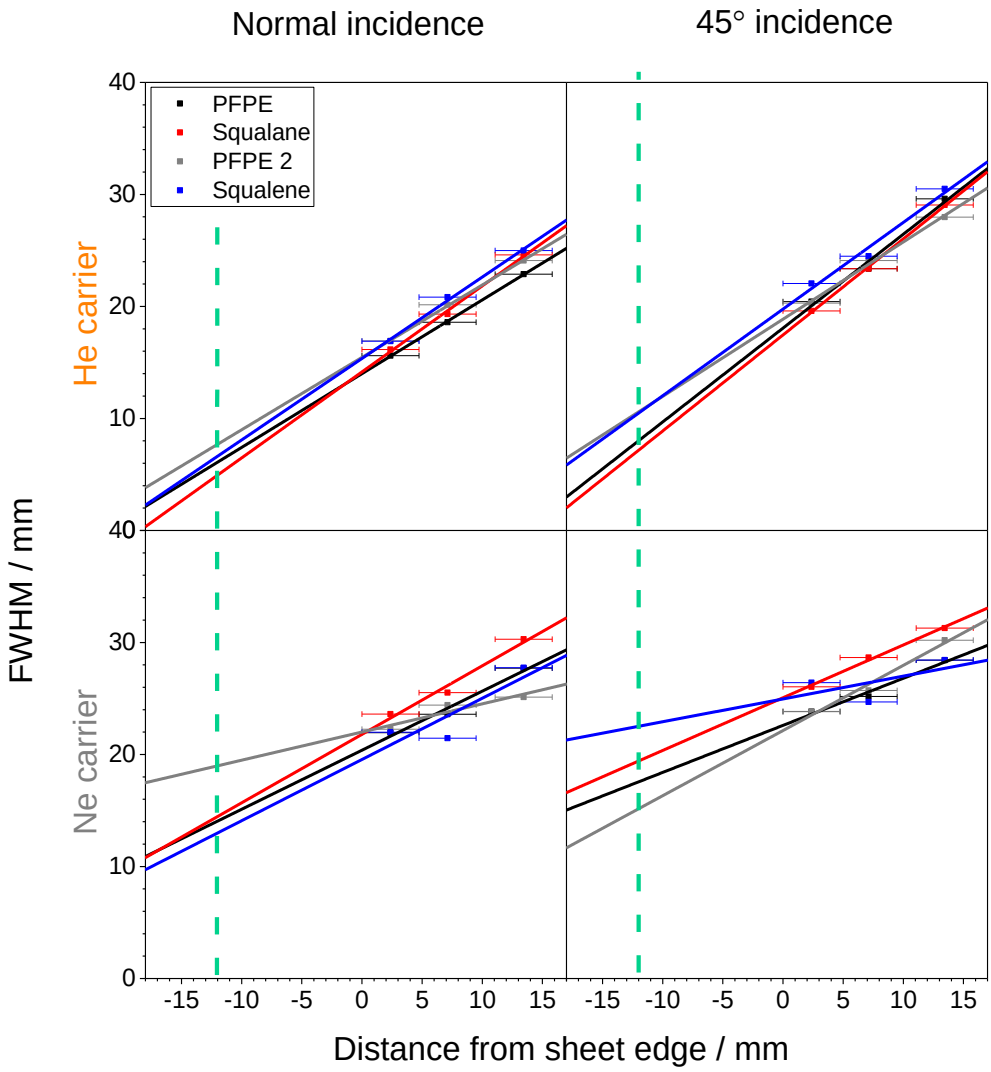

Figure 5.34: Representative plot of FWHM over distance from the edge of the sheet, where the distance increases away from the liquid surface, obtained from slices of image sections shown between Figure 5.24 and Figure 5.29. Plots include the linear fit to the FWHM for each set. The FWHM were extracted from slices taken from OD scattered off PFPE (black for data acquired alongside squalane, grey for data acquired alongside squalene), squalane (red) and squalene (blue) at both normal (left) and 45° incidence (right) with respect to the surface, using He (top) and Ne (bottom) as the carrier gas, and probed on the $Q_1(6)$ transition at the 'early' discharge-probe delay as described in the captions of the source figures. Green dashed line indicates the position of the surface, assumed to be at -12 mm with respect to the edge of the sheet.

When comparing the FWHM obtained as a function of the angle of incidence (Figures 5.32 and 5.33), the results for the He carrier data show that there are no systematic differences in the rate of expansion of the FWHM from the different sets of data at the low rotational level, after accounting for the errors in the FHWM values. There are, however, clear differences in the relative sizes of the FWHM between the two angles of incidence, with the values obtained from 45° incidence being larger than those obtained from normal incidence, suggesting the differences are due to the larger area on the surface dosed by the 45° incidence beam. At the higher *N* level, the rate of expansion of the OD radicals is clearly systematically different between data from normal and 45° incidence. These differences are clearly reproducible between the two sets of PFPE data, and appear to indicate that the rate of expansion for the 45° incidence data increases with increasing delay, whereas the data from normal incidence stays roughly the same regardless of the delay. The fact that the fitted lines from different angles of incidence appear to converge on the same FWHM at the position where the surface is expected to be suggests that the differences in the rates of expansion are due to dynamical effects in the way OD scatters off the surfaces. With regards to the Ne results, the scatter in the FWHM values obtained from the slices and their associated errors, and the lack of reproducibility between the two sets of PFPE data makes it difficult to determine whether the differences are due to any dynamical effect based on the linear fits alone. However, the fact that in all cases the relative differences of the slopes of the graphs within each set of PFPE data is small and within error would suggest that any dynamical effect on the scattering of OD at the lower collision energy is likely going to be small, if not negligible. This is supported by the considerable overlap between the slices from OD scattered at the two angles of incidence observed in Figures 5.24 and 5.25.

Finally, a comparison of the FWHM obtained as a function of the liquid surface (Figure 5.34) shows that, at the higher collision energy, there is no noticeable systematic difference in the angular distribution of OD between the different liquids, as all the fitted lines fall within error of all the different sets of data. This is observed regardless of the angle of incidence of the incoming projectiles. With regards to the data obtained at the lower collision energy, once again the scatter in the FWHM at the different distances from the surface makes it difficult to determine with any degree of accuracy if there are systematic differences between the different liquids. Nevertheless, close observation of the spread in the FWHM between different sets of data, and a careful

analysis of the slices from which the FWHM are derived from, would suggest that the differences between liquids will also be small at the lower collision energy.

5.5 Discussion

The results reported in this chapter are, to our knowledge, the first use of pLIF in a gas-liquid scattering experiment using molecular beams. This detection method allows the user to probe the inelastically scattered radicals over a wide range of final scattering angles with a single measurement, including 'back'-scattering angles in the same direction as that of the 45° angle of incidence. This is an improvement over the more conventional LIF method of resolving the angular distribution used by Nesbitt *et al.* [244], in which each final scattering angle had to be probed separately by moving the detector with each measurement. It is also an advance over the MS detection method used by Nathanson *et al.* [1-2, 4, 92, 116-120] and Minton *et al.* [68, 78, 88-91], overcoming the constraint in their experimental set-up that allows them to probe only 'forward' final scattering angles with respect to the surface normal, in addition to providing information on the internal energy distribution of the radicals probed.

This discussion of the results will focus on the scattered OD data obtained for $N = 2$ and $N = 6$, which correspond to the lowest and highest common rotational level probed at both collision energies and from both angles of incidence. The analysis presented in this chapter was obtained with proof-of-concept custom-analysis programs, used to determine the best method to extract a full, comprehensive set of results from the sequences of images acquired, and identify any issues in the analysis that need to be addressed. Despite the limited and preliminary analysis of the results, both the raw images and the results extracted from the image sections offer some interesting insights on the scattering dynamics of OD that complement the dynamical information from the single-point detection chapter (Chapter 4 Section 4.5.1).

Considering first the analysis from the TOF profiles (Section 5.4.2), the profiles extracted by integrating an RoI closely approximating the detection region of the single-point detection set-up shows that OD scatters off the liquid surfaces probed with qualitatively similar trends and relative magnitude in the survival probability to the results shown in Chapter 4 Section 4.4.1. As previously observed, more OD is lost from scattering off squalene than from squalane, which in turn has a lower signal size than

OD scattered off the inert PFPE surface. The results show that, in principle, survival probabilities comparable to those obtained with the single-point detection results could be obtained using the same methods used to analyse the TOF profiles in Chapter 4 Section 4.4. Furthermore, the angular distribution of scattered OD in the plane of detection could also be used to determine the extent of out-of-plane scattering off the liquid surface, allowing the user to obtain, in principle, the total survival probability of OD over all final scattering angles, unlike the single-point detection method, where the angular distribution of the radicals has to be assumed, resulting in a potential source of systematic error. The calculation of the survival probabilities would, however, require further optimization of the analysis programs in order to systematically account for any attenuation of the incident beam, and obtain well resolved data to determine the global T_{rot} of the scattered species, and in turn, account for differences in the rotational energy distribution of the scattered radicals, as described in sections 4.4.3 and 4.4.4, respectively.

A proof-of-concept analysis of the TOF profiles acquired from smaller RoI placed at different distances from the surface also demonstrated that the most-probable speeds of the scattered radicals can be determined from the images. The speeds reported in Table 5.2 clearly show that, at the higher collision energy, the radicals are scattering with significantly higher than thermal speeds. Furthermore, there are noticeable differences in the speeds depending on the liquid surface probed, where OD scatters off squalane at slower speeds compared to the other surfaces. This complements the dynamical information obtained from the single-point detection set-up (Chapter 4, Section 4.5.1), indicating that the radicals are being scattered with IS-like trajectories. Though the results were obtained from scattering at normal incidence to the surface, and probed on the normal incidence final scattering angle, it would be reasonable to suggest that these differences will also be present at different final scattering angles, and when OD is scattered at 45° incidence. As for the results obtained at the lower collision energy, the speeds obtained are slightly higher but still within error of the predicted Maxwell-Boltzmann most-probable speed for thermal desorption. Any IS-like scattering behaviour is not immediately apparent from the speeds obtained under the conditions probed, and would require a more comprehensive analysis on a wider range of final scattering angles from results obtained from both angles of incidence to definitely rule out the presence of IS-like trajectories on the basis of the speeds alone. This can be achieved by using smaller RoIs positioned at different angles with respect

to the centre of the dosage area on the surface (provided the position of the surface in the image has been determined), which would further improve the spatial resolution of the results.

Additional interesting insights on the scattering dynamics of OD were observed in the raw images, and more specifically in the slices obtained from the image sections taken at selected discharge-probe delays (Sections 5.4.3 and 5.4.4). An initial survey of the results shown between Figures 5.24 and 5.29 reveals that all the slices share two common features, regardless of the condition probed. The first common feature is that OD scatters of the liquid surfaces with a broad angular distribution in the plane of detection. This feature is observed for all scattered OD data, regardless of the carrier gas used, the angle of incidence, the liquids surface or the rotational level probed. A consequence of this is that a substantial proportion of the radicals will scatter out of the plane of detection, which was also confirmed in all of the data analysed (Figure 5.30). The second most common feature is that the overall peak pixel intensity obtained from the slices is always centred within a few pixels from the surface normal axis, regardless of the scattering parameters. There is no evidence of any systematic movement in the position of the peak towards a particular direction on either side of the axis as a function of the distance from the surface and the discharge-probe delay. Small but noticeable differences between the slices obtained at the two different angles of incidence can be observed between sets of data, particularly in the data taken at the higher collision energy, which would suggest that some of the projectiles scatter with IS-like trajectories in a given direction. However, the fact that those differences do not impact the overall distribution of OD signal in the slices suggest that the radicals scattered with IS-like trajectories do not have a strong, directed narrow angular distribution, such as the ones observed by the Minton group at the collision energies of 451-486 kJ mol^{-1} in the centre of mass frame [68, 78, 88-91]. Rather, the angular distribution of the results appears to broadly resemble those observed by Nesbitt *et al.* [244] for NO scattered off liquid surfaces at the moderate collision energy of 11 kJ mol^{-1} , and lack the clear but modest asymmetry identified at the higher one of 84 kJ mol^{-1}.

Though the slices extracted from the images are generally broad, and there is considerable overlap between them after normalizing each to the peak of their signal (Figures 5.17 to 5.22), some systematic differences between the slices were observed for certain parameters through an analysis of the FWHM shown in Figures 5.31 to 5.34.

To determine whether these differences are due to actual dynamical effects of the scattering, the FWHM of incident and scattered OD slices were compared in Figure 5.22. The figure shows that, at the higher collision energy, the scattered OD distribution is significantly broader than the incident OD distribution across comparable slices, whereas at the lower collision energy, there is considerable overlap between the incident and scattered OD slices. The narrow FWHM of incident OD when using the He carrier indicates that the angular distribution of scattered OD will be well-resolved, and thus any dynamical effect as a function of the different parameters tested is expected to be readily apparent from the FWHM analysis. As for the results from the Ne carrier, the overlap between the incident and scattered OD slices suggest that the scattered OD distribution will be poorly resolved, which would make it difficult to identify any systematic differences between the angular distribution as a function of the different parameters tested without further reductions in the width of the incident beam.

With regards to the scattered OD results, when considering first the data obtained at the higher collision energy, the FWHM analysis shows that there are clear differences in how the width of the distribution of OD increases with increasing discharge-probe delay as a function of the angles of incidence. These differences are likely mainly due to a dynamical effect of scattering at 45° incidence compared to normal incidence, though at the lower rotational level probed, the geometry of the dosed area on the liquid surface may also have an effect on the results. There is also some evidence of small effects resulting from differences in the size of the dosed area as a function of the rotational level probed, which, if confirmed via a more refined analysis of the scattered angular distribution, may be due to corresponding differences in the FWHM of the incident beam. This would, in turn, imply that there is a tendency for scattered OD probed at the higher rotational level to have formed from the scattering of incident OD radicals occupying higher rotational levels. Any further analysis of the scattered OD distribution would thus have to take into account the incident OD radicals from all rotational levels, and not simply assume that all of the scattered radicals have emerged from scattering out of the low rotational levels in the incident beam, which would result in the analysis becoming intractably complex. This issue could be resolved in future scattering experiments by using a rotationally colder molecular beam, or ideally a molecular beam with perfect state-selection. When comparing the liquid surfaces, there appears to be no systematic differences between the distribution of OD regardless of the angle of incidence probed, after accounting for the errors in the values. If any

difference is present, is it likely to be subtle, and a more refined analysis will be needed to detect such differences.

With regards to the FWHM analysis using the Ne carrier, the low levels of OD LIF signal in the scattered data have affected the reliability of the cubic spline fit to the raw data, which in many cases have resulted in FWHM values leading to poor linear fits through the data. This makes drawing any solid conclusions much harder than the equivalent results obtained at the higher collision energy. Nevertheless, if the results were confirmed to be true followed a more careful analysis of the data, the analysis would indicate that the differences between sets of data analysed will be small and likely within error, regardless of the angle of incidence, the rotational level probed, or the liquid surface being studied. When considered alongside the data on the scattered OD velocities, and the rotational energy distribution discussed in Chapter 4 Section 4.5.1, the results would suggest that OD scatters with predominantly TD-like trajectories at the lower collision energy.

The above observations point towards the conclusion that all the liquid surfaces tested are rough and corrugated under the conditions used in the scattering experiments. This will have an impact on both the IS and TD-like trajectories with which the radicals scatter off the liquid surface. The highly corrugated surface will promote multiple collisions on the surface, which would increase the proportion of radicals emerging from the surface with TD-like trajectories, especially if they arrive at the surface with low speeds. It will also have a direct broadening effect on the angular distribution of the radicals, even if they scatter with an IS like mechanism. The scattering dynamics of OD radicals may also be affected by the fact that OD is an asymmetric rotor, which would lead to different scattering trajectories compared to those observed from scattering homonuclear or near-homonuclear diatomic molecules such as NO (Figure 5.1) or single atoms such as $O(^3P)$ radicals (Figure 5.2). MD simulations of the scattered projectiles off the liquid surfaces may be required to properly determine the contribution of those two factors to the scattering angle distribution, and thus such considerations are beyond the scope of this preliminary analysis.

5.6 Summary Points

1) OD radicals, generated from the new molecular beam and electric discharge source described in the previous chapter, were scattered from the surfaces of squalane, squalene and PFPE. The radicals were then detected by planar-LIF using the image acquisition set-up described in section 2.7.2. As before, He and Ne were chosen as the carrier gas.

2) A preliminary analysis of the results was conducted from observation of the images themselves and by obtaining TOF profiles and slices from image sections at different distances from the surface within the region of detection. An instrument function correction, accounting for the uneven distribution of the probe beam power across the sheet and differences in the detection sensitivity across the instrument function, was applied to the slices results obtained, and a pixel-to-real space conversion factor was determined

3) The speeds of the scattered OD radicals, extracted from a proof-of-concept analysis of the TOF profiles for scattering from normal incidence and probed at the final scattering angle normal to the surface, indicate that at the higher collision energy, OD scatters with superthermal speeds, whereas as the low collision energy, OD scatters with near-thermal speeds. At the higher collision energy, there are also noticeable differences in the speeds as a function of the liquid surface, which are consistent with but more definitive than the dynamical information obtained in Chapter 4

4) OD radicals appears to scatter off the liquid surfaces with a broad angular distribution, resulting in significant out-of-plane scattering, regardless of the angle of incidence of the projectiles, the liquid surface, the carrier gas and the rotational level probed. There is also no evidence of the overall peak of the slices shifting in any specific direction as a function of the distance from the surface and the discharge-probe delay, suggesting that the radicals scattered with IS-like trajectories are not strongly directed.

5) Both features suggest that all these liquid surfaces are highly corrugated, which promotes multiple collisions on the surface, and makes the surface itself rougher, which increases the width of the angular distribution of IS-like scattering trajectories. The

effect of the surface may also be compounded by the slower incident speeds used in this experimental set-up, compared to the higher incident speeds reported in the literature, and the fact that the OD radical is asymmetric.

6) Subtle differences between the normal and 45° incidence results provide some evidence that the radicals with IS-like trajectories scatter with some directionality from the surface. Some of the results, particularly from squalane and squalene at the higher collision energy, show that the radicals are preferentially scattered in a 'forward' direction close to the specular angle to the surface, as expected.

7) At the lower rotational level probed when using the He carrier, and at both rotational levels for Ne, there are hints that, at early delays, OD scatters towards the same direction of the incident beam with respect to the surface. This effect then disappears at the later delays probed. This result is surprising, and without precedent in other experiments reported in the literature, though further analysis will be required to determine whether it is a dynamical effect from gas-liquid scattering, or an effect of gas-phase collisions with the carrier gas atoms scattered off the liquid surface prior to the arrival of the OD packet.

8) With scattering experiments conducted using the He carrier, subtle differences between the normal incidence slices and the 45° incidence slices show that there is some hint at scattering directionality from the surface within the broad angular distribution, which is expected from IS-type trajectories. This is especially evident when comparing results from normal and 45° incidence. However, there doesn't appear to be any noticeable differences in the angular distribution between the liquids probed.

9) The results obtained from using the Ne carrier, on the other hand, indicate that there is little difference in the distribution of scattered OD as a function of rotational level probed, angle of incidence, and liquid surface. This suggest that scattering with TD-like trajectories is predominant at the lower collision energies, although the presence of OD scattered with IS-like trajectories cannot entirely be ruled out without a comprehensive analysis of the data with improved data analysis programs.

Chapter 6 – Conclusions and Final Remarks

The objective of the work presented in this thesis was to implement and test two new improvements to an experimental set-up designed for scattering OH (or OD for technical reasons) radicals off liquids surfaces. The improvements consist of a molecular beam source, used to scatter rotationally cold OD radicals off the surfaces with a well-defined incident speed and angle of incidence, and an image acquisition set-up, used to image the OD LIF signal from a 2D region in the plane of scattering with a pulsed laser beam expanded into a sheet. Both methods have been successfully implemented and tested, and provide interesting new insights into the scattering dynamics of OD off the surfaces, which will be summarised in this chapter.

6.1 Single-Point Detection Results

The inelastic scattering and potential reactivity of rotationally 'cold' OD with a range of liquid surfaces was studied using the new molecular beam and electric discharge source of radicals. OD was then detected by LIF using a conventional single-point detection set-up. The molecular beam source allowed for the speed of the incident OD radicals, and thus the collision energy with the surface, to be controlled by changing the carrier gas, providing access for the first time to low collision energies comparable to atmospheric conditions.

Direct measurements of the survival probability of OD scattered off the organic liquid surfaces squalane and squalene were obtained at the two collision energies of 7.5 kJ mol^{-1} and 30 kJ mol^{-1} from this experimental set-up, and compared with previous results at even higher collision energies of ~54 kJ mol^{-1} from the 'bulk photolysis' set-up used previously by our group [10-12]. The results from the squalene surface show an increase in the survival probability of OD with increasing collision energy. This confirms previous molecular-dynamics predictions that the vinyl sites in squalene are present at the gas-surface interface, and provides the first direct evidence that uptake of OH (or OD) via addition reactions to the vinyl sites is negatively activated. With regards to squalane, the measured survival probabilities remain the same within error at all three collision energies probed. The latter result is somewhat surprising, as comparisons with equivalent reactions from gas phase scattering studies with large alkanes [219-222] suggest that the increased reactivity at primary C-H sites, which is

subject to higher activation energies and hence expected to be suppressed at lower collision energies, would have decreased the overall survival probability from squalane by more than factor of 2 at the higher collision energies. A possible explanation for this observation is that it may be due to the decrease in reactivity from impulsively scattered OD being compensated by the increase in thermally accommodated radicals at lower collision energies, which then migrate on the surface until they encounter a more reactive secondary or tertiary C-H bond. This would, in turn, imply more generally that the application of simple gas-phase-like Arrhenius behaviour to the temperature dependence of interfacial reactions in atmospheric models may be unreliable. Further experimental and theoretical work will be required to confirm this result. Nevertheless, the essentially flat survival probability of OD off squalane within the range of collision energies tested provides some reassurance to groups invoking and interpreting our previous results [3, 17, 26, 54, 80, 211-216] that their conclusions are unlikely to be affected by the difference in collision energy between our 'bulk photolysis' set-up and their own more atmospherically relevant experimental conditions.

Dynamical information was also obtained from the scattering experiments. At the higher collision energy, OD radicals scatter off the liquid surfaces with clear superthermal translational energies and rotational distributions, indicating the presence of a significant IS-like component. There is also some evidence of IS-like scattering at the lower collision energy, however, its contribution with respect to the TD scattered molecules could not be unambiguously distinguished from the data obtained with the single-point detection set-up.

6.2 Image Acquisition Results

In the second set of scattering experiments, the single-point detection set-up was replaced with the image-acquisition set-up, where OD was detected in a 2D area within the scattering plane via planar-LIF. This set-up represents the first example of pLIF applied to the study of gas-liquid interface collisions, allowing the scattered OD distribution to be resolved both spatially and temporally over a wide range of final scattering angles. From these results, the projectile's speed and final scattering angle distribution can be determined. The scattering experiments from the three liquid surfaces were repeated with the new detection set-up for both collision energies, with the molecular beam arriving at both normal incidence and at 45° with respect to the

surface. Due to time constraints, only a preliminary analysis of the results was conducted on the images obtained, which nevertheless provide some interesting dynamical information that complements the results observed above.

The key feature that all sets of scattering experiments have in common is that OD scatters off all liquid surfaces with a broad angular distribution, regardless of angle of incidence, the collision energy of the projectiles, and the rotational level probed. The scattered OD distribution also appears to be largely symmetric with respect to the surface normal. Furthermore, in all cases, the peak signal density declines strongly as a function of distance from the surface. This indicates that a significant amount of OD radicals scatter out of the plane of detection. The results appear to be in broad agreement with similar angle-resolved gas-liquid scattering experiments with NO at collision energies close to our experimental set-up [244], compared to the modest angular asymmetry observed when NO is scattered at a higher collision energy [244], and the more directed angular distribution observed from scattering O atoms at very high collision energies [68, 78, 88-91, 244], which is expected for IS-like trajectories.

A closer analysis of the data, however, suggests that there are subtle differences in the scattering angle distribution as a function of the angle of incidence and the rotational level probed, though not as a function of the liquid surface. These differences were also more evident at the higher collision energy compared to the lower collision energy. By comparing the incident and scattered OD slices for each of the carrier gases used, it was determined that, at the higher collision energy, the molecular beam dosed a small area of the liquid surface. This suggested that any differences in the angular distribution of the scattered radicals was likely due to dynamical effects of the scattering. At the lower collision energy, however, the area dosed by the molecular beam using the Ne carrier is larger, which makes it difficult to distinguish any real dynamical effect from OD scattered at the lower collision energy. In some of the results, and particularly for PFPE, an apparent preference towards ‘back’-scattering was also observed. This is likely to be an artefact caused by gas-phase collisions of incident OD with the carrier gas from earlier in the gas pulse which has scattered off the liquid surface prior to the arrival of the OD packet, though this would need to be determined more accurately via a more refined analysis of the results.

Further analysis of the results aimed at determining the speed of the scattered OD radicals revealed that, at the higher collision energy, OD scatters with overall superthermal speeds, whereas at the lower collision energy, OD scatters with near thermal speeds. Subtle differences between the speeds as a function of the liquid surface were also observed at the higher collision energy, which were found to be consistent with the dynamical information obtained with the single-point detection set-up. When combined with the information on the angular distribution of OD described above, the results indicate that a noticeable component of scattered OD has some directionality consistent with IS-like trajectories at the higher collision energy, whereas TD-like scattering trajectories are more predominant at the lower collision energy.

6.3 Conclusions and future work

There have been recent reports in the literature of methods aimed at obtaining the speed and angular resolution of scattered projectiles from liquid surfaces and SAMs using spectroscopic techniques, including moving the detector along the direction of the probe beam in more conventional LIF measurements [244], and velocity map imaging [245, 264]. Within this context, the image acquisition set-up shows that planar-LIF can also be applied to gas-liquid scattering experiments, providing a new spectroscopic method that can spatially and temporally resolve the OD LIF signal. This method can be used to gain further insights on the scattering dynamics, including at low collision energies close to atmospheric conditions when combined with the molecular beam experimental set-up.

There are still further improvements to be made to the experimental set-up, the analysis methodology and the custom LabVIEW™ programs used, in order to obtain clearer information from the images. With regards to the scattering experiment itself, the results could be made clearer by using a shorter incident OD packet with lower translational energy spreads and rotationally colder radicals. This may initially be achieved by using a higher performance molecular-beam valve. A further improvement would be to introduce Stark-decelerator technology [265-268] to the experimental set-up, which would provide the ultimate translational energy selection and resolution, and absolute initial state-selection, of the incident projectiles. The spatial resolution of the incident beam could also be improved by adding a second skimmer, acting as a

collimating aperture. This would be especially useful when using Ne or heavier gases as the carrier gas. Finally, a higher-gain image intensifier could provide better discrimination between signal and background noise in the images. As for the analysis programs, one improvement currently under development would allow the user to extract TOF profiles from smaller regions of interest placed at a given final scattering angle and radial distance from the focus point on the surface. This would provide specific angle-dependent information of the scattered OD, including its speed and rotational energy distribution at a given final scattering angle. When studying organic liquid surfaces, the angle-dependent survival probability can also be extracted. Indeed, the information on the angular distribution of the scattered species in the plane of detection would, in principle, allow the user to compensate for scattering out of the plane of detection when determining the overall survival probability and internal energy distribution, obtained by expanding the region of interest to the entire region of detection. This would provide the user with truly integral yields of scattered OD, which would be an advance over the single-point detection method, where the angular distribution of the radicals could introduce systematic errors in the analysis. Monte Carlo and QM/MM simulations are also currently under development in order to gain further insights on the scattering dynamics.

In the future, once the methodology to analyse the images has been established, it would be interesting to use this method to explore the scattering of OH or OD from a range of other liquid surfaces. A particular area of interest for atmospheric chemistry would be to study liquids with functional groups similar to the more polar and oxidized surfaces of secondary organic aerosols [13, 15-17]. Self-assembled monolayers (SAMs) could also be used to create a surface interface densely populated with a specific functional group, allowing it to be determined whether intermolecular interactions between the groups affect the scattering dynamics of the projectiles, and disentangle competing reaction mechanisms with the surface. Another area of interest would be to scatter the projectiles at a range of different incident speeds to explore the collision energy dependence on the scattering dynamics of the projectiles, and the excitation function for reactions of OD with the surface, especially at collision energies lower than the activation energies for a given reaction. Finally, the method could be extended to use other molecular projectiles that can be probed via LIF.

References

1. King, M. E.; Saecker, M. E.; Nathanson, G. M., The thermal roughening of liquid surfaces and its effect on gas-liquid collisions. *J. Chem. Phys.* **1994,** *101* (3), 2539-2547.

2. King, M. E.; Fiehrer, K. M.; Nathanson, G. M.; Minton, T. K., Effects of thermal roughening on the angular distributions of trapping and scattering in gas-liquid collisions. *J. Phys. Chem. A* **1997,** *101* (36), 6556-6561.

3. Lu, J. W.; Day, B. S.; Fiegland, L. R.; Davis, E. D.; Alexander, W. A.; Troya, D.; Morris, J. R., Interfacial energy exchange and reaction dynamics in collisions of gases on model organic surfaces. *Prog. Surf. Sci.* **2012,** *87* (9-12), 221-252.

4. Nathanson, G. M., Molecular beam studies of gas-liquid interfaces. *Annu. Rev. Phys. Chem.* **2004,** *55*, 231-255.

5. Faust, J. A.; Nathanson, G. M., Microjets and coated wheels: versatile tools for exploring collisions and reactions at gas-liquid interfaces. *Chem. Soc. Rev.* **2016,** *45* (13), 3609-3620.

6. Phillips, L. F., Processes at the gas-liquid interface. *Int. Rev. Phys. Chem.* **2011,** *30* (3), 301-333.

7. Davidovits, P.; Kolb, C. E.; Williams, L. R.; Jayne, J. T.; Worsnop, D. R., Mass accommodation and chemical reactions at gas-liquid interfaces. *Chem. Rev.* **2006,** *106* (4), 1323-1354.

8. Tesa-Serrate, M. A.; Smoll, E. J.; Minton, T. K.; McKendrick, K. G., Atomic and molecular collisions at liquid surfaces. *Annu. Rev. Phys. Chem.* **2016,** *67*, 515-540.

9. Faust, J. A.; House, J. E., Physical chemistry of gas-liquid interfaces. *Elsevier*: **2018**.

10. Bagot, P. A. J.; Waring, C.; Costen, M. L.; McKendrick, K. G., Dynamics of inelastic scattering of OH radicals from reactive and inert liquid surfaces. *J. Phys. Chem. C* **2008,** *112* (29), 10868-10877.

11. Waring, C.; King, K. L.; Bagot, P. A. J.; Costen, M. L.; McKendrick, K. G., Collision dynamics and reactive uptake of OH radicals at liquid surfaces of atmospheric interest. *PCCP* **2011,** *13* (18), 8457-8469.

12. King, K. L.; Paterson, G.; Rossi, G. E.; Iljina, M.; Westacott, R. E.; Costen, M. L.; McKendrick, K. G., Inelastic scattering of OH radicals from organic liquids: isolating the thermal desorption channel. *PCCP* **2013,** *15* (31), 12852-12863.

13. Donaldson, D. J.; Vaida, V., The influence of organic films at the air-aqueous boundary on atmospheric processes. *Chem. Rev.* **2006,** *106* (4), 1445-1461.

14. Rudich, Y., Laboratory perspectives on the chemical transformations of organic matter in atmospheric particles. *Chem. Rev.* **2003,** *103* (12), 5097-5124.

15. Finlayson, P.; Pitts, Chemistry of the upper and lower atmosphere : theory, experiments, and applications. *Academic P.*: **2000**.

16. Ellison, G. B.; Tuck, A. F.; Vaida, V., Atmospheric processing of organic aerosols. *J. Geophys. Res.: Atmos.* **1999,** *104* (D9), 11633-11641.

17. Enami, S.; Sakamoto, Y.; Hara, K.; Osada, K.; Hoffmann, M. R.; Colussi, A. J., "Sizing" heterogeneous chemistry in the conversion of gaseous dimethyl sulfide to atmospheric particles. *Environ. Sci. Technol.* **2016,** *50* (4), 1834-1843.

18. Finlayson-Pitts, B. J., Reactions at surfaces in the atmosphere: integration of experiments and theory as necessary (but not necessarily sufficient) for predicting the physical chemistry of aerosols. *PCCP* **2009,** *11* (36), 7760-7779.

19. Laskin, A.; Laskin, J.; Nizkorodov, S. A., Mass spectrometric approaches for chemical characterisation of atmospheric aerosols: critical review of the most recent advances. *Environ. Chem.* **2012,** *9* (3), 163-189.

20. Heard, D. E.; Pilling, M. J., Measurement of OH and HO_2 in the troposphere. *Chem. Rev.* **2003,** *103* (12), 5163-5198.

21. Chapleski, R. C.; Zhang, Y.; Troya, D.; Morris, J. R., Heterogeneous chemistry and reaction dynamics of the atmospheric oxidants, O_3, NO_3, and OH, on organic surfaces. *Chem. Soc. Rev.* **2016,** *45* (13), 3731-46.

22. Yang, Y. D.; Shao, M.; Wang, X. M.; Nolscher, A. C.; Kessel, S.; Guenther, A.; Williams, J., Towards a quantitative understanding of total OH reactivity: A review. *Atmos. Environ.* **2016,** *134*, 147-161.

23. Enami, S.; Hoffmann, M. R.; Colussi, A. J., OH-radical specific addition to glutathione S-Atom at the air-water interface: Relevance to the redox balance of the lung epithelial lining fluid. *J. Phys. Chem. Lett.* **2015,** *6* (19), 3935-3943.

24. Che, D. L.; Smith, J. D.; Leone, S. R.; Ahmed, M.; Wilson, K. R., Quantifying the reactive uptake of OH by organic aerosols in a continuous flow stirred tank reactor. *PCCP* **2009,** *11* (36), 7885-7895.

25. Crowley, J. N.; Ammann, M.; Cox, R. A.; Hynes, R. G.; Jenkin, M. E.; Mellouki, A.; Rossi, M. J.; Troe, J.; Wallington, T. J., Evaluated kinetic and photochemical data for atmospheric chemistry: Volume V - heterogeneous reactions on solid substrates. *Atmos. Chem. Phys.* **2010,** *10* (18), 9059-9223.

26. Houle, F. A.; Hinsberg, W. D.; Wilson, K. R., Oxidation of a model alkane aerosol by OH radical: the emergent nature of reactive uptake. *PCCP* **2015,** *17* (6), 4412-4423.

27. Smith, J. D.; Kroll, J. H.; Cappa, C. D.; Che, D. L.; Liu, C. L.; Ahmed, M.; Leone, S. R.; Worsnop, D. R.; Wilson, K. R., The heterogeneous reaction of hydroxyl radicals with sub-micron squalane particles: a model system for understanding the oxidative aging of ambient aerosols. *Atmos. Chem. Phys.* **2009,** *9* (9), 3209-3222.

28. Atkinson, R., Kinetics of the gas-phase reactions of OH radicals with alkanes and cycloalkanes. *Atmos. Chem. Phys.* **2003,** *3*, 2233-2307.

29. D'Anna, B.; Andresen, W.; Gefen, Z.; Nielsen, C. J., Kinetic study of OH and NO_3 radical reactions with 14 aliphatic aldehydes. *PCCP* **2001,** *3* (15), 3057-3063.

30. George, I. J.; Vlasenko, A.; Slowik, J. G.; Broekhuizen, K.; Abbatt, J. P. D., Heterogeneous oxidation of saturated organic aerosols by hydroxyl radicals: uptake kinetics, condensed-phase products, and particle size change. *Atmos. Chem. Phys.* **2007,** *7* (16), 4187-4201.

31. Mitroka, S.; Zimmeck, S.; Troya, D.; Tanko, J. M., How solvent modulates hydroxyl radical reactivity in hydrogen atom abstractions. *JACS* **2010,** *132* (9), 2907-2913.

32. Zhang, J. X.; Yang, L.; Troya, D., Chemical dynamics simulations of the hydroxyl radical reaction with ethene. *Chin. J. Chem. Phys.* **2013,** *26* (6), 765-773.

33. Ruehl, C. R.; Nah, T.; Isaacman, G.; Worton, D. R.; Chan, A. W. H.; Kolesar, K. R.; Cappa, C. D.; Goldstein, A. H.; Wilson, K. R., The influence of molecular structure and aerosol phase on the heterogeneous oxidation of normal and branched alkanes by OH. *J. Phys. Chem. A* **2013,** *117* (19), 3990-4000.

34. Kolesar, K. R.; Buffaloe, G.; Wilson, K. R.; Cappa, C. D., OH-Initiated heterogeneous oxidation of internally-mixed squalane and secondary organic aerosol. *Environ. Sci. Technol.* **2014,** *48* (6), 3196-3202.

35. Nah, T.; Kessler, S. H.; Daumit, K. E.; Kroll, J. H.; Leone, S. R.; Wilson, K. R., Influence of molecular structure and chemical functionality on the heterogeneous OH-initiated oxidation of unsaturated organic particles. *J. Phys. Chem. A* **2014,** *118* (23), 4106-4119.

36. Nah, T.; Zhang, H. F.; Worton, D. R.; Ruehl, C. R.; Kirk, B. B.; Goldstein, A. H.; Leone, S. R.; Wilson, K. R., Isomeric product detection in the heterogeneous reaction of hydroxyl radicals with aerosol composed of branched and linear unsaturated organic molecules. *J. Phys. Chem. A* **2014,** *118* (49), 11555-11571.

37. Browne, E. C.; Franklin, J. P.; Canagaratna, M. R.; Massoli, P.; Kirchstetter, T. W.; Worsnop, D. R.; Wilson, K. R.; Kroll, J. H., Changes to the chemical composition of soot from heterogeneous oxidation reactions. *J. Phys. Chem. A* **2015,** *119* (7), 1154-1163.

38. Nah, T.; Kessler, S. H.; Daumit, K. E.; Kroll, J. H.; Leone, S. R.; Wilson, K. R., OH-initiated oxidation of sub-micron unsaturated fatty acid particles. *PCCP* **2013,** *15* (42), 18649-18663.

39. Vlasenko, A.; George, I. J.; Abbatt, J. P. D., Formation of volatile organic compounds in the heterogeneous oxidation of condensed-phase organic films by gas-phase OH. *J. Phys. Chem. A* **2008,** *112* (7), 1552-1560.

40. George, I. J.; Chang, R. Y. W.; Danov, V.; Vlasenko, A.; Abbatt, J. P. D., Modification of cloud condensation nucleus activity of organic aerosols by hydroxyl radical heterogeneous oxidation. *Atmos. Environ.* **2009,** *43* (32), 5038-5045.

41. Slade, J. H.; Knopf, D. A., Heterogeneous OH oxidation of biomass burning organic aerosol surrogate compounds: assessment of volatilisation products and the role of OH concentration on the reactive uptake kinetics. *PCCP* **2013,** *15* (16), 5898-5915.

42. Lai, C. Y.; Liu, Y. C.; Ma, J. Z.; Ma, Q. X.; He, H., Degradation kinetics of levoglucosan initiated by hydroxyl radical under different environmental conditions. *Atmos. Environ.* **2014,** *91*, 32-39.

43. Lai, C. Y.; Liu, Y. C.; Ma, J. Z.; Ma, Q. X.; He, H., Laboratory study on OH-initiated degradation kinetics of dehydroabietic acid. *PCCP* **2015,** *17* (16), 10953-10962.

44. Pflieger, M.; Monod, A.; Wortham, H., Heterogeneous oxidation of terbuthylazine by "dark" OH radicals under simulated atmospheric conditions in a flow tube. *Environ. Sci. Technol.* **2013,** *47* (12), 6239-6246.

45. Al Rashidi, M.; Chakir, A.; Roth, E., Heterogeneous oxidation of folpet and dimethomorph by OH radicals: A kinetic and mechanistic study. *Atmos. Environ.* **2014,** *82*, 164-171.

46. Segal-Rosenheimer, M.; Linker, R.; Dubowski, Y., Heterogeneous oxidation of the insecticide cypermethrin as thin film and airborne particles by hydroxyl radicals and ozone. *PCCP* **2011,** *13* (2), 506-517.

47. Liu, Y. C.; Liggio, J.; Harner, T.; Jantunen, L.; Shoeib, M.; Li, S. M., Heterogeneous OH initiated oxidation: A possible explanation for the persistence of organophosphate flame retardants in air. *Environ. Sci. Technol.* **2014,** *48* (2), 1041-1048.

48. Liu, Y.; Huang, L.; Li, S. M.; Harner, T.; Liggio, J., OH-initiated heterogeneous oxidation of tris-2-butoxyethyl phosphate: implications for its fate in the atmosphere. *Atmos. Chem. Phys.* **2014,** *14* (22), 12195-12207.

49. McNeill, V. F.; Yatavelli, R. L. N.; Thornton, J. A.; Stipe, C. B.; Landgrebe, O., Heterogeneous OH oxidation of palmitic acid in single component and internally mixed aerosol particles: vaporization and the role of particle phase. *Atmos. Chem. Phys.* **2008,** *8* (17), 5465-5476.

50. Lambe, A. T.; Zhang, J.; Sage, A. M.; Donahue, N. M., Controlled OH radical production via ozone-alkene reactions for use in aerosol aging studies. *Environ. Sci. Technol.* **2007,** *41* (7), 2357-2363.

51. Lambe, A. T.; Miracolo, M. A.; Hennigan, C. J.; Robinson, A. L.; Donahue, N. M., Effective rate constants and uptake coefficients for the reactions of organic molecular markers (n-alkanes, hopanes, and steranes) in motor oil and diesel primary organic aerosols with hydroxyl radicals. *Environ. Sci. Technol.* **2009,** *43* (23), 8794-8800.

52. Weitkamp, E. A.; Lambe, A. T.; Donahue, N. M.; Robinson, A. L., Laboratory measurements of the heterogeneous oxidation of condensed-phase organic molecular makers for motor vehicle exhaust. *Environ. Sci. Technol.* **2008,** *42* (21), 7950-7956.

53. Bertram, A. K.; Ivanov, A. V.; Hunter, M.; Molina, L. T.; Molina, M. J., The reaction probability of OH on organic surfaces of tropospheric interest. *J. Phys. Chem. A* **2001,** *105* (41), 9415-9421.

54. Moussa, S. G.; Finlayson-Pitts, B. J., Reaction of gas phase OH with unsaturated self-assembled monolayers and relevance to atmospheric organic oxidations. *PCCP* **2010,** *12* (32), 9419-9428.

55. Dilbeck, C. W.; Finlayson-Pitts, B. J., Hydroxyl radical oxidation of phospholipid-coated NaCl particles. *PCCP* **2013,** *15* (24), 9833-9844.

56. Mysak, E. R.; Smith, J. D.; Ashby, P. D.; Newberg, J. T.; Wilson, K. R.; Bluhm, H., Competitive reaction pathways for functionalization and volatilization in the heterogeneous oxidation of coronene thin films by hydroxyl radicals and ozone. *PCCP* **2011,** *13* (16), 7554-7564.

57. Ausfelder, F.; McKendrick, K. G., The dynamics of reactions of $O(^3P)$ atoms with saturated hydrocarbons and related compounds. *Prog. React. Kinet. Mech.* **2000,** *25* (4), 299-370.

58. Kelso, H.; Kohler, S. P. K.; Henderson, D. A.; McKendrick, K. G., Dynamics of the gas-liquid interfacial reaction of $O(^3P)$ atoms with hydrocarbons. *J. Chem. Phys.* **2003,** *119* (19), 9985-9988.

59. Kohler, S. P. K.; Allan, M.; Kelso, H.; Henderson, D. A.; McKendrick, K. G., The effects of surface temperature on the gas-liquid interfacial reaction dynamics of $O(^3P)$ plus squalane. *J. Chem. Phys.* **2005,** *122* (2), 024712.

60. Kohler, S. P. K.; Allan, M.; Costen, M. L.; McKendrick, K. G., Direct gas-liquid interfacial dynamics: The reaction between O(^{3}P) and a liquid hydrocarbon. *J. Phys. Chem. B* **2006,** *110* (6), 2771-2776.

61. Allan, M.; Bagot, P. A. J.; Costen, M. L.; McKendrick, K. G., Temperature dependence of OH yield, translational energy, and vibrational branching in the reaction of O(^{3}P)(g) with liquid squalane. *J. Phys. Chem. C* **2007,** *111* (40), 14833-14842.

62. Allan, M.; Bagot, P. A. J.; Koehler, S. P. K.; Reed, S. K.; Westacott, R. E.; Costen, M. L.; McKendrick, K. G., Dynamics of interfacial reactions between O(^{3}P) atoms and long-chain liquid hydrocarbons. *Phys. Scr.* **2007,** *76* (3), C42-C47.

63. Allan, M.; Bagot, P. A. J.; Westacott, R. E.; Costen, M. L.; McKendrick, K. G., Influence of molecular and supramolecular structure on the gas-liquid interfacial reactivity of hydrocarbon liquids with O(^{3}P) atoms. *J. Phys. Chem. C* **2008,** *112* (5), 1524-1532.

64. Waring, C.; Bagot, P. A. J.; Raeisaenen, M. T.; Costen, M. L.; McKendrick, K. G., Dynamics of the reaction of O(^{3}P) atoms with alkylthiol self-assembled monolayers. *J. Phys. Chem. A* **2009,** *113* (16), 4320-4329.

65. Waring, C.; Bagot, P. A. J.; Bebbington, M. W. P.; Raisanen, M. T.; Buck, M.; Costen, M. L.; McKendrick, K. G., How penetrable are thioalkyl self-assembled monolayers? *J. Phys. Chem. Lett.* **2010,** *1* (13), 1917-1921.

66. Waring, C.; Bagot, P. A. J.; Slattery, J. M.; Costen, M. L.; McKendrick, K. G., O(^{3}P) atoms as a chemical probe of surface ordering in ionic liquids. *J. Phys. Chem. A* **2010,** *114* (14), 4896-4904.

67. Waring, C.; Bagot, P. A. J.; Slattery, J. M.; Costen, M. L.; McKendrick, K. G., O(^{3}P) atoms as a probe of surface ordering in 1-alkyl-3-methylimidazolium-based ionic liquids. *J. Phys. Chem. Lett.* **2010,** *1* (1), 429-433.

68. Wu, B.; Zhang, J.; Minton, T. K.; McKendrick, K. G.; Slattery, J. M.; Yockel, S.; Schatz, G. C., Scattering dynamics of hyperthermal oxygen atoms on ionic liquid surfaces: [emim] [NTf_2] and [C_{12}mim][NTf_2]. *J. Phys. Chem. C* **2010,** *114* (9), 4015-4027.

69. Waring, C.; Bagot, P. A. J.; Costen, M. L.; McKendrick, K. G., Reactive scattering as a chemically specific analytical probe of liquid surfaces. *J. Phys. Chem. Lett.* **2011,** *2* (1), 12-18.

70. Waring, C.; King, K. L.; Costen, M. L.; McKendrick, K. G., Dynamics of the gas-liquid interfacial reaction of O(^{1}D) with a liquid hydrocarbon. *J. Phys. Chem. A* **2011,** *115* (25), 7210-7219.

71. Waring, C.; Bagot, P. A. J.; King, K. L.; Costen, M. L.; McKendrick, K. G., Dynamics of collisions of O(^{1}D) and OH radicals with organic liquid surfaces. *Abstr. Pap. Am. Chem. Soc.* **2011,** *241*, 44-PHYS.

72. Wu, B. H.; Zhang, J. M.; Minton, T. K.; McKendrick, K. G.; Slattery, J. M.; Yockel, S.; Schatz, G. C., Scattering dynamics of hyperthermal oxygen atoms on ionic liquid surfaces: [emim][NTf_2] and [C_{12}mim][NTf_2]. *Abstr. Pap. Am. Chem. Soc.* **2011,** *241*, 43-PHYS.

73. Wu, B. H.; Zhang, J. M.; Minton, T. K.; McKendrick, K. G.; Slattery, J. M.; Yockel, S.; Schatz, G. C., Inelastic and reactive scattering dynamics of hyperthermal oxygen atoms on ionic liquid surfaces: [emim][NTf_2] and [C_{12}mim][NTf_2]. *27th*

International Symposium on Rarefied Gas Dynamics, 2010, Pts One and Two **2011,** *1333*, 516-521.

74. Tesa-Serrate, M. A.; King, K. L.; Paterson, G.; Costen, M. L.; McKendrick, K. G., Site and bond-specific dynamics of reactions at the gas-liquid interface. *PCCP* **2014,** *16* (1), 173-183.

75. Tesa-Serrate, M. A.; Marshall, B. C.; Smoll, E. J.; Purcell, S. M.; Costen, M. L.; Slattery, J. M.; Minton, T. K.; McKendrick, K. G., Ionic liquid-vacuum interfaces probed by reactive atom scattering: Influence of alkyl chain length and anion volume. *J. Phys. Chem. C* **2015,** *119* (10), 5491-5505.

76. Purcell, S. M.; Tesa-Serrate, M. A.; Marshall, B. C.; Bruce, D. W.; D'Andrea, L.; Costen, M. L.; Slattery, J. M.; Smoll, E. J.; Minton, T. K.; McKendrick, K. G., Reactive-atom scattering from liquid crystals at the liquid-vacuum interface: $[C_{12}mim][BF_4]$ and 4-Cyano-4 '-Octylbiphenyl (8CB). *Langmuir* **2016,** *32* (39), 9938-9949.

77. Tesa-Serrate, M. A.; Smoll, E. J.; D'Andrea, L.; Purcell, S. M.; Costen, M. L.; Bruce, D. W.; Slattery, J. M.; Minton, T. K.; McKendrick, K. G., Hiding the headgroup? Remarkable similarity in alkyl coverage of the surfaces of pyrrolidinium- and imidazolium-based ionic liquids. *J. Phys. Chem. C* **2016,** *120* (48), 27369-27379.

78. Marshall, B. C.; Smoll, E. J.; Purcell, S. M.; Costen, M. L.; McKendrick, K. G.; Minton, T. K., Scattering dynamics of oxygen atoms on imidazolium tetrafluoroborate ionic liquid surfaces: Dependence on alkyl chain length. *J. Phys. Chem. C* **2016,** *120* (23), 12472-12483.

79. Vasudev, R.; Zare, R. N.; Dixon, R. N., State-selected photodissociation dynamics - Complete characterization of the OH fragment ejected by the HONO A-approximately state. *J. Chem. Phys.* **1984,** *80* (10), 4863-4878.

80. Enami, S.; Hoffmann, M. R.; Colussi, A. J., Stepwise oxidation of aqueous dicarboxylic acids by gas-phase OH radicals. *J. Phys. Chem. Lett.* **2015,** *6* (3), 527-534.

81. Enami, S.; Hoffmann, M. R.; Colussi, A. J., In situ mass spectrometric detection of interfacial intermediates in the oxidation of RCOOH(aq) by gas-phase OH-radicals. *J. Phys. Chem. A* **2014,** *118* (23), 4130-4137.

82. Roeselova, M.; Vieceli, J.; Dang, L. X.; Garrett, B. C.; Tobias, D. J., Hydroxyl radical at the air-water interface. *JACS* **2004,** *126* (50), 16308-16309.

83. D'Andrea, T. M.; Zhang, X.; Jochnowitz, E. B.; Lindeman, T. G.; Simpson, C. J. S. M.; David, D. E.; Curtiss, T. J.; Morris, J. R.; Ellison, G. B., Oxidation of organic films by beams of hydroxyl radicals. *J. Phys. Chem. B* **2008,** *112* (2), 535-544.

84. Lednovich, S. L.; Fenn, J. B., Absolute evaporation rates for some polar and nonpolar liquids. *AlChE J.* **1977,** *23* (4), 454-459.

85. Scoles, G., Atomic and molecular beam methods. Vol.1, Page 33, Equation 2.19. *OUP*: **1988**.

86. Whitehead, J. C., Molecular beam studies of free-radical processes: Photodissociation, inelastic and reactive collisions. *Rep. Prog. Phys.* **1996,** *59* (8), 993-1040.

87. Blomberg, S.; Zhou, J. F.; Gustafson, J.; Zetterberg, J.; Lundgren, E., 2D and 3D imaging of the gas phase close to an operating model catalyst by planar laser induced fluorescence. *J. Phys.: Condens. Matter* **2016,** *28* (45), 453002.

88. Garton, D. J.; Minton, T. K.; Alagia, M.; Balucani, N.; Casavecchia, P.; Volpi, G. G., Reactive scattering of ground-state and electronically excited oxygen atoms on a liquid hydrocarbon surface. *Faraday Discuss.* **1997,** *108*, 387-399.

89. Garton, D. J.; Minton, T. K.; Alagia, M.; Balucani, N.; Casavecchia, P.; Volpi, G. G., Comparative dynamics of Cl(^{2}P) and O(^{3}P) interactions with a hydrocarbon surface. *J. Chem. Phys.* **2000,** *112* (13), 5975-5984.

90. Zhang, J. M.; Garton, D. J.; Minton, T. K., Reactive and inelastic scattering dynamics of hyperthermal oxygen atoms on a saturated hydrocarbon surface. *J. Chem. Phys.* **2002,** *117* (13), 6239-6251.

91. Zhang, J. M.; Upadhyaya, H. P.; Brunsvold, A. L.; Minton, T. K., Hyperthermal reactions of O and O_2 with a hydrocarbon surface: Direct C-C bond breakage by O and H-atom abstraction by O_2. *J. Phys. Chem. B* **2006,** *110* (25), 12500-12511.

92. Lipkin, N.; Gerber, R. B.; Moiseyev, N.; Nathanson, G. M., Atom scattering studios of liquid structure and dynamics - Collisions of Xe with a model of squalane. *J. Chem. Phys.* **1994,** *100* (11), 8408-8417.

93. Benjamin, I.; Wilson, M. A.; Pohorille, A.; Nathanson, G. M., Scattering of water from the glycerol liquid-vacuum interface. *Chem. Phys. Lett.* **1995,** *243* (3-4), 222-228.

94. Peng, Y. X.; Liu, L.; Cao, Z.; Li, S.; Mazyar, O. A.; Hase, W. L.; Yan, T. Y., Chemical dynamics simulation of Ne atom scattering off a squalane surface. *J. Phys. Chem. C* **2008,** *112* (51), 20340-20346.

95. Kohler, S. P. K.; Reed, S. K.; Westacott, R. E.; McKendrick, K. G., Molecular dynamics study to identify the reactive sites of a liquid squalane surface. *J. Phys. Chem. B* **2006,** *110* (24), 11717-11724.

96. Bosio, S. B. M.; Hase, W. L., Energy transfer in rare gas collisions with self-assembled monolayers. *J. Chem. Phys.* **1997,** *107* (22), 9677-9686.

97. Yan, T. Y.; Hase, W. L.; Barker, J. R., Identifying trapping desorption in gas-surface scattering. *Chem. Phys. Lett.* **2000,** *329* (1-2), 84-91.

98. Yan, T. Y.; Hase, W. L., Comparisons of models for simulating energy transfer in Ne-atom collisions with an alkyl thiolate self-assembled monolayer. *J. Phys. Chem. B* **2002,** *106* (33), 8029-8037.

99. Yan, T. Y.; Isa, N.; Gibson, K. D.; Sibener, S. J.; Hase, W. L., Role of surface intramolecular dynamics in the efficiency of energy transfer in Ne atom collisions with a *n*-hexylthiolate self-assembled monolayer. *J. Phys. Chem. A* **2003,** *107* (49), 10600-10607.

100. Wick, C. D.; Martin, M. G.; Siepmann, J. I., Transferable potentials for phase equilibria. 4. United-atom description of linear and branched alkenes and alkylbenzenes. *J. Phys. Chem. B* **2000,** *104* (33), 8008-8016.

101. Isa, N.; Gibson, K. D.; Yan, T.; Hase, W.; Sibener, S. J., Experimental and simulation study of neon collision dynamics with a 1-decanethiol monolayer. *J. Chem. Phys.* **2004,** *120* (5), 2417-2433.

102. Nogueira, J. J.; Vazquez, S. A.; Mazyar, O. A.; Hase, W. L.; Perkins, B. G., Jr.; Nesbitt, D. J.; Martinez-Nunez, E., Dynamics of CO_2 scattering off a perfluorinated self-assembled monolayer. Influence of the incident collision energy, mass effects, and use of different surface models. *J. Phys. Chem. A* **2009,** *113* (16), 3850-3865.

103. Martinez-Nunez, E.; Rahaman, A.; Hase, W. L., Chemical dynamics simulations of CO_2 scattering off a fluorinated self-assembled monolayer surface. *J. Phys. Chem. C* **2007,** *111* (1), 354-364.

104. Scott Day, B.; Morris, J. R.; Troya, D., Classical trajectory study of collisions of Ar with alkanethiolate self-assembled monolayers: Potential-energy surface effects on dynamics. *J. Chem. Phys.* **2005,** *122* (21), 214712.

105. Alexander, W. A.; Troya, D., Theoretical study of the Ar-, Kr-, and Xe-CH_4, -CF_4 intermolecular potential-energy surfaces. *J. Phys. Chem. A* **2006,** *110* (37), 10834-10843.

106. Sun, L. P.; Hase, W. L., Born-Oppenheimer direct dynamics classical trajectory simulations. *Rev. Comput. Chem.* **2003,** *19*, 79-146.

107. Wiens, J. P.; Nathanson, G. M.; Alexander, W. A.; Minton, T. K.; Lakshmi, S.; Schatz, G. C., Collisions of sodium atoms with liquid glycerol: Insights into solvation and ionization. *JACS* **2014,** *136* (8), 3065-3074.

108. Kim, D.; Schatz, G. C., Theoretical investigation of hyperthermal reactions at the gas-liquid interface: O(^{3}P) and squalane. *J. Phys. Chem. A* **2007,** *111* (23), 5019-5031.

109. Radak, B. K.; Yockel, S.; Kim, D.; Schatz, G. C., Modeling reactive scattering of F(^{2}P) at a liquid squalane interface: A hybrid QM/MM molecular dynamics study. *J. Phys. Chem. A* **2009,** *113* (26), 7218-7226.

110. Yockel, S.; Schatz, G. C., Modeling O(^{3}P) and Ar scattering from the ionic liquid [emim][NO_3] at 5 eV with hybrid QM/MM molecular dynamics. *J. Phys. Chem. B* **2010,** *114* (45), 14241-14248.

111. Li, X.; Schatz, G. C.; Nesbitt, D. J., Anion effects in the scattering of CO2 from the room-temperature ionic liquids [bmim][BF_4] and [bmim][Tf_2N] : Insights from Quantum Mechanics/Molecular Mechanics trajectories. *J. Phys. Chem. B* **2012,** *116* (11), 3587-3602.

112. Yockel, S.; Schatz, G. C., Dynamic QM/MM: A hybrid approach to simulating gas-liquid interactions. In "Multiscale Molecular Methods in Applied Chemistry", Kirchner, B.; Vrabec, J., Eds. **2012;** Vol. 307, 43-67.

113. Troya, D.; Pascual, R. Z.; Schatz, G. C., Theoretical studies of the O(^{3}P) plus methane reaction. *J. Phys. Chem. A* **2003,** *107* (49), 10497-10506.

114. Troya, D.; Pascual, R. Z.; Garton, D. J.; Minton, T. K.; Schatz, G. C., Theoretical studies of the O(^{3}P) plus ethane reaction. *J. Phys. Chem. A* **2003,** *107* (37), 7161-7169.

115. Troya, D.; Schatz, G. C., Theoretical studies of hyperthermal O(^{3}P) collisions with hydrocarbon self-assembled monolayers. *J. Chem. Phys.* **2004,** *120* (16), 7696-7707.

116. Saecker, M. E.; Govoni, S. T.; Kowalski, D. V.; King, M. E.; Nathanson, G. M., Molecular-beam scattering from liquid surfaces. *Science* **1991,** *252* (5011), 1421-1424.

117. King, M. E.; Nathanson, G. M.; Hanninglee, M. A.; Minton, T. K., Probing the microscopic corrugation of liquid surfaces with gas-liquid collisions. *Phys. Rev. Lett.* **1993,** *70* (7), 1026-1029.

118. Saecker, M. E.; Nathanson, G. M., Collisions of protic and aprotic gases with hydrogen-bonding and hydrocarbon liquids. *J. Chem. Phys.* **1993,** *99* (9), 7056-7075.

119. Saecker, M. E.; Nathanson, G. M., Collisions of protic and aprotic gases with a perfluorinated liquid. *J. Chem. Phys.* **1994,** *100* (5), 3999-4005.

120. Nathanson, G. M.; Davidovits, P.; Worsnop, D. R.; Kolb, C. E., Dynamics and kinetics at the gas-liquid interface. *J. Phys. Chem.* **1996,** *100* (31), 13007-13020.

121. Rettner, C. T.; Auerbach, D. J.; Tully, J. C.; Kleyn, A. W., Chemical dynamics at the gas-surface interface. *J. Phys. Chem.* **1996,** *100* (31), 13021-13033.

122. Kenyon, A. J.; McCaffery, A. J.; Quintella, C. M.; Zidan, M. D., Investigation of dynamical processes at liquid surfaces by molecular-scattering. *J. Chem. Soc. Faraday Trans.* **1993,** *89* (21), 3877-3884.

123. Perkins, B. G., Jr.; Nesbitt, D. J., Quantum-state-resolved CO_2 scattering dynamics at the gas-liquid interface: Incident collision energy and liquid dependence. *J. Phys. Chem. B* **2006,** *110* (34), 17126-17137.

124. Cohen, S. R.; Naaman, R.; Sagiv, J., Rotational and state-resolved translational distributions of NO scattered from organized amphiphilic monolayers. *J. Chem. Phys.* **1988,** *88* (4), 2757-2763.

125. Alexander, W. A.; Zhang, J.; Murray, V. J.; Nathanson, G. M.; Minton, T. K., Kinematics and dynamics of atomic-beam scattering on liquid and self-assembled monolayer surfaces. *Faraday Discuss.* **2012,** *157*, 355-374.

126. Cohen, S. R.; Naaman, R.; Balintkurti, G. G., Energy-distribution between spin-orbit states in NO scattered from organized amphiphilic monolayers. *Chem. Phys. Lett.* **1988,** *152* (2-3), 269-273.

127. Kenyon, A. J.; McCaffery, A. J.; Quintella, C. M.; Zidan, M. D., Dynamics of the gas-liquid interface from laser molecular-beam scattering. *Faraday Discuss.* **1993,** *96*, 245-254.

128. Quintella, C. M.; McCaffery, A. J.; Zidan, M. D., Direct observation of the kinetics and dynamics of molecular desorption from liquid surfaces. *Chem. Phys. Lett.* **1993,** *214* (6), 563-568.

129. Perkins, B. G.; Haber, T.; Nesbitt, D. J., Quantum state-resolved energy transfer dynamics at gas-liquid interfaces: IR laser studies of CO_2 scattering from perfluorinated liquids. *J. Phys. Chem. B* **2005,** *109* (34), 16396-16405.

130. Perkins, B. G., Jr.; Nesbitt, D. J., Quantum-state-resolved CO_2 scattering dynamics at the gas-liquid interface: Dependence on incident angle. *J. Phys. Chem. A* **2007,** *111* (31), 7420-7430.

131. Perkins, B. G., Jr.; Nesbitt, D. J., Quantum state-resolved CO_2 collisions at the gas-liquid interface: Surface temperature-dependent scattering dynamics. *J. Phys. Chem. B* **2008,** *112* (2), 507-519.

132. Perkins, B. G.; Nesbitt, D. J., High resolution Dopplerimetry of correlated angular and quantum state-resolved CO_2 scattering dynamics at the gas-liquid interface. *PCCP* **2010,** *12* (42), 14294-14308.

133. Perkins, B. G.; Nesbitt, D. J., Stereodynamics at the gas-liquid interface: Orientation and alignment of CO_2 scattered from perfluorinated liquid surfaces. *J. Phys. Chem. A* **2010,** *114* (3), 1398-1410.

134. Nogueira, J. J.; Vazquez, S. A.; Lourderaj, U.; Hase, W. L.; Martinez-Nunez, E., Chemical dynamics simulations of CO_2 in the ground and first excited bend states colliding with a perfluorinated self-assembled monolayer. *J. Phys. Chem. C* **2010,** *114* (43), 18455-18464.

135. Perkins, B. G.; Nesbitt, D. J., Toward three-dimensional quantum state-resolved collision dynamics at the gas-liquid interface: Theoretical investigation of incident angle. *J. Phys. Chem. A* **2009,** *113* (16), 4613-4625.

136. Zolot, A. M.; Harper, W. W.; Perkins, B. G.; Dagdigian, P. J.; Nesbitt, D. J., Quantum-state resolved reaction dynamics at the gas-liquid interface: Direct absorption detection of HF(v,J) product from F(^{2}P) plus squalane. *J. Chem. Phys.* **2006,** *125* (2), 021101.

137. Andresen, P.; Luntz, A. C., The chemical-dynamics of the reactions of O(^{3}P) with saturated-hydrocarbons .1. Experiment. *J. Chem. Phys.* **1980,** *72* (11), 5842-5850.

138. Zolot, A. M.; Dagdigian, P. J.; Nesbitt, D. J., Quantum-state resolved reactive scattering at the gas-liquid interface: F plus squalane ($C_{30}H_{62}$) dynamics via high-resolution infrared absorption of nascent HF(v,J). *J. Chem. Phys.* **2008,** *129* (19), 194705.

139. Layfield, J. P.; Troya, D., Theoretical study of the dynamics of F plus alkanethiol self-assembled monolayer hydrogen-abstraction reactions. *J. Chem. Phys.* **2010,** *132* (13), 134307.

140. Adusei, G. Y.; Fontijn, A., Comparison of the kinetics of O(^{3}P) reactions with the 4 butenes over wide temperature ranges. *J. Phys. Chem.* **1994,** *98* (14), 3732-3739.

141. Quandt, R.; Min, Z. Y.; Wang, X. B.; Bersohn, R., Reactions of O(^{3}P) with alkenes: H, CH_2CHO, CO, and OH channels. *J. Phys. Chem. A* **1998,** *102* (1), 60-64.

142. Min, Z. Y.; Wong, T. H.; Su, H. M.; Bersohn, R., Reaction of O(^{3}P) with alkenes: Side chain vs double bond attack. *J. Phys. Chem. A* **2000,** *104* (44), 9941-9943.

143. Ringeisen, B. R.; Muenter, A. H.; Nathanson, G. M., Collisions of DCl with liquid glycerol: Evidence for rapid, near-interfacial D -> H exchange and desorption. *J. Phys. Chem. B* **2002,** *106* (19), 4999-5010.

144. Ringeisen, B. R.; Muenter, A. H.; Nathanson, G. M., Collisions of HCl, DCl, and HBr with liquid glycerol: Gas uptake, D -> H exchange, and solution thermodynamics. *J. Phys. Chem. B* **2002,** *106* (19), 4988-4998.

145. Chorny, I.; Benjamin, I.; Nathanson, G. M., Scattering, trapping, and ionization of HCl at the surface of liquid glycerol. *J. Phys. Chem. B* **2004,** *108* (3), 995-1002.

146. Muenter, A. H.; DeZwaan, J. L.; Nathanson, G. M., Collisions of DCl with pure and salty glycerol: Enhancement of interfacial D -> H exchange by dissolved NaI. *J. Phys. Chem. B* **2006,** *110* (10), 4881-4891.

147. Brastad, S. M.; Nathanson, G. M., Molecular beam studies of HCl dissolution and dissociation in cold salty water. *PCCP* **2011,** *13* (18), 8284-8295.

148. Govoni, S. T.; Nathanson, G. M., Exploring the fate of water-molecules striking concentrated sulfuric-acid - scattering versus solvation. *JACS* **1994,** *116* (2), 779-780.

149. Behr, P.; Morris, J. R.; Antman, M. D.; Ringeisen, B. R.; Splan, J. R.; Nathanson, G. M., Reaction and desorption of HCl and HBr following collisions with supercooled sulfuric acid. *Geophys. Res. Lett.* **2001,** *28* (10), 1961-1964.

150. DeZwaan, J. L.; Brastad, S. M.; Nathanson, G. M., Evidence for interfacial $[FDCl]^-$ in collisions between DCl and F^- in KF-glycerol solutions. *J. Phys. Chem. C* **2008,** *112* (39), 15449-15457.

151. DeZwaan, J. L.; Brastad, S. M.; Nathanson, G. M., The roles of salt concentration and cation charge in collisions of Ar and DCl with salty glycerol solutions of NaI and CaI_2. *J. Phys. Chem. C* **2008,** *112* (8), 3008-3017.

152. Dempsey, L. P.; Brastad, S. M.; Nathanson, G. M., Interfacial acid dissociation and proton exchange following collisions of DCl with salty glycerol and salty water. *J. Phys. Chem. Lett.* **2011,** *2* (6), 622-627.

153. Muenter, A. H.; DeZwaan, J. L.; Nathanson, G. M., Interfacial interactions of DO with salty glycerol solutions of KI, NaI, LiI, and NaBr. *J. Phys. Chem. C* **2007,** *111* (41), 15043-15052.

154. Brastad, S. M.; Albert, D. R.; Huang, M. W.; Nathanson, G. M., Collisions of DCl with a solution covered with hydrophobic and hydrophilic ions: Tetrahexylammonium bromide in glycerol. *J. Phys. Chem. A* **2009,** *113* (26), 7422-7430.

155. Alexander, W. A.; Wiens, J. P.; Minton, T. K.; Nathanson, G. M., Reactions of solvated electrons initiated by sodium atom ionization at the vacuum-liquid interface. *Science* **2012,** *335* (6072), 1072-1075.

156. Waclawik, E. R.; Goh, M. C.; Donaldson, D. J., Inelastic scattering of atoms and molecules from liquid crystal surfaces. *J. Chem. Phys.* **1999,** *110* (16), 8098-8103.

157. Kenyon, A. J.; McCaffery, A. J.; Quintella, C. M.; Zidan, M. D., Liquid surface dynamics - A quantum-resolved scattering study. *Chem. Phys. Lett.* **1992,** *190* (1-2), 55-58.

158. Ocko, B. M.; Wu, X. Z.; Sirota, E. B.; Sinha, S. K.; Gang, O.; Deutsch, M., Surface freezing in chain molecules: Normal alkanes. *Phys. Rev. E* **1997,** *55* (3), 3164-3182.

159. Plechkova, N. V.; Seddon, K. R., Applications of ionic liquids in the chemical industry. *Chem. Soc. Rev.* **2008,** *37* (1), 123-150.

160. Lovelock, K. R. J., Influence of the ionic liquid/gas surface on ionic liquid chemistry. *PCCP* **2012,** *14* (15), 5071-5089.

161. Grenoble, Z.; Baldelli, S., Ionic liquids at the gas-liquid and solid-liquid interface - Characterization and properties. In "Supported Ionic Liquids: Fundamentals and Applications", Fehrmann, R.; Riisager, A.; Haumann, M., Eds. *Wiley-V C H Verlag Gmbh*: Weinheim, **2014;** 145-175.

162. Ziemkiewich, M. P.; Zutz, A.; Nesbitt, D. J., Inelastic scattering of radicals at the gas-ionic liquid interface: Probing surface dynamics of [bmim][Cl], [bmim][BF_4], and [bmim][Tf_2N] by rovibronic scattering of NO [$^2\Pi_{1/2}(0.5)$]. *J. Phys. Chem. C* **2012,** *116* (27), 14284-14294.

163. Roscioli, J. R.; Nesbitt, D. J., State-resolved scattering at room-temperature ionic liquid-vacuum interfaces: Anion dependence and the role of dynamic versus equilibrium effects. *J. Phys. Chem. Lett.* **2010,** *1* (4), 674-678.

164. Roscioli, J. R.; Nesbitt, D. J., Quantum state resolved scattering from room-temperature ionic liquids: The role of cation versus anion structure at the interface. *J. Phys. Chem. A* **2011,** *115* (34), 9764-9773.

165. Iwahashi, T.; Nishi, T.; Yamane, H.; Miyamae, T.; Kanai, K.; Seki, K.; Kim, D.; Ouchi, Y., Surface structural study on ionic liquids using metastable atom electron spectroscopy. *J. Phys. Chem. C* **2009,** *113* (44), 19237-19243.

166. Hammer, T.; Reichelt, M.; Morgner, H., Influence of the aliphatic chain length of imidazolium based ionic liquids on the surface structure. *PCCP* **2010,** *12* (36), 11070-11080.

167. Ridings, C.; Lockett, V.; Andersson, G., Effect of the aliphatic chain length on electrical double layer formation at the liquid/vacuum interface in the [$C_n$mim][BF_4] ionic liquid series. *PCCP* **2011,** *13* (38), 17177-17184.

168. Bruce, D. W.; Cabry, C. P.; Lopes, J. N. C.; Costen, M. L.; D'Andrea, L.; Grillo, I.; Marshall, B. C.; McKendrick, K. G.; Minton, T. K.; Purcell, S. M.; Rogers, S.; Slattery, J. M.; Shimizu, K.; Smoll, E.; Tesa-Serrate, M. A., Nanosegregation and structuring in the bulk and at the surface of ionic-liquid mixtures. *J. Phys. Chem. B* **2017,** *121* (24), 6002-6020.

169. Smoll, E. J.; Tesa-Serrate, M. A.; Purcell, S. M.; D'Andrea, L.; Bruce, D. W.; Slattery, J. M.; Costen, M. L.; Minton, T. K.; McKendrick, K. G., Determining the composition of the vacuum-liquid interface in ionic-liquid mixtures. *Faraday Discuss.* **2018,** *206*, 497-522.

170. Gisler, A. W.; Nesbitt, D. J., On probing ions at the gas-liquid interface by quantum state-resolved molecular beam scattering: the curious incident of the cation in the night time. *Faraday Discuss.* **2012,** *157*, 297-305.

171. Lawrence, J. R.; Glass, S. V.; Nathanson, G. M., Evaporation of water through butanol films at the surface of supercooled sulfuric acid. *J. Phys. Chem. A* **2005,** *109* (33), 7449-7457.

172. Lawrence, J. R.; Glass, S. V.; Park, S. C.; Nathanson, G. M., Surfactant control of gas uptake: Effect of butanol films on HCl and HBr entry into supercooled sulfuric acid. *J. Phys. Chem. A* **2005,** *109* (33), 7458-7465.

173. Glass, S. V.; Park, S. C.; Nathanson, G. M., Evaporation of water and uptake of HCl and HBr through hexanol films at the surface of supercooled sulfuric acid. *J. Phys. Chem. A* **2006,** *110* (24), 7593-7601.

174. Burden, D. K.; Johnson, A. M.; Krier, J. M.; Nathanson, G. M., The entry of HCl through soluble surfactants on sulfuric acid: Effects of chain branching. *J. Phys. Chem. B* **2014,** *118* (28), 7993-8001.

175. Scoles, G., Atomic and molecular beam methods. Vol.1. *OUP*: **1988**.

176. Tkáč, O. PhD Thesis: Inelastic scattering of symmetric top molecules. *University of Bristol*, Bristol, **2013**.

177. van Beek, M. C.; ter Meulen, J. J., An intense pulsed electrical discharge source for OH molecular beams. *Chem. Phys. Lett.* **2001,** *337* (4-6), 237-242.

178. Ikejiri, K.; Ohoyama, H.; Nagamachi, Y.; Teramoto, T.; Kasai, T., A highly intense state-selected OH beam source by the pulsed electric DC discharge method. *Chem. Phys. Lett.* **2003,** *379* (3-4), 255-260.

179. Schultz, A.; Zare, R. N.; Cruse, H. W., Laser-Induced Fluorescence - method to measure internal state distribution of reaction products. *J. Chem. Phys.* **1972,** *57* (3), 1354-1355.

180. Cessou, A.; Meier, U.; Stepowski, D., Applications of planar laser induced fluorescence in turbulent reacting flows. *Meas. Sci. Technol.* **2000,** *11* (7), 887-901.

181. Greene, C. H.; Zare, R. N., Determination of product population and alignment using Laser-Induced Fluorescence. *J. Chem. Phys.* **1983,** *78* (11), 6741-6753.

182. Kinsey, J. L., Laser-Induced Fluorescence. *Annu. Rev. Phys. Chem.* **1977,** *28*, 349-372.

183. Dyer, M. J.; Crosley, D. R., Two-dimensional imaging of OH Laser-Induced Fluorescence in a flame. *Opt. Lett.* **1982,** *7* (8), 382-384.

184. Kychakoff, G.; Howe, R. D.; Hanson, R. K.; McDaniel, J. C., Quantitative visualization of combustion species in a plane. *Appl. Opt.* **1982,** *21* (18), 3225-3227.

185. Gorbatšov, S., BSc Dissertation Project: Developing a new molecular beam source of OH radicals to be used in gas-organic liquid interfacial experiments. In *Chemical Dynamics research group data archives*, Heriot Watt University, March 2, **2012**.

186. LabVIEW Profiessional Development System, 13.0; *National Instruments,*: **2013**.

187. Luque, J.; Crosley, D. R. LIFBASE: Database and spectral simulation for diatomic molecules (version 1.6), Version 1.6; *SRI International*: **1999**.

188. Schindelin, J.; Arganda-Carreras, I.; Frise, E.; Kaynig, V.; Longair, M.; Pietzsch, T.; Preibisch, S.; Rueden, C.; Saalfeld, S.; Schmid, B.; Tinevez, J. Y.; White, D. J.; Hartenstein, V.; Eliceiri, K.; Tomancak, P.; Cardona, A., Fiji: an open-source platform for biological-image analysis. *Nat. Methods* **2012,** *9* (7), 676-682.

189. Rueden, C. T.; Schindelin, J.; Hiner, M. C.; DeZonia, B. E.; Walter, A. E.; Arena, E. T.; Eliceiri, K. W., ImageJ2: ImageJ for the next generation of scientific image data. *Bmc Bioinformatics* **2017,** *18*, 529.

190. Droege, A. T.; Engelking, P. C., Supersonic expansion cooling of electronically excited OH radicals. *Chem. Phys. Lett.* **1983,** *96* (3), 316-318.

191. Engelking, P. C., Corona excited supersonic expansion. *Rev. Sci. Instrum.* **1986,** *57* (9), 2274-2277.

192. Bai, H.; Ault, B. S., Matrix-isolation study of the products and reaction pathways in the corona excited discharge of C_6F_6. *Chem. Phys.* **1993,** *169* (3), 317-326.

193. Hain, T. D.; Weibel, M. A.; Backstrand, K. M.; Pope, P. E.; Curtiss, T. J., State-selected beams of hydroxyl radicals via electric hexapole focusing. *Chem. Phys. Lett.* **1996,** *262* (6), 723-728.

194. Ploenes, L.; Haas, D.; Zhang, D. D.; van de Meerakker, S. Y. T.; Willitsch, S., Cold and intense OH radical beam sources. *Rev. Sci. Instrum.* **2016,** *87* (5), 053305.

195. Tang, Q.; Jiang, W. J.; Cheng, Y.; Lin, S.; Lim, T. M.; Xiong, J. R., Generation of reactive species by gas-phase Dielectric Barrier Discharges. *Ind. Eng. Chem. Res.* **2011,** *50* (17), 9839-9846.

196. Luria, K.; Lavie, N.; Even, U., Dielectric barrier discharge source for supersonic beams. *Rev. Sci. Instrum.* **2009,** *80* (10), 104102.

197. Schlachta, R.; Lask, G.; Tsay, S. H.; Bondybey, V. E., Pulsed discharge source of supersonically cooled transient species. *Chem. Phys.* **1991,** *155* (2), 267-274.

198. Xin, J.; Ionescu, I.; Kuffel, D.; Reid, S. A., On the energy dependence of the Zeeman and hyperfine parameters in the $\tilde{A}^2\Sigma^+$ state of OH and OD. *Chem. Phys.* **2003,** *291* (1), 61-72.

199. Thoma, A.; Wurfel, B. E.; Schlachta, R.; Lask, G. M.; Bondybey, V. E., A pulsed discharge source of transients for matrix-isolation spectroscopy. *J. Phys. Chem.* **1992,** *96* (18), 7231-7235.

200. Xin, J.; Fan, H. Y.; Ionescu, I.; Annesley, C.; Reid, S. A., Fluorescence excitation spectroscopy of the $\tilde{A}^2A_1 \leftarrow \tilde{X}^2B_1$ system of jet-cooled NH_2 in the region 2900-4300 Å. *J. Mol. Spectrosc.* **2003,** *219* (1), 37-44.

201. Mukarakate, C.; Tao, C.; Jordan, C. D.; Polik, W. F.; Reid, S. A., Stimulated emission pumping spectroscopy of the $[\tilde{X}]^1A'$ state of CHF. *J. Phys. Chem. A* **2008,** *112* (3), 466-471.

202. Chapman, W. B.; Blackmon, B. W.; Nizkorodov, S.; Nesbitt, D. J., Quantum state-resolved reactive scattering of $F+H_2$ in supersonic jets: Nascent HF(v,J) rovibrational distributions via IR laser direct absorption methods. *J. Chem. Phys.* **1998,** *109* (21), 9306-9317.

203. Rupp, M. T., Research Project: Generation of cold free radicals by electrical discharge. In *Chemical Dynamics research group data archives*, Heriot-Watt University, June 20, **2016**.

204. Lieberman M. A.; Lichtenberg A. J., Principles of plasma discharges and materials processing. 2nd ed.; *Wiley-Interscience*: **2005**.

205. Krishnavedala Paschen curves. https://en.wikipedia.org/wiki/Paschen%27s_law#/media/File:Paschen_curves.svg (accessed 15/01/2018).

206. Scoles, G., Atomic and molecular beam methods. Vol.1, Page 17, Equation 2.2. *OUP*: **1988**.

207. Anderson, D. T.; Davis, S.; Zwier, T. S.; Nesbitt, D. J., An intense slit discharge source of jet-cooled molecular ions and radicals (T_{rot}<30 K). *Chem. Phys. Lett.* **1996,** *258* (1-2), 207-212.

208. Lewandowski, H. J.; Hudson, E. R.; Bochinski, J. R.; Ye, J., A pulsed, low-temperature beam of supersonically cooled free radical OH molecules. *Chem. Phys. Lett.* **2004,** *395* (1-3), 53-57.

209. Bochinski, J. R.; Hudson, E. R.; Lewandowski, H. J.; Ye, J., Cold free-radical molecules in the laboratory frame. *Phys. Rev. A* **2004,** *70* (4), 043410.

210. Radenovic, D. C.; van Roij, A. J. A.; Wu, S. M.; Ter Meulen, J. J.; Parker, D. H.; van der Loo, M. P. J.; Janssen, L. M. C.; Groenenboom, G. C., Photodissociation of vibrationally excited OH/OD radicals. *Mol. Phys.* **2008,** *106* (2-4), 557-572.

211. Renbaum, L. H.; Smith, G. D., Artifacts in measuring aerosol uptake kinetics: the roles of time, concentration and adsorption. *Atmos. Chem. Phys.* **2011,** *11* (14), 6881-6893.

212. Wiegel, A. A.; Liu, M. J.; Hinsberg, W. D.; Wilson, K. R.; Houle, F. A., Diffusive confinement of free radical intermediates in the OH radical oxidation of semisolid aerosols. *PCCP* **2017,** *19* (9), 6814-6830.

213. Socorro, J.; Durand, A.; Temime-Roussel, B.; Gligorovski, S.; Wortham, H.; Quivet, E., The persistence of pesticides in atmospheric particulate phase: An emerging air quality issue. *Sci. Rep.* **2016,** *6*, 7.

214. Arangio, A. M.; Slade, J. H.; Berkemeier, T.; Poschl, U.; Knopf, D. A.; Shiraiwa, M., Multiphase chemical kinetics of OH radical uptake by molecular organic markers of biomass burning aerosols: Humidity and temperature dependence, surface reaction, and bulk diffusion. *J. Phys. Chem. A* **2015,** *119* (19), 4533-4544.

215. Enami, S.; Hoffmann, M. R.; Colussi, A. J., Extensive H-atom abstraction from benzoate by OH-radicals at the air-water interface. *PCCP* **2016,** *18* (46), 31505-31512.

216. Enami, S.; Sakamoto, Y., OH-Radical oxidation of surface-active cis-pinonic acid at the air-water interface. *J. Phys. Chem. A* **2016,** *120* (20), 3578-3587.

217. Bianchini, R. H.; Tesa-Serrate, M. A.; Costen, M. L.; McKendrick, K. G., Collision-energy dependence of the uptake of hydroxyl radicals at atmospherically relevant liquid surfaces. *J. Phys. Chem. C* **2018,** *122* (12), 6648-6660.

218. Levine, R. D., Molecular Reaction Dynamics. *Cambridge University Pr ess*: Cambridge, **2005**.

219. Atkinson, R.; Arey, J., Atmospheric degradation of volatile organic compounds. *Chem. Rev*. **2003,** *103* (12), 4605-4638.

220. Wilson, E. W.; Hamilton, W. A.; Kennington, H. R.; Evans, B.; Scott, N. W.; DeMore, W. B., Measurement and estimation of rate constants for the reactions of hydroxyl radical with several alkanes and cycloalkanes. *J. Phys. Chem. A* **2006,** *110* (10), 3593-3604.

221. Badra, J.; Farooq, A., Site-specific reaction rate constant measurements for various secondary and tertiary H-abstraction by OH radicals. *Combust. Flame* **2015,** *162* (5), 2034-2044.

222. Liu, D. P.; Khaled, F.; Giri, B. R.; Assaf, E.; Fittschen, C.; Farooq, A., H-Abstraction by OH from large branched alkanes: Overall rate measurements and site-specific tertiary rate calculations. *J. Phys. Chem. A* **2017,** *121* (5), 927-937.

223. Laidler, K. J., Chemical Kinetics. 3rd edition ed.; *Harper & Row*: New York, **1987**.

224. Diamanti, A.; Adjiman, C. S.; Piccione, P. M.; Rea, A. M.; Galindo, A., Development of predictive models of the kinetics of a hydrogen abstraction reaction combining quantum-mechanical calculations and experimental data. *Ind. Eng. Chem. Res.* **2017,** *56* (4), 815-831.

225. Loison, J. C.; Daranlot, J.; Bergeat, A.; Caralp, F.; Mereau, R.; Hickson, K. M., Gas-phase kinetics of hydroxyl radical reactions with C_3H_6 and C_4H_8: Product branching ratios and OH addition site-specificity. *J. Phys. Chem. A* **2010,** *114* (51), 13326-13336.

226. Troya, D., Dynamics of collisions of hydroxyl radicals with fluorinated self-assembled monolayers. *Theor. Chem. Acc.* **2012,** *131* (1), 1072.

227. Park, J.-H.; Ivanov, A. V.; Molina, M. J., Effect of relative humidity on OH uptake by surfaces of atmospheric importance. *J. Phys. Chem. A* **2008,** *112* (30), 6968-6977.

228. Molina, M. J.; Ivanov, A. V.; Trakhtenberg, S.; Molina, L. T., Atmospheric evolution of organic aerosol. *Geophys. Res. Lett*. **2004,** *31* (22), L22104.

229. Cooper, P. L.; Abbatt, J. P. D., Heterogeneous interactions of OH and HO_2 radicals with surfaces characteristic of atmospheric particulate matter. *J. Phys. Chem.* **1996,** *100* (6), 2249-2254.

230. George, I. J.; Abbatt, J. P. D., Heterogeneous oxidation of atmospheric aerosol particles by gas-phase radicals. *Nature Chem*. **2010,** *2* (9), 713-722.

231. Hearn, J. D.; Smith, G. D., A mixed-phase relative rates technique for measuring aerosol reaction kinetics. *Geophys. Res. Lett*. **2006,** *33* (17), L17805.

232. Park, J. H.; Christov, C. I.; Ivanov, A. V.; Molina, M. J., On OH uptake by sea salt under humid conditions. *Geophys. Res. Lett*. **2009,** *36*, L02802.

233. Yan, B.; Claus, P. F. H.; van Oorschot, B. G. M.; Gerritsen, L.; Eppink, A.; van de Meerakker, S. Y. T.; Parker, D. H., A new high intensity and short-pulse molecular beam valve. *Rev. Sci. Instrum.* **2013,** *84* (2), 023102.

234. Abad, L.; Bermejo, D.; Herrero, V. J.; Santos, J.; Tanarro, I., Performance of a solenoid-driven pulsed molecular-beam source. *Rev. Sci. Instrum.* **1995,** *66* (7), 3826-3832.

235. Shaw, D. G., Hydrocarbons with water and seawater. *Pergamon*: **1989**.

236. Johansson, S. M.; Kong, X. R.; Thomson, E. S.; Hallquist, M.; Pettersson, J. B. C., The dynamics and kinetics of water interactions with a condensed nopinone surface. *J. Phys. Chem. A* **2017,** *121* (35), 6614-6619.

237. Isakson, M. J.; Sitz, G. O., Adsorption and desorption of HCl on ice. *J. Phys. Chem. A* **1999,** *103* (13), 2044-2049.

238. Halfmann, T.; Koensgen, J.; Bergmann, K., A source for a high-intensity pulsed beam of metastable helium atoms. *Meas. Sci. Technol.* **2000,** *11* (10), 1510-1514.

239. Feng, P. X.; Weiner, B., A collimated pulsed supersonic metastable helium atomic beam. *Phys. Scr.* **2007,** *75* (4), 565-571.

240. Ohno, K.; Takami, T.; Mitsuke, K.; Ishida, T., State-resolved collision energy-dependence of penning ionization cross-sections for N_2 and CO_2 by He*2^3S. *J. Chem. Phys.* **1991,** *94* (4), 2675-2687.

241. Laidler, K. J., Elementary processes in the radiation chemistry of water. *J. Chem. Phys.* **1954,** *22* (10), 1740-1745.

242. Atkins, Physical chemistry. 6th ed.; *OUP*: **1998**.

243. Harris, K. R., Viscous calibration liquids for self-diffusion measurements. *J. Chem. Eng. Data* **2015,** *60* (12), 3506-3517.

244. Zutz, A.; Nesbitt, D. J., Angle-resolved molecular beam scattering of NO at the gas-liquid interface. *J. Chem. Phys.* **2017,** *147* (5), 054704.

245. Hadden, D. J.; Messider, T. M.; Leng, J. G.; Greaves, S. J., Note: Velocity map imaging the scattering plane of gas surface collisions. *Rev. Sci. Instrum.* **2016,** *87* (10), 106104.

246. Zetterberg, J.; Blomberg, S.; Zhou, J. F.; Gustafson, J.; Lundgren, E., Planar Laser Induced Fluorescence applied to catalysis. In "Operando Research in Heterogeneous Catalysis", Frenken, J.; Groot, I., Eds. *Springer International Publishing Ag*: Cham, **2017;** Vol. 114, 131-149.

247. Hedman, T. D.; Cho, K. Y.; Pfeil, M. A.; Satija, A.; Mongia, H. C.; Groven, L. J.; Lucht, R. P.; Son, S. F., High speed OH PLIF applied to multiphase combustion (Review). *Combust. Explos. Shock Waves* **2016,** *52* (1), 1-13.

248. Alden, M.; Bood, J.; Li, Z. S.; Richter, M., Visualization and understanding of combustion processes using spatially and temporally resolved laser diagnostic techniques. *Proc. Combust. Inst.* **2011,** *33*, 69-97.

249. Kohsehoinghaus, K., Laser techniques for the quantitative detection of reactive intermediates in combustion systems. *Prog. Energy Combust. Sci.* **1994,** *20* (3), 203-279.

250. Eckbreth, A. C., Laser diagnostics for combustion temperature and species. 2nd ed.; *Gordon & Breach*: Amsterdam ; United Kingdom, **1996**.

251. Zhou, J. F.; Pfaff, S.; Lundgren, E.; Zetterberg, J., A convenient setup for Laser-Induced Fluorescence imaging of both CO and CO_2 during catalytic CO oxidation. *Appl. Phys. B-Lasers O.* **2017,** *123* (3), 87.

252. Crimaldi, J. P., Planar laser induced fluorescence in aqueous flows. *Exp. Fluids* **2008,** *44* (6), 851-863.

253. Peterson, B.; Sick, V., Simultaneous flow field and fuel concentration imaging at 4.8 kHz in an operating engine. *Appl. Phys. B-Lasers O.* **2009,** *97* (4), 887-895.

254. Heeger, C.; Bohm, B.; Ahmed, S. F.; Gordon, R.; Boxx, I.; Meier, W.; Dreizler, A.; Mastorakos, E., Statistics of relative and absolute velocities of turbulent non-premixed edge flames following spark ignition. *Proc. Combust. Inst.* **2009,** *32*, 2957-2964.

255. McDonell, V. G.; Samuelsen, G. S., Measurement of fuel mixing and transport processes in gas turbine combustion. *Meas. Sci. Technol.* **2000,** *11* (7), 870-886.

256. Fridell, E.; Westblom, U.; Alden, M.; Rosen, A., Spatially resolved Laser-Induced Fluorescence imaging of OH produced in the oxidation of hydrogen on platinum. *J. Catal.* **1991,** *128* (1), 92-98.

257. Gudmundson, F.; Persson, J. L.; Forsth, M.; Behrendt, F.; Kasemo, B.; Rosen, A., OH gas phase chemistry outside a Pt catalyst. *J. Catal.* **1998,** *179* (2), 420-430.

258. Fridell, E.; Rosen, A.; Kasemo, B., A Laser-Induced Fluorescence study of OH desorption from Pt in H_2O/O_2 and H_2O/H_2 mixtures. *Langmuir* **1994,** *10* (3), 699-708.

259. Fridell, E.; Elg, A. P.; Rosen, A.; Kasemo, B., A Laser-Induced Fluorescence study of OH desorption from Pt(111) During oxidation of hydrogen in O_2 and decomposition of water. *J. Chem. Phys.* **1995,** *102* (14), 5827-5835.

260. Forsth, M.; Gudmundson, F.; Persson, J. L.; Rosen, A., The influence of a catalytic surface on the gas-phase combustion of H_2+O_2. *Combust. Flame* **1999,** *119* (1-2), 144-153.

261. Gudmundson, F.; Fridell, E.; Rosen, A.; Kasemo, B., Evaluation of OH desorption rates from Pt using spatially-resolved imaging of Laser-Induced Fluorescence. *J. Phys. Chem.* **1993,** *97* (49), 12828-12834.

262. Greenaway, A.; Lee, D., Fused Silica Lens Analysis. In *Chemical Dynamics research group data archives*, Heriot Watt University, July 28, **2011**.

263. Atkins, P. W.; Atkins, P. W. P. c.; De Paula, J., Atkins' Physical chemistry, Page 820, Equation 24.8. 7th ed. / Peter Atkins, Julio de Paula. ed.; *Oxford University Press*: Oxford, **2002**.

264. Hoffman, C. H.; Nesbitt, D. J., Quantum state resolved 3D Velocity Map Imaging of surface scattered molecules: Incident energy effects in HCl plus self-assembled monolayer collisions. *J. Phys. Chem. C* **2016,** *120* (30), 16687-16698.

265. van de Meerakker, S. Y. T.; Vanhaecke, N.; Meijer, G., Stark deceleration and trapping of OH radicals. In "Annu. Rev. Phys. Chem.", *Annual Reviews*: Palo Alto, **2006;** Vol. 57, 159-190.

266. Vogels, S. N.; Gao, Z.; van de Meerakker, S. Y. T., Optimal beam sources for Stark decelerators in collision experiments: a tutorial review. *EPJ Tech. Instrum.* **2015,** *2* (1), 12.

267. Onvlee, J.; Vogels, S. N.; van de Meerakker, S. Y. T., Unraveling cold molecular collisions: Stark decelerators in crossed-beam experiments. *ChemPhysChem* **2016,** *17* (22), 3583-3595.

268. Haas, D.; Scherb, S.; Zhang, D. D.; Willitsch, S., Optimizing the density of Stark decelerated radicals at low final velocities: a tutorial review. *EPJ Tech. Instrum.* **2017,** *4* (1), 6.

Appendix A– Publications

A.1 Published papers

- Bianchini, R. H.; Tesa-Serrate, M. A.; Costen, M. L.; McKendrick, K. G., Collision-energy dependence of the uptake of hydroxyl radicals at atmospherically relevant liquid surfaces. *Journal of Physical Chemistry C* **2018,** *122* (12), 6648-6660.

A.2 Papers in preparation

- Roman, M. J.; Bianchini, R. H.; Costen, M. L.; McKendrick, K. G., 2D LIF imaging of gas-liquid scattering of OH from liquid surfaces.